TECHNISCHE UNIVERSITÄT MÜNCHEN
INGENIEURFAKULTÄT BAU GEO UMWELT
LEHRSTUHL FÜR INGENIEURGEOLOGIE

Geophysical and engineering geological karst reconnaissance on the Swabian Alb high plain, new line Wendlingen–Ulm, southwestern Germany

Constantin Prins

Vollständiger Abdruck der von der Ingenieurfakultät Bau Geo Umwelt der Technischen Universität München zur Erlangung des akademischen Grades eines Doktors der Ingenieurwissenschaften genehmigten Dissertation.

Vorsitzender: Prof. Dr.-Ing. Christoph Gehlen

Prüfer der Dissertation:

1. Prof. Dr. rer. nat. habil. Kurosch Thuro
2. Prof. Dr. rer. nat. Michael Krautblatter
3. Prof. Dr.-Ing. Roberto Cudmani

Die Dissertation wurde am 19.07.2018 bei der Technischen Universität München eingereicht und durch die Ingenieurfakultät Bau Geo Umwelt am 30.11.2018 angenommen.

I. Affidavit (in German)

Ich erkläre an Eides statt, dass ich die bei der Ingenieurfakultät Bau Geo Umwelt der TUM zur Promotionsprüfung vorgelegte Arbeit mit dem Titel *Geophysical and engineering geological karst reconnaissance on the Swabian Alb high plain, new line Wendlingen–Ulm, southwestern Germany* in München am Lehrstuhl für Ingenieurgeologie unter der Anleitung und Betreuung durch Univ.-Prof. Dr. habil. Kurosch Thuro ohne sonstige Hilfe erstellt und bei der Abfassung nur die gemäß § 6 Ab. 6 und 7 Satz 2 angebotenen Hilfsmittel benutzt habe.

_____

München, 19.07.2018

II. Acknowledgments (in German)

Die vorliegende Dissertation entstand auf Anregung von Univ.-Prof. Dr. rer. nat. habil. Kurosch Thuro in den Jahren 2015 bis 2018 am Lehrstuhl für Ingenieurgeologie der Technischen Universität München. Ihm gegenüber möchte ich meinen ganz besonderen Dank zum Ausdruck bringen – für seine große und stets fortlaufende Unterstützung, für sein reges Interesse am Werdegang dieser Arbeit sowie dessen wertvolle Anregungen und stete Diskussionsbereitschaft. Er war mir ein vortrefflicher Doktorvater. Herrn Prof. Dr. Kurosch Thuro danke ich außerdem zusammen mit Herrn Univ.-Prof. Dr. rer. nat. Michael Krautblatter (TU München) für deren tatkräftige Mitarbeit bei der Datenerhebung im Projektgebiet. Bei Herrn Prof. Dr. Michael Krautblatter bedanke ich mich ferner für kritische Diskussionen und die zur Verfügung gestellte Zeit, die er unter anderem für das Startgespräch bei der DB Projekt Stuttgart–Ulm GmbH investiert hat.

Diese Arbeit wäre nicht entstanden ohne das wohlwollende Entgegenkommen der DB Projekt Stuttgart–Ulm GmbH. Herrn Dr.-Ing. Stefan Kielbassa und Herrn M.Eng. André Reinhardt (NBS Wendlingen–Ulm, Projektabschnitt 7, PFA 2.3 / 2.4 / 2.5a1) bin ich zu großem Dank verpflichtet, insbesondere für deren Zustimmung bezüglich der Verwendung der Projektunterlagen, der Ausführung von Messungen auf der Baustelle und der Veröffentlichung aller Ergebnisse.

Herrn Dipl.-Geol. Uwe Kaufmann und Herrn M.Sc. Dominik Spitzenberger (Bauüberwachung NBS Wendlingen–Ulm, PFA 2.3) sowie Herrn M.Sc. Maximilian Wunderle (ARGE Tunnel Albabstieg, PFA 2.4) gilt ein spezieller Dank für die mir zugänglich gemachten Unterlagen, zielführende Diskussionen und uneingeschränkte Hilfe vor Ort.

Bei Herrn Dr.-Ing. Christian Wawrzyniak und Herrn Dipl.-Ing. Marco Meier (CDM Smith Consult GmbH) bedanke ich mich ganz herzlich für die Möglichkeit, mich parallel zur beruflichen Tätigkeit meiner Promotion widmen zu können. Herr Dr.-Ing. Christian Wawrzyniak verdient darüber hinaus meine dankbare Anerkennung für seine Bereiterklärung, mich als mein Mentor zu betreuen, sowie für viele anregende Gespräche.

Anlässlich seiner ausnehmend großen Hilfsbereitschaft bei Datenerhebung und -auswertung, äußerst zahlreicher Fachgespräche und seiner stets konstruktiven Diskussionsfreudigkeit bedanke ich mich vielmals bei Herrn Dipl.-Geophys. Reinhard Schulz (CDM Smith Consult GmbH).

Ferner möchte ich Herrn B.Sc. Lokman Ahmo (CDM Smith Consult GmbH) sowie Herrn Dipl.-Geogr. Philipp Mamot und Frau B.Sc. Julia Stamnitz (TU München) für deren Mithilfe bei der Datengewinnung im Projektgebiet danken.

Mein innigster Dank gebührt meiner langjährigen Lebensgefährtin, Frau B.Eng. Patricia Heichele, die mich nicht nur durch ihre hilfreichen Anregungen bei der Vortrags- und Abbildungsgestaltung, sondern auch ganz allgemein, über die gesamte Doktorandenzeit hinweg, geduldig und einfühlsam unterstützt hat.

Aus vollem Herzen bringe ich schließlich meinen Eltern Sabine und Lodewijk Prins sowie meiner Schwester Gwendolin Prins, die mich ein Leben lang auf jegliche Art und Weise liebevoll begleitet haben, tiefste Dankbarkeit entgegen.

III. Guiding principle (in German)

„Bei der Realisierung von Großbauprojekten sollte neben dem Wohl der Gesellschaft auch immer der nachhaltige Umgang mit unserem Planeten im Vordergrund stehen – denn die Erde ist unser aller Heimat.“

(Constantin Prins 2018)

IV. Abstract

Karstic rock arise from a combination of high rock solubility and well developed secondary (fracture) porosity and can cause a wide range of hazard scenarios that (i) do not or only to a small extent exist in other rock types and that (ii) have a considerable impact on tunnel and underground constructions worldwide. According to the current state of scientific and technical knowledge, the predictability of the spatial distribution and the characteristics of geological defective karst voids and other karstic features underground remains challenging.

On the Swabian Alb high plain, southwestern Germany, the new high-speed railway line Wendlingen–Ulm of the German Railway Company (Deutsche Bahn AG) is currently under construction. 2D / 2.5D electrical resistivity tomography (ERT) measurements were performed at the excavation bottom level in addition to the investigation program of the construction company including microgravimetric and seismic methods. The aim was to (i) explore geological defective karst voids and other karstic features including their geometry and type of filling and to (ii) test the effectiveness of an inverse Wenner-Schlumberger array for geoelectrical karst (void) reconnaissance in a highly heterogeneous karstic environment. Extensive direct probing investigations served for calibration and discussion: 2 exploration drillings, 7 core drillings with 1 camera inspection, 61 destructive drillings with 14 camera inspections and 2 laser scans, 2 trial pits and 1 excavation pit.

The 2D ERT surveys (conducted with Wenner-Schlumberger, Dipole-dipole and inverse Wenner-Schlumberger electrode arrays) in most cases accurately revealed the size, shape and spatial distribution of clayey / loamy deposits (< 60 Ωm) and delineated them from a fractured and/or weathered limestone bedrock (60 – 960 Ωm), respectively. The comparatively low resistivity values of the limestones can be seen as possible geoelectrical indicators of the limestone host rock in karstic environments. Comparative measurements have further shown that the inverse Wenner-Schlumberger array delivered the same results as those obtained from the standard Wenner-Schlumberger array; a larger potential electrode spacing had no negative effect on the resistivity results. Model refinements (meaning the use of model cells with widths of half the unit electrode spacing) produced small near-surface artifacts, which significantly disturbed the data set, respectively; this approach was not expedient in the present research work, for unclear reasons. The adjustment of inversion parameters including the damping factor and flatness filter had no appreciable impact on the apparent resistivity pseudosections.

The 2.5D ERT survey (parallel 2D lines, conducted with an inverse Wenner-Schlumberger electrode array) provided resistivity values of (i) moderately fractured and medium weathered marls and marlstones (7.5 – 120 Ωm), (ii) a coarsely fractured and lowly to medium weathered limestone bedrock (20 – 960 Ωm), (iii) a collapse doline composed of cobbly, blocky limestone fragments embedded in a loamy matrix (15 – 320 Ωm) and of (iv) an air-filled cavity, partly backfilled loosely with stone and other debris (320 – 960 Ωm). It could be concluded that air-filled cavities can be characterized by lower resistivity values than typically expected. Exploring the geometrical and geophysical properties of dolines still remains complex due to their differentiated morphologic properties at different scales. Outside the area of influence of the collapse doline, the

actual limestone bedrock surface was depicted clear and even non-transitional by means of the used inverse Wenner-Schlumberger array.

The 2.5D ERT survey could reliably be used to test the effectiveness of an inverse Wenner-Schlumberger array for exploring the geometry of known air-filled voids; one of three air-filled voids could be derived accurately in location and roughly in size and shape from the ERT profiles. In general, the ERT method gave greater importance to shallow, especially high-resistive anomalies. Based on the findings of the present research work, the use of (i) an inter-electrode spacing of 0.5 m and thus 0.33 times the opening width of construction-relevant voids and (ii) a line spacing of 1 m and thus two times the advised inter-electrode spacing of 0.5 m is recommended, in order to obtain sufficient safety in karst building ground evaluation. As postulated in previous studies for ERT application on bedrock, it was elaborated that the robust inversion routine was more suitable for detecting the limestone bedrock surface and the air-filled voids. The used inverse Wenner-Schlumberger array (applied in the multi-channel system ABEM Terrameter SAS 4000) afforded the same advantages as the standard Wenner-Schlumberger array, but, in addition, reduced the survey time significantly (by a factor of almost 4). If it is ensured that the larger potential electrode spacing has no negative effect on the resistivity results, a combination of an inverse Wenner-Schlumberger and the Dipole-dipole array can thus be recommended for data acquisition in a highly heterogeneous karstic environment, with different geological units/karst features within narrow space.

The bottom line of this research work: The 2D / 2.5D ERT measurements complemented the microgravimetric and seismic results of the previously conducted investigation program of the construction company and provided a reliable and consistent contribution to karst (void) reconnaissance and building ground evaluations in a highly heterogeneous karstic environment like the Swabian Alb high plain, on the new line Wendlingen–Ulm.

V. Zusammenfassung

Verkarstetes Gebirge entsteht durch eine Kombination aus hoher Gesteinslöslichkeit und stark ausgeprägter, sekundärer Porosität und weist eine Vielzahl an unterschiedlichsten Gefährdungsbildern auf, welche nicht oder nur zu einem geringen Anteil in anderen Gesteinstypen vorkommen und weltweit einen erheblichen Einfluss auf Tunnel- und Tiefbauwerke ausüben. Bezogen auf den derzeitigen Stand der Wissenschaft und der Technik, besteht die Schwierigkeit nach wie vor darin, die Geometrie, als auch das Verfüllmaterial von geologisch und bautechnisch relevanten Karsthohlräumen und anderen Karststrukturen exakt zu bestimmen bzw. vorherzusagen.

Auf der Schwäbischen Albhochfläche, Südwestdeutschland, befindet sich derzeit die neue Hochgeschwindigkeits-Bahnstrecke von Wendlingen nach Ulm der Deutschen Bahn AG in der Bauausführung. In Ergänzung zu den bereits ausgeführten Erkundungsmaßnahmen der Baufirma (darunter mikrogravimetrische und seismische Verfahren) wurden geoelektrische Messungen in 2D / 2,5D von der Aushubsohle aus durchgeführt. Ziel war es, geologisch und bautechnisch relevante Karsthohlräume und andere Karststrukturen inkl. deren Geometrie und Verfüllmaterial zu erkunden und die Effektivität einer inversen Wenner-Schlumberger-Konfiguration für die geoelektrische Karst(hohlraum)erkundung in einem stark heterogenen Karstgebiet abzuleiten. Umfangreiche direkte Baugrunderkundungen standen für die Kalibrierung und die anschließende Diskussion zur Verfügung: 2 Erkundungsbohrungen, 7 Kernbohrungen mit 1 Kamerabefahrung, 61 Meisselbohrungen mit 14 Kamerabefahrungen und 2 Laserscans, 2 Schürfe und 1 Baugrubenaushub.

Die 2D geoelektrische Erkundung (ausgeführt mit Wenner-Schlumberger, Dipol-Dipol und inversen Wenner-Schlumberger-Elektrodenkonfigurationen) lieferte in den meisten Fällen präzise die Größe, Form und räumliche Ausdehnung von tonigen / lehmigen Ablagerungen (< 60 Ωm) und grenzte diese jeweils von einem geklüfteten und/oder verwitterten Kalksteinuntergrund (60 – 960 Ωm) ab. Die vergleichsweise niedrigen Resistivitätswerte des Kalksteins können in anderen Karstgebieten als mögliche geoelektrische Indikatoren für ein anstehendes Kalksteingebirge angesehen werden. Vergleichsmessungen haben des Weiteren gezeigt, dass die inverse Wenner-Schlumberger-Konfiguration dieselben Ergebnisse wie die „normale“ Wenner-Schlumberger-Konfiguration geliefert hat – ein größerer Potentialelektrodenabstand hatte keinen negativen Einfluss auf die geoelektrischen Ergebnisse. Verfeinerungen im Modell (d.h. das Verwenden von Zelleinheiten halb so groß wie der verwendete Elektrodenabstand) führten jeweils zu kleinen, oberflächennahen Artefakten, welche den Datensatz erheblich störten – diese Vorgehensweise war in der vorliegenden Forschungsarbeit nicht zielführend, aus bislang noch ungeklärten Gründen. Die Anpassung der Inversionsparameter inkl. des Dämpfungsfaktors und des Ebenheitsfilters hatte keine erkennbare Auswirkung auf die Widerstandstomogramme.

Die 2,5D geoelektrische Erkundung (parallel verlaufende 2D Profile, ausgeführt mit einer inversen Wenner-Schlumberger-Konfiguration) lieferte Resistivitätswerte von geklüfteten und verwitterten Mergeln und Mergelsteinen (7,5 – 120 Ωm), einem grob geklüfteten und gering bis mäßig verwitterten Kalksteinuntergrund (20 – 960 Ωm), einer Versturzdoline bestehend aus steinigen, blockigen Kalksteinbruchstücken in einer tonig-lehmigen Matrix (15 – 320 Ωm) und einem

luftgefüllten Hohlraum, teilweise verstürzt mit losen Steinen und anderem Bodenmaterial (320 – 960 Ωm). Es konnte geschlussfolgert werden, dass luftgefüllte Hohlräume durch niedrigere Resistivitätswerte als üblicherweise erwartet gekennzeichnet sein können. Das Erkunden der geometrischen und geophysikalischen Charakteristika von Dolinen stellt sich aufgrund der differenzierten morphologischen Eigenschaften auf engstem Raum nach wie vor schwierig dar. Außerhalb des Einflussbereichs der Doline wurde die tatsächliche Kalksteinoberfläche mit Hilfe der verwendeten inversen Wenner-Schlumberger-Konfigurationen deutlich und als scharfe Grenzlinie abgebildet.

Die 2,5D geoelektrischen Messungen konnten verlässlich dazu genutzt werden, die Effektivität einer inversen Wenner-Schlumberger-Konfiguration bzgl. der Erkundung der Geometrie von bekannten luftgefüllten Hohlräumen zu untersuchen. Einer von drei luftgefüllten Hohlräumen konnte präzise in seiner Lage und grob in seiner Größe und Form von den geoelektrischen Profilen abgeleitet werden. Generell ließ das geoelektrische Verfahren oberflächennahen, insbesondere hochresistiven Anomalien eine größere Bedeutung zukommen. Auf Grundlage der Erkenntnisse aus der vorliegenden Forschungsarbeit kann die Verwendung eines Elektrodenabstands von 0,5 m und damit 0,33 mal der Öffnungsweite von bautechnisch relevanten Hohlräumen sowie ein Profilabstand von 1 m und damit zwei Mal der angeratene Elektrodenabstand von 0,5 m empfohlen werden, um eine ausreichende Sicherheit in der Karstbaugrundbeurteilung zu gewährleisten. Wie bereits durch frühere geoelektrische Untersuchungen auf felsigem Untergrund postuliert, konnte ferner herausgearbeitet werden, dass das robuste Inversionsverfahren besser dazu geeignet war, die Kalksteinoberfläche und die luftgefüllten Hohlräume zu detektieren. Die verwendete inverse Wenner-Schlumberger-Konfiguration (ausgeführt mit dem mehrkanaligen Messsystem ABEM Terrameter SAS 4000) brachte die gleichen Vorteile mit sich wie die normale Wenner-Schlumberger-Konfiguration, jedoch bei einer nahezu 4-fach reduzierten Erkundungszeit. Sofern sichergestellt ist, dass der größere Potentialelektrodenabstand keinen negativen Einfluss auf die geoelektrischen Ergebnisse ausübt, kann demnach eine Kombination aus der inversen Wenner-Schlumberger-Konfiguration und der Dipol-Dipol-Konfiguration für die Datenerhebung in einem stark heterogenen Karstgebiet, mit unterschiedlichsten geologischen Einheiten/Karststrukturen auf engstem Raum, empfohlen werden.

Das Fazit dieser Forschungsarbeit: Die 2D / 2,5D geoelektrischen Messungen ergänzten die mikrogravimetrischen und seismischen Ergebnisse aus dem vorangegangenen Erkundungsprogramm der Baufirma und leisteten einen belastbaren und konsistenten Beitrag in der Karst(hohlraum)erkundung und der Baugrundbeurteilung in einem stark heterogenen Karstgebiet wie der Schwäbischen Albhochfläche, auf der Neubaustrecke Wendlingen–Ulm.

VI. Table of contents

List of figures

List of tables

1. Introduction

With development of society and economy, many large-scale projects are under construction all over the world, such as high-speed railways, highways, water storage and hydropower stations, energy storage and transportation systems, tunnels, underground mines and other infrastructure constructions. Especially in the past decades, a soaring progress in tunneling and underground construction has taken place. Tunnel construction projects of long distances (> 50 km) and large diameters (> 13 m) are currently planned or realized (RECHLIN et al. 2011: 14). Due to the rapid development of traffic tunnel constructions in mountain areas, many of these projects are located in geologically complex areas. Thus the geological, hydrogeological and geotechnical conditions in tunneling are becoming unprecedentedly complex and a series of environmental and geotechnical problems, such as fault systems, ground subsidence, large overburden, high stresses, rock bursts, collapse, groundwater, high water pressure, high risk of water inflow and mud gushing become more conspicuous and frequent. **Karstic rock**, in particular, can cause a wide range of hazard scenarios that do not or only to a small extent exist in other rock types. Tab. 1 illustrates only some typical **karst hazard scenarios** for tunnel constructions, which can generally be assigned to the three karst key problems "void filled with air", "void filled with water" and "void filled with soil material", whereas a combination thereof is commonly present.

Approximately 20 % of the ice-free land surface is composed of karstifiable rock formations worldwide (FORD & WILLIAMS 2007: 5). In Germany, karstified strata take about 12 % of the total area (www-01). Switzerland is covered with karstic rock by around 20 %, which resulted in various difficulties during tunnel construction (e.g. FILIPPONI et al. 2012: 39ff.). Karstifiable limestone or other soluble rock is present at or near the surface over 25 % of the United States (DAVIES et al. 1984). In western China, more than 52 % of building tunnel cross the limestone karst region, and the geological hazard of karst caused serious influences (XU et al. 2013: 1). Within the Alps, where currently the longest tunnels in the world are under construction or planned (LÜTH et al. 2005: 98, PESENDORFER 2006: 2, WAGNER et al. 2009: 601, FASCHING et al. 2010: 119, GRANDORI et al. 2011, RECHLIN et al. 2011: 14, REHBOCK-SANDER et al. 2014: 551), carbonates and thus karstifiable rocks are even present in all four main geological units: Helvetic, Penninic, Austroalpine and South Alpine (cf. SCHMID et al. 2004).

Against this background, the exploration of geological defective karst voids and other karstic features plays an important role in tunnel construction all over the world (in both driven and cut-and-cover tunneling). According to the current state of scientific and technical knowledge, the predictability of the spatial distribution and the characteristics of karst voids and other karstic features underground remains challenging. This is where the present Ph.D. thesis comes in:

Geophysical and engineering geological karst reconnaissance on the Swabian Alb high plain, new line Wendlingen–Ulm, southwestern Germany.

Tab. 1: Some common hazard scenarios for tunnel constructions in karstic rock (modified and supplemented from FILIPPONI et al. 2012: 43).

Hazard scenario	Karst void filled with air	Karst void filled with water	Karst void filled with soil material	Hazard to the entire construction	Hazard to the environment	Hazard during the construction phase	Hazard during the operation phase
Geological overbreak of several m² due to the heterogeneity of the karst medium and thus mixed-face-conditions	X	X	X	X		X	
Instabilities of tunnel walls, roof and face up to rock bursts, sinkholes and surface collapses	X	X	X	X	X	X	X
Disturbance of ground load-bearing capacity due to differences in rock and soil resistance/stiffness, especially over pinnacles or dolines	X	X	X	X		X	X
Loose rock fall in a nearby, not excavated karst void	X	X	X	X		X	X
Problem for anchoring	X	X	X	X		X	
Lowering of cutterhead (mechanized heading)	X	X	X	X		X	
Sticking together of cutterhead (mechanized heading)			X	X		X	
Jamming of cutterhead (mechanized heading)	X	X	X	X		X	
Bit abrasion (mechanized heading)	X	X	X	X		X	
Problem for tightening of Gripper (mechanized heading)	X	X	X	X		X	
Problem for bedding of lining segment (mechanized heading)	X	X	X	X		X	
Problem for boring/blasting/digging and rock bolting (drill-and-blast heading)	X	X	X	X		X	
Stopping round (drill-and-blast heading)	X	X	X	X		X	
Loose rock fall of soil material			X	X		X	
Instability of excavated sediment fillings			X	X		X	
Loose rock fall of sediment fillings in the rear area			X	X		X	X
Congelifraction due to gelivity of sediment fillings			X	X		X	X
Settlement or erosion of sediment filling			X	X		X	X
Swelling of sediment filling			X	X		X	X
Mud gushing, sudden debris flow of karst sediments		X	X	X		X	X
Water inflow of up to several m³/s, exposure of water pockets		X		X	(X)	X	
Temporary water inflow following heavy rainfall events and/or snowmelt of up to several m³/s, also in the rear area		X		X	(X)	X	X
Permanent water inflow of several m³/s		X		X	(X)	X	X
Hydraulic ground failure due to rising groundwater table and/or high water pressure and/or confined groundwater conditions		X		X	(X)	X	X
Instabilities of tunnel walls, roof and face due to high head water and/or high water pressure		X		X		X	X
Change in rock mass permeability		X		X	X	X	X
Instabilities/settlements at ground surface due to lowering/changes in groundwater table (doline reactivation, initiating doline formation)		X	X		X	X	X
Drying-up of springs, effect on the discharge rate		X			X	X	X
Effect on the water quality and dissolved mineral content		X			X	X	X
New karst void formation along the tunnel's outer shell		X		X			X
Accelerated corrosion through tunnel drainage, concrete corrosion		X		X	X		X
Sintering of tunnel drainage system		X		X			X

This Ph.D. thesis includes the following research questions:

- How reliable can the geometry and the characteristics of karst voids and other karstic features underground be determined by means of electrical resistivity tomography (ERT) measurements?
- To what degree do the ERT results agree (i) with the results gathered from direct probing investigations and (ii) with the microgravimetric and seismic results of the previously conducted investigation program of the construction company?
- How effective and reliable is an inverse Wenner-Schlumberger array, which is yet very rarely used for geoelectrical karst reconnaissance?
- What are the physical resolution limitations of the ERT method in terms of karst (void) reconnaissance in a highly heterogeneous karstic environment?

2. Study site – the Swabian Alb high plain on the new line Wendlingen–Ulm

Presently, the new railway line from Stuttgart to Ulm, part of the new trans-European Main Line from Paris to Budapest (Fig. 1), is under construction in southwestern Germany by the German Railway Company (Deutsche Bahn AG).

Fig. 1: Central European west-east railway main line (DB Projekt Stuttgart–Ulm GmbH © 2015).

The Stuttgart–Ulm rail project is composed of two subsections: Stuttgart–Wendlingen (Stuttgart 21) and the new line Wendlingen–Ulm. The project section Stuttgart–Wendlingen is divided into seven planning sections (PFA), covering the rail junction at Stuttgart, the rearrangement of Stuttgart main station, the Filder station at the airport, the new line from the airport to Wendlingen and associated access lines (EDELHOFF et al. 2015: 16). The construction works comprise altogether 18 bridges, 16 tunnels and culverts. The largest tunnel in this section (PFA 1.2) is named Filder Tunnel with a length of 9,468 m.

The new high-speed railway line Wendlingen–Ulm, the second part of the Stuttgart–Ulm rail project, which is designed for running speeds of up to 250 km/h, has a total length of approximately 60 km with about 50 % running through tunnel constructions (KIELBASSA et al. 2015b: 27). The new line Wendlingen–Ulm is divided into five planning sections: Alb foreland, Alb ascent, Alb high plain and Alb descent (Albvorland, Albaufstieg, Albhochfläche und Albabstieg) and the conversion of Ulm railway station (Appendix A.1). The construction works include altogether 37 bridges and 9 tunnels. The largest Tunnel in this section (PFA 2.2) is the Boßler Tunnel with a length of 8,806 m.

One significant project section on the new line Wendlingen–Ulm is the PFA 2.3 **Alb high plain**, which ranges from line km 53+811 near Hohenstadt over Merklingen and Temmenhausen to line km 75+250 near Dornstadt (Fig. 2, Fig. 3). The approximately 21.4 km long Alb high plain is mainly characterized by open-air line and smaller tunnels. The excavation bottom level on the Alb

high plain is predominantly situated in limestones of the Upper Jurassic (Kimmeridgian, ~ 152.1 – 157.3 Ma), which are primarily affected by karstification and can be classified as slightly to heavily karstified (KIELBASSA et al. 2015a: 130f.).

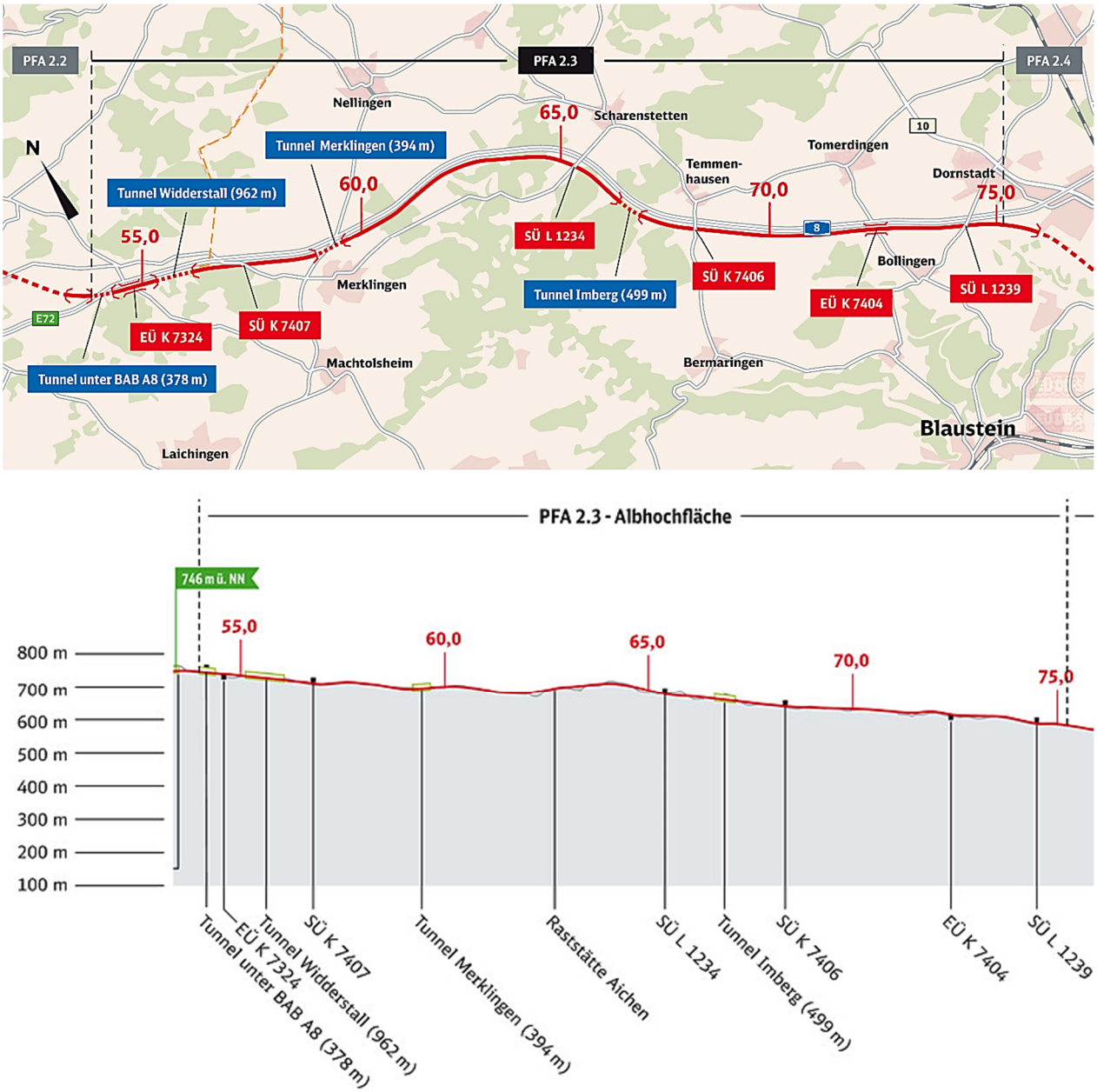

Fig. 2: Overview of the PFA 2.3 Alb high plain with open air lines, tunnels, railway viaducts (EÜ) and road overpasses (SÜ) (in German, DB Projekt Stuttgart–Ulm GmbH © 2015).

Fig. 3: Aerial photograph, 2nd line section, view from Merklingen to Temmenhausen (DB Projekt Stuttgart–Ulm GmbH © 2014).

The Upper Jurassic limestone shows varying karst forms and extents, with karst fractures and cavities of various sizes and shapes (KIELBASSA et al. 2015a: 130f.). The following karst features are particularly expected on the Alb high plain:

- Karst voids with sizes ranging from mm to cm,
- Karst development along bedding planes and joints with opening widths of up to 0.1 m,
- Karst conduits with opening widths of up to 0.1 m,
- Enlarged karst fractures with opening widths of more than 0.1 m,
- Karst shafts at intersections of joints with diameters in the meter range,
- Karst cavities with sizes of several meters, mainly at locations where several fractures or conduits coincide,
- Occasionally karst caves with dimensions of tens of meters (comparison: deep cave of Laichingen (Laichinger Tiefenhöhle) only a few kilometers from the line with an absolute depth of 86 m and a total length of 1348 m (www-02)),
- Dolines, mainly at intersections of fractures in the range of meters to tens of meters,
- Karst depressions above heavily fractured zones with widths in the range of tens to hundreds of meters. Along the line, karst depressions may be encountered for kilometers.

3. Karst hydrogeology and geomorphology – an overview

3.1. Introduction to karst

Karstifiable rock formations are widespread and their surface and near-surface outcrops occupy overall 20 % of the Earth's ice-free continental area and a complete range of altitude and latitude (FORD & WILLIAMS 2007: 5). Karstification itself typically occurs in biogenic, biochemical and chemical sedimentary rocks, predominantly in carbonate rocks, such as limestone, dolomite and marble (JOHNSON & STIEGLITZ 1990, WALTHAM & FOOKES 2003, GOLDSCHEIDER & GÖPPERT 2004, GROVES & MEIMAN 2005, FORD & WILLIAMS 2007, DE WAELE et al. 2009, ZHOU & BECK 2011, ZHAO et al. 2013, THIENERT et al. 2016), but also in evaporites, such as gypsum, anhydrite and halite (BLACK 1997, CALAFORRA & PULIDO-BOSCH 2003, FORD & WILLIAMS 2007, ZHOU & BECK 2011, THIENERT et al. 2016), and rarely in conglomerates (SCHOLZ & STROHMENGER 1999, GÖPPERT et al. 2011), sandstones and quartzites (FILIPPONI et al. 2012). Not all carbonate rocks display distinctive karst landforms and/or significant karst groundwater circulations. This is because some are impure and their insoluble residues clog developing conduits (FORD & WILLIAMS 2007: 5). Thus, estimates from FORD & WILLIAMS (2007: 5) amount that carbonate karst occur over 10 – 15 % of the continental area (Fig. 4); while limestones are usually more karstifiable than dolomites, both are generally more karstifiable than marbles (GOLDSCHEIDER & DREW 2007: 11).

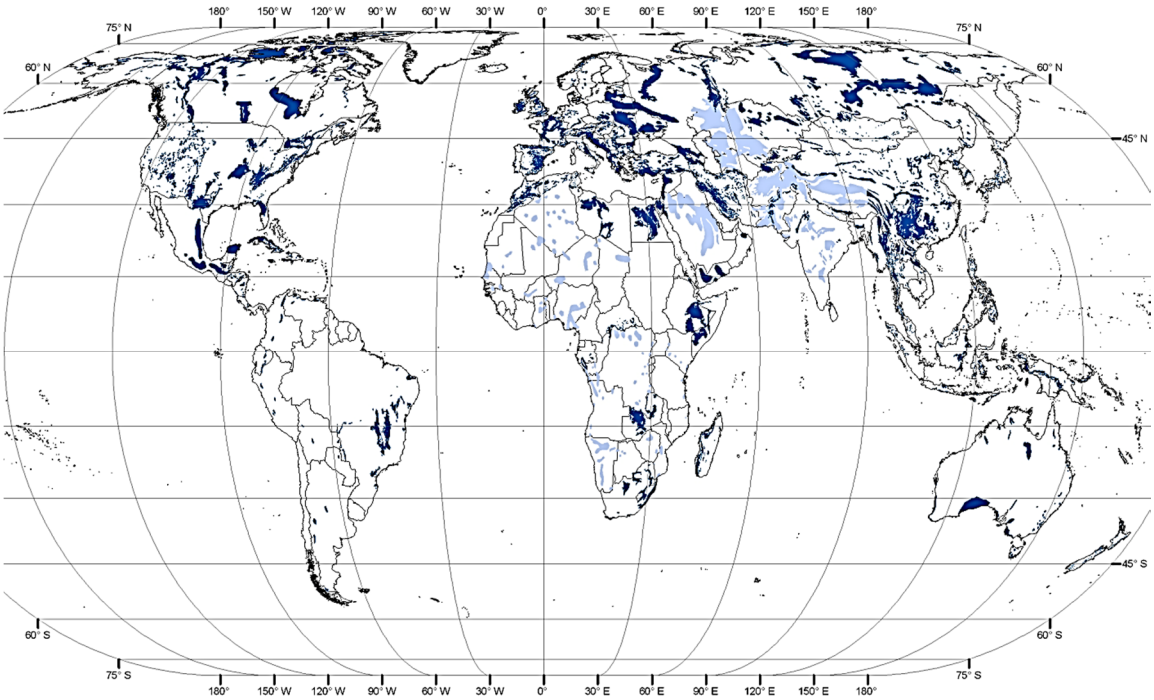

Fig. 4: Global distribution of major outcrops of carbonate rocks. Accuracy varies according to detail of mapping. Generalization occurs in areas with interbedded lithologies and where superficial deposits mask outcrops. A differentiation between areas, where carbonate rocks are relatively pure and continuous, from those, where they are abundant but discontinuous or impure, is established. Most carbonate rocks are susceptible to karstification, although not all are well karstified. Thus, the area of carbonate rock outcrop provides an upper limit on the area of exposed karst terrain. Extensive karstified carbonate rock also exists in subcrop, but is not mapped here (www-03 based on FORD & WILLIAMS 2007: 2, map assembled using GIS on Eckert IV equal-area projection).

The following specifications concerning karst are mainly related to carbonate rocks, in particular limestones. For a detailed description of non-carbonate karst rocks as well as for a fundamental and profound introduction in terms of karst hydrogeology, geomorphology and speleogenesis, reference is made to the appropriate specialized literature (e.g. BONACCI 1987, DREYBRODT 1988, WHITE 1988, SOWERS 1996, KLIMCHOUK et al. 2000, WALTHAM et al. 2005, FORD & WILLIAMS 2007, PALMER 2007).

We may define karst as comprising terrain with distinctive hydrogeology and landforms that arise from a combination of high rock solubility and well developed secondary (fracture) porosity (FORD & WILLIAMS 2007: 1). Substantial rock solubility alone is insufficient to produce karst; the latter also depends on rock structure and lithology (FORD & WILLIAMS 2007: 1). While dense, massive, pure and coarsely fractured rocks develop the best karst, soluble rocks with extremely high primary porosity (30 – 50 %) usually show poorly developed karst features (FORD & WILLIAMS 2007: 1f.). In contrast, soluble rocks with negligible primary porosity (< 1 %) with a subsequently evolved large secondary porosity support excellent karst (FORD & WILLIAMS 2007: 2). Karstification generally begins when the carbonate content exceeds about 75 % (GOLDSCHEIDER & DREW 2007: 12, GOEPPERT et al. 2011: 298).

Karst development is primarily affected by the occurrence of discontinuities (such as joints, faults, bedding planes and beds) within the rock massif, which represent the primary flow paths for groundwater and along which dissolution effects can take place (e.g. KIRALY 1975). Most dissolution occurs at or near the bedrock surface, where it is manifested as surface and subsurface karst landforms (FORD & WILLIAMS 2007: 2), such as poljes, dry and blind valleys, bare rock, karren, enclosed depressions, dolines (sinkholes), fluted rock outcrops, swallow holes, estavelles, springs, highly irregular top of rock profile, dissolutionally enlarged joints or bedding planes, conduits, cavities and caves (BEYNEN 2011: 1, BENSON & YUHR 2016: 3, FORD & WILLIAMS 2007: 1, GOLDSCHEIDER & DREWS 2007: 21, ZHOU & BECK 2011: 9). While some karst features can evolve on a human time scale (e.g. dolines), the dissolution of carbonate rock and void forming processes generally develop over much longer periods of many thousands of years or more (BENSON & YUHR 2016: 3). Sediments or younger rock strata may cover karst features with no visible evidence of their presence at the surface (BENSON & YUHR 2016: 3) and karst groundwater circulation can develop even though surface karst is not apparent (FORD & WILLIAMS 2007: 1). Most groundwater in the majority of karst systems is of meteoric origin, circulating at comparatively shallow depths and with short residence times in the underground (FORD & WILLIAMS 2007: 2). This groundwater circulation causes progressive solutional enlargement of discontinuity and void space and a commensurate increase in permeability (FORD & WILLIAMS 2007: 5). Although karst rocks may have a primary intergranular porosity and a secondary fracture porosity, most water flow through them is transmitted by conduits (tertiary porosity) developed by solution (FORD & WILLIAMS 2007: 5).

3.2. Effects of lithological properties upon karst development

The karstifiability of a rock is controlled by three key factors: (i) the bulk mineralogical-chemical composition, (ii) the mineralogical purity of the rock and (iii) the degree of diagenetic compaction

and cementation (LAMOREAUX et al. 1984, DREYBRODT 1988, WHITE 1988, FORD & WILLIAMS 1989, MORSE & MACKENZIE 1990).

It is a widespread finding that small percentages of non-soluble components, such as clays or silts, significantly decrease the karstifiability of carbonate rocks; limestones that contain more than about 25 % of such impurities form only little karst (GOLDSCHEIDER & DREW 2007: 12, FORD & WILLIAMS 2007: 28). The greatest karst development is usually recognizable in pure, dense, massive, highly-cemented, mechanically strong (unconfined compressive strength: 30 – 100 MPa), thick-bedded and coarsely fractured limestones (WALTHAM & FOOKES 2003: 101, WALTHAM et al. 2005: 305, FORD & WILLIAMS 2007: 1, GOLDSCHEIDER & DREW 2007: 12). In general, the finer a rock's grain size, the more soluble it tends to be due to the increasing area of exposed grain surfaces. However, if the grains are uniform in their size and packing, the finest grained limestones are sometimes less soluble because of smooth surfaces, with exposed grain areas being reduced (FORD & WILLIAMS 2007: 28). The greater the heterogeneity of the grain size, the greater is the roughness of a dissolving surface, which increases solubility, up to a limit (FORD & WILLIAMS 2007: 28f.).

While sedimentologists define primary porosity as that created during deposition of the rock and secondary porosity as that produced subsequently during diagenesis, hydrogeologists determine all types of bulk rock porosity as primary (or matrix) porosity. Fracture (or fissure) porosity, arising from rock folding and faulting, and channel (or conduit) porosity, developing from dissolution along penetrable fissures by circulating groundwaters, are deemed secondary and tertiary, respectively (FORD & WILLIAMS 2007: 29, 104, GOLDSCHEIDER & DREW 2007: 4, BENSON & YUHR 2016: 8). When the primary rock porosity is high, the groundwater flow will tend to be widely diffuse and tertiary porosity development will be minimized (SOWERS 1996: 75, 78f., GOLDSCHEIDER & DREW 2007: 12). In general, hydrogeological and geomorphological active karst terrains are concerned largely or entirely with large-scale, interconnected, non-fabric-selective porosity – meaning penetrable bedding planes and fractures as well as dissolutional channels and caverns – in rocks, where the fabric-selective porosity is low (< 15 %) (FORD & WILLIAMS 2007: 29).

3.3. Effects of lithological frameworks upon karst development

Research carried out by karst scientists during the last 40 years have demonstrated that the development of dissolution voids is not random, but is related to discontinuities within the rock massif (KIRALY 1968, RAUCH & WHITE 1970, WALTHAM 1971, PALMER 1989, KLIMCHOUK & FORD 2000, FILIPPONI & JEANNIN 2006, FILIPPONI 2009). Discontinuities such as bedding planes, joints and faults (often collectively referred to as fractures) pervade karstic rock and host and guide almost all parts of the underground solution conduit networks; they are planar breaks in the rock that can be significantly penetrated and modified (by dissolution or precipitation) by circulating groundwater (FORD & WILLIAMS 2007: 31) and thus promote conduit, cavity and cave development (KIRALY 1975). The minima for effective dissolutional karst genesis barely exceed fracture apertures of 10 μm, probably (FORD & WILLIAMS 2007: 33). Groundwater penetration to initiate karst is often easier at the contact between limestone and adjoining rock with deviating solubility

than it is at bedding planes, joints etc. within the limestone (FORD & WILLIAMS 2007: 31). The hydrogeological function of a three-dimensional fracture network generally depends on the spatial orientation and extension of separating fractures, their frequency, the degree of connectivity between them, their aperture width, their roughness and the existing filling material with its respective hydraulic properties (WITTHÜSER 2002).

Bedding planes are only significant concerning karst development if they are sufficiently open to be penetrable by water under natural pressure gradients or if they are impenetrable and will rupture under mechanical stress (FORD & WILLIAMS 2007: 31). It is widely recognized that the finest karst features require medium to massive bedding; the solutional attack is dispersed, where beds are thin (FORD & WILLIAMS 2007: 31). While penetrable joints and most faults are discrete (i.e. terminate in comparatively short distances), major bedding planes can be regarded to be continuous entities when solution conduits and caves are propagating through them (FORD & WILLIAMS 2007: 31). RAUCH & WHITE (1970), WALTHAM (1971) and PALMER (1989), among others, observed that only a restricted number of karstifiable bedding planes within the limestone series is accountable for conduit and cave development along them. LOWE (1992, 2000) termed such features **inception horizons**, which mainly have a thickness of some centimeters to decimeters and are identifiable (LOWE 1992, FILIPPONI 2009). In recent studies, FILIPPONI (2009) and FILIPPONI et al. (2009) showed quantitatively that 3 to 5 discrete inception horizons guided more than 70 % of the phreatic conduits in the investigated karst systems.

In uniform bedded rocks, most **joints** are oriented perpendicular to bedding planes, but they may be inclined (FORD & WILLIAMS 2007: 32). With reference to VAN DER PLUIJM & MARSHAK (2003: 144ff.), FORD & WILLIAMS (2007: 32) and GOLDSCHEIDER & DREWS (2007: 16f.), it can be summarized that:

(i) parallel joints constitute a **joint set**,
(ii) two or more sets intersecting at regular angles form a **joint system**,
(iii) **rectangular** and **60°/120° systems** are the most frequent, caused by simple tension and shear forces, respectively,
(iv) **release joints**, forming parallel to the topography (often along bedding planes) when the load of the overlying rock masses is removed due to uplift and erosion, favor the development of subhorizontal karst conduits, cavities and caves,
(v) **systematic tectonic joints** are roughly planer joints, always following preferential directions, as they form perpendicular to the minimum principal stress field; they occur as part of a set in which joints parallel one another and are evenly spaced,
(vi) **cross joints** cut across the rock between two systematic joints, are restricted to one or a few beds and terminate at systematic or major joints with a high angle,
(vii) **major** (or **master**) **joints** extend through several or more beds to a depth of some tens of meters and may be several hundred meters to many kilometers long (in thick to massive rocks); they terminate at other master joints and control the orientation of master conduits (DREYBRODT 1988, FORD & WILLIAMS 1989).

Joint fracture openings may be tiny and impenetrable to water, or larger but filled by secondary calcite or quartz, rendering them effectively impermeable (FORD & WILLIAMS 2007: 32). Most master joints exposed at the surface will be penetrable, however, in addition to many cross joints (FORD & WILLIAMS 2007: 32). With increasing depth and under lithostatic pressure, joints are more readily closed to impenetrable dimensions than are bedding planes, reducing their significance in deeper karst systems (FORD & WILLIAMS 2007: 32). However, open fractures can also exist in greater depth, mainly in an extensional stress field environment (VAN DER PLUIJM & MARSHAK 2003: 144ff.), which enables the development of deep karst (GOLDSCHEIDER & DREW 2007: 17); joints are generally well penetrable by percolating waters when under tension (FORD & WILLIAMS 2007: 122). The karstifiability of joints mainly depends on the fracture frequency, extension and aperture width (which in turn are largely proportional to bed thickness) as well as on the orientation to the hydraulic gradient, respectively (FILIPPONI et al. 2012: 56). Joints running parallel to the hydraulic gradient and/or developed parallel to the main stress field of the rock (parallel to σ_1 striking joints) (ERASO 1985) are predominantly karstified, with tendency to larger aperture widths. As with bedding, the best development of karst features is found, where joint spacing is wide to very wide; many caves are rectangular mazes guided rigidly by joint patterns (FORD & WILLIAMS 2007: 33, GOLDSCHEIDER & DREW 2007: 17). Subhorizontal conduits often follow the intersections between bedding planes and joints, while shafts and dolines are often located at the intersections of two vertical joints (GOLDSCHEIDER & DREW 2007: 17). Statistically, most conduits lie at the intersections of joints and bedding planes (FILIPPONI & JEANNIN 2006: 25).

Faults are fractures with some displacement of rock up, down and/or laterally and may be considered to grade into shear fractures or joints, if this displacement is less than about 1 cm (FORD & WILLIAMS 2007: 33). In contrast to nearly vertical faults, **low-angle reversed faults** (such as thrust or décollement faults) are areally extensive and thus emulate very penetrable bedding planes in their capacity to host interconnected solution conduits (FORD & WILLIAMS 2007: 33). **Fracture traces** (or linears, lineaments) are narrow linear trends, manifested on the karstic ground as zones of closely spaced high-angle faults of minor displacement, plus their feathering fractures etc. (FORD & WILLIAMS 2007: 33). While some faults may direct the predominant flow in a groundwater basin or have dolines aligned along them, **large normal** and **reversed faults** are often characterized by low permeability and serve as barriers due to clayey crush fillings (mylonite) or precipitated calcite in them (FORD & WILLIAMS 2007: 33). Instead, there is higher permeability in zones of **feathering fractures**, which frequently guide major karst depressions, whereby the latter may be centered where two traces intersect (FORD & WILLIAMS 2007: 33). Although the overall trend of karst cave development may follow the fault-trace zone, fault planes themselves often control local passage segments, only; in intermediate cases, cave systems extend between fault zones and beyond them (FORD & WILLIAMS 2007: 33).

Folds such as **anticlinal** and **synclinal structures** are associated with tension and compression, respectively, and thus with joint patterns reflecting these conditions (FORD & WILLIAMS 2007: 122). While extensional stress and open fractures occur in the outer parts of folds, compressional stress and closed fractures predominate in the inner parts (GOLDSCHEIDER & DREWS 2007: 14).

Consequently, karstification is often increasing with depth in synclines, whereas the opposite pattern is found in anticlines (RODRÍGUEZ ESTRELLA 2002).

3.4. Dissolution of carbonate rocks in normal meteoric waters

The solubility of carbonate minerals, such as calcite or dolomite, by dissociation in pure deionized water is very low with only 14 mg L^{-1} (as $\mathbf{CaCO_3}$) at 25 °C (FORD & WILLIAMS 2007: 45). Most of the enhanced solubility of carbonate minerals that occurs is due to the hydration of atmospheric $\mathbf{CO_2}$ (ROQUES 1962, 1964), producing carbonic acid:

$$\mathbf{CO_2}(\text{aq}) + \mathbf{H_2O} \Leftrightarrow \mathbf{H_2CO_3^0}\ (\text{carbonic acid})$$

which, in turn, dissociates rapidly to provide H^+:

$$\mathbf{H_2CO_3^0} \Leftrightarrow \mathbf{H^+} + \mathbf{HCO_3^-}$$

Bicarbonate ion may then dissociate to carbonate:

$$\mathbf{HCO_3^-} \Leftrightarrow \mathbf{H^+} + \mathbf{CO_3^{2-}}$$

Additional $\mathbf{H^+}$ may be provided by other acids, while other complexing effects may further increase solubility. The effect of $\mathbf{CO_2}$ from the atmosphere and soil air is predominant in most carbonate karsts, which are created by meteoric waters that can circulate only to comparatively shallow depths underground and, consequently, have not been geothermally heated to a significant extent (FORD & WILLIAMS 2007: 46, BENSON & YUHR 2016: 8).

The pH of water in limestone and dolomite terrains is usually between 6.5 and 8.9; in this range, $\mathbf{HCO_3^-}$ is the predominant species, $\mathbf{CO_3^{2-}}(\text{aq})$ being negligible below pH 8.3 (FORD & WILLIAMS 2007: 47). Based on laboratory experiments, PLUMMER et al. (1978) regard calcite dissolution to be the sum of three forward rate processes:

- the reaction of solid calcite with $\mathbf{H^+}$,

$$\mathbf{CaCO_3}(\text{s}) + \mathbf{H^+} \Leftrightarrow \mathbf{Ca^{2+}} + \mathbf{HCO_3^-}$$

- plus the direct reaction with carbonic acid

$$\mathbf{CaCO_3}(\text{s}) + \mathbf{H_2CO_3}(\text{aq}) \Leftrightarrow \mathbf{Ca^{2+}} + 2\mathbf{HCO_3^-}$$

- and the dissolution in water (a double dissociation)

$$\mathbf{CaCO_3}(\text{s}) + \mathbf{H_2O} \Leftrightarrow \mathbf{Ca^{2+}} + \mathbf{HCO_3^-} + \mathbf{OH^-}$$

This full sequence of the aforementioned reactions is commonly summarized:

$$\mathbf{CaCO_3} + \mathbf{CO_2} + \mathbf{H_2O} \Leftrightarrow \mathbf{Ca^{2+}} + 2\mathbf{HCO_3^-}$$

The solubility of calcite in water equilibrated to the standard atmosphere ($\mathbf{P_{CO_2}}$ = 0.03 %) at 25 °C is 55 mg L^{-1}, increasing to 75 mg L^{-1} at 0 °C. Since the water's temperature usually decreases when passing underground, its solvent potential enhances (FORD & WILLIAMS 2007: 57). Addition of large quantities of ions such as $\mathbf{Na^+}$, $\mathbf{K^+}$ and $\mathbf{Cl^-}$ to a bicarbonate water decreases the activity of $\mathbf{Ca^{2+}}$, $\mathbf{HCO_3^-}$ etc. and thus increases the solubility of calcite and dolomite (FORD & WILLIAMS 2007: 60). In contrast, the solution rate strongly decreases when the solution reaches about 90 % of the saturation of dissolved calcite (e.g. PLUMMER & WIGLEY 1976, DREYBRODT 1988), which, however, favors the long-term solution of calcite in a fissure or conduit, extensively. The solubility of calcite additionally enhances with increasing $\mathbf{Mg^{2+}}$ content (DAVIS et al. 2000). Other chemical impurities in the crystal lattice of calcite and dolomite may further influence solubility (GOLDSCHEIDER & DREW 2007: 10). Increasing the hydrostatic pressure has only negligible effects on dissolved species (FORD & WILLIAMS 2007: 57).

The solution kinetics of calcite dissolution can be expressed as standard rate equation:

$$\frac{\mathrm{d}\mathbf{C}}{\mathrm{d}\mathbf{t}} = \frac{\mathbf{K_C A}}{\mathbf{V}\left(\mathbf{C_{eq}} - \mathbf{C}\right)^{\mathrm{n}}}$$

where $\mathbf{K_C}$ is the surface dissolution rate constant for calcite, $\mathbf{C_{eq}}$ the concentration at saturation (i.e. at the solid surface) and $\mathbf{C}$ the concentration in the bulk flow (BERNER & MORSE 1974, PLUMMER & WIGLEY 1976, PLUMMER et al. 1978, PLUMMER & BUSENBERG 1982). The comprehensive rate equation of the aforementioned three forward rate processes (PLUMMER et al. 1978) is:

$$\mathbf{r} = \mathbf{k}_1 \times \mathbf{a}_{\mathbf{H^+}} + \mathbf{k}_2 \times \mathbf{a}_{\mathbf{H_2CO_3^0}} + \mathbf{k}_3 \times \mathbf{a}_{\mathbf{H_2O}} - \mathbf{k}_4 \times \mathbf{a}_{\mathbf{Ca^{2+}}} \times \mathbf{a}_{\mathbf{HCO_3^-}}$$

where $\mathbf{a}$ represents activity and the three forward rates were fitted as functions of temperature: $\log \mathbf{k}_1$ = 0.98 – 444/T, $\log \mathbf{k}_2$= 2.84 – 217/T and $\log \mathbf{k}_3$= –5.86 – 317/T, with T in °K. The final term expresses the back reaction (FORD & WILLIAMS 2007: 68).

3.5. Water flow through fractured carbonate rocks and network development

Water flow in karst systems is routed underground in channels created by dissolutional widening of fissures. Fissure apertures are very small, initially, offering high resistance to water flow. Early penetration will occur under closed-system conditions with laminar flow, which prohibits eddy diffusion (FORD & WILLIAMS 2007: 72). **Kinetic breakthrough** begins when a fissure or conduit becomes sufficiently enlarged to permit solution kinetics operating throughout its length (WHITE 1977a); this threshold is crossed when fracture apertures exceed about 0.01 m (WHITE 2002). Further enlargement to permit turbulent flow with eddy diffusion may then follow rapidly, accelerating the process of dissolution (FORD & WILLIAMS 2007: 72) and thus the development of channels and conduits. Subsequently, these tertiary pathways can be progressively enlarged by a combination of continuous dissolution, mechanical erosion and transport of rock and soil material associated with groundwater circulation; cavities and caves may develop.

When considering interconnected fissures with solid intervening blocks of rock constituting the matrix being relatively impermeable, information is required about the orientation of fracture

patterns, the fissure frequency (i.e. fracture density), the extent of their interconnectivity, and the size and smoothness of the fracture openings (FORD & WILLIAMS 2007: 112). Where laminar flow conditions exist in the jointed rock, the **volumetric flow rate Q** through a single fracture of unit length represented by two smooth parallel plates separated by a constant distance can be determined from the expression:

$$\mathbf{Q} = \frac{\boldsymbol{\rho}\mathbf{g}\mathbf{w}^3}{12\boldsymbol{\mu}} \times \frac{\mathrm{d}\mathbf{h}}{\mathrm{d}\mathbf{l}}$$

where **ρ** is the fluid density of water, **g** is the gravitational acceleration, **μ** is the dynamic viscosity and d**h**/d**l** is the change of head with distance along the fracture (also termed the hydraulic gradient); while porosity increases linearly with the fracture aperture **w**, permeability increases with the cube of the aperture (FORD & WILLIAMS 2007: 109, 112). The **hydraulic conductivity K** of the fracture can be calculated by:

$$\mathbf{K} = \frac{\boldsymbol{\rho}\mathbf{g}\mathbf{w}^2}{12\boldsymbol{\mu}}$$

with varying values of fluid density and dynamic viscosity for different water temperatures, respectively (FORD & WILLIAMS 2007: 112). For a set of planar fractures, the hydraulic conductivity **K** ($\mathbf{K_x}$, $\mathbf{K_y}$ for horizontal and $\mathbf{K_z}$ for vertical directions) and the permeability **k** may be equivalently derived from:

$$\mathbf{K} = \frac{\boldsymbol{\rho}\mathbf{g}\mathbf{N}\mathbf{w}^3}{12\boldsymbol{\mu}}$$

and

$$\mathbf{k} = \frac{\mathbf{N}\mathbf{w}^3}{12}$$

where **N** is the number of fissures per unit distance across the rock face and **Nw** is the planar porosity (FORD & WILLIAMS 2007: 112). In most well-karstified rock, the vertical hydraulic conductivity $\mathbf{K_z}$, in particular, decreases considerably with depth below the surface, because secondary permeability is usually greatest near the surface (FORD & WILLIAMS 2007: 115). Natural conditions are of course more complex than the aforementioned due to the uneven openness and roughness of fractures and the three-dimensional complexity of fracture patterns (FORD & WILLIAMS 2007: 113).

Concentrated inflows of water sinking underground can be of vertical point-inputs from perforated overlying beds and lateral point-inputs from adjacent impervious rocks; the flow may originate from (i) a retreating overlying caprock, (ii) the updip margin of a stratigraphically lower impermeable formation that is tilted, or (iii) an impermeable rock across a fault boundary (FORD & WILLIAMS 2007: 118). While a perforated impermeable caprock will funnel water underground in much the same way as solution dolines, favoring the development of large shafts beneath, lateral point-inputs are often being derived from large catchment areas and are commonly associated with

major river caves (FORD & WILLIAMS 2007: 118). After the ingress of water underground, flow direction is determined by the direction of the hydraulic gradient, except of local deviations where flow direction is determined by pathways made available by interconnected fissures and pores (FORD & WILLIAMS 2007: 122). Factors that determine the density, size and distribution of voids dictate the potential flow paths and thus control the throughput and storage of water in the karst system (FORD & WILLIAMS 2007: 122). The vertical position of a spring controls the outflow of the karst system, whereby the difference in elevation between the spring and the water table upstream determines the water head and thus the energy available to drive a deep circulation (FORD & WILLIAMS 2007: 118f.).

3.6. Karst hydrographic zones

Karst aquifers are commonly differentiated into the three end-member types granular (or matrix), fracture and conduit, according to the nature of the voids, in which the water is stored and through which it is transmitted (FORD & WILLIAMS 2007: 104). A single karst system can be hydrographically divided into the saturated (or phreatic) zone, the intermittently saturated zone and the unsaturated (or vadose) zone with further subdivisions, respectively (Tab. 2). While the top of the saturated (or phreatic) zone is delimited by the water table, which is the surface defined by the level of free-standing water in fissures and pores, the unsaturated (or vadose) zone is above the water table, where voids in the rock are only partially filled with water, except after heavy rain when some are completely filled (FORD & WILLIAMS 2007: 106f.).

Tab. 2: Subdivisions of the saturated and unsaturated zones (unconfined conditions); not all categories may be present in any given karst and each may be traversed by caves, permanently flooded in the saturated zone (modified after FORD & WILLIAMS 2007: 107).

Karst hydrographic zones	
Unsaturated (vadose) zone	Soil Epikarst (subcutaneous) zone Free-draining percolation (transmission) zone
Intermittently saturated zone	Epiphreatic zone (zone of fluctuation of water table)
Saturated (phreatic) zone	Shallow phreatic zone Deep phreatic (bathyphreatic) zone Stagnant phreatic zone

The **phreatic zone** is strongly karstified and thus hydraulic conductive, whereas its underlying rock, in which dissolution processes are still in an initial phase, is usually less conductive due to the missing conduit network (FILIPPONI et al. 2012: 46). In both the phreatic and the vadose zone, discontinuities such as beddings planes, major joints and faults often operate hydrologically due to their vertical and lateral continuity and thus control the orientation of water flow; however, fault planes can be highly compressed or filled and may considerably interrupt groundwater flow and karst development (FORD & WILLIAMS 2007: 123). Phreatic conduits form in the saturated zone or slightly above (epiphreatic zone) and usually show elliptical cross-sections (expanded either horizontally, oblique or vertically), which are often quite constant along flow paths (GOLDSCHEIDER & DREW 2007: 36). While a new generation of karst conduits may develop in the

phreatic zone, previously phreatic karst conduits and cavities can transform into vadose ones and finally dry up or become filled with sediment (GOLDSCHEIDER & DREW 2007: 22).

Significant fracture porosity development in the **epiphreatic zone** results in (i) an increase in horizontal hydraulic conductivity favoring greater water movement in the shallow phreatic zone rather than at depth and (ii) an increase in storage lowering the water table gradient and thereby extending the vadose zone (FORD & WILLIAMS 2007: 130).

The **vadose zone** is determined by the relative rates of movement of its upper and lower boundaries and thus the rate of surface lowering associated with the rate of water table lowering (FORD & WILLIAMS 2007: 132). With subsequent dissolutional widening of the fissures, systems' void space is gradually increasing at depth and the zone of saturation in the rock is falling, thus deepening the vadose zone (FORD & WILLIAMS 2007: 132). Its thickness in well-karstified rock is often more than 100 m and sometimes extends as much as 2 km below the surface (FILIPPONI et al. 2012: 39). Bedding planes in the vadose zone link joint-dominated routes for water percolation downwards, while the latter is characterized by a multiphase process, with air and water coexisting in the pores and fissures (FORD & WILLIAMS 2007: 107). The development of vertical shafts and cavities is favored by gravitational and thus subvertical water percolation, cascading vertically down through fractures, continuously enlarging them; their diameter is typically significantly larger than the conduits feeding and draining them (GOLDSCHEIDER & DREW 2007: 36, FILIPPONI et al. 2012: 39).

The **epikarst** (also referred to as the subcutaneous zone, "top of rock" or "rockhead") is characterized by highly fractured and weathered rock lying immediately beneath a possible soil cover and above the main body of the vadose zone that comprises largely unweathered bedrock (Tab. 2, Fig. 5) (FORD & WILLIAMS 2007: 132). Its thickness is typically 3 – 15 m, but can range from greater 0.1 m to 30 m or more in especially massive rock with low density of fissuring (FORD & WILLIAMS 2007: 132, BENSON & YUHR 2016: 27, GOLDSCHEIDER & DREW 2007: 19). With increasing depth, the effectiveness of corrosional attack and thus the extent and frequency of widened fissures gradually diminishes due to the lower $\mathbf{CO_2}$ supply; therefore, 50 – 80 % of solutional denudation in a karstic limestone catchment is accomplished within the top 10 m beneath the surface and thus mainly in the epikarst (FORD & WILLIAMS 2007: 343). The amount of rock removed by dissolution within this zone varies from less than 1 % to more than 50 % and the amount of the fracture and bedrock void volume that is filled with sediment can range from less than 5 % to more than 95 %, with the higher percent values being the most common (ALEY 1997). While porosity in the epikarst usually exceeds 20 %, it is commonly less than 2 % in the relatively unweathered rock beneath, wherefore water tends to accumulate at the base of the epikarst due to the contrast in hydraulic conductivity (FORD & WILLIAMS 2007: 133). This concentration of flow encourages the formation of shafts and conduits developing downwards from the base of the epikarst (KLIMCHOUK 1995: 46). Since not all fissures are closed, some penetrate as major openings through the rock funneling water and draining the epikarst downwards, act as distal tributaries through the vadose zone and transmit diffuse autogenic recharge to conduits in the vadose and thence to the phreatic zone (FORD & WILLIAMS 2007: 133f.). The development of karst conduits in the phreatic zone is even partly dependent on the temporal evolution of the distribution of recharge from the epikarst (CLEMENS et al. 1999). With the enlargement of paths of rapid percolation from

the epikarst, the amount of undersaturated water flowing into the underlying conduit system enhances, and therefore the growth of phreatic conduits and cavities is accelerated (FORD & WILLIAMS 2007: 163).

Fig. 5: Epikarst zone with partly highly weathered limestones. Imberg Tunnel, Swabian Alb high plain, southwestern Germany, 2016.

3.7. Karst conduits, cavities and caves – development, erosional forms and infillings

As previously described, karst conduits develop from dissolution along penetrable fissures and can be progressively enlarged by a combination of continuous dissolution, mechanical erosion and transport of rock and soil material associated with groundwater circulation, respectively. As karstification proceeds, patterns of interconnected conduits may form secondary cavities and caves, whereby a decoupling of flow will gradually occur between that passing relatively rapidly and turbulently through the karst pipes and that penetrating slowly and laminar through the surrounding porous and fissured rock (WHITE 1977b). Such dissolutional cave systems may develop in the phreatic, epiphreatic and vadose zone (FILIPPONI et al. 2012: 60f.) and are among the most complex of all landforms, because they ramify in a great variety of three-dimensional patterns in the rock massif (Fig. 6) (FORD & WILLIAMS 2007: 209, FILIPPONI et al. 2012: 39, GOLDSCHEIDER & DREW 2007: 27). However, even a karst cave system can initially be defined as an opening enlarged by dissolution to a diameter sufficient for breakthrough kinetics, meaning a conduit greater than 5 – 15 mm in diameter or width (FORD & WILLIAMS 2007: 209). A conduit of breakthrough diameter or greater extending continuously between the input and output points of a karst rock constitutes an **integrated cave system** (FORD & WILLIAMS 2007: 209). While **protocaves** extend from an input or an output point and may connect them, but are not yet enlarged to cave dimensions, **isolated**

caves are voids that are and were not connected to any water input or output points by conduits of these minimum dimensions; these latter non-integrated caves may range from vugs to some large rooms, possibly (FORD & WILLIAMS 2007: 209). **Periodic caverns** within a cave most likely develop along intersections of fractures with zones of weakened rock (BENSON & YUHR 2016: 30). Contrasting with **deep phreatic** conditions where flow and dissolution rates and thus the size of the dissolution voids are very slight, the void size distribution changes dramatically near the water table (FILIPPONI & JEANNIN 2010: 436). Although caves are often initially guided by the early networks of phreatic primary tubes, more than 90 % of the cave volume might be created by later erosion under vadose conditions (FORD & WILLIAMS 2007: 229). The extent of **vadose caves** depends on the depth of the vadose zone and on lithological and other effects tending to divert groundwater from a vertical descent with topographic relief above the springs as the most effective; the magnitude of vadose caves is a function of the size of their streams and the duration of erosion (FORD & WILLIAMS 2007: 229). The majority of the deepest vadose caves are simple systems of vertical shafts down fractures, almost homogeneous in altitude and drained by short basal meanders leading to the next shaft; the meanders commonly develop along inception horizons (FORD & WILLIAMS 2007: 228, FILIPPONI & JEANNIN 2010: 437). Because of varying hydrogeological boundary conditions within most cave catchment areas over time, a superposition of different phases (i.e. coexistence of voids at different states of karstification close together) can often be observed (FILIPPONI & JEANNIN 2010: 437). As already stated, ground cavities and cave systems develop best in massive competent limestones, whose intact unconfined compressive strength is generally 30 – 100 MPa (WALTHAM & FOOKES 2003: 101).

Fig. 6: Karst cave close to the Widderstall Tunnel, Swabian Alb high plain, southwestern Germany (DB Projekt Stuttgart–Ulm GmbH © 2016).

The **erosional form** of a **cave passage** may be attributable entirely to dissolution under phreatic (pressure flow), vadose (free-flow) or alternating (floodwater) conditions, whereby many passages are compound forms displaying, first, phreatic and then vadose erosion; however, dissolutional forms of every kind may be modified or destroyed by collapse of roof or walls (FORD & WILLIAMS 2007: 249). When first connected, **phreatic passages** show a subcircular cross-section or are expanded along the fissure, if resistance is very low; diameter or width is no more than a few centimeters and dissolution processes occur in all parts of the perimeter (FORD & WILLIAMS 2007: 249, GOLDSCHEIDER & DREW 2007: 36, GOEPPERT et al. 2011: 295). With further passage enlargement, the developing form depends on the interaction between passive variables (lithological, structural) and active mass transfer variables (fluid velocity, dissolution potential, type and abundance of clastic load); the minimum friction cross-section (a circular pipe) is maintained (FORD & WILLIAMS 2007: 249, GOEPPERT et al. 2011: 295). While isotropic geology with slow mass transfer will permit the simple fissure to enlarge uniformly to great size, passive variables are more often anisotropic normal to bedding planes (i.e. properties change significantly from bed to bed), however, and irregular profiles will evolve; the extent of irregularity may be a function of size, and thus of the aggregate amount of erosion time (FORD & WILLIAMS 2007: 250). Although the variety of phreatic cross-sections is enormous, all are variations on these themes (FORD & WILLIAMS 2007: 250). **Anastomoses** comprise a network of branching, intersecting and rejoining channels in a two dimensional system or may be independent forms (SLABE 1995), that originally develop along a fissure through dissolution by slow, poorly directed phreatic flows (FILIPPONI & JEANNIN 2006: 26); independent anastomoses are the subsidiaries of primary tubes (FORD & WILLIAMS 2007: 251). While anastomoses can form excellently where stratal dip is low, features such as vertical joints, steeply dipping bedding planes etc. show relatively little anastomosing (FORD & WILLIAMS 2007: 251f.). The form of **vadose passages** is that of entrenchment, with or without widening; it might be an underfit in the floor of a phreatic passage at its minimum development (FORD & WILLIAMS 2007: 252). Where the rock is hard and channel gradients are steep, **stream potholes** may develop; they are most frequent and display the most regular form in hard limestones, dolomites and marbles, pre-eminently (FORD & WILLIAMS 2007: 253f.).

Karst conduits, cavities and caves may be partly or completely **filled with air**, **water** or **soil material**, whereas a combination thereof is commonly present. They may be (i) abandoned when their water is captured by other preferred routes, (ii) wholly or partially filled with clastic sediment or secondary calcite deposits, or (iii) may collapse when their dimensions create unstable roof spans (ZHOU & BECK 2011: 13, FILIPPONI & JEANNIN 2006: 26). They function as sediment traps, accumulating clastic, chemical and organic debris (FORD & WILLIAMS 2007: 271). Allogenic fluvial sediments and local breakdown are the predominant categories of clastic deposits (FORD & WILLIAMS 2007: 271). Deposits of gravel to boulder-sized material are the typical bedload in many hilly karst regions if extensive allogenic catchment areas exist; however, they can also be generated from autogenic breakdown (FORD & WILLIAMS 2007: 273). Allogenic sand is an abundant constituent of cave sediments in basins composed of limestones and sandstones together (FORD & WILLIAMS 2007: 275). The dissolution of limestone often leads to the formation of residual clays (and rarely silica), which may occur as cavity infillings (GOLDSCHEIDER & DREW 2007: 10). Clays

and silts are widespread because they are transported in suspension; they may coat cave walls and even ceilings, although most accumulation is on the floors (FORD & WILLIAMS 2007: 276). All categories of the aforementioned sediments can be observed in common phreatic caves (FORD & WILLIAMS 2007: 276). Within the solid rock, filled caves may appear as sand or clay-filled pipes, whereas progressive roof collapse propagating upward may create a pile of fallen rock in a breccia pipe (ZHOU & BECK 2011: 13).

Tab. 3 summarizes the characteristics of the different karst hydrographic zones with respect to the dominating dissolution process and the occurrence of conduits, cavities, water flow and soil material, respectively.

3.8. Rate of karst denudation and karst maturity

Karst erosion occurs underground as well as on slopes and is referred to a surface-area-dependent process, in which precipitation rather than temperature is the principal control (FORD & WILLIAMS 2007: 77f.). The **karst denudation rate** is the sum of both chemical and mechanical erosion processes, expressed in units of volume/area per year (m^3 km^{-2} a^{-1}) or, most commonly, in millimeters per thousand years (mm ka^{-1}), equivalently (FORD & WILLIAMS 2007: 78). The spatial distribution of denudation depends upon the distribution of water flow and the distribution of solute concentrations (FORD & WILLIAMS 2007: 95). Spatial inequalities in the availability of solvent (water) arise from the distribution of runoff following rain, whereas spatial variability in soil $\mathbf{CO_2}$ production arises from variations in biological activity associated with soil thickness, soil moisture and aspect (FORD & WILLIAMS 2007: 95). The **downcutting rate** (e.g. of cave streams) is equivalent to the rate of **baselevel lowering** and is equal to or less than the rate of **tectonic uplift**; in stable alpine karst areas, longterm denudation and uplift will tend to balance (FORD & WILLIAMS 2007: 97).

Karst can be described in terms of (i) maturity, (ii) complexity and (iii) geomorphology along with specific features; WALTHAM & FOOKES (2003) classified **karst maturity** into five levels (Tab. 4, Fig. 7) generally increasing in number, size and variety of karst features from Juvenile to Extreme. However, the stages of karst development and maturity are always to be placed in context with time (BENSON & YUHR 2016: 35). The process from initiation to enlargement proceeds over a period of 3000 – 5000 years, degradation may occur after about 10 000 – 100 000 years and finally decay after about 1 – 10 million years (WHITE 1988, ESTEBAN & WILSON 1993); this corresponds roughly to the evolution of the karst stages Juvenile, Youthful, Mature, Complex and Extreme karst from WALTHAM & FOOKES (2003) (BENSON & YUHR 2016: 36).

Tab. 3: Characterization of the different karst hydrographic zones with respect to the dominating dissolution process and the occurrence of conduits, cavities, water flow and soil material (modified after FILIPPONI et al. 2012: 161).

Karst hydrographic zone		Common thickness	Dominating dissolution process	Conduits	Cavities	Water flow	Soil material
Vadose zone	Epikarst	3 – 15 m	Near-surface erosion; diffuse and/or directed infiltration of percolating water with high dissolution potential; widening of fissures	Strongly loosened zone with many corrosively widened fissures and conduits	Many, rather small and mostly subvertical cavities; unstable; common size: < 50 cm	Vadose; slow to rapid percolation; accumulation at base of epikarst	Rather less soil; predominantly boulders and debris; inflow of material
	Transmission zone	20 – 50 m; up to 2000 m	Dissolution of subvertical structures due to gravitational penetrating, corrosive water	Vertically directed conduits (gravitationally); shafts and meanders, increasing with depth	Subvertical cavities; common size: 1– >10 m; h: < 20 m to > 100 m in depth	Vadose; gravitational draining towards karst water table; permanently and periodically aquiferous up to > 1 m³/s	Less soil; predominantly boulders; inflow of material
Flood level							
Epiphreatic zone		30 – 50 m; up to 300 m	Predominantly dissolution of subvertical structures due to gravitational penetrating water; in depth: phreatic conduit network development	Vertically directed conduits (gravitationally); shafts and meanders; vadose forms dominate; isolated phreatic forms possible; in depth: mainly subhorizontally directed conduits (following hydraulic gradient); phreatic forms (circular to elliptical cross-sections)	Subvertical cavities; common size: 1– >10 m; h: up to > 100 m; in depth: subhorizontal cavities; common size: 1– >10 m	Predominantly vadose; phreatic in times of greater flood events; in depth: phreatic or vadose; permanently and periodically aquiferous up to several m³/s	Predominantly boulders, decreasing with depth; partly fine-grained clastic material (sand, silt, clay), strongly increasing with depth
Low water level							
Phreatic zone		30 – 50 m; up to several 100 m (up to base of karstifi-able rock)	Phreatic conduit network development; in depth: corrosive widening (mm) of karstifiable fissures	mainly subhorizontally directed conduits (following hydraulic gradient); phreatic forms (circular to elliptical cross-sections); in depth: little conduits in proper sense (> 1 cm); widening predominantly along inception horizons, rather decreasing frequency with depth	subhorizontal cavities; common size: 1– >10 m; in depth: cavities negligible; common size: < 1 cm	Phreatic; directed flow; permanently aquiferous up to several m³/s; in depth: phreatic; diffuse flow; permanently aquiferous; very rarely large volumes of water	Large quantities of fine-grained clastic material (sand, silt, clay); in depth: no significant soil material

Tab. 4: Karst classification based upon maturity (modified after WALTHAM & FOOKES 2003: 110).

Classification	Location	Rockhead	Fissuring	Caves	Sinkholes	NSH (new sinkholes per km^2 per year)
Juvenile karst	Deserts and periglacial zones; on impure carbonates	Almost uniform; minor fissures	Minimal; low secondary permeability	Rare and small; some isolated relict features	Rare	< 0.001
Youthful karst	Minimum in temperate regions	Many small fissures	Widespread in the few meters nearest surface	Many small caves; most < 3 m across	Small suffosion or dropout sinkholes; Open stream sinks	0.001 – 0.05
Mature karst	Temperate regions; the minimum in wet tropics	Extensive fissuring; relief < 5 m; loose blocks in cover soil	Extensive secondary opening of most fissures	Many < 5 m across at multiple levels	Many suffosion and dropout sinkholes; large dissolution sinkholes; small collapse and buried sinkholes	0.05 – 1.0
Complex karst	Temperate regions; normal in tropical regions	Pinnacled; relief 5 – 20 m; loose pillars	Extensive large dissolutional openings, on and away from major fissures	Many > 5 m across at multiple levels	Many large dissolution sinkholes; numerous subsidence sinkholes; scattered collapse and buried sinkholes	0.5 – 2.0
Extreme karst	Wet regions	Tall pinnacles; relief > 20 m; loose pillars undercut between deep soil fissures	Abundant and very complex dissolution cavities	Numerous complex 3D cave systems; galleries and chambers > 15 m across	Very large sinkholes of all types; remanent arches; soil compaction in buried sinkholes	>> 1.0

3.9. Typical karst features and landforms of humid regions

Karst features can generally be classified into **exokarstic** (subaerial), **epikarstic** (subcutaneous) and **endokarstic** (subterranean) forms (GOLDSCHEIDER & DREW 2007: 19). The drainage of a karst system is subterranean and the initiation of karst plumbing represents a significant precondition for the early development of medium- to large-scale surface landforms (FORD & WILLIAMS 2007: 321). Karst features and landforms result from processes operating in coupled geochemical and hydrological systems and are characteristic of humid regions, where water usually occurs in its liquid phase, contrasting with arid and extremely cold climatic conditions that provide limiting circumstances, consequently (FORD & WILLIAMS 2007: 321). In most cases, chemical dissolution and thus true karstification is the predominant geomorphological process (GOEPPERT et al. 2011: 296).

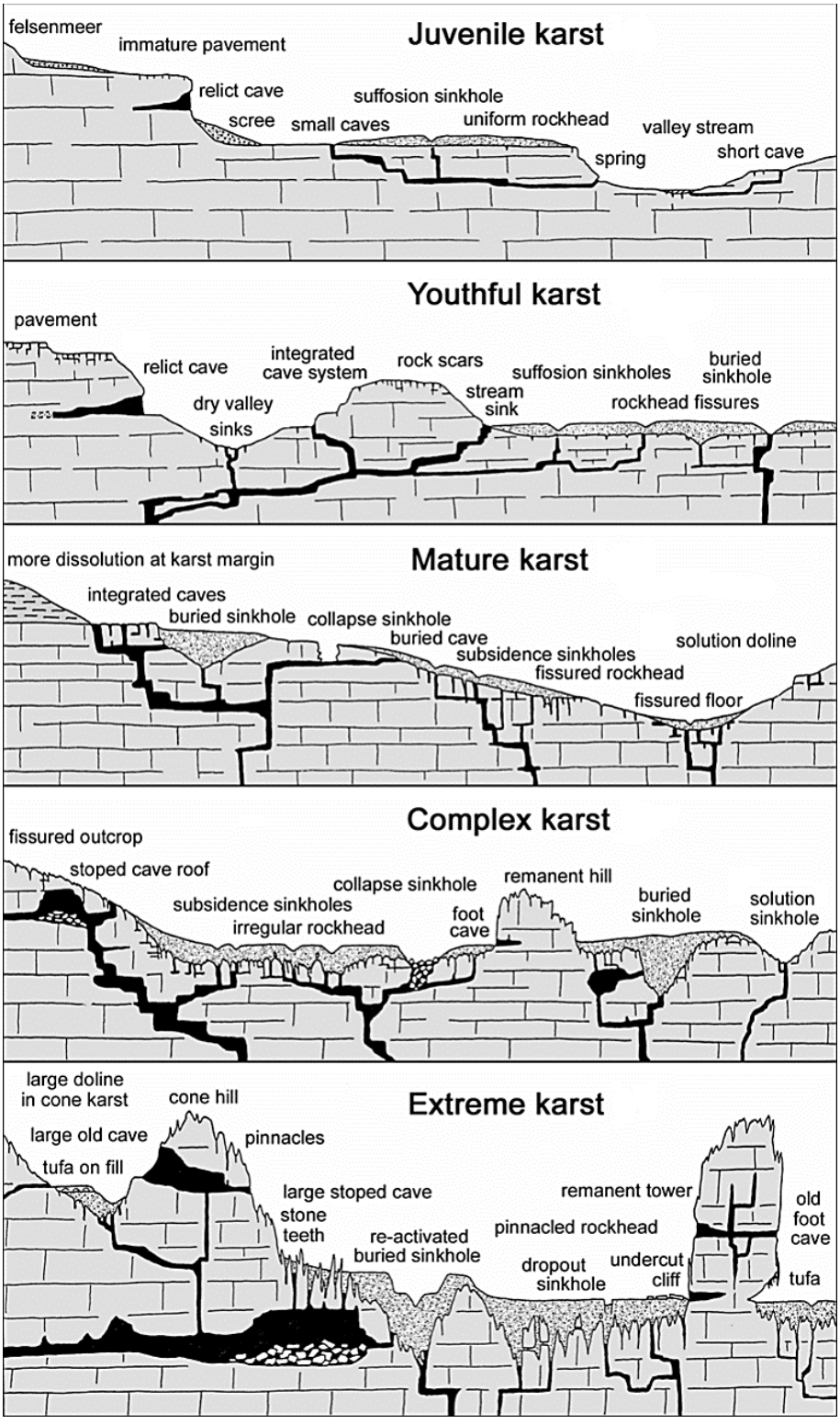

Fig. 7: Typical morphological features of karstic ground conditions within the five classes of karst maturity, illustrated in horizontally bedded limestones; dipping bedding planes and inclined fractures may add complexity to most of the features. The dotted ornaments represent any type of clastic soil or surface sediment (modified after WALTHAM & FOOKES *2003: 111).*

The **top of karstic bedrock** is commonly buried beneath the soil and usually characterized by a highly **irregular rockhead** with deep, solution-widened discontinuities alternating with **pinnacles** of more competent rock that have not been dissolved yet (Fig. 8). The deep v-shaped, sediment-filled fissures (commonly referred to as cutters) may become several tens of meters deep and just as wide, while the residual blocks of rock may be of similar dimensions or larger depending on the frequency of fractures (ZHOU & BECK 2011: 12).

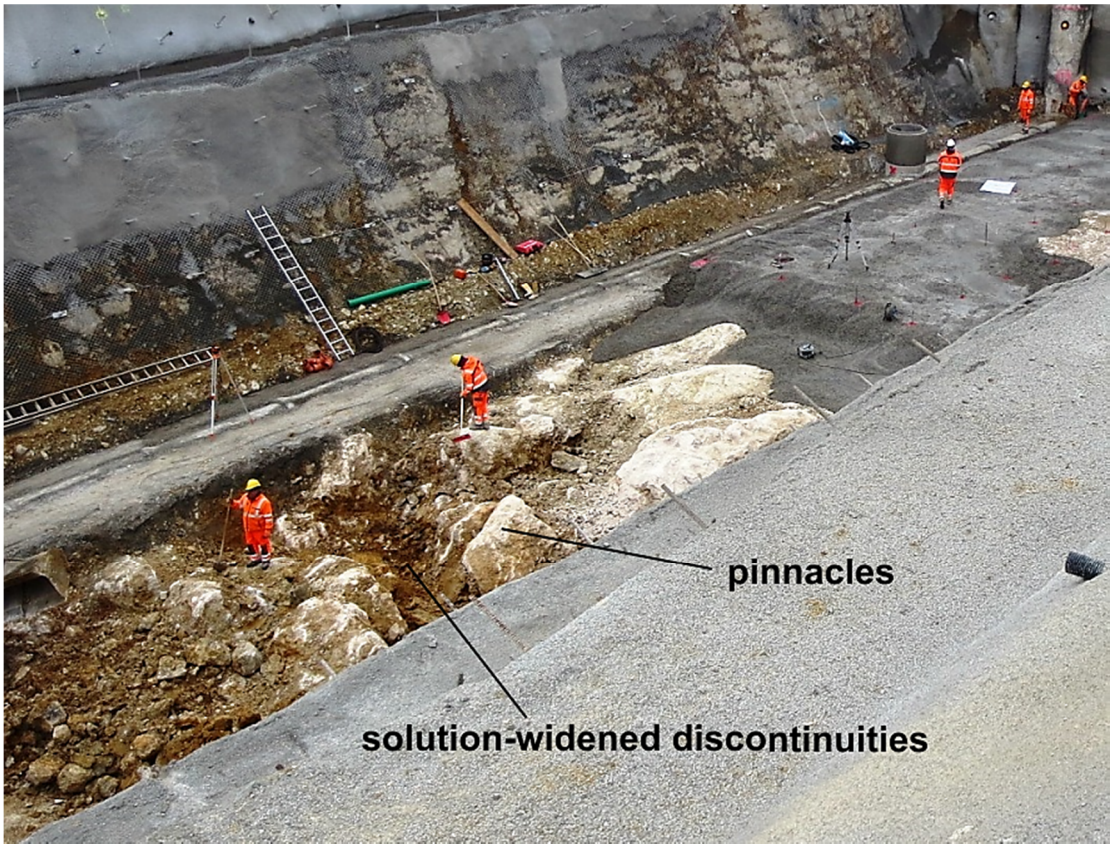

Fig. 8: The top of karstic bedrock characterized by a highly irregular rockhead. Solution-widened discontinuities alternate with pinnacles of limestone that have not been dissolved yet. Merklingen Tunnel, Swabian Alb high plain, southwestern Germany, 2016.

Karren are referred to as channels or furrows, separated by ridges and caused by chemical and/or mechanical dissolution on massive bare limestone surfaces; they typically range from a few millimeters to more than 1 m in depth and from 1 cm to more than 10 meters in dimension (FIELD 2002, FORD & WILLIAMS 2007: 322, BENSON & YUHR 2016: 27). Karren are strongly affected by texture and thus only develop on fine-grained and high homogeneous rock (FORD & WILLIAMS 2007: 29, 322). Assemblages of many individual karren are denoted as **karrenfield** and may cover large areas (Fig. 9) (FORD & WILLIAMS 2007: 322). **Karren shafts** constitute vertical, horizontal or inclined drains into the epikarst and are usually guided by joints, bedding planes etc.; length (depth) varies from a few centimeters to 2 – 3 m and cross-sections tend to be elliptical or circular and up to 1 m in diameter, with great variety (FORD & WILLIAMS 2007: 325). **Kluftkarren** are fracture-controlled linear karren developing along major joint sets or systems and thus tend to

intersect at angles of 60°, 90° and 120° (tension and shear systems) (FORD & WILLIAMS 2007: 326). The slow release of water from storage may permit meandering and favors the development of striking meander incisions into bare rock surfaces (**mäanderkarren**) (FORD & WILLIAMS 2007: 331).

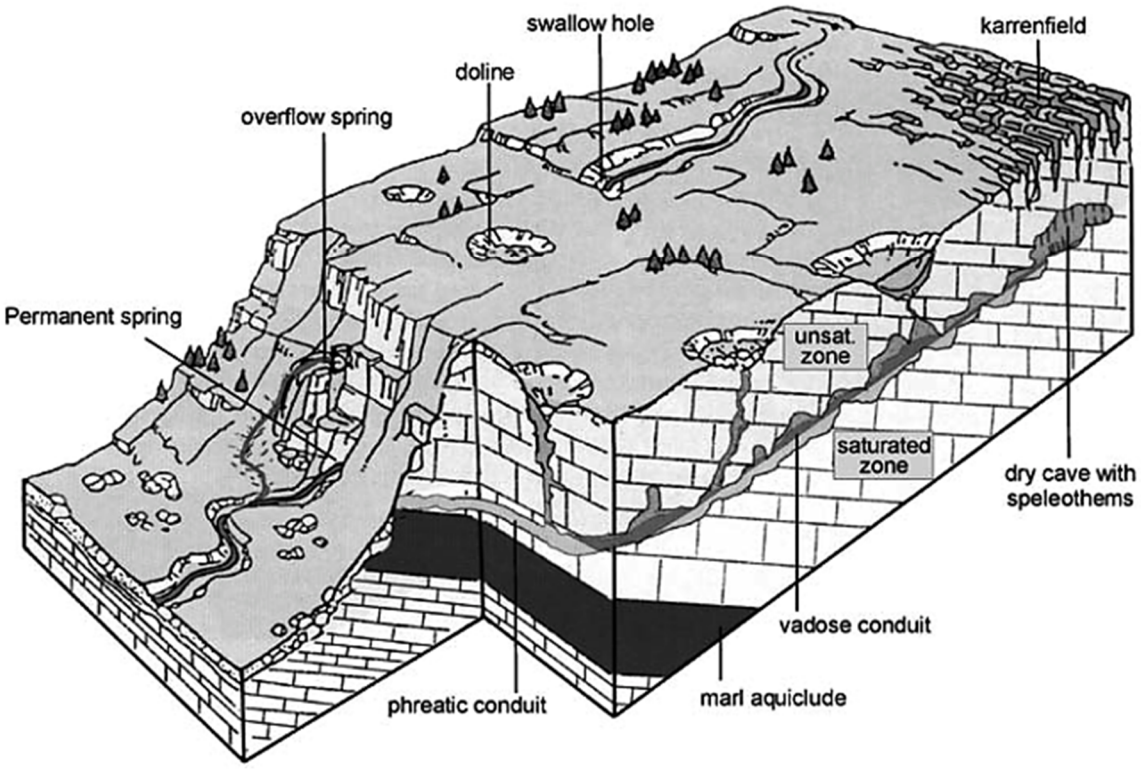

Fig. 9: Block diagram of a karst landscape with some typical surface and underground karst landforms and their relation to the hydrogeological system (SCHAER et al. 1998).

Dolines (or **sinkholes**) are referred to as any small to intermediate enclosed karst depressions, formed by various processes including dissolution, collapse and subsidence; a spectrum of features from bowl-sloped hollows, to funnels to cylindrical pits can be observed (Fig. 9) (FORD & WILLIAMS 2007: 339, GOLDSCHEIDER & DREW 2007: 20, ZHOU & BECK 2011: 10). Dolines represent index landforms of karst development, although they may be rare or even absent in some karst areas. They may occur as isolated individuals or as densely packed groups in terrain, with number and density depending on thickness of soil cover, type of underlying rock, depth to water table, degree of dissolution and karst maturity (FORD & WILLIAMS 2007: 339, BENSON & YUHR 2016: 22). The spatial orientation of dolines (and other karst landforms) may provide indications on the geometry of the underground conduit network, because they are often aligned along the strike of the strata, situated at the intersection of two fractures and follow master joints or faults (GOLDSCHEIDER & DREW 2007: 21, GOEPPERT et al. 2011: 293, BENSON & YUHR 2016: 22). Dolines are usually circular to subcircular in plan form, varying in diameter from a few meters to about 1 km; sides range from gently sloping to vertical and vary from a few to several hundred meters in depth (FORD & WILLIAMS 2007: 339, GOLDSCHEIDER & DREW 2007: 20). They may be open and dry (like in typical upland limestone karst areas) or be filled with water and/or sediment;

when buried, little, if any, surface evidence is remaining (BENSON & YUHR 2016: 17f.). Dolines constitute zones of preferential infiltration and may have an active **ponor** at their bottom, sometimes in the form of an open but narrow shaft, which acts as a permanent or intermittent **swallow hole** for surface waters (Fig. 9) (GOEPPERT et al. 2011: 293, GOLDSCHEIDER & DREW 2007: 20, FORD & WILLIAMS 2007: 134, ZHOU & BECK 2011: 10f.). Dolines are usually characterized by either a slow imperceptible subsidence or a sudden catastrophic collapse of the ground surface (ZHOU & BECK 2011: 10). WALTHAM & FOOKES (2003: 106) classified sinkholes (or dolines) into six different types: (i) solution sinkhole, (ii) dropout sinkhole, (iii) collapse sinkhole, (iv) suffosion sinkhole, (v) caprock sinkhole and (vi) buried sinkhole (Fig. 7, except for (v)). Water related factors such as heavy rainfall and low water table seem to be the dominant triggering factors for doline collapses; a declining water table shows an accelerating effect (NEWTON 1976, 1987). The speed at which a doline collapse occurs depends on the rock structure and lithology, the content of fine-grained material, partial cementation, hydraulic head differences and the size of the opening into the rock along with the size and interconnection of the void space within the rock (BENSON & YUHR 2016: 73). While the collapse process may proceed rapidly in loosely bedded sediments such as sands, the mature slope may develop quite slowly where the sediments contain a significant amount of fine-grained material or are weakly cemented (BENSON & YUHR 2016: 73). Most doline collapses develop over a few hours or a few days after a triggering event (BENSON & YUHR 2016: 72).

Poljes are large, flat-floored, enclosed depressions in karst terrains, associated with the input and throughput of water, often covered with alluvial sediments and soil, and ranging between tens and many hundreds of square kilometers (FORD & WILLIAMS 2007: 361f., GOLDSCHEIDER & DREW 2007: 20, GOEPPERT et al. 2011: 294). Poljes (like dolines) often drain underground via **swallow holes** and follow major geological structures, like synclines or grabens (GOLDSCHEIDER & DREW 2007: 20f.). In many respects, they can be considered as inliers of a normal fluvial landscape (FORD & WILLIAMS 2007: 361f.).

Swallow holes that transform into springs during high-flow conditions are referred to as **estavelles**, which occur rarely and almost exclusively in karstic terrain (GOEPPERT et al. 2011: 295, GOLDSCHEIDER & DREW 2007: 21).

Baselevelled corrosional plains form by solutional removal of irregularities down to a water table controlled surface; slopes can be very low indeed (< 0.1°), since mechanical work is not involved and no significant insoluble residues exist (FORD & WILLIAMS 2007: 365f.). The complex of processes producing baselevelled corrosional plains in karst can be regarded as a combination of (i) vertical dissolution of upstanding remnants by direct rainfall, (ii) lateral undercutting of hillsides by accelerated corrosion in swampy zones at their base and (iii) spring head sapping (FORD & WILLIAMS 2007: 366). After corroding the topography down to the level of frequent inundation (the epiphreatic zone), the plain may expand by gradual retreat of adjoining karst uplands and by elimination of residual hills (FORD & WILLIAMS 2007: 366). Longterm denudation results in the merger of neighbouring valleys and in the production of a **karst margin plain** (FORD & WILLIAMS 2007: 365).

A landscape of residual carbonate hills scattered across a plain is referred to as **tower karst**, whereby the residual hills display a variety of shapes from tall sheer-sided towers to cones or even hemispheres (Fig. 7); massive bedding and low fissure frequency is necessary to sustain the verticality of the tower walls (FORD & WILLIAMS 2007: 227, 370). While some are symmetrical in form, others may be asymmetric, reflecting the influence of dip or erosional processes (FORD & WILLIAMS 2007: 370). Only some residual hills rise directly from the plain; many surmount pedestals (FORD & WILLIAMS 2007: 370f.). Some towers are isolated, whereas others are in groups rising from a common base (FORD & WILLIAMS 2007: 371).

4. General state of research in terms of engineering geological and geophysical karst reconnaissance

The accurate prediction and the effective governance of geological defective karst voids and other karstic features are of decisive importance in hazards control worldwide and become major engineering problems to be solved urgently (BAUER & THURO 2005, PLINNINGER et al. 2005, DANIELSEN & DAHLIN 2009, LI et al. 2010, LI et al. 2013, XU et al. 2013, KIELBASSA et al. 2015a, KIELBASSA et al. 2015b, RAITHEL et al. 2015, THIENERT & LEISMANN 2015). To decide, which exploration technique for karst reconnaissance should be used for tunnel constructions in karstifiable areas, numerous parameters are of interest. Besides geological, geometrical and technical tunnel parameters, dimension and properties of geotechnically and constructionally relevant karst voids and features, so the resolution requirement, are significant (THIENERT et al. 2016: 2). In particular, this shall include:

- geology (type of soil/rock, stratification/cleavage, spatial distribution of joints, faults, fracture zones, grade of loosening etc.)
- geometry of karst void or feature (size, shape, spatial position referring to tunnel axis)
- karst void/feature filling (non, partially or almost completely filled with soil material and/or water)
- filling material (blocky material with high volume of voids, fine material with small volume of voids, mixture of both, cohesive or noncohesive soil aggregate, partially with enclosed blocks of rock)
- hydrogeology (groundwater table above/below tunnel, groundwater confined/unconfined, water head)
- type of tunneling (driven or cut-and-cover)
- tunnel geometry (thickness of overlying beds, tunnel diameter)
- type of heading (mechanized or conventional due to accessibility of the ground for measuring tools)

In terms of karst reconnaissance, tunnel construction depends primarily on a qualitative and quantitative description of the underground conditions. Engineering geology and hydrogeology offer a number of methods in order to investigate these conditions with the desired precision. These methods (e.g. DIN 4020, DIN 4021, SIA 199, EC: ENV 1991) are generally recognized to be state of the practice and/or technical knowledge and are regulated in a wide range of standards (LEHMANN et al. 2009: 105). Engineering geological and hydrogeological studies usually include the application of near-surface mapping along exposures or the use of direct probing by destructive drillings and/or deep vertical/horizontal drillings with core recovery and geotechnical analyses. In potentially karstified areas, these methods can predict e.g. large-scale faults, karst caves or underground rivers and are capable of providing further information of geological karst hazard sources (LI et al. 2010: 233).

However, in most cases, a detailed **geotechnical exploration** and rock mass classification in the run-up to the construction work is possible to a limited degree only (RECHLIN et al. 2011: 14). Even

within intensive, expensive and time-consuming investigations of the underground, distances between drillings can easily range between 50 m and 200 m (LEHMANN et al. 2009: 105) and unfavorable geological and hydrogeological conditions can be predicted grossly and macroscopically only (LI et al. 2010: 233). ZISMAN (2001) showed that more than 2000 borings per hectare would be needed for a 90 % certainty of detecting a cavity 2 – 3 m in diameter. In the case of deeply buried tunnels, the nearest boreholes are commonly drilled more than 1000 m apart. Especially in potentially karstified areas, the common engineering geology and hydrogeology methods will not deliver reliable information about the dimension of karstification and the type and location of karst voids and other karstic features (PRINZ & STRAUß 2011: 472, ROTH & NYQUIST 2003: 1); drillings several meters apart may yield very different depth to rock (GOLDSCHEIDER & DREW 2007: 171, ROTH & NYQUIST 2003: 1) and highly variable rock conditions of a soil-covered epikarst are difficult to define by drilling alone (WALTHAM & FOOKES 2003: 113). Therefore, to overcome uncertainties in the description of physical underground properties determined from drillings, the geotechnical investigations can be complemented with exhaustive **geophysical investigations** (GIRMSCHEID 2013: 18, LEHMANN et al. 2009: 105, ULUSAY 2015: 11f. etc.). The geophysical investigations complete and condense the grid of the drillings and, in a next step, can be calibrated with these (GIRMSCHEID 2013: 18, LEHMANN et al. 2009: 106). Due to the indirect nature of geophysical explorations, a relation between the measured variables (e.g. electrical resistivity, seismic velocity) and the actual subsurface constituents (solid bedrock, soil material, water, air) is always required (HAUCK et al. 2011: 453).

Geophysical high resolution prospecting is a simple, fast, economic, non-intrusive and effective method in exploring geological structures in front of tunneling working site and can yield continuous information along profiles or about the complete area under investigation of relevant physical underground properties. The geophysical response depends on the size of the target in relation to its depth as well as on the contrast between the physical properties of the target and the surrounding rock, respectively (ABDALLATIF et al. 2015: 508, CHALIKAKIS et al. 2011: 1174, KAUFMANN & DECEUSTER 2014: 21). Thereby, the geophysical signature of the target itself can be decisively influenced by the thickness and consistency of overburden sediments (percentage of clay, density, presence of water etc.), also with increasing depth of the target (CHALIKAKIS et al. 2011: 1177). The amplitude of geophysical anomalies is, furthermore, an inverse function of the distance between the measurement point and the structure (CHALIKAKIS et al. 2011: 1174). The lateral limits of geophysical methods are related to the measurement sampling (investigation step), whereas the vertical limits correspond to the investigation depth, which is also linked to the equipment, the configuration array and, in terms of karst reconnaissance, to the physical properties of the carbonate matrix (CHALIKAKIS et al. 2011: 1174). During tunnel constructions with less overburden, for instance, it is suitable to use initially geophysical measuring procedures to prospect the depth and irregularity of rock surfaces, tectonic weakness zones, sinkhole structures, air-/water-/sediment-filled cavities and zones of strong karstification (PRINZ & STRAUß 2011: 472, YASSIN et al. 2014: 63). With regard to the prediction of geological defective karst features in karst terrains, geophysical methods are very beneficial because of the intrinsic heterogeneity of the medium (cf. MOCHALES et al. 2007, NEUKUM et al. 2010, SMITH 2005, ŠUMANOVAC & WEISSER 2001, VAN SCHOOR 2002, VOUILLAMOZ et al. 2003 etc.), even if this heterogeneity might sometimes be

associated with a high level of geophysical noise (VAN SCHOOR 2002: 393). As is generally known (e.g. VADILLO et al. 2012: 153), the main heterogeneities in karst terrains are due to the existence of voids (minor and major cavities, conduits, fractures and fault zones). Any geophysical method should involve **void detection** as its main objective, consequently. VADILLO et al. (2012: 153) outlined furthermore, that the geophysical exploration of karst heterogeneities needs to be able to encompass the following singularities involved:

- target depths may vary within one to hundreds of meters,
- karst void sizes may range from centimeters to tens of meters,
- surfaces of karst areas are often rough / consist of a combination of soil and compact rock,
- investigation sites often belong to protected environmental areas,
- groundwater and its seasonal variations plays an important role in that it changes physical parameters at different times.

Although all these points might sometimes be disadvantageous, the vadose zone in karstified areas, in particular, affords the advantage of not being a fully saturated medium and thus provides a sharp contrast between the geophysical properties of air-filled voids and the limestones, dolomites or marbles of the carbonate media (VADILLO et al. 2012: 153f.). In addition, karstified and intensively fractured rock is often disturbed when surrounding karst voids and thus creates a larger bulk anomalous volume than the void itself; this again favors the detection of the void by means of geophysical investigations (CHALIKAKIS et al. 2011: 1172f.). Ultimately, it is important to choose the best of the methods available for detecting the difference between compact rock and karst voids (VADILLO et al. 2012: 154).

A review of the different **geophysical techniques** applicable to karst systems is given by CHALIKAKIS et al. (2011). Tab. 5 presents the adequacy of frequently used ground-based geophysical methods and their measuring techniques for the most common issues in karst formations.

Apparently, there is no single method that can forecast geological karst defects accurately and counterweigh all the disadvantages of the karstic medium (SMITH 2005, WALTHAM & FOOKES 2003 etc.). Especially with respect to the size of voids that can be detected and the depth below the surface that can be explored with confidence, all common remote geophysical techniques have their limitations (FORD & WILLIAMS 2007: 152). Thus, the usual approach to detect karst voids and other karstic features is to combine different geophysical methods (VADILLO et al. 2012: 154).

Tab. 5: Adequacy of frequently used ground-based geophysical methods for karst-system exploration (modified after CHALIKAKIS et al. 2011: 1176).

Ground based geophysics		Adequacy of the method											
		With sedimentary covering					Without sedimentary covering					Sedimentary covering	
Method	Measurement technique	Boundaries	Fractured zone	Preferential pathways	Cavities		Boundaries	Fractured zone	Preferential pathways	Cavities		Type	Thickness
					Air-filled	Water-filled				Air-filled	Water-filled		
Electrical	ES	+++	++	+	0	0	+++	+	+	0	0	++	+++
	SP	0	++	+++	0	++	0	++	+++	0	++	+	0
	Mise-à-la-masse	0	0	++	0	++	0	+	++	0	++	0	0
	ERT	++	++	++	++	++	+++	++	++	+++	++	+++	++
EM	Slingram	++	++	++	+	+	++	++	++	++	++	+++	++
	TDEM	+++	+	0	0	0	+++	+	0	0	0	+++	+++
	CSAMT	+++	++	++	+	+	+++	+++	++	+	+	+++	+++
	VLF EM	+++	+++	+++	+	+	++	+++	+++	+	+	++	+
	GPR	0	+	+	+	+	+	+++	++	+++	++	+	0
Seismic	Tomography	+++	++	++	++	++	+++	++	++	++	++	++	++
	MASW	++	++	++	++	++	++	+++	++	++	++	++	++
Microgravimetry	Profiling or mapping	0	++	+	+++	++	0	+	+	+++	++	0	0
Magnetic	Profiling or mapping	0	0	0	0	0	0	0	0	0	0	++	0
MRS	Sounding	0	0	0	0	+++	0	0	0	0	+++	+	0

+++ recommended; ++ appropriate but incomplete; + appropriate but limited; 0 not recommended

ES electrical sounding; SP self potential; ERT electrical resistivity tomography; EM electromagnetic; TDEM time domain electromagnetic; CSAMT controlled source audio magnetotelluric; VLF very low frequency; GPR ground penetrating radar; MASW multichannel analysis of surface waves; MRS magnetic resonance sounding

5. Description of frequently used ground-based geophysical methods for karst reconnaissance

5.1. Microgravity (or Microgravimetry) – Methodology

Gravity surveying measures variations in the Earth's gravitational field produced by density differences in subsurface rocks (McGRATH et al. 2002: 552, FORD & WILLIAMS 2007: 149, BATAYNEH 2013: 1381f.). Caves and depressions cause a reduction in the gravitational acceleration over them due to the missing mass associated with the void (McGRATH et al. 2002: 552, FORD & WILLIAMS 2007: 149f.), whereas topographic highs on the bedrock surface will exert greater gravity pull than the surrounding less dense material (FORD & WILLIAMS 2007: 149f.). These gravity anomalies are typically a few parts in a billion of **g** and expressed in milliGals (1 Gal = 1 cm/s^2) (McGRATH et al. 2002: 552, BATAYNEH 2013: 1378). Because **microgravity** variations are so small, very high-precision instruments and meticulous field techniques are required in order to detect karst voids (McGRATH et al. 2002: 552, FORD & WILLIAMS 2007: 150). Microgravity surveys involve the establishment of a regular grid of observation points over the study area with station spacing depending on the possible size and depth of the voids that are to be detected (McGRATH et al. 2002: 553, FORD & WILLIAMS 2007: 150). The microgravity data recorded are then to be corrected for latitude, elevation, topography, tide and instrument drift (minute changes in the calibration of the gravity meter) before they can be modeled and presented on profiles and/or maps referred to as Bouguer gravity anomalies (GIBSON et al. 2004: 35, GOLDSCHEIDER & DREW 2007: 181f.). In order to remove regional effects and focus on local karst features, the residual gravity is calculated by subtracting a smooth regional trend from the Bouguer gravity (McGRATH et al. 2002: 553, GOLDSCHEIDER & DREW 2007: 182).

As described before, the detectability of karst features using microgravity measurements depends on the dimension and depth of the feature as well as on the density contrast between the feature and the surrounding rock (GOLDSCHEIDER & DREW 2007: 182). Subsurface mass excesses such as locally shallow bedrock pinnacles, float blocks in the soil profile or zones of particularly massive bedrock cause residual Bouguer gravity highs (positive gravity anomalies) (GOLDSCHEIDER & DREW 2007: 182). In contrast, residual Bouguer gravity lows (negative gravity anomalies) are caused by mass deficiencies such as locally deep bedrock cutters or clay seams where less dense soil displaces more dense bedrock (GOLDSCHEIDER & DREW 2007: 182). In general, the lighter (less dense), larger, thicker and shallower the karst feature is, the easier it will be detected and delineated using a microgravity survey; the narrower or "spikier" the observed gravity anomaly is, the shallower its source must be (GOLDSCHEIDER & DREW 2007: 182). Cavities within bedrock also produce residual Bouguer gravity lows: (i) air-filled cavities provide the largest anomalies for gravity surveying because of the complete absence of material in the target (density contrast: –2.5 g/cm^3), (ii) water-filled cavities provide anomalies 60 % that of the same cavity containing air (density contrast: –1.5 g/cm^3) and (iii) rubble-filled cavities about 40 % that of air (density contrast: –1.0 g/cm^3) (McGRATH et al. 2002: 554). However, this simplified picture of an isolated cavity is not usually the case, because rock surrounding any cavity is often disturbed and associated fracturing may extend for two or more diameters away from the cavity (DANIELS 1988). This is

particularly true in karst terrains where the associated dissolution of rock enlarges faults and fractures; this secondary effect is termed 'halo' effect and normally serves to increase the effective target size (McGRATH et al. 2002: 554).

Microgravity surveying is used for determining karst features in urban areas, near underground or overhead utilities, where the application of electrical/electromagnetic or seismic methods would be impossible due to noise limitations or existing infrastructure (GOLDSCHEIDER & DREW 2007: 182). Of all geophysical methods, gravity surveys may be least susceptible to interference or noise (GOLDSCHEIDER & DREW 2007: 182). Since microgravity alone cannot discriminate between a void and a local bedrock deep, it should always be interpreted with complementary geophysical (e.g. seismic) or boring data (GOLDSCHEIDER & DREW 2007: 182). The main drawbacks of microgravity are: (i) the long acquisition time and the associated costs, (ii) the large number of corrections – latitudinal, elevational, topographical, tidal and instrument drift – that have to be applied to the data before they can be modeled, (iii) the limited density contrast in areas with a high saturation ratio and (iv) the low frequency ground vibration from heavy construction equipment or earthquakes (even distant ones) that may cause the gravity meter to sway during a measurement (ROTH et al. 2002: 225, GIBSON et al. 2004: 35, GOLDSCHEIDER & DREW 2007: 181f., 183, KAUFMANN & DECEUSTER 2014: 20); the latter can be overcome by averaging readings over relatively long periods or by performing measurements when the vibrations are not active (GOLDSCHEIDER & DREW 2007: 183).

5.2. Microgravity – State of research in terms of karst reconnaissance

Microgravity methods are often used to map shallow subsurface karst features (BUTLER 1984, PATTERSON et al. 1995, RODRIGUEZ 1995, CRAWFORD et al. 1999, McGRATH et al. 2002). KAUFMANN et al. (2006), for instance, performed intensive 2D microgravity surveys to locate wide palaeokarst slots under a 10 – 15 m thick unconsolidated overburden. The microgravity technique has also been successfully applied in the detection of sinkholes when the density of the sinkhole's filling material was markedly lower than the density of the host rock (e.g. ARGENTIERI et al. 2015). However, microgravity is only able to detect large sinkholes or those located close to the ground surface but cannot be used to track the presence of buried sinkholes; this might inter alia be the case because the only presence of open conduits does not provide a strong perturbation of the gravity field (CHALIKAKIS et al. 2011: 1175). Microgravity, conducted with close spacing and careful implementation in order to ensure high-resolution and accuracy, remains one of the geophysical methods best suited to the detection of voids in the uppermost 20 m, even when these voids might be relatively small (CHALIKAKIS et al. 2011: 1175). Especially air-filled cavities will yield as unequivocal anomalous response (VAN SCHOOR 2002: 393, CARRIÈRE et al. 2013: 32). Therefore, microgravity (including microgravity vertical-gradient (MVG)) is shown to be a very effective and adaptable non-destructive tool for the detection of naturally occurring cavities (McGRATH et al. 2002: 557, GAMBETTA et al. 2011: 11). The MVG technique, in particular, emphasizes shallow gravity anomalies with a strong reduction in geologic noise to allow the determination of the horizontal position of voids (GAMBETTA et al. 2011: 11). However, ROTH et al. (2000) studied microgravity testing in areas of irregular bedrock surface and found the data insufficient for locating voids. Microgravity can be accurate in delineating near-surface zones of

increased fracture density or in revealing major fractures with significant gravity anomaly amplitude (CHALIKAKIS et al. 2011: 1175). Moreover, microgravity can be combined with resistivity tomography to identify rock head and to distinguish buried sinkholes from caves (which have similar gravity signatures) (YOUSSEF et al. 2012a: 32).

5.3. Seismic – Methodology

Seismic techniques operate by transmitting seismic (acoustic) energy into the ground through a seismic source (such as dynamite, hammers, air guns or seismic vibrators) and by recording the seismic waves that are reflected or refracted at interfaces between materials with different rheological properties (i.e. seismic velocities). Thereby, arrays of geophones can be used as recording tools and depth penetration is about one-third of the geophone spread (FORD & WILLIAMS 2007: 483f.). The seismic velocity of a material is proportional to its stiffness (defined by elastic moduli) and inversely proportional to its density; the stiffness in turn is strongly dependent upon the porosity of the rock material (GOLDSCHEIDER & DREW 2007: 177f.). Because of the fact that the stiffness increases faster than density with decreasing porosity, the seismic velocity also increases with decreasing porosity, empirically; as a consequence, higher density and lower porosity rock materials are usually characterized by higher seismic velocities (GOLDSCHEIDER & DREW 2007: 178). While dry, unconsolidated sediments and soils generally show compressional or primary (P-) wave velocities between approximately 300 – 1400 m/s, saturated soils might have P-wave velocities in the range of 1400 – 2300 m/s (GOLDSCHEIDER & DREW 2007: 178, MILSOM 2003: 181). In karst terrains, where bedrock weathering is predominately controlled by dissolution rather than decomposition, a distinct velocity contrast at the top of carbonate bedrock is commonly present; P-wave velocities might easily exceed > 2500 m/s (GOLDSCHEIDER & DREW 2007: 178). In contrast, irregular karst cavities, fractures and fault zones may significantly decrease seismic velocities (CHALIKAKIS et al. 2011: 1172).

Once a seismic wave strikes a density contrast, a portion of the seismic energy is reflected at the angle of incidence, while the remainder is refracted into the underlying layer (Fig. 10) (GOLDSCHEIDER & DREW 2007: 178, MILSOM 2003: 182). The reflected and refracted seismic waves at each subsurface density contrast combined with the generation of surface waves (ground roll) and sound (i.e. air-coupled waves or air blasts) produce a complex sequence of ground motion at the geophones near a shot point; this ground motion is typically displayed as a simple curve (wiggle trace) or as a wave train for each geophone (GOLDSCHEIDER & DREW 2007: 178). Seismic wave arrival times for certain events can subsequently be analyzed to determine the velocity structure of the subsurface beneath the geophone array; thereby, the velocity structure may be depicted as boundary lines between layers with different inferred velocities or as velocity contours (GOLDSCHEIDER & DREW 2007: 178). In order to improve the signal-to-noise ratio and besides a number of recommended corrections, several traces obtained with identical source and receiver positions (common midpoint or CMP traces) can be added together (stacking); the number of traces in a CMP stack defines the fold of coverage (GUÉRIN et al. 2009: 813, MILSOM 2003: 203, SIART et al. 2011: 319). When a constant seismic wave velocity of the geological environment is known, the depth of an imaged target (visible through an anomaly in the wave transmission rate) can be computed from the two-way travel time of the seismic waves; a time-to-depth inversion can finally

be performed (FORD & WILLIAMS 2007: 484, GÉLIS et al. 2010: 1416, GUÉRIN et al. 2009: 813, KAUFMANN & DECEUSTER 2014: 22, SIART et al. 2011: 319).

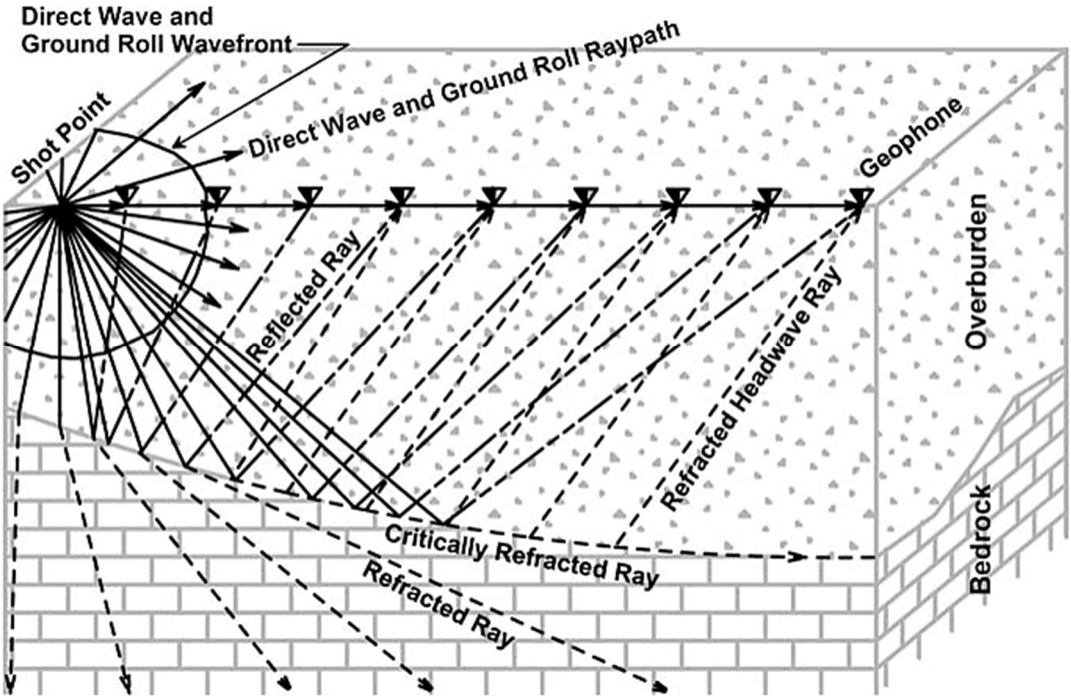

Fig. 10: Schematic diagram of selected seismic ray paths from a shot point to an array of geophones (GOLDSCHEIDER & DREW 2007: 178).

In **seismic reflection** surveys, specialized field and data processing procedures are applied to maximize the energy reflected by subsurface density contrasts along near-vertical ray paths (GOLDSCHEIDER & DREW 2007: 180). Reflected seismic energy is never a first arrival and thus must be identified in a generally complex set of overlapping seismic arrivals (which is usually done by collecting and filtering highly redundant or multi-fold data sets (e.g. STEEPLES & MILLER 1990)). Particularly in shallow seismic reflection surveys (depth penetration less than approximately 15 m), the reflected energy from subsurface density contrasts will reach all geophones in an array almost simultaneously with the near-surface waves (ground roll, air blast and refractions); ground roll and air blast are characterized by a comparatively much higher amplitude and might significantly overlap the seismic reflection arrivals (GOLDSCHEIDER & DREW 2007: 180f., MILSOM 2003: 201). Moreover, separating shallow reflections from shallow refractions might be difficult, if not impossible (KAUFMANN & DECEUSTER 2014: 20). In deeper seismic reflection surveys (depth penetration more than approximately 15 m), the reflected energy will reach the geophones subsequent to the near-surface waves and, as a consequence, can be identified more easily (GOLDSCHEIDER & DREW 2007: 181).

Seismic refraction techniques measure the travel time of the portion of seismic energy, which is refracted along a distinct density contrast (e.g. top of rock) and partially returns to the surface as a head wave that leaves the interface at the original angle of incidence (Fig. 10) (GOLDSCHEIDER & DREW 2007: 179, MILSOM 2003: 182); the refracted rays always represent the first arrival of

seismic energy for geophones at a certain distance from the shot point (LANKSTON 1990). Seismic refraction requires geophone arrays with lengths of approximately 4 to 5 times the depth to density contrast of interest and is thus limited to penetration depths typically less than 30 m (GOLDSCHEIDER & DREW 2007: 179). In standard seismic refraction methods, a subhorizontal layered subsurface is assumed, with no seismic velocity variations in the vertical direction within each layer. In **seismic refraction tomography (SRT)**, the seismic velocity may change gradually within each layer both vertically and horizontally; this might particularly be decisive in the case of overburden soils overlying karstic bedrock. SRT generally needs more shot points per receiver than standard seismic refraction surveys in order to obtain high-resolution profiles and besides involves more complex mathematical algorithms for inversion.

5.4. Seismic – State of research in terms of karst reconnaissance

High-resolution seismic methods are frequently used in karstic environments due to their advantageous penetration depth and spatial resolution (GUÉRIN et al. 2009: 813). Seismic reflection can be used to delineate karst voids from compact rock and to detect subvertical faults, fractures and geologic contacts as well as horizontal limits, if a velocity contrast at the top or bottom of the karst medium is present, for instance (BALLARD et al. 1983, ODUM et al. 1999, ŠUMANOVAC & WEISSER 2001, EVANS & LIZARRALDE 2003, THIERRY et al. 2005, GOLDSCHEIDER & DREW 2007: 181, GÉLIS et al. 2010: 1407, 1416, CHALIKAKIS et al. 2011: 1175). Seismic reflection is rarely used in terms of sinkhole detection, although some recent and moderately successful applications are known (e.g. KAUFMANN & DECEUSTER 2014). While the presence of a karst void can often be determined by means of seismic reflection, the delineation of its shape and dimension is not usually possible (GOLDSCHEIDER & DREW 2007: 181). The seismic signature of a void in a karstified medium, measured via compression (P) waves, is highly variable due to (i) the influence of diffraction patterns, (ii) local attenuations, (iii) perturbations caused by reflecting material deeper than the target and (iv) the P-wave low velocity anomaly; a water-filled conduit might be difficult to detect due to the lower acoustic impedance contrast (GUÉRIN et al. 2009: 813). In comparison to standard refraction techniques, seismic reflection (i) can be performed in the presence of low velocity zones (velocity inversions), (ii) generally has lateral resolution superior to seismic refraction (and thus is better suited to a karstic setting with typically strong lateral heterogeneities) and (iii) can delineate very deep density contrasts with much less shot energy and shorter profile lengths than would be required to achieve a comparable depth using seismic refraction (GOLDSCHEIDER & DREW 2007: 181, GUÉRIN et al. 2009: 813). The main limitations of seismic reflection methods are (i) its higher cost compared to seismic refraction, (ii) its possible weakness in karst terrains due to uneven reflectors and a high level of noise (such as when the refraction energy is dominant in recordings) and (iii) its physical limitation to depths generally greater than approximately 15 m (CHALIKAKIS et al. 2011: 1175, GÉLIS et al. 2010: 1407, 1416, GOLDSCHEIDER & DREW 2007: 181, GUÉRIN et al. 2009: 813); in areas of shallow bedrock with an irregular surface, seismic reflection does not provide reliable data (ROTH et al. 2002: 225). Very shallow (< 5 m), extremely high-resolution reflection seismics (using high-frequency signal sources/receivers and ultra-high-fold data) proved to be useful (BAKER et al. 1999), but are not yet in wide use for karst geophysics (GOLDSCHEIDER & DREW 2007: 181).

Seismic refraction seems to be the most commonly used geophysical method in tunnel construction in the past (CARDARELLI et al. 2003, GANERØD et al. 2006, KLOSE et al. 2007, LÜTH et al. 2008) and can provide information on velocity field anomalies due to near-surface karst heterogeneities such as near-surface cavities and preferential pathways (BALLARD et al. 1983, ODUM et al. 1999, ŠUMANOVAC & WEISSER 2001, EVANS & LIZARRALDE 2003, THIERRY et al. 2005, CHALIKAKIS et al. 2011: 1175). Seismic refraction works best for relatively flat, dipping layers (GOLDSCHEIDER & DREW 2007: 179). In karst terrains with commonly pinnacled bedrock, successful refraction surveys require highly redundant data sets (with many shot points per receiver) to be able to resolve the irregular bedrock profile; however, even the best refraction data often produce a smoothed version of the top of bedrock (GOLDSCHEIDER & DREW 2007: 179). Seismic refraction is mainly limited (i) by practicality to mapping the tops of layers at depths typically less than 30 m and (ii) by the fact that seismic velocity has to increase with depth for a sufficient investigation depth; a near-surface fast layer with high velocities (e.g. clay) could hide underground structures and may yield incorrect results (CHALIKAKIS et al. 2011: 1175, GOLDSCHEIDER & DREW 2007: 179). Seismic refraction tomography (SRT) operates excellently in detecting the basal boundary between unconsolidated soil material/overburden and solid bedrock (SIART et al. 2011: 331). In contrast, the SRT method exhibits only a moderate precision for subtle substrate changes and thus is limited in determining the internal stratification of overburden and in delineating smaller karst features from solid bedrock (SIART et al. 2011: 319, 331, SIART et al. 2013: 1141). In addition, SRT seems to be limited in detecting cavities, if they are located beneath weathered layers with increasing thicknesses, and in reconstructing vertical karst structures (such as palaeokarst slots) (CARDARELLI et al. 2010: 694, KAUFMANN & DECEUSTER 2014: 23). Furthermore, also SRT is rarely used in terms of sinkhole detection, although some recent and relatively successful applications are known (e.g. ARGENTIERI et al. 2015).

5.5. Ground Penetrating Radar (GPR) – Methodology

Ground penetrating radar (GPR) operates by emitting radiofrequency electromagnetic (EM) energy as a short-pulse or swept frequency from a transmitter antenna and by recording the reflected, refracted or diffracted scattered-back waves that formed at interfaces between materials with different electromagnetic properties (OLHOEFT 2000); thereby, the same antenna (monostatic) or a separate antenna (bistatic) can be used as receiving antenna (SLOB et al. 2010: 106). The radar signal itself is determined by the properties of the radar system and controlled by the geometry of the antennas and the properties of the ground, including coupling and buried-object (target) responses (SLOB et al. 2010: 106). The propagation of EM waves is fundamentally based on coupled electrical and magnetic vector fields (as described by Maxwell's equations) and depends upon the electrical conductivity and the dielectric permittivity of the medium of travel (GOLDSCHEIDER & DREW 2007: 193, VADILLO et al. 2012: 156). Once the EM wave has leaved the transmitter antenna, some part of the field leaks through the air directly to the receiver antenna (direct air wave) and is scattered from nearby above-ground objects (despite possible attempts to shield the antenna) (SLOB et al. 2010: 105f., VADILLO et al. 2012: 156). While the above-ground wavefield will travel with the speed of light in air (which is always faster than in the ground), the below-ground wavefield will travel through the earth materials with the speed of light in the

material, with a part of that wave directly traveling to the receiving antenna (direct ground wave) (SLOB et al. 2010: 106). If the EM wave passes a small reflector such as a pipe, a stone or a cavity in the subsurface, reflections occur not only above the object, but also in its nearest surrounding; this effect leads to a diffraction hyperbola in the radargram, where the vertex of the hyperbola marks the position of the object (VADILLO et al. 2012: 153). In the same way, hyperbolas can be caused by surface and near-surface reflectors such as houses, cars, trees, bushes, power lines and boreholes (if they are cased in concrete reinforcement), which may be mistaken for subsurface karst structures and, therefore, need to be identified (VADILLO et al. 2012: 153). The shape of a hyperbola depends on the object's burial depth, size and orientation with regard to its elongation as well as on the average wave velocity in the material above the object (OLHOEFT 2000); on that basis, a differentiation between small and large cavities is possible (VADILLO et al. 2012: 153). As EM waves propagate at 0.3 m/ns in air and ~ 0.1 m/ns in karst limestone, surface and subsurface reflectors may reliably be distinguished (VADILLO et al. 2012: 153). When the EM wave velocity is known, the depth of an imaged target can be computed from the two-way travel time of the EM waves (NEAL 2004). The EM wave velocity can possibly be estimated from the diffraction pattern in fixed-offset GPR data, when the target is present in an approximately homogeneous embedding (SLOB et al. 2010: 111). If the velocity estimation is hampered by fixed-offset data quality, because the target cannot be considered small in comparison to the dominant wavelength or due to weak scattering, velocity profiles should be obtained from multiple offset data (common-midpoint gathers or CMPs) or from running several imaging procedures using different velocities; while the first option slows the acquisition operation (because multichannel systems are uncommon), the second option requires detailed knowledge of the antenna positions (SLOB et al. 2010: 111).

Horizontal and vertical resolutions are not equal in GPR surveys, vary with position and depth and are a function of wavelength and geometry (including depth) (SLOB et al. 2010: 107). The vertical resolution additionally depends on the scatterer size/layer thickness as well as on the signal-to-noise (S/N) and signal-to-clutter ratio (SLOB et al. 2010: 107). For pulse radars, the vertical resolution is generally estimated to be one-third to one-fourth of the dominant wavelength with normal noise and clutter (YILMAZ 2001: 46f.). For frequency-domain GPR, the vertical resolution is expressed in terms of the bandwidth used to determine the ability to distinguish between (resolve) two targets closely spaced in depth; it is given as the propagation velocity divided by the square root of two times the bandwidth (SLOB et al. 2010: 107). In contrast to seismic signals, GPR's very high frequency of 50 – 500 MHz (used for most karst applications) is generally providing a much higher resolution, although often at the expense of lower depth of investigation (GOLDSCHEIDER & DREW 2007: 192).

A raw GPR recording depicts the reflection/backscatter amplitude as a function of time and can roughly be read as a cross-section of the dielectric properties of the subsurface (GOLDSCHEIDER & DREW 2007: 193). In order to improve and enhance the GPR results and to remove undesirable noises, different processing functions are applied on the acquired data; these may inter alia include: a time-zero correction, background removal by subtracting the mean trace from each measured trace, dewow filtering (filtering out low frequencies), the removal of the gain that was used in the data acquisition, the use of an energy decay gain, average filtering, frequency band pass filtering,

different migration algorithms (diffraction stack, Kirchhoff migration, fk-migration Stolt) and a topographic correction (ABDALLATIF et al. 2015: 510, CARRIÈRE et al. 2013: 35, REIS JÚNIOR et al. 2015: 373f., SLOB et al. 2010: 111, VADILLO et al. 2012: 153). Finally, the time-to-depth conversion and the diffraction hyperbola analysis can be performed (ABDALLATIF et al. 2015: 510, CARRIÈRE et al. 2013: 35, REIS JÚNIOR et al. 2015: 374, VADILLO et al. 2012: 153). Qualitative GPR detection applications require minimal signal processing and the recorded data, from which only the low-frequency content is filtered out (dewow), may already be used for interpretation (SLOB et al. 2010: 104). In contrast, quantitative GPR applications (to determine e.g. burial depth, size and orientation of objects, moisture content etc.) require imaging and/or inversion (SLOB et al. 2010: 104).

The effectiveness of GPR is based on its wave-propagation nature in combination with its sensitivity to changes in electromagnetic material properties, particularly to changes in the presence of water (SLOB et al. 2010: 104, VADILLO et al. 2012: 153). Subsurface GPR imaging is thus useful in the case of geological bodies with differing dielectric constants (e.g. water-/air-filled cavities or sinkholes in a limestone bedrock environment) (BILLI et al. 2016: 70, VADILLO et al. 2012: 153). GPR applications are generally possible when the topography is rather smooth and when the material penetrated is fine grained, no more than a few meters thick and dry (REYNOLDS 2011: 537ff.). GPR's penetration depth is significantly limited in the presence of high conductive zones or surface foundations (ABDALLATIF et al. 2015: 510). In addition, several sources of error may affect the determination of depth, e.g. (i) the distance from the antenna to the bedrock surface that may have changed due to vegetation and uneven paths, (ii) the uncertainty in recognizing the apex of a hyperbola that may lead to false depths or (iii) wave velocities that are not constant throughout the entire study area (VADILLO et al. 2012: 154).

5.6. Ground Penetrating Radar (GPR) – State of research in terms of karst reconnaissance

GPR appears to be the most popular geophysical method for identifying and locating subsurface karst features such as cavities, conduits and solutionally enlarged fractures (MCMECHAN et al. 1998, AL-FARES et al. 2002, PUEYO-ANCHUELA et al. 2009, CHALIKAKIS et al. 2011: 1175, CARRIÈRE et al. 2013: 39). Although penetration depths are relatively shallow (only up to some tens of meters), the high resolution of this method is advantageous (cf. BALLARD et al. 1983, COLLINS et al. 1990, DOOLITTLE & COLLINS 1998, MCMECHAN et al. 1998, AL-FARES et al. 2002, CUNNINGHAM 2004, THIERRY et al. 2005, MOCHALES et al. 2007, PUEYO-ANCHUELA et al. 2009, NEUKUM et al. 2010). GPR is particularly well-adapted to the analysis of the near-surface (< 30 m depth) structure of karst, especially when clay or soil that would otherwise absorb and attenuate the radar signal is thin or discontinuous (AL-FARES et al. 2002). GPR seems to be very efficient in describing near surface karst features when rock permittivity is low, the epikarst in detail and the infiltration zone of karst aquifers, where limestone crops out at the surface (ABDALLATIF et al. 2015: 510, AL-FARES et al. 2002, CHALIKAKIS et al. 2011: 1175). Moreover, GPR is partially capable of a three-dimensional definition of stratal surfaces and underground cavities (MCGRATH et al. 2002: 557). But even if the extent of underground cavities can often be determined by means of GPR, their precise shape and height may often not be ascertained; this is caused by the circumstance that the propagation and reflection of radar waves inside subsurface cavities are unpredictable and not reconstructable if the exact geometry of the relevant feature is unknown

(VADILLO et al. 2012: 153f.). GPR is, in particular, extremely limited when the overburden is electrically conductive (as it is common in temperate lowland karst with thick residual clay soil covers or in areas of shallow groundwater aquifers) (ABDALLATIF et al. 2015: 510, ABDELTAWAB 2013: 268, CARRIÈRE et al. 2013: 39, CHALIKAKIS et al. 2011: 1175, GOLDSCHEIDER & DREW 2007: 194, ROTH & NYQUIST 2003: 1); in such conditions, the GPR investigation depth can easily be limited to around 2 m (CARRIÈRE et al. 2013: 39, KAUFMANN & DECEUSTER 2014: 21). GPR can be practicable to a restricted extent when the soil mantle is thin or clay-rich but dry (e.g. temperate karst belts during drought) (AL-FARES et al. 2002, GOLDSCHEIDER & DREW 2007: 194). The general absence or discontinuity of electrically conducting sediments on the surface and the use of low frequencies (less than 100 MHz) make the application of GPR effective and useful to limestone formations due to the weak attenuation of the radar waves (AL-FARES et al. 2002, CHALIKAKIS et al. 2011: 1175).

6. The direct-current geoelectrical imaging method, electrical resistivity tomography (ERT), electrical resistivity imaging (ERI)

6.1. Elementary theory

The purpose of geoelectrical resistivity measurements is to determine the resistivity distribution in the subsurface. By introducing an artificial current into the ground via point electrodes, the potentials at other electrodes (geometrically arranged) can be measured and the effective or apparent resistivity of the subsurface can be derived. By using a controlled source of specific dimensions, quantitative results are obtained.

Considering a continuous **current flow in an isotropic homogeneous medium**, with $\delta\mathbf{A}$ is an element of surface and **J** the current density in amperes per square meters, the current passing through $\delta\mathbf{A}$ is $\mathbf{J} \cdot \delta\mathbf{A}$. The current density **J** can be described by Ohm's law (in vector form):

$$\mathbf{J} = \boldsymbol{\sigma}\,\mathbf{E}$$

where $\boldsymbol{\sigma}$ is the conductivity of the medium in siemens per meter and **E** is the electric field in volts per meter. It should be noted that in geoelectrical imaging, the medium resistivity $\boldsymbol{\rho}$ given in ohm-meters (Ωm), which is equal to the reciprocal of the conductivity ($\boldsymbol{\rho} = 1/\boldsymbol{\sigma}$), is commonly used. The electric field **E** is the gradient of a scalar potential:

$$\mathbf{E} = -\,\boldsymbol{\nabla}\,\boldsymbol{\Phi}$$

As a result, we get:

$$\mathbf{J} = -\,\boldsymbol{\sigma}\,\boldsymbol{\nabla}\,\boldsymbol{\Phi}$$

In general, the current is introduced into the ground via point electrodes. Therefore, the current density **J** and the current **I** are related through:

$$\boldsymbol{\nabla}.\mathbf{J} = \left(\frac{\mathbf{I}}{\Delta\mathbf{V}}\right)\boldsymbol{\delta}(x - x_s)\boldsymbol{\delta}(y - y_s)\boldsymbol{\delta}(z - z_s)$$

where $\Delta\mathbf{V}$ is an elemental volume surrounding a current source **I** at location (x_s, y_s, z_s) and $\boldsymbol{\delta}$ is the Dirac delta function (DEY & MORRISON 1979a: 107f.).

By rewriting this equation, we get the basic equation for describing the potential distribution in the subsurface due to a **point current source**:

$$-\boldsymbol{\nabla}.[\boldsymbol{\sigma}(x,y,z)\boldsymbol{\nabla}\boldsymbol{\Phi}(x,y,z)] = \left(\frac{\mathbf{I}}{\Delta\mathbf{V}}\right)\boldsymbol{\delta}(x - x_s)\boldsymbol{\delta}(y - y_s)\boldsymbol{\delta}(z - z_s)$$

In practically all resistivity field works, four electrode spreads are normally used. By injecting current into the subsurface via two current electrodes C_1 and C_2, the difference in potential between the two potential electrodes P_1 and P_2 over a homogeneous half space is measurable, given by:

$$\Delta\boldsymbol{\Phi} = \frac{\mathbf{I}\boldsymbol{\rho}}{2\pi}\left(\frac{1}{\mathbf{r}_{C_1P_1}} - \frac{1}{\mathbf{r}_{C_2P_1}} - \frac{1}{\mathbf{r}_{C_1P_2}} + \frac{1}{\mathbf{r}_{C_2P_2}}\right)$$

where **r** represents the respective inter-electrode distances. It is worth mentioning that in a four electrodes array, the current flow lines and equipotentials are bent by the proximity of the second current electrode C_2. Thereby, the distortion from the spherical equipotentials is most evident in the area between the two current electrodes C_1 and C_2. Furthermore, a distortion of current flow lines and equipotentials at the plane boundary can be recognized, always when $\boldsymbol{\rho_1 \neq \rho_2}$ (Fig. 11). If $\boldsymbol{\rho_1 < \rho_2}$, the current lines would be bent toward the normal and vice versa.

The potential difference $\boldsymbol{\Delta\Phi}$ is directly proportional to the apparent resistivity $\boldsymbol{\rho_a}$. Thus, at a known current **I** and a potential difference $\boldsymbol{\Delta\Phi}$, the apparent resistivity $\boldsymbol{\rho_a}$ can be derived from:

$$\boldsymbol{\rho_a = k\frac{\Delta\Phi}{I}}$$

where **k** is the **geometric factor** corresponding to the four electrode arrangement:

$$\mathbf{k} = \frac{2\pi}{\left(\frac{1}{\mathbf{r}_{C_1P_1}} - \frac{1}{\mathbf{r}_{C_2P_1}} - \frac{1}{\mathbf{r}_{C_1P_2}} + \frac{1}{\mathbf{r}_{C_2P_2}}\right)}$$

It should be outlined that the calculated apparent resistivity $\boldsymbol{\rho_a}$ is not the true resistivity. This would only be the case over an isotropic homogeneous ground with constant resistivity for any current and electrode arrangement. If the ground is inhomogeneous, however, the ratio will, in general, change. Consequently, we will get a different apparent resistivity value for each measurement and, as a result, a measured quantity, which is known as the **apparent resistivity** $\boldsymbol{\rho_a}$.

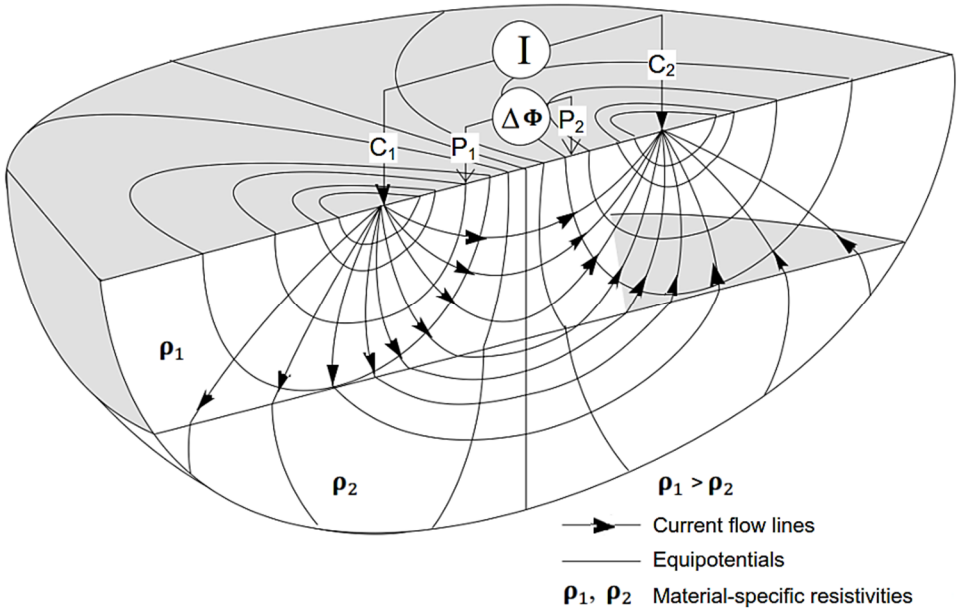

Fig. 11: Exemplary resistivity measurement with a four electrodes spread (modified after KNÖDEL et al. 2005: 129). Current flow lines and equipotentials for the two point current electrodes C_1 and C_2 on surface are displayed. Note that the current flow lines and equipotentials are bent by the proximity of the second current electrode C_2. Thereby, the distortion from the spherical equipotentials is most evident in the area between the two current electrodes C_1 and C_2. Furthermore, a distortion of current flow lines and equipotentials at the plane boundary can be recognized.

6.2. Effect of inhomogeneous ground

Considering a current source and potential point, both located on ground surface, above a horizontal boundary separating two media, the upper resistivity $\boldsymbol{\rho}_1$, the lower $\boldsymbol{\rho}_2$, there are altogether **three media**, **separated by two interfaces**, as described by TELFORD et al. (1990: 529f.) and shown in Fig. 12. This results in an infinite set of images above and below the current electrode C_1. The original image C_1', at a depth $2\mathbf{z}$ below surface, is reflected in the surface boundary and produces an image C_1'' at distance $2\mathbf{z}$ above C_1. This second image, reflected in the lower boundary, is leading to a third C_1''' at depth $4\mathbf{z}$ and so on.

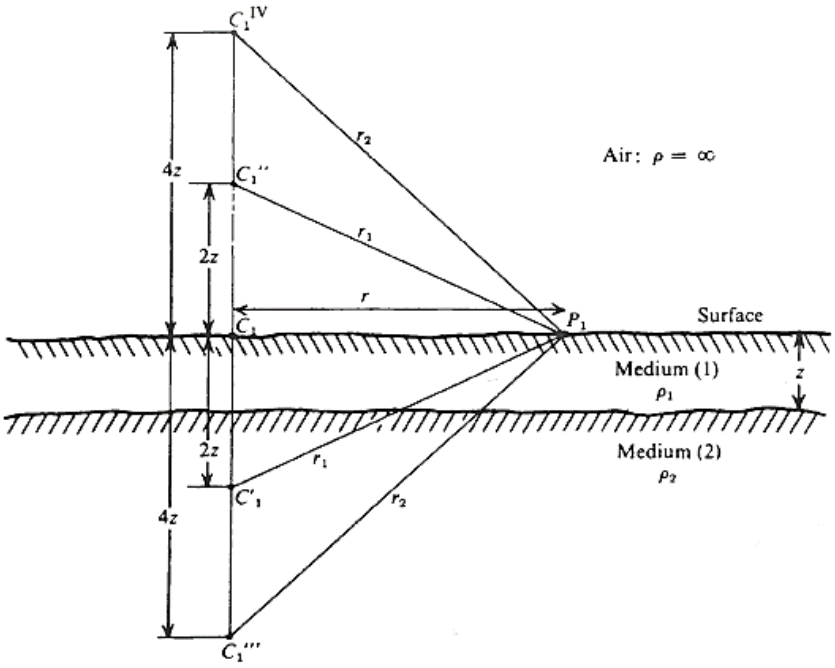

Fig. 12: Images resulting from two horizontal beds (TELFORD et al. 1990: 530).

The effect of each consecutive image on the potential at P_1 is reduced by the reflection coefficient between the boundaries (TELFORD et al. 1990: 529f.). For the current source and its first image below the ground, the potential is:

$$\boldsymbol{\Phi}' = \frac{\mathbf{I}\boldsymbol{\rho}_1}{2\pi}\left(\frac{1}{\mathbf{r}} + \frac{\mathbf{k}}{\mathbf{r}_1}\right)$$

The effect of the second image at C_1'', at distance $2\mathbf{z}$ above ground, is:

$$\boldsymbol{\Phi}'' = \frac{\mathbf{I}\boldsymbol{\rho}_1}{2\pi}\left(\frac{\mathbf{k} \times \mathbf{k}_a}{\mathbf{r}_1}\right)$$

with $\mathbf{k}_a$ as the reflection coefficient at the surface boundary. Due to the fact that $\boldsymbol{\rho}_a$ is essentially infinite, this coefficient is unity, hence:

$$\boldsymbol{\Phi}' + \boldsymbol{\Phi}'' = \frac{\mathbf{I}\boldsymbol{\rho}_1}{2\pi}\left(\frac{1}{\mathbf{r}} + \frac{2\mathbf{k}}{\mathbf{r}_1}\right)$$

The potential due to the third image C_1''', at depth $4\mathbf{z}$ below ground, will be further reduced, as will that of its image $4\mathbf{z}$ above ground, therefore:

$$\boldsymbol{\Phi}''' + \boldsymbol{\Phi}^{\mathrm{IV}} = \frac{\mathbf{I}\boldsymbol{\rho}_1}{2\pi}\left(\frac{\mathbf{k} \times \mathbf{k}}{\mathbf{r}_2} + \frac{\mathbf{k} \times \mathbf{k} \times \mathbf{k}_\mathbf{a}}{\mathbf{r}_2}\right) = \frac{\mathbf{I}\boldsymbol{\rho}_1}{2\pi}\left(\frac{2\mathbf{k}^2}{\mathbf{r}_2}\right)$$

The resultant total potential at P_1 can thus be expressed as an infinite series:

$$\boldsymbol{\Phi} = \frac{\mathbf{I}\boldsymbol{\rho}_1}{2\pi}\left\{\frac{1}{\mathbf{r}} + \frac{2\mathbf{k}}{\mathbf{r}_1} + \frac{2\mathbf{k}^2}{\mathbf{r}_2} + \cdots + \frac{2\mathbf{k}^{\mathrm{m}}}{\mathbf{r}_{\mathrm{m}}} + \cdots\right\}$$

with:

$$\mathbf{r}_1 = \{\mathbf{r}^2 + (2\mathbf{z})^2\}^{1/2}$$

$$\mathbf{r}_2 = \{\mathbf{r}^2 + (4\mathbf{z})^2\}^{1/2}$$

$$\mathbf{r}_{\mathrm{m}} = \{\mathbf{r}^2 + (2\mathrm{m}\mathbf{z})^2\}^{1/2}$$

In a compact form, the series can be written as follows:

$$\boldsymbol{\Phi} = \frac{\mathbf{I}\boldsymbol{\rho}_1}{2\pi}\left[\frac{1}{\mathbf{r}} + 2\sum_{\mathrm{m}=1}^{\infty}\frac{\mathbf{k}^{\mathrm{m}}}{\{\mathbf{r}^2 + (2\mathrm{m}\mathbf{z})^2\}^{1/2}}\right] = \frac{\mathbf{I}\boldsymbol{\rho}_1}{2\pi\mathbf{r}}\left[1 + 2\sum_{\mathrm{m}=1}^{\infty}\frac{\mathbf{k}^{\mathrm{m}}}{\{1 + (2\mathrm{m}\mathbf{z}/\mathbf{r})^2\}^{1/2}}\right]$$

Because $|\mathbf{k}| < 1$, this series is convergent, whereas the denominator increases indefinitely. To get a reasonable answer, the number of terms necessary depends primarily on the value of $\mathbf{k}$ and partly on the ratio $\mathbf{z}/\mathbf{r}$. If the value of $\mathbf{r}$ is fixed, the potential differs from that measured over uniform ground. The latter is given by the first term in the bracket of the aforementioned equation and is called normal potential, whereas the portion expressed by the infinite series is named the disturbing potential (TELFORD et al. 1990: 529f.). With $\mathbf{k}$ positive and approximately unity, the total potential at P_1 might be increasing by a factor of 2 and more.

Considering **a three dimensional body** for which the external potential might be developed is the **sphere**, as illustrated by TELFORD et al. (1990: 530f.) and Fig. 13. The sphere is assumed to be in a uniform field $\mathbf{E}_0$ parallel to the x-axis, for simplicity. This assumption is attributable to having the current electrode at substantial distance from the sphere. Using spherical coordinates, with the sphere center as origin and the polar axis parallel to the x-axis, and applying the boundary conditions $\mathbf{E}_{x_1} = \mathbf{E}_{x_2}$, $\boldsymbol{\sigma}_1\mathbf{E}_{z_1} = \boldsymbol{\sigma}_2\mathbf{E}_{z_2}$, $\boldsymbol{\Phi}_1 = \boldsymbol{\Phi}_2$, a solution of Laplace's equation can be derived, satisfying potential relations inside and outside the sphere (TELFORD et al. 1990: 530f.). For $\mathbf{r} > \mathbf{a}$, the potential is:

$$\boldsymbol{\Phi}_1 = -\mathbf{E}_0\mathbf{r}\cos\theta\left\{1 - \frac{(\boldsymbol{\rho}_1 - \boldsymbol{\rho}_2)}{(\boldsymbol{\rho}_1 + 2\boldsymbol{\rho}_2)}\left(\frac{\mathbf{a}}{\mathbf{r}}\right)^3\right\}$$

The sphere will show an image that will double the second term, if the potential is measured at the ground surface (TELFORD et al. 1990: 530f.). Considering the field to be generated by a current source C_1 at a distance **R** from the origin, additionally, the potential can be written:

$$\mathbf{\Phi_1 = -\frac{I\rho_1}{2\pi R^2}\left\{1 - 2\frac{(\rho_1 - \rho_2)}{(\rho_1 + 2\rho_2)}\left(\frac{a}{r}\right)^3\right\} r\cos\theta}$$

Again, the first term is the normal potential, the second the disturbing potential caused by the sphere (TELFORD et al. 1990: 530f.). In the section shown in Fig. 14, the current flow lines and equipotentials are displayed, respectively.

It should be noted that two assumptions were made for the aforementioned derivation, which are not necessarily valid. On the one hand, that the external or normal field is uniform and, on the other, that no interaction takes place between the sphere and its image. Only if the sphere is at great distance from both, the current source and the ground surface, both assumptions are strictly true, in which case the anomaly could not be detected anyway. With a distance between the sphere's center and the ground surface not less than 1.3 times the radius, the approximation proved reasonably good, however (TELFORD et al. 1990: 530f.).

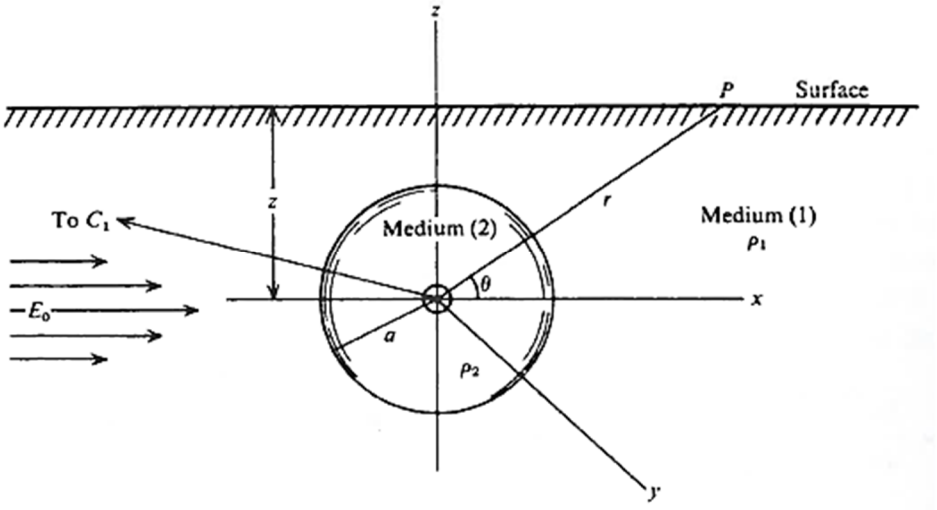

Fig. 13: Buried conducting sphere in uniform field (TELFORD et al. 1990: 530).

So far we have considered current flow and potential in and over homogeneous ground. In general, most rock masses are anything but homogeneous and isotropic in the electrical sense. Shales, slates, and frequently schists and limestones, in particular, show a definite **anisotropic character**, especially with respect to the bedding planes.

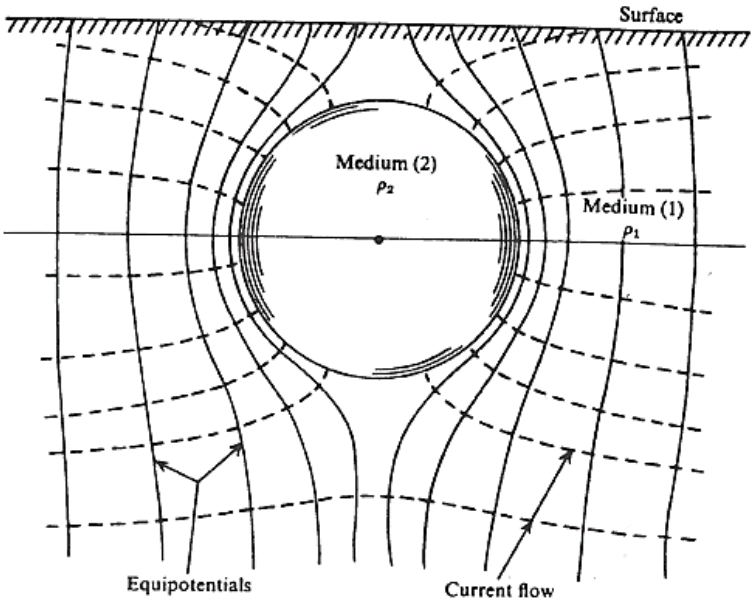

Fig. 14: Equipotentials and current flow lines for buried conducting sphere (TELFORD et al. 1990: 531).

Considering a point source at the ground surface of a semi-infinite medium in which the resistivity is uniform in both the horizontal direction ($\boldsymbol{\rho}_h$) and the vertical direction ($\boldsymbol{\rho}_v$), as described by TELFORD et al. (1990: 531f.). $\boldsymbol{\rho}_v$ has a different magnitude and is almost invariably being larger than $\boldsymbol{\rho}_h$. Applying modifications to allow for the difference between horizontal and vertical directions, the equipotential surfaces appear ellipsoidal and symmetrical about the z-axis, which may be expressed mathematically by:

$$\boldsymbol{\Phi} = -\mathbf{I}\boldsymbol{\rho}_h\boldsymbol{\lambda}/2\pi(x^2 + y^2 + \boldsymbol{\lambda}^2z^2)^{1/2}$$

where $\boldsymbol{\lambda} = (\boldsymbol{\rho}_v/\boldsymbol{\rho}_h)^{1/2}$ is the coefficient of anisotropy. The term $\boldsymbol{\lambda}/(x^2 + y^2 + \boldsymbol{\lambda}^2z^2)^{1/2}$ represents the departure from spherical symmetry (TELFORD et al. 1990: 531f.).

The potential at a ground surface point P and a distance $\mathbf{r}_1$ from the current electrode C_1 can be calculated through:

$$\boldsymbol{\Phi}_P = \frac{-\mathbf{I}\boldsymbol{\rho}_h\boldsymbol{\lambda}}{2\pi\mathbf{r}_1} = \frac{-\mathbf{I}(\boldsymbol{\rho}_h\boldsymbol{\rho}_v)^{1/2}}{2\pi\mathbf{r}_1}$$

which means that the potential is equivalent to that for an isotropic medium of resistivity $(\boldsymbol{\rho}_h\boldsymbol{\rho}_v)^{1/2}$. Due to this, it is impossible to detect this type of anisotropy from field measurements (TELFORD et al. 1990: 531f.).

Based on the aforementioned equation, it is trivial that the resistivity measured over horizontal beds is larger than the actual horizontal resistivity in the beds, but smaller than the vertical resistivity. Otherwise, when the beds are dipping steep and the measurement is carried out with a spread normal to the strike, the apparent resistivity will be smaller than the true resistivity perpendicular

to the bedding, just the opposite to the result previously illustrated over horizontal layers; this phenomena is known as the "paradox of anisotropy" (BHATTACHARYYA & SEN 1981). If the array is parallel to the strike of the dipping beds, the apparent resistivity might be too large, depending on the used current-electrode separation (TELFORD et al. 1990: 532).

Besides local variations in ground surface conductivity, **rugged topography** shows a strong influence on resistivity measurements, too. Because the current flow lines are concentrated or focused in valleys and dispersed or diverged beneath hills, the equipotential surfaces will be distorted and produce false anomalies due to the topography alone. Thus, a real anomaly might be distorted or masked.

FOX et al. (1980) determined that resistivity is anomalously low on ridges and hills and high in valleys or 3D depressions, with regard to a surface of homogeneous ground. Fig. 15 illustrates the distortion of a uniform field produced by a 2D ridge.

The terrain effect increases with surface relief and can be seen as insignificant for slopes of less than 10° (TELFORD et al. 1990: 532). In addition, the chosen resistivity array, in particular its direction, shows a sensitive response; for 2D structures the anomaly is smaller, when the spread is running parallel, rather than perpendicular, to strike (TELFORD et al. 1990: 532). Overall, it should be focused on removing or at least minimizing the terrain anomaly.

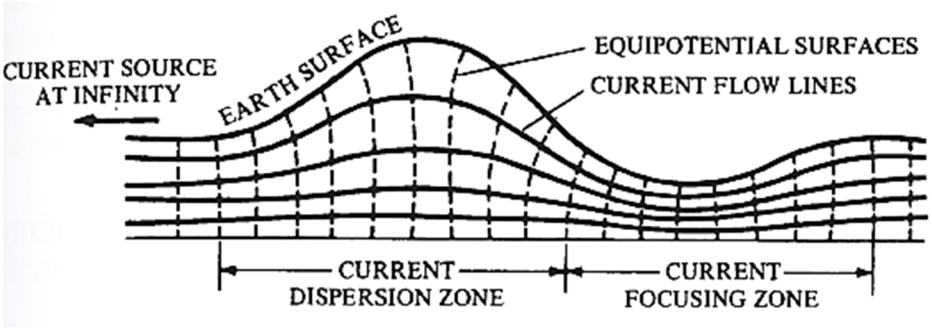

Fig. 15: Distortion of a uniform field by a 2D ridge (modified after FOX et al. 1980: 76).

Anisotropic ground and terrain effects can lead to errors in estimating both depth $\mathbf{z}$ and resistivity $\boldsymbol{\rho_1}$. Aside from these errors, ambiguity in sounding interpretation may occur owing to the **principle of equivalence**; it covers the impossibility to distinguish between two highly resistive beds of different depth $\mathbf{z}$ and resistivity $\boldsymbol{\rho}$ values if the product $\mathbf{z\rho}$ is the same, or between two highly conductive beds if the ratio $\mathbf{z/\rho}$ is the same. As illustrated by TELFORD et al. (1990: 553) and shown in Fig. 16a, a block of cross section $\Delta\mathbf{A}$ offers a resistance to vertical current flow given by $\mathbf{R} = \boldsymbol{\rho_2 z_2/\Delta A}$; thus layers having an identical product $\mathbf{z\rho}$ are equivalent and the two parameters cannot be measured separately. In Fig. 16b, the vertical current flow in the conductive bed is deflected almost perpendicular to the vertical stack, making $\mathbf{R} = \boldsymbol{\rho_2 h/z_2 l}$. As a result, beds having the same ratio $\mathbf{z/\rho}$ are equivalent and again depth $\mathbf{z}$ and resistivity $\boldsymbol{\rho}$ cannot be determined separately. For both configurations, the bed resistivity and thickness might vary within wide limits with respect to

layers above and below it. However, these limits might be found by performing optimization methods (TELFORD et al. 1990: 553).

As a second factor, ambiguity in sounding interpretation may occur owing to the **suppression principle**, stating that if a bed is very thin compared to those above and below, its effect on the image is insignificant unless its resistivity is extremely low or high (TELFORD et al. 1990: 554).

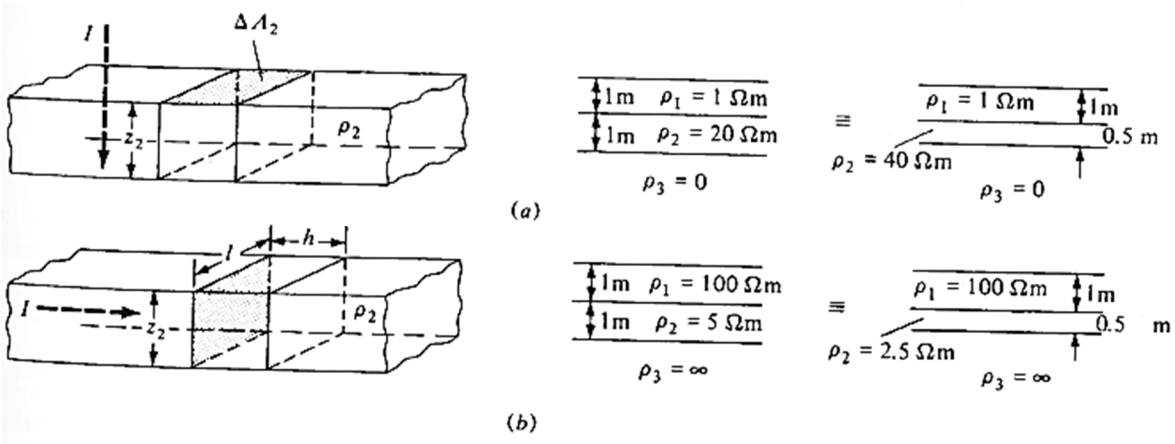

Fig. 16: The equivalence principle (schematic). (a) $\boldsymbol{\rho_1 < \rho_2 > \rho_3}$, $\boldsymbol{\rho_2 z_2}$ *= constant. (b)* $\boldsymbol{\rho_1 > \rho_2 < \rho_3}$, $\boldsymbol{\rho_2 / z_2}$ *= constant (modified after TELFORD et al. 1990: 553).*

6.3. Electrical properties of various rocks, sediments and karst features

Because most rock-forming minerals are very poor conductors, current flow in the ground is primarily conducted through interstitial water by ionic transport (i.e. by dissolved salts, mainly sodium chloride). Hence, the ground resistivity varies with mobility, concentration and degree of dissociation of the ions, while the latter in turn depends on the dielectric constant of the solvent. The relationship between the resistivity of a porous rock and the fluid saturation factor is obtained by the empirical formula due to ARCHIE (1942):

$$\boldsymbol{\rho = a \times \rho_w \times \phi^{-m}}$$

where $\boldsymbol{\rho_w}$ is the fluid resistivity and $\boldsymbol{\phi}$ is the fraction of rock filled with the fluid, whereas **a** and **m** are two empirical parameters (KELLER & FRISCHKNECHT 1966); for most rocks, **a** is about 1 and **m** is about 2, depending on the shape of the pores. This equation is applicable for certain types of rocks and sediments, especially for those characterized by low clay contents.

Resistivities of various rocks and sediments are listed in Tab. 6. Igneous and metamorphic rocks are typically characterized by high resistivities, whereby the resistivity here strongly depends on the degree of fracturing and the percentage of fractures filled with groundwater. As a result, these rock types can show a wide range of resistivity values, from about 1000 Ωm to 10 000 000 Ωm, depending on their moisture content, respectively (LOKE 2004b: 5, MILSOM 2003: 86). Sedimentary rocks, which are basically defined by higher porosities and higher water contents, usually show lower resistivities compared to igneous and metamorphic rocks; resistivity values between 10 Ωm and 30 000 Ωm are achieved, with most values below 1000 Ωm (KRAUTBLATTER et al. 2010: 1,

LOKE 2004b: 5, MILSOM 2003: 86). These resistivity values can be directly related to the porosity of the rocks and the salinity of the contained water. Unconsolidated sediments, in general, have even lower resistivities than sedimentary rocks, with values varying from about 10 Ωm to less than 1000 Ωm (LOKE 2004b: 5, MILSOM 2003: 86); these on their part depend on porosity (assuming all the pores are saturated) as well as on the amount of fine grains. Thus, clayey soils usually show lower resistivities than sandy soils. The presence of clay in the ground, in general, decreases resistivities more than water (which is valid for fresh water, not for salt water) (CHALIKAKIS et al. 2011: 1174). The resistivity of soil water/fresh groundwater ranges from 10 to 100 Ωm, depending on the concentration of dissolved salts (LOKE 2004b: 5, TELFORD et al. 1990: 285).

Tab. 6: Resistivities of various rocks and sediments in ohm-meters (after KNÖDEL et al. 2005: 98, KRAUTBLATTER et al. 2010: 1, LOKE 2004b: 6, MILSOM 2003: 88, TELFORD et al. 1990: 285, 290).

Rock material	**Resistivity range [Ωm]**
Surface/soil water, fresh groundwater	10 – 100
Topsoil	50 – 100
Unconsolidated wet clay	20
Clay	1 – 100
Loose Sand	500 – 5000
Gravel	100 – 600
Weathered bedrock	100 – 1000
Conglomerates	3000 – 10 000
Sandstone	200 (fissured, wet) – 8000 (compact, dry)
Limestone	50 (fissured, wet) – 30 000 (compact, dry)
Marls	5 – 80
Dolomite	500 – 8000
Gabbro	100 – 500 000
Granite	200 – 100 000
Diorite	2000 – 40 000
Basalt	200 – 100 000
Graphitic schist	10 – 500
Slate	500 – 500 000
Quartzite	500 – 800 000

In carbonate karst terrains, geoelectrical imaging methods are routinely used to characterize the (for common) highly heterogeneous subsurface, inter alia composed of undisturbed soils, carbonate rock, clay in-fills and air-/water-filled voids, all generally characterized by very different resistivity values. **Clays** and **clayey deposits/infills** tend to retain moisture and generally show a comparatively high ion concentration to conduct electricity; they are usually characterized by low resistivities (less than 100 Ωm), with variable resistivity values depending on moisture content, purity and unit shape/size (ISMAIL & ANDERSON 2012: 282, 291, TELFORD et al. 1990: 283ff., ZHOU et al. 2000: 761). **Residual soils** are typically characterized by intermediate resistivities (between 25 and 600 Ωm), with variable resistivity values depending on clay and moisture content (ISMAIL & ANDERSON 2012: 282). **Weathered to intact carbonate rock** is generally characterized by higher resistivities (typically more than 400 Ωm, but variable depending on layer thickness,

moisture content and impurities) (ISMAIL & ANDERSON 2012: 282). **Relatively intact carbonate rock** in general has a significantly higher resistivity than clayey soils due to its much smaller primary porosity and fewer interconnected pore spaces; it is characterized by high resistivities (typically more than 1000 Ωm, but again variable depending on layer thickness, moisture content and impurities) (ISMAIL & ANDERSON 2012: 291, TELFORD et al. 1990: 283ff., ZHOU et al. 2000: 761). Dry **air-filled voids** (such as fractures, conduits and cavities) always provide a significant resistivity contrast between the void and the surrounding host rock; they are generally characterized by very high resistivities (typically more than 2000 Ωm), depending on the conductivity of the encompassing material and the size/shape of the void (ISMAIL & ANDERSON 2012: 282, KIDANU et al. 2016: 107, YASSIN et al. 2014: 71). However, isolated areas of anomalously high resistivity values may also be characteristic for air-filled voids, which were backfilled loosely with stone and/or other debris (LABUDA & BAXTER 2001: 4). If a **void** is partially or almost completely **filled with water**, the void may show a resulting electrical conductivity ranging from very conductive to relatively resistive (compared to the host rock), depending on the composition of the water, respectively (CHALIKAKIS et al. 2011: 1171). For usual, the resistivity values will be relatively low if a karst void is filled with water (CHALIKAKIS et al. 2011: 1174, FORD & WILLIAMS 2007: 149). One of the largest subsurface resistivity contrasts in karst terrains exists between intact carbonate rock and **air-filled caves** (or **cave systems**); the latter are usually associated with extremely high (near-infinite) resistivity values (typically varying from several thousands to more than 15 000 Ωm), depending on the conductivity of the encompassing material and the size/shape of the cave (BERMEJO et al. 2017: 396, GAMBETTA et al. 2011: 13, GIBSON et al. 2004: 37). The raveling zone of a **doline** (or **sinkhole**) is generally characterized by increased porosity and reduced percentage of finer grain sizes. Depending on the fraction filled with water, it may be shown as a high-resistive anomaly (if relatively dry) or as a low-resistive anomaly (if relatively saturated), compared to the host rock (FESTA et al. 2012: 140). Deeper void space within the raveling zone is typically characterized by lower resistivities, which are indicative of carbonate materials being replaced by looser clastic sediments or water (FESTA et al. 2012: 140).

6.4. Measuring process for a multi-electrode earth resistivity system

In order to obtain a 2D high-resolution image of the resistivity distribution in the ground, numerous single measurements with varying current and potential electrode positions are required. For this purpose, multi-electrode earth resistivity systems are commonly used with 25 or more electrodes (usually metal stakes) connected to a resistivity meter via multi-core cables. An internal switching circuitry controlled by a programmable microcomputer/microprocessor within the resistivity meter automatically selects the appropriate 4 electrodes for each measurement. The electrodes are commonly spaced between 1 and 20 m. In general, increasing the electrode spacing leads to an increase in penetration depth with a simultaneous decrease in resolution. The maximum penetration depth is typically 20 – 25 % of the maximum field layout (LOKE 1994); it might be reduced when the overburden/surface layers are electrically conductive or highly resistive.

LOKE (2004b: 17) and Fig. 17 demonstrate a possible measuring process for a system with 20 electrodes with spacing between adjacent electrodes is “a”, exemplarily. In a first measuring sequence, all feasible measurements with an electrode spacing of “1a” are carried out. Thereby,

electrodes number 1, 2, 3 and 4 are used. Note that electrode 1 represents the first current electrode C_1, electrode 2 the first potential electrode P_1, electrode 3 the second potential electrode P_2 and electrode 4 the second current electrode C_2. For the second measuring cycle, electrodes number 2, 3, 4 and 5 are used for C_1, P_1, P_2 and C_2, respectively. This series of measurements continuous down the line of electrodes until the last measurement with spacing "1a" is performed for electrodes 17, 18, 19 and 20. After these first 17 measurements with an electrode spacing of "1a", a second measuring sequence with an electrode spacing of "2a" is carried out. At the beginning, electrodes 1, 3, 5 and 7 are used for the first measuring cycle, electrodes 2, 4, 6 and 8 for the second and so on. This series of measurements continuous in turn down the line until electrodes 14, 16, 18 and 20 are used for the last measurement with spacing "2a". The same measuring process is repeated for electrode spacings "3a", "4a", "5a" and "6a", finally.

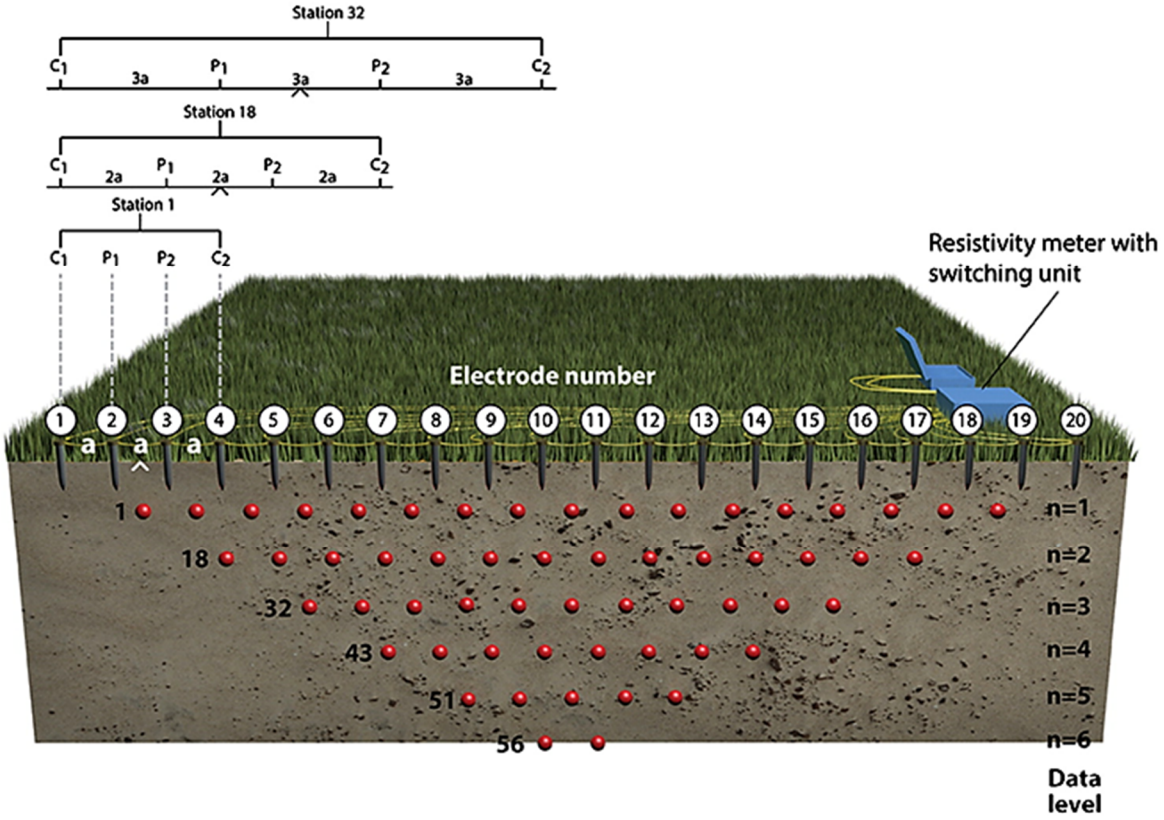

Fig. 17: Schematic diagram of a multi-electrode system, and a possible sequence of measurements to create a 2D pseudosection (British Geological Survey © NERC 2013). Note that the resolution of resistivity data decreases with depth because of the number of measured points decreasing with depth as a function of electrode spacing and electrode configuration.

To extend the area covered by a survey horizontally, the **roll-along method** is commonly used. After completing all possible measurement sequences, the cable is moved past one end of the line by several unit electrode spacings. All the measurements involving the electrodes on part of the cable that do not overlap the original end of the survey line are repeated.

6.5. Commonly used electrode arrays for resistivity acquisition (in a karstic environment)

Fig. 18 illustrates some commonly used electrode arrays with their respective geometric factors. The suitability of an array depends on its sensitivity to the target of interest, the signal-to-noise ratio, the depth of investigation, the lateral data coverage and more recently the efficiency of using it in a multi-channel system (i.e. while two electrodes serve as current electrodes, voltage measurements can be made between many different pairs of potential electrodes at a single time); the multiple gradient array, for instance, was specifically designed for the use in a multi-channel system (DAHLIN & ZHOU 2006). Arrays are often (at least partly) chosen for their penetration depth, which is almost impossible to define, because the depth to which a given fraction of current penetrates into the ground depends on the layering as well as on the separation between the current electrodes. In terms of detecting geological defective karst features, an electrode array responding best to the material change between the respective karst feature and its non-karstic/karstic surrounding is primarily required. Besides the occurrence of noise (i.e. effects of near-surface local variations in resistivity limiting the detectability and resolution of the karst feature), also the application of an inappropriate array might affect its recognition in the apparent resistivity pseudosections. An overview of the main advantages and disadvantages of the different electrode arrays is given by e.g. DAHLIN & ZHOU (2004) or ZHOU et al. (2002).

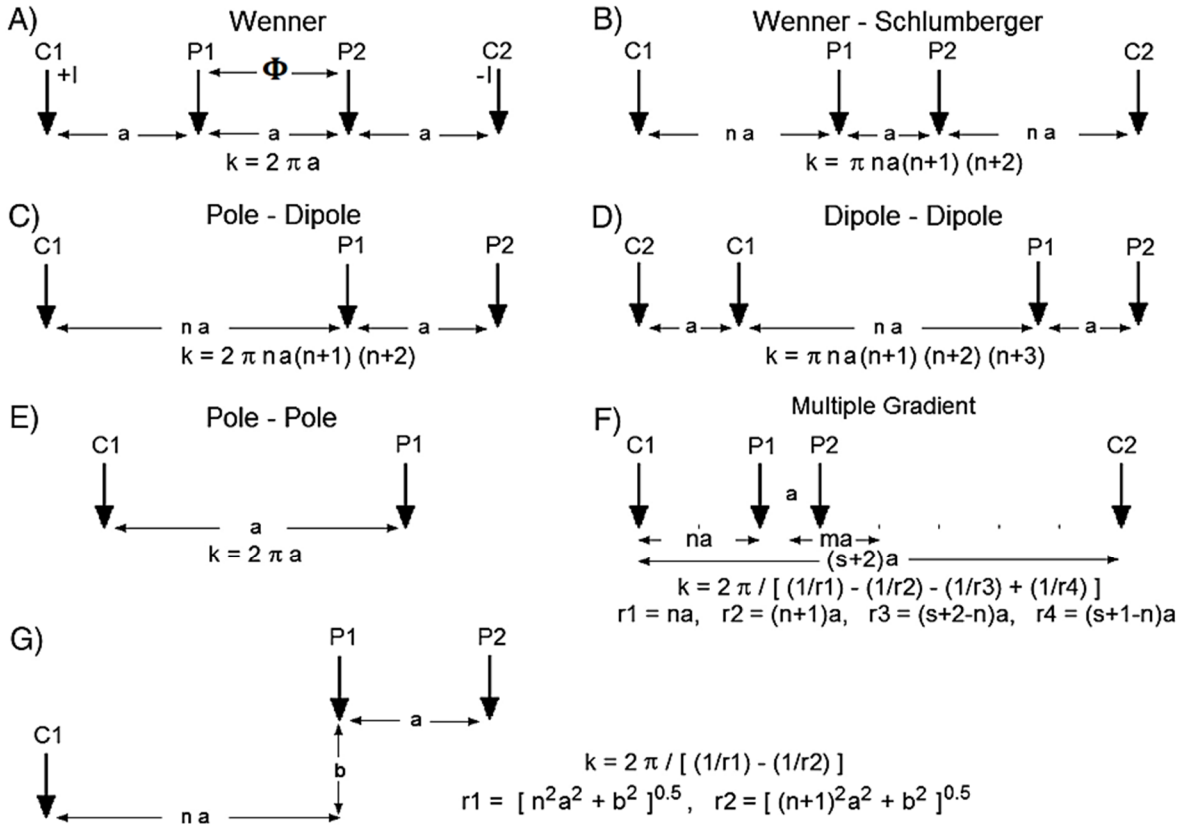

Fig. 18: Some commonly used electrode arrays and their geometric factor (modified after British Geological Survey © NERC 2013). Note that for the multiple gradient array, the total array length is '(s + 2)a', while the distance between the center of the potential dipole pair P_1P_2 and the center of the current pair C_1C_2 is given by 'ma'.

ZHOU et al. (2002) recommend a combination of the Wenner-Schlumberger and the Dipole-dipole array for ERT data acquisition in a karstic environment.

The **Wenner-Schlumberger** array is a relatively new hybrid between the Wenner and the Schlumberger array and arose during the past two decades within electrical imaging surveys (PAZDIREK & BLAHA 1996). Compared to the classical Wenner array, the horizontal data coverage is slightly better with the Wenner-Schlumberger array, but narrower than that obtained with the Dipole-dipole array (LOKE 2004b: 33). The Wenner-Schlumberger array shows a moderate sensitivity to both horizontal (for low **n** values) and vertical structures (for high **n** values). In a highly heterogeneous karstic environment, where both types of geological structures are commonly expected, this array can deliver a good compromise between the high vertical resolution of the classical Wenner array, on the one hand, and the high horizontal resolution of the Dipole-dipole array, on the other. Compared to the Dipole-dipole array, the Wenner-Schlumberger is thus superior in accurately localizing flat-laying interfaces, for instance (MILSOM 2003: 106). Furthermore, the signal strength (which is approximately inversely proportional to the square of the **n** value) as well as the median depth of investigation of the Wenner-Schlumberger array are significantly higher / larger than that of the Dipole-dipole array (LOKE 2004b: 33). In addition, the Wenner-Schlumberger array is characterized by its comparatively lower susceptibility to near-surface inhomogenities (MILSOM 2003: 106), while its resistivity results in turn are generally less affected by artifacts (CARRIÈRE et al. 2013: 34). To summarize, the application of the Wenner-Schlumberger array (with overlapping data levels) is a reasonable all-round alternative in a highly heterogeneous karstic environment, where both good horizontal and vertical resolutions are needed, particularly if good signal strength is also required (LOKE 2004b: 39). An **inverse Wenner-Schlumberger** array can be obtained by the simple exchange of the current and potential electrodes, i.e. current is passed through P_1 and P_2 and the potential is measured between C_1 and C_2 (Fig. 19). Identical apparent resistivity values result from this interchange (even for an anisotropic ground) as a consequence of the theorem of reciprocity (KELLER & FRISCHKNECHT 1966). The only significant disadvantage of the inverse array is the increased telluric noise / the possibly minimized resolution at large potential electrode spacings. This might be the reason why the inverse Wenner-Schlumberger array is yet very rarely used in terms of karst reconnaissance, although it can be applied in a multi-channel system and thus reduces the survey time significantly.

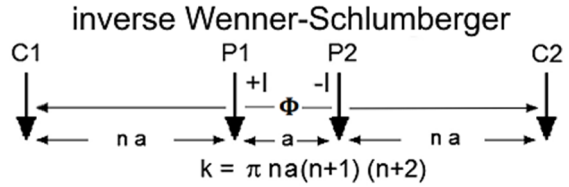

Fig. 19: Inverse Wenner-Schlumberger array with its geometric factor, obtained by the simple exchange of the current and potential electrodes, i.e. current is passed through P_1 and P_2 and the potential is measured between C_1 and C_2.

In comparison with the Wenner-Schlumberger array, the **Dipole-dipole** array is characterized by its better horizontal data coverage and its greater sensitivity to horizontal changes in resistivity (LABUDA & BAXTER 2001: 10, LOKE 2004b: 30f.). While the Dipole-dipole array is thus superior in mapping vertical karst structures such as voids or rock pinnacle / cutter interfaces, it is relatively

poor in mapping horizontal structures such as flat-laying interfaces (LABUDA & BAXTER 2001: 10, LOKE 2004b: 30f., ZHOU et al. 2000: 761). The Dipole-dipole array shows a very small signal strength (LOKE 2004b: 31); its data set might easily be affected by near-surface resistivity variations (GRIFFITHS & BARKER 1993: 213). To summarize, the Dipole-dipole array might be the more suitable choice if good horizontal resolution and data coverage is important (LOKE 2004b: 39).

ZHOU et al. (2002: 923) tested the effectiveness of the Wenner, the Wenner-Schlumberger and the Dipole-dipole array in delineating a collapsed sinkhole (approximately 0.6 m in diameter and 1 m deep, treated as an air-filled cavity due to the absence of soil) along a resistivity section with 3 m electrode spacing in Frederick County, Maryland, USA. While the classical Wenner array could not provide a recognizable signature of the collapsed sinkhole area, the Dipole-dipole array (followed by the Wenner-Schlumberger array) provided the highest precision in delineating the collapsed sinkhole feature and showed the greatest sensitivity to vertical resistivity boundaries (ZHOU et al. 2002: 925ff.). ZHOU et al. (2002: 926) further compared the Dipole-dipole and the Wenner-Schlumberger arrays in locating a water-saturated void (between 1.5 and 2 m deep) along a resistivity section with 1.5 m electrode spacing in Maryville, Tennessee, USA. The Dipole-dipole array was also superior in delineating the water-saturated void (ZHOU et al. 2002: 926). Based on these results, ZHOU et al. (2002) concluded that a combination of the Dipole-dipole (preferred) and the Wenner-Schlumberger array should be used for ERT data acquisition in a karstic environment.

6.6. Resistivity processing

By means of the previously mentioned basic equation for describing the potential distribution in the subsurface due to a point current source:

$$-\boldsymbol{\nabla}.\left[\boldsymbol{\sigma}(x,y,z)\boldsymbol{\nabla\Phi}(x,y,z)\right] = \left(\frac{\mathbf{I}}{\Delta\mathbf{V}}\right)\boldsymbol{\delta}(x-x_s)\boldsymbol{\delta}(y-y_s)\boldsymbol{\delta}(z-z_s)$$

the potential at any point in the subsurface can be calculated if the resistivity distribution is known. This is the **forward problem**, which should specifically be separated from the inverse problem discussed below. For modeling of field data, the forward problem is commonly solved using finite-difference and associated finite volume methods (DEY & MORRISON 1979a,b, PIDLISECKY et al. 2007) as well as the finite-element (COGGON 1971, HOLCOMBE & JIRACEK 1984) method, discretizing the subsurface into a large number of cells, respectively. By using an adequately fine mesh and proper boundary conditions, an accurate solution for the potential over complex distributions of resistivity can be obtained.

The modern application of resistivity processing involves **inverse modeling**. In 1D resistivity surveys, a commonly used method for sounding data inversion is the damped least-squares method (INMAN 1975), based on the equation:

$$(\mathbf{J^T J} + \boldsymbol{\lambda}\mathbf{I})\Delta\mathbf{q} = \mathbf{J^T}\Delta\mathbf{g}$$

where $\Delta\mathbf{g}$ is the discrepancy vector (including the difference between the logarithms of the measured and the calculated apparent resistivity values) and $\Delta\mathbf{q}$ is the deviation vector (including the deviation of the estimated model parameters from the true model; here, the model parameters

are the logarithms of the resistivity and the thickness of the model layers). While **J** is the Jacobian matrix of partial derivatives of apparent resistivity with respect to the model parameters, **λ** is a damping or regularization factor that stabilizes the ill-condition Jacobian matrix usually encountered for geophysical problems (LOKE et al. 2013: 137). Considering a homogeneous ground model, the damped least-squares inversion iteratively refines the model in order to reduce the data misfit to a desired level (usually less than 5 %) (LOKE et al. 2013: 137).

In 2D electrical imaging surveys, fast and stable automatic data inversion techniques (DEGROOT-HEDLIN & CONSTABLE 1990, LI & OLDENBURG 1992, LOKE & BARKER 1996) are recently used. These methods again subdivide the subsurface into a large number of rectangular cells; while the resistivity of the cells may change in the vertical and one horizontal direction, the size and position of the cells are fixed. Different numerical techniques are used to calculate the potentials for the 2D forward model (**forward modeling subroutine**), whereas inverse techniques are subsequently used to back calculate the resistivity that gave rise to the measured potential measurements (**inversion routine**). Considering again a homogeneous half-space model, an optimization method is used to iteratively change the resistivity of the model cells in order to minimize the difference between the measured and calculated apparent resistivity values. This difference between the measured and calculated apparent resistivity values between the pair of **m** data points (**i** = 1, 2, 3,…, **m**) can be quantified by the **Root-Mean-Square** (**RMS**) **error**, given by:

$$\boldsymbol{\varepsilon_{RMS}} = \sqrt{\frac{\sum_{\mathbf{i=1}}^{\mathbf{m}} \left\{ \left(\ln(\boldsymbol{\rho}_{\mathbf{mea\,i}}) - \ln(\boldsymbol{\rho}_{\mathbf{cal\,i}}) \right)^2 \right\}}{\mathbf{m}}} \times 100\%$$

while a small RMS error indicates a close match. The acceptable match is defined by the convergence limit; the default value is normally in the range of 2 – 5 % change in the RMS value between two iterations.

The inversion problem is frequently ill-posed and ill-constrained because of incomplete, inconsistent or noisy data (LOKE et al. 2013: 137). In order to stabilize the inversion procedure to avoid numerical artifacts, smoothness or other constraints are usually incorporated. As described by LOKE et al. (2013: 137) and as an example, the following equation includes a model smoothness constraint to the least-squares optimization method:

$$(\mathbf{J^T J} + \boldsymbol{\lambda}\mathbf{F})\Delta\mathbf{q_k} = \mathbf{J^T}\Delta\mathbf{g_k} - \boldsymbol{\lambda}\mathbf{F}\mathbf{q_{k-1}}$$

where:

$$\mathbf{F} = \boldsymbol{\alpha}_x\mathbf{C}_x^T\mathbf{C}_x + \boldsymbol{\alpha}_z\mathbf{C}_z^T\mathbf{C}_z$$

While $\mathbf{C}_x$ and $\mathbf{C}_z$ are the roughness filter matrices in the horizontal (x) and vertical (z) directions, $\boldsymbol{\alpha}_x$ and $\boldsymbol{\alpha}_z$ are the respective relative weights of the roughness filters; **k** represents the iteration number. One common form of the roughness filter is the first-order difference matrix (DEGROOT-HEDLIN & CONSTABLE 1990), whereby the elements of the matrices can be modified to introduce other desired characteristics into the inversion model (FARQUHARSON 2008, PELLERIN & WANNAMAKER 2005). The **smoothness-constrained least-squares method** (**L2-norm criterion**)

(DEGROOT-HEDLIN & CONSTABLE 1990) delivers a model with a smooth variation in the resistivity values, which is advisable when detecting subsurface bodies with gradational boundaries, for instance. A **robust inversion** (**L1-norm criterion**) can be used to produce 'blocky' models for regions that are piecewise constant and separated by sharp boundaries (FARQUHARSON & OLDENBURG 1998, LOKE et al. 2003). A robust inversion is thus more suitable for detecting karst conduits and cavities as well as sharpening linear features such as faults and contacts within carbonate rock (PUTIŠKA et al. 2014: 158, ZHU et al. 2011: 529). The robust inversion is principally superior to the smoothness-constrained least-squares inversion, because the former attempts to find a model that minimizes the absolute values of the data misfit (L1-norm), whereas the latter seeks a smooth model that minimizes the squares of the data misfit (L2-norm) (DAHLIN & ZHOU 2004: 386f.). In addition, the robust inversion is less sensitive to noise levels and produces fewer artifacts in the inverted models, while the smoothness-constrained least-squares inversion tends to give greater importance to data points with a larger misfit, making it more sensitive to the outliers in a data set (DAHLIN & ZHOU 2004: 387). Joint inversion algorithms using other geophysical or geological data to constrain the model have also been implemented to help produce models that are consistent with known information (e.g. BOUCHEDDA et al. 2012). In order to test a solution's robustness and to minimize numerical artifacts, some inversion parameters may be adjusted, respectively, including **the damping factor**, **flatness filters** and the initial model for the inversion (LOKE 2004b: 56ff., DAHLIN & ZHOU 2004: 387). **Mesh sizes** may also be changed, within certain constraints (LOKE 2004b: 57f.).

6.7. Limitations of the resistivity method (in karst reconnaissance)

The **inverse resistivity problem** has a unique solution for 1D, 2D and 3D resistivity distributions within a boundary (FRIEDEL 2003), but only under strict conditions, where the current and voltage distributions are known continuously and accurately over the boundary for a complete set of current injection patterns (LOKE et al. 2013: 148). In practice, resistivity inversion is non-unique and ill-posed, because only a finite number of electrodes covering part of the surface is in use. As a consequence, more than one resistivity model will produce responses consistent with the observed data to the limits of the data accuracy (HOFFMANN & DIETRICH 2004). Regularization (often in the form of a smoothing matrix (LOKE et al. 2003)) is applied to enforce uniqueness without sacrificing too much resolution.

High-contrast heterogeneities in the subsurface that are small compared to the **model cell-size** cannot be accurately modeled and thus can hinder convergence between the measured data and the resistivity model during the inversion process (LOKE et al. 2013: 149). However, reducing the model cell-size leads to an increase in computer memory and time required for the data inversion; a higher damping constraint to stabilize the inversion model may also be needed (LOKE & DAHLIN 2010, LOKE & LANE 2004). On the basis of numerical tests with 2D models, SASAKI (1992) and LOKE (2012) illustrated that using a model cell-size of half the unit electrode spacing seems to provide the optimum balance.

The measured resistivity data as well as the resulting resistivity images (LABRECQUE et al. 1996) are prone to error from a variety of sources including (i) that introduced by the measurement device,

(ii) **poor electrode contact** (usually identifiable through high contact resistances), (iii) **electrode polarization** and (iv) other indeterminate external effects (DAHLIN 2000, MERRIAM 2005, WILKINSON et al. 2012, ZHOU et al. 2000). These possibly occurring errors are commonly addressed by the appropriate selection and conditioning of electrodes to reduce contact resistance, by using appropriate filters (including reciprocal error analysis) prior to inversion (FERAHTIA et al. 2009, ZHOU & DAHLIN 2003) and by employing measurement sequences that reduce the influence of electrode polarization. During data acquisition, polarization can be reduced by ensuring an adequate time between using an electrode alternately as current or potential electrode (WILKINSON et al. 2012). While the electrode position is usually assumed to be known and fixed for the purposes of geoelectrical monitoring, the accurate positioning of electrodes can be complicated for difficult ground conditions such as steep or heavily vegetated areas. The selection of measurement array geometries less sensitive to positional errors (WILKINSON et al. 2008) as well as estimating the electrode position using a position inversion routine (in the case of moving electrodes on unstable ground) (WILKINSON et al. 2010) might reduce the impact of insufficient electrode positions.

Besides the electrode spacing, the reliability of the ERT method depends on the **orientation of the line** and the **line spacing**. In the presence of nearby **conductive obstacles** (such as utilities etc.), a survey design is recommended, in which the current is traveling perpendicular to the obstacle and thus will only make minimal use of this conductive pathway (ROTH & NYQUIST 2003: 6). Where a single line orientation is used, linear features parallel to the line direction might be poorly resolved (CHAMBERS et al. 2002) and banding or herring-bone effects might be present in the model (LOKE & DAHLIN 2010). Mitigation measures include: roll-along (or multiple line) data acquisition methodologies (DAHLIN et al. 2002), orthogonal line directions (CHAMBERS et al. 2002, GHARIBI & BENTLEY 2005, ROTH et al. 2002, ZHOU et al. 2000), line separations of no more than two electrode spacings (CHAMBERS et al. 2002, GHARIBI & BENTLEY 2005, ROTH et al. 2002) and appropriate inversion settings (e.g. horizontal diagonal roughness filters) (FARQUHARSON 2008, LOKE & DAHLIN 2010). **Off-line three-dimensional structures** (including topography) cannot be accurately modeled by 2D inversion and thus might distort the resistivity model (AHMED & CARPENTER 2003, BENTLEY & GHARIBI 2004, CHAMBERS et al. 2002, NIMMER et al. 2008, ZHOU et al. 2000). Bedrock-surface features such as pinnacles or cutters, for instance, might be shown on the resistivity transect, even if they are actually caused by features lying laterally offset from the transect (AHMED & CARPENTER 2003: 710, ZHOU et al. 2000: 765). Data values near the base of the model section, in particular, often incorporate 3D effects or offline information projected onto the section due to lateral current spreading at wide electrode spacings (AHMED & CARPENTER 2003: 710, ZHOU et al. 2000: 763ff.). These distortion effects can be reduced by ensuring lines are oriented **perpendicular to the strike** of elongated structures or by using a 3D survey approach in complex settings; although it should be noted that the edges of 3D models might also be influenced by 3D structures outside of the survey area (LOKE et al. 2013: 149, ZHOU et al. 2000: 763). Anomalies near the **edge of a model section** should, in general, be interpreted with caution due to the reduced data coverage near the respective end of the electrode layout; a large number of iterations with different inversion parameters might be necessary to ensure an anomaly near the edge of a model section is not a processing artifact (AHMED & CARPENTER 2003: 710). Distortions in the resistivity model might also be produced by the influence of even moderately **anisotropic**

media on the results of the resistivity inversion assuming isotropic conditions (e.g. GREENHALGH et al. 2010, HERWANGER et al. 2004). These distortions might be even more momentous, when using a 3D survey with orthogonal line directions in an anisotropic media, due to differing lateral resistivities in different line directions.

When **exploring geological defective karst voids** and other karstic features, the effectiveness of the ERT method depends on (i) the orientation of the test line, (ii) the horizontal offset from the karst void/feature to the test line and (iii) on the quality of the bedrock surrounding the karst void/feature (ROTH & NYQUIST 2003: 1, 8). The geophysical influence of a karst void (alternatively feature) cannot be determined in real exploration because of the unknown and irregular shape of the void and the (most of the time) unknown degree of filling (CHALIKAKIS et al. 2011: 1174). However, the effective geophysical size of a void is usually larger than its true size, because karstic rock surrounding any void is often disturbed and intensively fractured, creating a larger anomalous volume; a circumstance, which ultimately favors the detection of the void (CHALIKAKIS et al. 2011: 1172f., MCGRATH et al. 2002: 554). A void will not be detected by means of ERT (regardless of line orientation), if it is insulated from low-resistive surface material by a surrounding (high-quality) bedrock, because the current will find a less resistive path and thus will not penetrate the void (ROTH et al. 2002: 229, ROTH & NYQUIST 2003: 8). If the void size increases or if a low-resistive connection such as a water- or soil-filled fracture exists between the void and the low-resistive material, the void may be detected (ROTH et al. 2002: 229, ROTH & NYQUIST 2003: 8). While resistivity lines running perpendicular to an **air-filled fracture** within the bedrock will show a high-resistivity anomaly, resistivity lines running parallel to an air-filled fracture will not indicate the fracture in the results, because the current will travel in the adjacent material; the same will be true for an enlarged opening in the bedrock, e.g. a small cave, if the opening is connected to an air-filled fracture (ROTH & NYQUIST 2003: 8). In contrast, if a **fracture or void contains water or soil** (the void does not need to be filled with these materials, but the water or soil must provide a continuous path for the current), resistivity lines running parallel to the feature will show a low-resistivity anomaly (even for a small fracture), whereas resistivity lines running perpendicular to a water- or soil-filled fracture may not indicate an anomaly unless the fracture is large with respect to the electrode spacing (ROTH & NYQUIST 2003: 8f.). Because fractures typically occur in orthogonal combinations or along bedding planes, it might be difficult to predetermine what orientation of resistivity lines will be optimum for locating voids (ROTH & NYQUIST 2003: 9). However, the likelihood of locating a void will be increased if multiple orientations of lines are used (e.g. both parallel and perpendicular to strike) and if lines are spaced at intervals of approximately 5 m or less (ROTH & NYQUIST 2003: 11). Horizontal offsets from a karst void to the test line of more than approximately 4 m will most probably not indicate the presence of the void anymore (ROTH et al. 2002: 231). Unfortunately, a region of high resistivity alone may not be sufficient to conclude that a void is present; this might also be due to unusually good-quality **bedrock** (ROTH & NYQUIST 2003: 9). Only in areas where the bedrock is of high quality (i.e. with very few fractures / unweathered), the resistivity section would show a continuing increase in resistivity with depth (ROTH et al. 1999: 299). Because resistivity tests only measure average values over a volume of soil and/or rock, a smoothing effect is often identifiable in the resistivity results when compared to the actual bedrock depth (ROTH et al. 2000: 362); even a sharply contrasting

limestone/clay boundary will appear transitional on the processed resistivity images (ZHOU et al. 2000: 762). In addition, it is very difficult to determine the in-situ resistivity values of a soil or bedrock (ZHOU et al. 2000: 762). Even if the ERT technique is well suited to **mapping dolines** (or **sinkholes**) due to its ability to detect resistive features and discriminate subtle resistivity variations in karst environments (FESTA et al. 2012: 140), exploring the geometrical and geophysical properties of dolines proved to be complex and unpredictable since dolines may have differentiated morphologic properties at different scales (SIART et al. 2011: 331).

The ERT method provides only **indirect** information of subsurface physical properties such as lithology, porosity, void ratio, moisture content, cementation or composition (LOKE et al. 2013: 143). Unfortunately, there is no direct causative relationship between electrical resistivity and, say, rock strength. The application of ERT requires other sources of **ground truth data** for a robust interpretation of the resistivity images. For ground investigation, resistivity imaging is routinely applied in combination with intrusive methods such as drillings or cone penetration tests (CPT) (WISEN et al. 2005). Intrusive methods, however, are (for common) spatially much more localized than the apparent resistivity data and local small-scale irregularities are often obscured by the volume-averaging method inherent in the ERT technique (ZHOU et al. 2002: 926ff.). In-situ measurements of resistivity (e.g. CPT resistivity profiles) as well as laboratory testing of subsurface materials (e.g. JACKSON et al. 2006, RUSSELL & BARKER 2010) can be used to directly constrain the inversion of resistivity data by fixing the resistivities of known regions of the model (e.g. GÜNTHER & RÜCKER 2009, PIDLISECKY et al. 2006). For in-situ or laboratory measurements of resistivity to be suitable for constraining inversion, they must provide information at a scale appropriate to the resolution of the ERT model; this is particularly crucial in the case of highly heterogeneous subsurface conditions (LOKE et al. 2013: 149). For CPT derived resistivity measurements, along-profile variability can be used to determine spatial averaging requirements; for laboratory measurements of resistivity, sample volumes and distributions representative of the ERT survey resolution and material heterogeneity are required (LOKE et al. 2013: 149).

6.8. The resistivity method – State of research in terms of karst reconnaissance

The use of the resistivity method has substantially increased in the last 20 years and has quickly becoming a common tool for geotechnical site investigation, particularly in karst areas overlain by clayey soils (CHALIKAKIS et al. 2011: 1175, LOKE et al. 2013: 139, ROTH & NYQUIST 2003: 1). Multi-electrode and multi-channel ERT systems have made it possible to perform large 2D, 3D and even 4D surveys efficiently to resolve complex geological and hydrogeological karst structures (LOKE et al. 2013: 135). Compared to other profiling methods, e.g. seismic refraction or microgravimetry, ERT became apparent as a relative fast and cost efficient method (DANIELSEN 2010: 20, KAUFMANN & DECEUSTER 2014: 24) and, in connection to the construction of a number of tunnels (DAHLIN et al. 1999, CAVINATO et al. 2006, GANERØD et al. 2006), delivered dependable results. As presented by DANIELSEN & DAHLIN (2009), geological and geotechnical parameters such as rock type, RQD, Q-Value, weathering, water leakage and amount of used grout can be qualitatively derived by means of the measured resistivity profiles. ERT measurements affect the entire rock mass and therefore can deliver dependable information on the lithology of the host rock (CHALIKAKIS et al. 2011: 1175). The overall effectiveness of ERT profiling in karst environments

is based on the contrast of different resistivity values, particularly between (i) the limestone host rock and detrital sediments/clayey soils and between (ii) compact limestone, water-saturated karstified limestone and dry karstified limestone (BERMEJO et al. 2017: 393, FORD & WILLIAMS 2007: 148f., ZHOU et al. 2000: 761). ERT has proved to be robust, reliable and efficient in delineating size, location and characterization of different karst features such as sinkholes, shallow conduits or enlarged fractures with high accuracy (CARDARELLI et al. 2006, GUÉRIN et al. 2009, ŠUMANOVAC & WEISSER 2001, VAN SCHOOR 2002, ZHOU et al. 2002, ZHU et al. 2011). Many other karst features including the irregular bedrock surface, overhanging rock ledges, air-/water-/clay-filled cavities within the bedrock or soil mantle, fracture and fault zones, raveling zones at the bedrock-overburden interface and preferential groundwater flow paths have also been detected efficiently by ERT investigations (DUNSCOMB & REHWOLDT 1999: 219ff., FESTA et al. 2012: 140, GAMBETTA et al. 2011: 11, GÉLIS et al. 2010: 1408, PARK et al. 2014: 2797, VAN SCHOOR 2002: 393, ZHOU et al. 2000: 761). The main limitations of the ERT method (in karst reconnaissance) are still (i) the rapid reduction of resolution with distance from the electrodes, (ii) the limited sensitivity to resistive zones beneath conductive zones, (iii) the assumption that the geological structures do not change in direction perpendicular to the survey line (in 2D ERT surveys) and (iv) the fact that the resistive influence of karst features cannot be determined in real exploration because of the unknown and irregular shape of the features and the (most of the time) unknown degree of filling (CHALIKAKIS et al. 2011: 1175, HARRO & KRUSE 2014: 213, KAUFMANN & DECEUSTER 2014: 20, LOKE et al. 2013: 139, 143). The rapid reduction of resolution with distance from the electrodes can be partly reduced by the use of subsurface electrodes located nearer to the region of interest and the use of other geotechnical and geophysical data (if available) to constrain the inversion model (LOKE et al. 2013: 143). The limited sensitivity to resistive zones beneath conductive zones may be restrictive when identifying the depth to limestone bedrock in covered karst terrain, for instance, because the sediments mantling the limestone rock are often clay-rich and highly conductive (HARRO & KRUSE 2014: 213). In contrast to other techniques such as GPR, however, ERT is much more integrative and successful in identifying shallow karst features even when an overlying clay-rich layer is present (CARRIÈRE et al. 2013: 34, GRGICH et al. 2004: 3). The common assumption in 2D ERT surveys that the geological karst structures do not change in the direction perpendicular to the survey line is a reasonable assumption when the survey line can be laid out perpendicular to the strike of the structure (LOKE et al. 2013: 139). However, when significant offline variations are present, distortions in the model produced can lead to erroneous interpretation (LOKE et al. 2013: 139). In some situations, correction factors can be calculated for the 3D effects (WIWATTANACHANG & GIAO 2011: 294ff.) to considerably reduce these distortions in the 2D model (LOKE et al. 2013: 139). In this context, where 2D models suffer from artifacts due to off-line karst structures, 3D ERT surveys play an increasingly important role and should deliver more accurate results as all geological karst structures are 3D in nature (DUNSCOMB & REHWOLDT 1999: 219ff., LOKE et al. 2013: 135, 139). While many of the early 3D surveys applied the Pole-pole array over rather small grids (up to about 20 by 20 electrodes) with measurements in different directions (LI & OLDENBURG 1992: 343ff., PARK & VAN 1991: 951ff.), the use of other arrays, such as the Wenner-Schlumberger or Dipole-dipole, is now becoming more common in surveys that involve thousands of electrode positions (LOKE et al. 2013: 139). To avoid a complete 3D

measuring setup, which requires placing of electrodes in the form of a 2D grid with measurements in different directions, 3D data sets are usually collated from independent parallel 2D survey lines with possibly orthogonal cross-lines; a cost-effective strategy (RUCKER et al. 2009: 150ff.). In this context, LOKE & DAHLIN (2010) describe some techniques to reduce artifacts in the 3D inversion model that could be caused in the use of parallel 2D lines. 3D ERT is generally sensitive to rock discontinuities and can resolve some spatial karst features that might be hidden to the application of 2D ERT (CHALIKAKIS et al. 2011: 1175).

6.9. Recent practical applications of the resistivity method in carbonate karst terrains

Exploration of various subsurface karst features

In the course of an extensive case study in southern Indiana, USA, 49 ERT transects in 2D / 3D associated with 39 pre-existing soil borings were effectively used to depict the karstified **limestone bedrock surface**, which was overlain by an unconsolidated clayey soil cover with a thickness of about 9 m (ZHOU et al. 2000: 760ff.). Nevertheless, ZHOU et al. (2000: 762) rightly noted that the exact depth to bedrock surface could not be determined from the ERT sections, because even a sharply contrasting limestone/clay boundary will appear transitional on the processed images; therefore, "ground-truth" data should always be available for interpreting the ERT transects. Furthermore, ZHOU et al. (2000: 763) stated that the incorporation of the boring data into the true resistivity profiles was not straightforward because boring data, in general, are spatially more localized than the apparent resistivity data and because the depth to bedrock does not correspond to a single value of resistivity. Therefore, ZHOU et al. (2000: 763) made two assumptions to facilitate their interpretation, namely that (i) the contact between limestone bedrock and soil is laterally continuous and corresponds to a single value of resistivity and that (ii) this contact is sharp rather than gradational. To evaluate the repeatability of the ERT technique, ZHOU et al. (2000: 760, 766) subsequently compared the limestone bedrock surface elevations determined from the borings with that interpreted from pairs of intersecting ERT transects. As a result, an average difference of 2.4 m, with a maximum of 10 m, between interpreted bedrock-surface elevations for a transect intersection was observed, possibly caused by variations in the subsurface geology normal to the transects (ZHOU et al. 2000: 760). Thereupon, ZHOU et al. (2000: 760, 765f.) averaged the elevation data interpreted from intersecting transects to increase the representativeness of the ERT interpretation; in the end, an average difference between interpreted and actual bedrock surface-elevations of less than 0.4 m was obtained. In this context, ZHOU et al. (2000: 766) emphasized that the three-dimensional variation of geological karst features such as the irregular distribution of pinnacles and cutters constitute an important factor affecting the reliability of the ERT technique in karst terrains. ERT setup: AGI Sting earth resistivity meter, Dipole-dipole array, 3 m electrode spacing, RMS error range: 1.8 – 118.2 %, average RMS error: 37.1 %.

At a study site in Nashville, Tennessee, USA, 2D ERT proved to be efficient in mapping vertical solution-enlarged **clay-filled fractures** within a horizontally bedded limestone formation and in differentiating between **clayey soil** (< 264 Ωm), transitional zones (264 – 1238 Ωm) and **limestone bedrock** (> 1238 Ωm); 10 boreholes drilled along the transect, including two directional boreholes, served for a reasonably good calibration (ZHOU et al. 2002: 926ff.). However, ZHOU et al. (2002:

926ff.) emphasized again that caution must constantly be taken when boring data are used to interpret the depth to bedrock surface, because boring data are much more localized than the resistivity measurements and local irregularities are often obscured by the volume-averaging method inherent in the resistivity technique. ERT setup: AGI Sting earth resistivity meter, Dipole-dipole array, 1.5 m electrode spacing, roll-along technique.

In two case studies in Short Gap, Mineral County, and near Front Royal, Warren County, Virginia, USA, 2D / 3D resistivity imaging techniques were applied over karstic limestone and dolomite bedrock to detect areas vulnerable to sinkhole development and to delineate subsurface karst features such as open and/or soil-filled caverns (LABUDA & BAXTER 2001: 1f., 6). In correlation with limited corehole data and surface mapping work, the 2D resistivity sections reached a penetration depth of around 20 m and revealed the **bedrock surface** at a depth of 3 – 20 m, **clay-** and **air-filled voids**, **rock ledges** and steeply dipping **fracture zones**/**solution cavities** (LABUDA & BAXTER 2001: 1ff., 6ff.). ERT setup: AGI Sting R1 earth resistivity meter, Dipole-dipole array, 3 m / 4 m / 5 m electrode spacing.

Building upon the findings obtained within two previous case studies, ROTH & NYQUIST (2003: 1ff.) evaluated multi-electrode resistivity testing over a two-year period at two karst sites in Northampton County, Pennsylvania, USA, by comparing over 140 resistivity tests with the results from 51 borings including bedrock samples and down-hole camera investigations. The results demonstrated that multi-electrode resistivity can reliably map the depth to soil-covered and fractured **limestone** and **dolomite bedrock** with excellent repeatability, although there was some smoothing in areas where the true bedrock surface is highly irregular; in this regard, the Dipole-dipole arrangement provided the greatest detail at both sites (ROTH & NYQUIST 2003: 1ff.). In terms of repeatability, the greatest differences in individual results were located in areas of very high resistivity values (> 4000 Ωm) (ROTH & NYQUIST 2003: 6). In contrast, the multi-electrode resistivity method was not as efficient at locating **voids** and **fractures** (ROTH & NYQUIST 2003: 1, 8). Its effectiveness depended on the orientation of the test line, the horizontal offset from the void to the test line and the quality of the bedrock surrounding the void/fracture (ROTH & NYQUIST 2003: 1, 8). For an exemplary 4-m-high void containing wet soil, resistivity lines in a particular line orientation indicated the void as a low-resistivity anomaly, whereas resistivity lines in a perpendicular line orientation showed up the same void as a large region of high resistivity that could easily be mistaken for bedrock; the results for most voids encountered at the sites indicated sensitivity with respect to line orientation (ROTH & NYQUIST 2003: 9). Direct probing investigation setup: drill rig equipped with hollow stem auger and core barrels. ERT setup: Dipole-dipole / Wenner-Schlumberger / Wenner array, 1 – 3 m electrode spacing, robust inversion, RMS error: 1.4 – 6.7 %.

At two sinkhole sites near Centurion, south of Pretoria, South Africa, 2D ERT profiles were conducted in a highly weathered dolomite bedrock environment through the center of the sinkhole's surface expression, respectively, to map the true extent of the **sinkholes** and to examine the existence of previously unknown cavities (VAN SCHOOR 2002: 393f., 396). The ERT measurements revealed two basin-shaped zones of highly weathered dolomite bedrock with a depth extent of about 10 – 15 m (250 – 600 Ωm) and with the perceived 'edges' of the sinkholes occurring directly above the regions of deepest weathering, respectively (VAN SCHOOR 2002: 394ff.).

Furthermore, the ERT survey allowed the interpretation of an **air-filled cavity** with a depth extent of 10 – 20 m (800 – 1000 Ωm) (VAN SCHOOR 2002: 398). ERT setup: Dipole-dipole array, 8 m electrode spacing.

In the town of Maynooth, County Kildare, eastern Ireland, 2D resistivity imaging indicated an unknown 210 m long, 70 m wide and 25 m deep infilled **collapse feature** within a limestone formation beneath 10 m thick surficial sediments (GIBSON et al. 2004: 35ff.). Another 2D resistivity survey taken over the Cloyne caves, County Cork, Ireland, moderately delineated position and extent of the **cave system** (30 000 Ωm) below a surficial sediment cover (GIBSON et al. 2004: 35ff.).

At the karst research area Metzgar Field, eastern Pennsylvania, USA, 2D resistivity data were collected using the traditional Dipole-dipole array and a computer-optimized array (STUMMER et al. 2004, increased coverage at depth due to many more widely spaced electrode pairs) to compare the method's relative ability to determine depth to limestone bedrock and to locate air-filled cavities within this limestone bedrock, which was overlain by a thin mantle of clayey soils (NYQUIST et al. 2007: 139f., 142). Against the hypothesis that the optimal array would offer significantly better resolution at depth, the Dipole-dipole and optimal arrays were equally effective in mapping the **karst bedrock topography** (1000 Ωm) and in delineating several **air-filled cavities** (> 3000 Ωm), as was confirmed by drilling logs and downhole camera tests; the few points where the augering and resistivity data disagreed dramatically were probably narrow soil-filled dissolution features – bedrock weathering on a scale too fine to be resolved (NYQUIST et al. 2007: 139f., 142f.). When the full grid of 2D lines were combined and analyzed using 3D inversion, however, the optimal array was able to resolve a crosscutting **bedrock fracture system** that was not visible in the Dipole-dipole data, but could be confirmed by drilling (NYQUIST et al. 2007: 139). ERT setup: AGI SUPERSTING R8 earth resistivity meter, 3 m electrode spacing, lines oriented both perpendicular and parallel to strike. Direct probing investigation setup: drill rig equipped with auger.

Another 2D geoelectrical resistivity survey was conducted in an abandoned quarry at Batu Caves, Kuala Lumpur, Malaysia, to investigate suspected subsurface karst features such as cavities, pinnacles and buried channels of a selected limestone bedrock area (ABU-SHARIAH 2002). In conjunction with borehole records, the 2D geoelectrical resistivity survey reached the bottom of a known subterranean **water-filled cavity** and was able to delineate its location and extent but not its exact geometry (ABU-SHARIAH 2009: 239f., 243). ERT setup: Wenner-alpha array, 2 m electrode spacing.

At the Torcas-Cueva Mayor endokarst system, Sierra de Atapuerca, Burgos, Spain, 2D ERT was applied in order to prospect and analyze endokarstic morphologies and sedimentary infills (ORTEGA et al. 2010: 233f.). By means of topographic, archaeological, geological and geomorphological data, the ERT measurements were able to identify the **limestone** and **dolomite bedrock** (> 1500 Ωm), **sediments** and **valley infills** up to a depth of 20 – 24 m (< 400 Ωm), **air-filled cavities** (> 1500 Ωm) as well as **endokarstic passages** filled with speleothems (400 – 1500 Ωm) or detrital materials (< 400 Ωm); the Wenner-Schlumberger profiles provided more realistic images in this context (ORTEGA et al. 2010: 236f., 242). ERT setup: IRIS SYSCAL R1 Plus Switch-72 resistivity meter, Dipole-dipole / Wenner-Schlumberger array, 1 – 5 m electrode spacing, RMS error: 2.5 – 64.4 % (Dipole-dipole) / 5.9 – 88.5 % (Wenner-Schlumberger).

In the Inner Bluegrass karst region, central Kentucky, USA, 2D / 3D ERT was conducted to detect and characterize unmapped karst conduits developed within a karstified limestone bedrock and covered by a continuous thin clay-rich soil layer (ZHU et al. 2011: 523f., 527ff.). The ERT measurements revealed the clay-rich **soil cover** and multiple low resistivity anomalies beneath the soil-bedrock interface, which were generally associated with moisture zones in the subsurface (ZHU et al. 2011: 525ff., 529). Among 15 exploratory boreholes, which were drilled to these low resistivity anomalies for verification, none actually intersected a major conduit; **water-filled conduits** and other **water-bearing zones** were undistinguishable by means of ERT (ZHU et al. 2011: 523, 527). ERT setup: AGI SUPERSTING R8 earth resistivity meter, Dipole-dipole array, 3.1 m electrode spacing, roll-along technique, lines oriented perpendicular to the direction of estimated conduits, smoothness-constrained least-squares inversion, RMS error: 4.88 – 7.97 %.

At Masseria Forte di Morello, Salento Peninsula, southern Italy, ERT measurements were implemented to study the deep geometry of a sinkhole developed within well-stratified carbonate bedrock (FESTA et al. 2012: 137). In conjunction with geological field mapping, the resulting 2D resistivity section allowed the detection of **carbonate bedrock** (> 1000 Ωm), a belt of **fractured carbonate rock** near the sinkhole (abrupt lateral resistivity lowering) and a funnel-shaped **sinkhole** body filled with clayey sand (3 – 30 Ωm) and carbonate breccia (30 – 100 Ωm) (FESTA et al. 2012: 143f.). ERT setup: Dipole-dipole array, 5 m electrode spacing, RMS error: 2.1 %.

In Chania, western Crete, Greece, 2D / 3D ERT, among others, was employed in order to image the complex tectonic structure of an active karstic system of the Omalos polje, to delineate the metamorphic karstified carbonate bedrock and to estimate the maximum thickness of the overlying deposits (terra rossa, clays, sands and gravels) (HAMDAN et al. 2012: 199ff.). Based on previous borehole-calibrated ERT surveys, the geoelectrical sections revealed the **carbonate bedrock** with a highly irregular relief at 25 – 70 m below the surface (300 Ωm), the **overlying deposits** with a varying thickness of 25 – 70 m (200 – 3500 Ωm) and another karstic structure at a depth of 25 – 55 m; the relatively high RMS error of 9.2 – 15.5 % was justified by the highly heterogeneous overlying deposits (HAMDAN et al. 2012: 199ff., 207). ERT setup: Wenner-Schlumberger array, 10 m electrode spacing, roll-along technique, 2D smoothness-constrained least-squares inversion / 3D robust inversion, RMS error: 9.2 – 15.5 %.

In a case study from the An Nu'ayriyah area, southwest of Al Khafji city, northeastern Kingdom of Saudi Arabia, 2D ERT was carried out across a shallow circular **karst depression** encountered at a subhorizontal sedimentary strata comprised of sandstones, marls and limestones and overlain by gravely deposits (YOUSSEF et al. 2012a: 30f.). The 2D ERT data proved to be successful in detecting and mapping the vertical and lateral dimensions of the 150 m wide and 50 m deep depression (YOUSSEF et al. 2012a: 33ff.). ERT setup: IRIS ELREC T resistivity/IP system / IRIS SYSCAL Pro resistivity meter, Wenner / Wenner-Schlumberger array, 10 m / 20 m / 40 m electrode spacing, smoothness-constrained least-squares inversion, RMS error: 3.5 – 4.0 % / 6.4 % / 9.2 – 16.6 %.

In another case study at Al Eitaliyah, northeast of Ar Riyad City, also Kingdom of Saudi Arabia, 2D ERT was applied to delineate buried sinkholes and associated subsurface cavities developed within a karstified limestone and dolomite bedrock and covered by a calcareous sandstone and overlying clasts of limestone in a calcareous sand and clay matrix (YOUSSEF et al. 2012b: 655ff.,

662). A first 2D ERT measuring sequence reached a maximum penetration depth of more than 65 m and probably delineated the karstified **limestone** and **dolomite bedrock** (> 140 Ωm) from the overlying layers (10 – 140 Ωm) at a depth of 45 m; however, this arrangement with an electrode spacing of 5 m failed in detecting a known **air-filled cavity** due to the relative small dimension of the cavity of less than 5 m (YOUSSEF et al. 2012b: 655, 659ff.). The second 2D ERT measuring sequence reached a maximum penetration depth of only 13 m, but now detected the known air-filled cavity at a depth of 2 – 4 m and determined its three-dimensional volume with a height of 2 – 4 m and a width of 5 – 7 m (2000 Ωm) (YOUSSEF et al. 2012b: 655, 659ff.). First ERT setup: IRIS SYSCAL Pro resistivity meter, Dipole-dipole array, 5 m electrode spacing, smoothness-constrained least-squares inversion, RMS error: 3.5 %. Second ERT setup: IRIS SYSCAL Pro resistivity meter, Dipole-dipole array, 1 m electrode spacing, smoothness-constrained least-squares inversion, RMS error: 2.4 – 3.8 %.

At two highway construction sites in Greene County and Jefferson County, Missouri, USA, 2D / 3D ERT data were acquired across and in proximity to an active sinkhole to identify and map air-filled karst cavities and the top of limestone bedrock (ISMAIL & ANDERSON 2012: 281f.). At site 1 (Greene County), after correlating the resistivity profiles with corresponding boreholes, the 2D / 3D ERT imaged the top of **limestone bedrock** (> 900 Ωm), a number of **clay-filled**, solution-widened **joints** (< 105 Ωm) and proved, furthermore, that the **sinkhole** was not underlain by a substantive **air-filled cavity** (ISMAIL & ANDERSON 2012: 281, 285ff., 289). At site 2 (Jefferson County), in conjunction with calibrated resistivity profiles, the 2D / 3D ERT enabled the interpretation of intact limestone (> 1000 Ωm), zones of **clay in-fill** or ponded **water-clay in-fill** in the base of the sinkhole (< 300 Ωm) and transitional zones probably consisting of wet fractured and/or weathered limestone and clay in-fill (300 – 1000 Ωm) (ISMAIL & ANDERSON 2012: 281, 285, 289). ERT setup site 1: AGI SUPERSTING R8 earth resistivity meter, Dipole-dipole array, 1.5 m electrode spacing, lines oriented perpendicular to the dominant solution-widened joint system, 2D robust inversion / 3D smoothness-constrained least-squares inversion. ERT setup site 2: AGI SUPERSTING R8 earth resistivity meter, Dipole-dipole array, 3.5 m electrode spacing, lines oriented perpendicular to the long axis of the oval-shaped sinkhole and the most prominent solution-widened joints, 2D robust inversion / 3D smoothness-constrained least-squares inversion.

In two case studies at Guanlu village and Momoshan village, Shangdong Province, China, the ERT method was used to constrain the vertical and horizontal extension of certain karstified and fractured zones within a karst water-bearing limestone bedrock, which was overlain by nearly 30 m thick sandy and gravely deposits (GAN et al. 2013: 255ff.). The ERT profiling reached a maximum penetration depth of about 150 m and, in conjunction with borehole logs, revealed several vertical **karst fissures** (GAN et al. 2013: 256ff.). ERT setup: WGMD-3 unit, Schlumberger array, 10 m electrode spacing, lines oriented perpendicular to the strike of the zone, RMS error: 2.0 – 3.3 %.

At the Abu Baara earth dam, northwestern Syria, the application of 2D ERT revealed the presence of several subsurface karst structures developed within a fractured and karstified limestone and dolomite bedrock and overlain by partly more than 25 m thick alluvial deposits (AL-FARES 2014: 1, 5f.). The ERT measurements proved to be efficient in detecting karst **cavities**, **faults**, **fractures** and **discontinuity features** and were compatible with lithological columns of piezometric boreholes (AL-FARES 2014: 3ff.). ERT setup: IRIS SYSCAL Pro Switch-72 resistivity meter, Wenner-

Schlumberger array, 5 m / 2 m electrode spacing, roll-along technique, smoothness-constrained least-squares inversion, RMS error: 6.0 – 7.2 %.

In the course of a cover collapse sinkhole investigation study at the Bordeaux Apartments, Tampa, west-central Florida, USA, HARRO & KRUSE (2014: 213f.) improved ERT's sensitivity and resolution by implanting an electrode array in a clay-rich karst cover at depths near the top of the limestone bedrock (~ 10 m) with direct push technology (Multi-Electrode Resistivity Implant Technique, MERIT), in addition to readings at the surface. The combination of both surface and deep measurements improved the resolution of the **epikarst** and the resolution of the **cover collapse development zone** at the sediment-limestone interface over that from surface measurements alone (HARRO & KRUSE 2014: 213, 216). ERT setup: Dipole-dipole / inverse-Schlumberger array, 3.3 m electrode spacing at surface and at 10 m depth, RMS error: 11.1 %.

In a karst area in Muan-gun, Jeollanam-do, Korea, crosshole ERT was conducted between six boreholes to examine the spatial distribution and shape of underground cavities and weak zones developed within a limestone bedrock and covered by a 4 – 10 m thick layer of alluvial deposits of high-viscosity clay (PARK et al. 2014: 2797ff.). Based on direct drilling and coring data, the field ERT results revealed a **clay-filled** vein-type **cavity** within an inclined fault and fracture zone (PARK et al. 2014: 2797ff., 2805). ERT setup: AGI SUPERSTING R8 IP earth resistivity/IP meter, Pole-pole / Pole-dipole array, 8 m / 12 m electrode spacing.

In a case study from the Tepal area, near Shahrood, northeastern Iran, ERT profiling was more or less successfully used on a macroscopic scale to recognize and explore **karstic water zones** within a thick-bedded to massive limestone bedrock up to a depth of approximately 176 m (SHARIFI et al. 2014: 1, 3, 8). ERT setup: ABEM Terrameter SAS 4000, Dipole-dipole array, 75 m electrode spacing, RMS error: 5.6 – 14 % for a maximum of 22 iterations.

At two construction sites north of Ipoh city, Perak, Peninsular Malaysia, 2D ERT surveys were performed in order to estimate the depth of karstic carbonate bedrock and to determine near-surface karst features such as cavities, sinkholes, intensely fractured zones and faults (YASSIN et al. 2014: 55, 81). The 2D ERT profiles indicated (i) the weathered and fractured marbleized **limestone bedrock** at depths between 1.25 m and more than 28 m, (ii) the intact marbleized limestone bedrock with asymmetrical topography at depths between 4 m and more than 28 m, (iii) several **pinnacles** at depths between 3 m and 19 m, (iv) two **clay-filled depressions** with a maximum extent of 75 m and a maximum depth of approximately 18 m (10 – 70 Ωm) and (v) **sinkholes** with a maximum extent of more than 55 m in diameter and more than 28.7 m in depth (YASSIN et al. 2014: 68f., 72f., 74ff., 79ff.). In addition, YASSIN et al. (2014: 73f., 77f.) tried to differentiate the sinkholes' sediment fillings varying from soft/stiff clay/silt to sand with/without ponded water, respectively (5 – 160 Ωm). ERT setup: ABEM Terrameter SAS 1000, Wenner array, 5 m electrode spacing, RMS error: 4.0 – 9.6 %.

At a test site within the limestone karst hydrosystem of the Fontaine de Vaucluse, Rustrel, France, a large-scale ERT surface-based time-lapse experiment was carried out during and after a rainy episode (17 days) to evaluate efficiency and limits of the ERT in monitoring water infiltration via previously recognized karst features (CARRIÈRE et al. 2015: 45f.). The ERT revealed **preferential pathways** without providing enough precision to determine their exact geometry and functioning

(CARRIÈRE et al. 2015: 45ff.). At the same study site, ERT and GPR were used earlier to study the geological structure of the karst unsaturated zone (CARRIÈRE et al. 2013: 31). ERT prospected down to a depth of 40 m and was able to detect **limestone bedrock** (> 2000 Ωm), a **clayey soil overburden** and a stratification change corresponding to slanted bedding (~ 900 Ωm) (CARRIÈRE et al. 2013: 31, 34f., 37ff.). Although GPR's investigation depth remained limited to around 12 m due to the conductive overburdened clayey soil, its results clearly identified the zone of stratification change and highlighted many **fractures** within the limestone, which were not or not well detected by ERT; this is because the chosen ERT arrays and inter-electrode space were not well fitted (CARRIÈRE et al. 2013: 31, 33f., 37ff.). ERT setup 2015: ABEM Terrameter SAS 4000. ERT setup 2013: ABEM Terrameter SAS 4000, Wenner-Schlumberger / Dipole-dipole / Gradient array, 2 m / 4 m electrode spacing, standard-constrained and least-squares inversion, model refinement with widths of half the unit inter-electrode spacing. GPR setup 2013: 250 MHz antenna, spacing traces: 0.2 m, recording time: ~ 420 ns, each trace stacked 128 times.

In a study at Tapah, Perak, Malaysia, 2D electrical resistivity imaging was conducted to map karst features within a limestone formation (FADHLI et al. 2015: 349, 355). The 2D inverted resistivity sections reached a penetration depth of around 80 m, were correlated with 14 boreholes (including standard penetration tests (SPT) and rock quality designation tests (RQD)) and revealed different karst features such as **filled cavities**, **boulders**, **pinnacles**, **discontinuities** and the **limestone rockhead** at a depth of 18 m (FADHLI et al. 2015: 349f., 353). ERT setup: ABEM Terrameter SAS 4000, Wenner-Schlumberger array, 5 m electrode spacing, roll-along technique, least-squares inversion.

In a case study from Amdoun, northwestern Tunisia, an ERT survey was conducted to examine the spatial distribution and shape of underground cavities developed within a fractured and karstic limestone bedrock and covered by a thin layer of clay (REDHAOUNIA et al. 2015: 1289). The 2D / 3D geoelectrical sections indicated the geometry and the position of several isolated **cavities** at various depths and the presence of an ovular **cave** (1000 – 5794 Ωm) with moderate resolution (REDHAOUNIA et al. 2015: 1289, 1294ff.). In addition, REDHAOUNIA et al. (2015: 1297) tried to delineate the **weathering zone** composed of clays and marls (4 – 16 Ωm) and the **epikarst zone** with large fractures and karstic features clearly visible on an outcrop (4 – 80 Ωm) from the underlying **endokarst zone** of the fractured limestone formation (80 – 1670 Ωm). ERT setup: ABEM Terrameter SAS 4000, Wenner array, 5 m electrode spacing, maximally smooth least-squares inversion, RMS error: 2.73 – 2.98 %.

In the sedimentary Acque Albule Basin, northeast of Rome, central Italy, which is superficially filled by a 50 – 90 m thick travertine body and characterized by intense karst processes with formation of sinkholes and caves, a detailed subsurface study was performed to obtain information about the lateral and vertical distribution of shallow rock resistivity (BILLI et al. 2016: 63, 66f., 73). Based on calibration tests, DPSH penetration tests, borehole logs, available exposures and previous borehole-calibrated ERT studies, lateral interruptions in the ERT cross-sections could be defined as a series of shallow **clay-filled sinkholes**, **cavities** and **caves** that were substantially hidden to the resolution of aerial photographs, DEMs and field surveys (BILLI et al. 2016: 63, 75ff.). ERT setup: PASI 16S24N electrical device, Wenner / Schlumberger array, 1 – 4 m electrode spacing, smoothness-constrained least-squares inversion, RMS error: < 6 %.

At the previously mentioned study site in Greene County, Missouri, USA, 2D ERT profiles were again acquired across and in proximity to an active sinkhole developed within fractured limestone bedrock to image and characterize the subsurface morphology (KIDANU et al. 2016: 99f., 107, 113). Based on confirmatory borehole data, the ERT measurements allowed the interpretation of the top of weathered **limestone bedrock** (125 Ωm), the top of competent limestone bedrock (> 600 Ωm), the presence of **moisture** and/or **clay-filled fractures** (< 125 Ωm) and, once again, indicated that the active sinkhole was not underlain by any substantive **air-filled cavities** (KIDANU et al. 2016: 107). Direct probing investigation setup: drill rig equipped with hollow stem auger and core barrels. ERT setup: AGI SUPERSTING R8 earth resistivity meter, Dipole-dipole array, 1.52 m electrode spacing, lines oriented perpendicular to major joints and regional geological structures.

At the Tuwaiq Mountain Limestone rock, Riyadh region, Kingdom of Saudi Arabia, 2D ERI associated with borehole records (penetration logs) clearly indicated the location of subsurface **cavities** at depths of 1 – 2 m (ABD EL AAL 2017: 220f.). ERI setup: 1 m electrode spacing, RMS error: 8.2 – 18.6 %.

Over the archaeological sites of Gran Dolina and Galería Complex, Sierra de Atapuerca, Burgos, Spain, 2D and 3D ERT imaging was applied to identify their karst system dimension and continuity, respectively (BERMEJO et al. 2017: 393). By means of the 2D and 3D profiles, it was possible to determine the extension of **conduits**, the presence of a filled **cave** entrance and, thanks to topographic maps, the exact location of the Cueva Peluda cave; resistivity values higher than 6575 Ωm could be assigned to the aerial part of the cave and lower than 500 Ωm to the detrital infillings (BERMEJO et al. 2017: 393, 396f.). ERT setup: IRIS SYSCAL Pro Switch-72 resistivity meter, Wenner-Schlumberger array, 2 m electrode spacing, robust inversion, RMS error: 1.9 – 11.4 %.

Combination with microgravity, seismic and GPR methods

At a karst site in Northampton County, northeastern Pennsylvania, USA, ROTH et al. (2000: 359f.) compared microgravity, multi-electrode resistivity and boring data to test the hypothesis that a combination of resistivity and gravity results can be used to locate **voids** in an area characterized by highly irregular **limestone** and **dolomite bedrock** surfaces with solution-enlarged fissures and pinnacles. Based on the results gained within this study, ROTH et al. (2000: 359ff., 365) concluded that 2D resistivity as well as microgravity can successfully be used to predict bedrock depths (~ 1500 Ωm); the actual bedrock depths were obtained from borings. Nevertheless, a smoothing effect was identifiable in the geophysical results when compared to the actual bedrock depth, because microgravity as well as resistivity tests only measure average values over a volume of soil and/or rock (ROTH et al. 2000: 362). In the course of this study, ROTH et al. (2000: 359) also illustrated the difficulty to distinguish anomalies caused by shallow voids from those caused by abrupt changes in bedrock depth (common in karst terrain) using resistivity or microgravity alone. ROTH et al. (2000: 359) further clarified that void locations cannot be reliably identified by a combination of resistivity and microgravity, because fluctuations observed in the gravity data in areas without voids were of a similar magnitude to those observed in areas with voids. In terms of interpreting boring data, ROTH et al. (2000: 362) stated that borings located in a fissure (which is often unavoidable due to the pinnacled nature of the karstic bedrock surface) might misleadingly be used to infer bedrock depths much greater than the average bedrock surface. In addition, ledges

(large areas of unweathered bedrock that remain in the soil profile) might be encountered and interpreted as areas of shallow bedrock if they caused refusal of the drilling auger; besides, rock ledges may also affect the geophysical results (ROTH et al. 2000: 362). ERT setup: AGI system, Dipole-dipole array, 3 m electrode spacing, lines oriented perpendicular to strike, least-squares inversion. Microgravity setup: Scintrex CG-3M autograv microgravity meter, resolution: 1 µGal, station spacing: 2 m, residual Bouguer gravity. Direct probing investigation setup: drill rig equipped with hollow stem auger, boring intervals: ~ 2.5 m.

At the Schwyll catchment area near Bridgend, South Wales, United Kingdom, microgravity surveying revealed areas of mass deficiency (–0.035 to –0.040 µGal) within the limestone host rock and, in-between, indicated the presence of interconnecting subsurface **karst channels** expressed by semi-linear gravity lows (–0.010 to +0.020 µGal); this anomaly amplitude might be smaller, if the interconnecting channels are either deeper or thinner or both (MCGRATH et al. 2002: 552, 555). In addition, 2D resistivity profiles clearly indicated the presence of a low resistivity area/layer around 2 – 4 m depth, which correlated very well with the gravity anomalies (MCGRATH et al. 2002: 553, 555f.). The resistivity results could be used to further constrain the location and size of the subsurface **cavities** (MCGRATH et al. 2002: 557). Microgravity setup: Scintrex CG-3M autograv microgravity meter, resolution: 1 µGal, nominal grid: 2.5 m, residual Bouguer gravity. ERT setup: Campus Geophysical Geopulse general-purpose earth resistance meter, Wenner array, 1 m electrode spacing, lines perpendicular to known negative gravity anomalies, RMS error: 1.3 – 2.3 %.

In Cartei da Colla plain in the Mount Armetta karst complex in Val Pennavair, northwestern Italy, ERT and microgravity vertical-gradient (MVG) measurements were performed over an explored shallow **cave** to test its geophysical response (GAMBETTA et al. 2011: 11). The high-resolution 2D ERT outlined the shape and vertical distribution of the known cave (6000 – 40 000 Ωm, high variability possibly due to micrometeorological effects inside the cave), shallow narrow passages and a fossil meander linking two large chambers at about 30 m below the cave entrance (GAMBETTA et al. 2011: 11ff.). The MVG minima were consistent with the horizontal geometry of the cave (~ 0.244 – 0.262 mGal m^{-1}), as it is expected from the large negative density contrast between voids and rock (–2400 kg/m^3), and with the presence of a large (about 20 x 20 x 80 m) collapsed pit partially filled by collapse debris (~ 0.244 – 0.262 mGal m^{-1}) (GAMBETTA et al. 2011: 13f.); the overall error of the MVG data including effects of nearby topography, tide and drift was approximately 4 – 5 µGal m^{-1} (STEFANELLI et al. 2008). ERT setup: IRIS SYSCAL R1 resistivity meter, Wenner-Schlumberger array, 5 m electrode spacing. Microgravity setup: LaCoste and Romberg model D gravity meter, resolution: 1 µGal (10^{-8} m/s^2).

At the location of Jarash City, north Jordan, ERT and high-resolution gravity were moderately effective in locating and tracing subterranean **cavities** in a marly limestone unit and in delineating their dimensions; the gravity data indicated a near-surface **paleochannel** (–10.57 to –10.52 mGal), whose existence could be confirmed by subsequent excavations (BATAYNEH 2013: 1377ff.). ERT setup: IRIS SYSCAL R2 resistivity meter, Wenner-Schlumberger array, 2 m electrode spacing. Gravity setup: LaCoste and Romberg D20 gravity meter, nominal grid: 5 m, residual Bouguer gravity.

In Komberek, western Slovakia, ERT and microgravity methods, among others, were used to obtain information about unknown or inaccessible continuations of known underground caves in a limestone and dolomite bedrock (PUTIŠKA et al. 2014: 155ff., 160). The ERT profiling yielded **carbonate bedrock** (500 Ωm), the presence of a known **loam-filled sinkhole** up to 25 m in

diameter and 9 m deep (< 100 Ωm) as well as a conductive **cavity** with indistinguishable filling at depths of approximately 50 – 60 m below the surface (PUTIŠKA et al. 2014: 155ff., 162). The microgravity measurements were able to delineate a porous rauhwackes formation (–0.2 mGal, comparatively lower density) from the limestone and dolomite host rock; a second major negative anomaly (–0.35 mGal) correlated with the conductive cavity in the ERT data (PUTIŠKA et al. 2014: 161f.). ERT setup: ARES instrument, Dipole-dipole array, 5.5 m electrode spacing, roll-along technique, robust inversion. Microgravity setup: single Scintrex CG-5 autograv microgravity meter, resolution: 1 µGal, station spacing: 5.5 m, residual Bouguer gravity, RMS error: 3.3 %.

In the previously mentioned northern Acque Albule Basin, northeast of Rome, central Italy, microgravity, SRT and ERT surveys, among others, were carried out to differentiate the geological structure of a rapidly developing sinkhole (ARGENTIERI et al. 2015: 36ff.). The 2.5D microgravity survey performed over the sinkhole delineated a low-density sedimentary deposit up to 40 m thick (−0.35 – 0 mGal) from the surrounding travertine lithoid (+0.40 mGal) and the underlying sedimentary sequence; the root-mean-square error of the gravity data was less than 5 µGal (ARGENTIERI et al. 2015: 40, 44f.). Comparing the results of 2.5D gravity with the 2D SRT section showed a good correlation between the lower density infill sediments (with density contrasts of −700 to −500 kg/m^3) and the lower P-wave velocities (300 – 500 m/s) down to a depth of approximately 24 m (ARGENTIERI et al. 2015: 40, 44). Moreover, they both showed a subvertical discontinuity along the depression (ARGENTIERI et al. 2015: 44f.). Besides, the 2D SRT section delineated the depression from the surrounding travertine lithoid and the sedimentary sequence (v_p ~ 1400 – 2000 m/s) with highlighting an asymmetric deepening of the depression (ARGENTIERI et al. 2015: 44f.). The 2D ERT effectively delineated the filling of the **sinkhole** (< 30 Ωm) from the surrounding **calcareous** and **travertine country rocks** (800 – 1000 Ωm) up to a depth of approximately 50 m, which was consistent with the lithotypes suggested from the gravity modeling (ARGENTIERI et al. 2015: 41, 43f.). In addition, the 2D ERT results indicated (i) a funnel-like, low resistivity pattern (5 – 30 Ωm) with a steep, near vertical transition from higher to lower resistivities within the depression and (ii) a horizontal stepwise decrease in resistivity corresponding to a subcircular minor depression probably reflecting a depression step in the underlying lithology (ARGENTIERI et al. 2015: 44f.). In summary, the combined microgravity, SRT and ERT observations imaged the developing sinkhole to a depth of some 50 m with at least 40 m of infill (characterized by lower density, seismic velocity and resistivity values), the presence of travertine lithoid around the depression (down to at least 40 m) and the absence of this lithotype within the depression (although its presence in secondary cavities could not be completely excluded) (ARGENTIERI et al. 2015: 36, 45). Microgravity setup: LaCoste and Romberg microgravity meter, standard field repeatability: < 5 µGal, nominal grid: 25 m, residual Bouguer gravity. SRT setup: vertical 14 Hz geophones, 10 m geophone spacing, recording time: 512 ms, source: 8 kg sledgehammer stroke. ERT setup: IRIS SYSCAL Pro Switch-72 resistivity meter, Wenner / Schlumberger array, 1 m / 3 m / 5 m electrode spacing, RMS error: 0.89 – 3 %.

At the Poumeyssen test site, southwestern France, electrical resistivity imaging and seismic tomography, among others, were performed to study a 5 – 9 m wide, 10 – 15 m deep, **water-filled conduit**, whose location and shape in compact limestone are known from cave mapping work (GUÉRIN et al. 2009: 810f.). While the seismic data provided the location and width of the conduit to within a few meters and thus more accurately than the electrical data, the latter additionally

revealed the presence of a conductive superficial layer inside the limestone, interpreted as altered limestone and/or soil (400 – 1000 Ωm), which correlated well with the location of the conduit (GUÉRIN et al. 2009: 810f., 813ff.). As a consequence, GUÉRIN et al. (2009: 816) concluded that several types of difficulties such as (i) a complex site topography (the conduit appears to be located in a slight structural hollow), (ii) a varying depth of the conduit, (iii) a moderately defined resistivity contrast between the conduit and the host rock and (iv) the presence of a superficially altered, conductive layer affected the electrical measurements. In the case of the seismic method, apart from the difficulties arising from near-surface heterogeneities as mentioned above, the main drawbacks were (i) the lower acoustic impedance contrast caused by the conduit, which was completely water-filled (no air-water interface) and (ii) the strong near-surface velocity gradient, which may reduce the depth of penetration by bending the seismic waves upwards (GUÉRIN et al. 2009: 816). Seismic setup: 1 m geophone spacing, 3 m shot spacing, source: hammer stroke, stacking used to enhance signal-to-noise ratio. ERT setup: IRIS SYSCAL Pro resistivity meter, Wenner-Schlumberger / Dipole-dipole / Pole-dipole array, 1 m / 2 m / 5 m electrode spacing, arrays merged before inversion, RMS error: 6.08 %.

At the Tournemire test site, Aveyron, France, a 2D large-scale ERT survey was carried out to supplement earlier 2D seismic investigations in detecting **fault zones** within a subhorizontal sedimentary succession of a clay-rock interbedded between two carbonate (limestone and dolomite) formations (GÉLIS et al. 2010: 1405, 1408f., 1417). The previously performed 2D seismic reflection lines clearly identified the interfaces between the clay-rock and the carbonate formations and highlighted a subvertical fault within the carbonate layer underlying the clay-rock (GÉLIS et al. 2010: 1407, 1416). However, the seismic data failed in revealing the faults in the upper carbonate and the clay-rock formation because of (i) the poor spatial coverage of the seismic data in the upper carbonate, (ii) the poor signal-to-noise ratio of the seismic data at shallow depths, (iii) the weak seismic impedance contrast in the clay-rock and (iv) the small vertical offset of the fracture structures of 2 m (GÉLIS et al. 2010: 1407, 1416). In contrast, the 2D ERT sections also delineated the upper, approximately 200 m thick, fractured carbonate formation (200 – 1500 Ωm in fractured conditions, up to 4000 – 5000 Ωm in unfractured zones) from the underlying clay-rock layer (90 – 150 Ωm) (GÉLIS et al. 2010: 1409ff.). Besides, the 2D ERT data now revealed several subvertical faults with approximate position (800 – 1500 Ωm), zones of faulted material (600 – 1200 Ωm) and 100 – 600 m wide fractured areas (150 – 200 Ωm) within the upper carbonate formation, mainly by the abrupt transition from these low resistivities to higher resistivity values (> 5000 Ωm) (GÉLIS et al. 2010: 1411, 1414ff.); the results were in general agreement with geological observations, laboratory data and borehole investigations on site (GÉLIS et al. 2010: 1408f., 1413). However, the 2D ERT was equally ineffective in imaging the faults in the clay-rock formation, possibly due to the influence of the overlying highly electrically resistive carbonate formation and a lack of resolution caused by the large range of electrical resistivity values (90 – 5000 Ωm) (GÉLIS et al. 2010: 1412, 1417). Seismic setup: 40 – 140 Hz geophones, 10 m geophone spacing, 10 m shot spacing, sweep source with a linearly increasing frequency. ERT setup: ABEM Terrameter SAS 4000, Wenner / Dipole-dipole array, 20 m / 40 m electrode spacing, RMS error: 3.2 – 17.5 %.

At the archaeological site of Zominthos, Central Crete, Greece, ERT and SRT were applied in 2D to assess the geometrical, geophysical and sedimentological attributes of doline-shaped karst depressions filled with loose sediments and developed within an intensively karstified limestone

and dolomite bedrock (SIART et al. 2011: 315, 317ff.). The 2D ERT profiles detected a thick filling of overlying fine-grained loose **sediments** up to a depth of 10 m (< 250 Ωm), a transition zone (mixture of coarse detritus, loose material and shattered limestone fragments) at depths ranging from 10 – 20 m (250 – 1200 Ωm) and the compact basal inclined **limestone** and **dolomite bedrock** with undulating topography at depths greater than 20 m (> 1200 Ωm) (SIART et al. 2011: 319ff., 323ff.). In addition, the ERT data clearly delineated the existence of a buried **sinkhole** filled with very fine-grained unconsolidated sediments up to a depth of more than 20 m as well as other typical buried karst features such as **bedrock ridges**, **pinnacles** and **cutters** (SIART et al. 2011: 315, 323, 325f.). The 2D SRT profiles also detected an overlying rather fine-grained loose substrate in the upper 8 – 10 m (v_p < 1000 m/s), a thick transition zone at depths ranging from 10 – 35 m (v_p = 1000 – 2000 m/s) and the massive limestone and dolomite bedrock at depths between 20 m and more than 35 m (v_p > 2000 m/s) (SIART et al. 2011: 319, 323). Even if less explicitly than the ERT measurements, the SRT data highlighted the buried sinkhole filled with fine-grained material (v_p < 1400 m/s, ray density ~ 0) and revealed its extremely coarse-grained covering possibly comprised of numerous debris fragments (v_p > 2000 m/s, ray density > 400) (SIART et al. 2011: 322f.). In summary, the ERT measurements proved to be very sensitive to directional changes respectively the separation of major layers and to the delineation of buried karst landforms such as subsurface sinkholes, bedrock ridges, pinnacles and cutters up to a maximum penetration depth of approximately 25 m (SIART et al. 2011: 321, 331). In contrast, the SRT operated excellently in detecting the basal boundary between the unconsolidated overburden and the solid limestone and dolomite bedrock due to its deeper penetration, but exhibited a slightly lower precision as for the internal stratification of the overburden and smaller karst features of the solid limestone and dolomite bedrock (SIART et al. 2011: 319, 331). Percussion drillings associated with sediment coring and grain size analysis, calibrated ERT measurements conducted on bare rock outcrops as well as sedimentological and stratigraphical findings served for calibration at this study site (SIART et al. 2011: 315, 320f., 327, 330). ERT setup: Geotom 100-electrode system, Schlumberger array, 1.0 m / 1.5 m electrode spacing, least-squares inversion, RMS error: 23.0 % / 2.1 %. SRT setup: Geometrics Geode 48-channel system, vertical 14 Hz geophones, source: 5 – 10 individual hammer blows per shot location. Direct probing investigation setup: drill rig equipped with liner tubes 5 cm in diameter.

At Kroustas, eastern Crete, Greece, ERT and SRT were applied in a similar way to analyze the sediment thickness, stratification and subsurface morphometry of karst depressions again filled with fine-grained loose sediments overlying solid limestone and dolomite bedrock (SIART et al. 2013: 1135f.). The 2D ERT transects clearly outlined a thick filling of overlying fine-grained loose **sediments** up to a depth of 17 m (< 150 Ωm) and a coarse-grained **alluvial fan** (800 Ωm) that protruded into the fine-grained sediment depression (SIART et al. 2013: 1139ff., 1144). In this case, neither the shatter zone nor the basal rockhead were detected due to the insufficient maximum penetration depth of 17 m (SIART et al. 2013: 1141). The 2D SRT transects reached penetration depths of up to 70 m and detected the fine-grained loose sediments with thicknesses of up to 20 m (v_p < 1000 m/s), an intermediate shatter zone (**epikarst**) with thicknesses of 15 m and the **basal limestone** and **dolomite bedrock** in depths of about 24 – 33 m below the surface (v_p > 2000 m/s) (SIART et al. 2013: 1138, 1140f.). The SRT was not able to delineate the zone of the coarse-grained alluvial fan because of the method's lower sensitivity for subtle substrate changes (SIART et al.

2013: 1141). In summary, the ERT measurements proved to be efficient in differentiating the overlying stratified sediments, in detecting buried micro-relief features and in providing information on local geomorphodynamics within the karstic depression up to a maximum penetration depth of 17 m (SIART et al. 2013: 1139, 1143, 1145f.). In contrast, the SRT performed rather moderately in terms of differentiating loose unconsolidated overburden, but allowed the detection of the actual rockhead, which properly defined the buried topography of the landform, and hence gave a deeper insight into the formation of the karstic depression (SIART et al. 2013: 1139, 1143ff.). The ERT and SRT results were calibrated by sediment core drillings, subsurface observations with geomorphometric calculations and tomographic mapping data from neighboring karst depressions (SIART et al. 2013: 1135, 1141). ERT setup: Geotom 100-electrode system, Schlumberger array, 0.5 m / 1.0 m / 1.2 m electrode spacing, least-squares inversion, RMS error: 2.1 % / 2.8 % / 3.2 %. SRT setup: Geometrics Geode 48-channel system, 14 Hz geophones, source: 5 – 10 individual hammer blows per shot location.

During construction of the Sol-an Tunnel, Kangwon Province, South Korea, electrical resistivity and tunnel seismic prediction (TSP) surveys presented the existence of multiple weak zones (< 300 Ωm), which were related to micro-scale **cavity networks** developed within massive limestone rock; the results were in good agreement with direct borehole-based investigations including ground surface boring and horizontal probe core drilling at the tunnel face (SONG et al. 2012: 92, 95ff.). ERT setup: ABEM Terrameter SAS 4000, 10 m electrode spacing.

At the Tournaisis area at Gaurain-Ramecroix, south-eastern Belgium, where GPR and other EM methods were strongly crippled due to the presence of conductive overburden materials (clays, argillaceous silts or marls; 50 – 100 Ωm), ERT and SRT / seismic reflection surveys were conducted to detect and map palaeokarst features encountered at a highly weathered limestone bedrock and overlain by a 3 – 4 m thick cover mainly consisting of silts and clayey sands (KAUFMANN & DECEUSTER 2014: 17f., 21f.). Based on the comparison with direct investigations (CPTs, boreholes, excavations), the 2D ERT measurements attained a maximum depth of investigation of about 12 m and allowed the detection of (i) a continuous 3 – 4 m thick layer of covering **silts** and **clayey sands** (< 50 Ωm), (ii) the depth to competent **limestone bedrock** at 4 – 8 m below the surface (> 250 Ωm), (iii) transitional zones of more or less intensively **weathered limestones** (50 – 200 Ωm) and (iv) up to 8 m thick vertical conductive anomalies corresponding to opened up **sinkholes** (< 150 Ωm) (KAUFMANN & DECEUSTER 2014: 22f.). In terms of sinkhole detection, the SRT survey was unsuccessful, while the seismic reflection survey was only moderately suitable for delineating a low velocity vertical anomaly at the sinkhole locations at depth (KAUFMANN & DECEUSTER 2014: 22f.). According to KAUFMANN & DECEUSTER (2014: 23), this was probably due to the limited width of the **palaeokarst slots** compared to the geophone spacing and to their vertical structure that is often poorly reconstructed, especially by surface seismic refraction tomography; moreover, P-waves might directly cross these thin weathered slots to gain high velocity zones (bedrock). ERT setup: Dipole-dipole / Wenner-Schlumberger array, 2.5 m electrode spacing, RMS error: 12.1 %. SRT setup: 4.5 Hz geophones, 1 m geophone spacing, roll-along technique, source: 8 kg sledgehammer stroke. Seismic reflection setup: 4.5 Hz geophones, 0.5 m geophone spacing.

At the previously mentioned study site in Northampton County, northeastern Pennsylvania, USA, where the presence of clayey silty soils overlying limestone and dolomite bedrock limited the

applicability of the GPR technique to a penetration depth of less than 1 m, ERT measurements were conducted to determine the depth to bedrock and the location, size and type of **karst voids** (ROTH et al. 2002: 225f.). Associated with 17 calibrating borings and several core samples, the ERT method revealed that the extremely irregular **limestone** and **dolomite bedrock** surface correlated well with resistivity values of approximately 600 Ωm and greater (ROTH et al. 2002: 226ff.). Based on the results achieved within this study, ROTH et al. (2002: 230) illustrated that the ERT data were influenced by three-dimensional effects related to the irregular bedrock surface and the joints and fractures in the rock. Especially in terms of void detection, three-dimensional effects might have been played a significant role (ROTH et al. 2002: 229). Voids, which were located during the subsurface sampling investigations, could be detected as anomalies in one line direction, but could not be observed in a perpendicular orientation (ROTH et al. 2002: 230). In general, line offsets greater than approximately 4 m from a known void did not indicate the presence of the void anymore (ROTH et al. 2002: 231). ROTH et al. (2002: 231) concluded that the reliability of the ERT method is still in question with regard to locating and determining the size of possible voids and that the three-dimensional variability, the effects of line orientation and the smoothing inherent in the inversion process might influence the ERT results significantly. GPR setup: 100 and 250 MHz antennas. Direct probing investigation setup: drill rig equipped with hollow stem auger and core barrels. ERT setup: Dipole-dipole array, 1 – 3 m electrode spacing, lines oriented both perpendicular and parallel to strike.

At the study site Perry Farm Park in Bourbonnais, east-central Illinois, USA, where GPR surveys failed due to the clayey sediment fillings of the sinkholes, which strongly attenuated the radar signals, and trees, which produced a myriad of air-wave reflections that interfered with subsurface signals, 2D resistivity profiles were collected to depict a sediment-filled sinkhole and soil pipes above deeply weathered dolomite bedrock fractures (AHMED & CARPENTER 2003: 705ff., 710). In accordance with the results obtained from 8 borings, the 2D inverted resistivity sections indicated the approximate extent of the **sinkhole**, the **bedrock surface**, a possible **clay-filled fracture** and **soil pipes** (AHMED & CARPENTER 2003: 709ff.). GPR setup: 50 and 100 MHz antennas. Direct probing investigation setup: AMS Powerprobe Model 9600 with Geoprobe Macro-Core sampler, providing continuous direct push soil core samples. ERT setup: AGI Sting R1 earth resistivity meter, Dipole-dipole array, 3 m electrode spacing, lines oriented perpendicular to the strike / subparallel to the trend of the sinkhole, least-squares inversion, RMS error: 2.9 – 4.1 %.

At a study area in the Sang Run quadrangle, Garrett County, Maryland, USA, GPR and electrical resistivity methods, among others, were applied to a stream loss problem near a limestone quarry, ultimately to distinguish between solution cavities containing air, sediment and water in order to best delineate groundwater flow paths (GRGICH et al. 2004: 2f.). While the GPR signal was completely interrupted by the high clay content in the soil and thus failed in delivering a conclusive subsurface image, the geoelectric survey indicated a relatively homogeneous overburden, an extremely irregular **limestone contact** with possible pinnacles, and **solution cavities** at approximately 9 – 10 m below the surface (GRGICH et al. 2004: 5ff.). ERT setup: Dipole-dipole array, 2 m / 3 m electrode spacing, RMS error: 5.0 – 8.0 %.

At a field test site in Yongweol-ri, southwestern Korea, which is underlain by limestone bedrock and overlain by alluvial deposits, a 2D / 3D electrical resistivity survey was carried out to determine the extent of karst voids and to delineate areas prone to ground subsidence beneath a proposed road

network (FAROOQ et al. 2012: 75ff.). While the use of GPR would have failed due to high salinity, the resistivity profiles provided a clear view of weathered **soils**, the distribution of weak rock and/or **water/clay-filled cavities** and the **limestone bedrock**; a shallow boring program verified the results (FAROOQ et al. 2012: 75ff.). ERT setup: AGI SUPERSTING R8 IP earth resistivity/IP meter, Dipole-dipole array, 5 m electrode spacing, smoothness-constrained least-squares inversion.

In the course of two projects in Riyadh City and Al Hofuf City, Kingdom of Saudi Arabia, several subsoil karst features (**empty caves**, **sinkholes** and **open fractures**) in karstic limestone bedrock could be identified using 2D ERT and GPR (ABDELTAWAB 2013). ERT setup: IRIS SYSCAL Pro Switch resistivity meter, Wenner-Schlumberger array, 2 m electrode spacing, RMS error: 5.8 – 7.7 %. GPR setup: 100 – 500 MHz antennas.

In a case study at the karstic limestone terrain of Al-Hassa, Kingdom of Saudi Arabia, where traditional application of probing techniques has not thoroughly covered the study area, GPR and 2D ERT were applied to image and detect hidden near-surface karst features encountered at a highly weathered and fractured limestone bedrock and overlain by a 2 m thick soil cover (ABDALLATIF et al. 2015). While the GPR technique could only delineate cavities located at a limited depth of 4 m beneath the soil cover due to the presence of very shallow scattered and conductive clay pockets, 2D ERT ensured the detection of around 14 **sediment-filled** (< 6 Ωm) and 18 **air-filled cavernous zones** (> 100 Ωm) at different shallow depths up to 11 m (ABDALLATIF et al. 2015: 511, 513). Following these geophysical investigations, an extensive cavity probing campaign was performed and confirmed the GPR and ERT results: percussion drillings with air track rigs provided 32 cavity probing zones and 660 probe holes; for each probe, the rate of penetration was recorded with depth (ABDALLATIF et al. 2015: 512). While the sudden drop of the drilling head and the loss of drilling fluids revealed voids, very high penetration rates indicated the occurrence of voids or soil-filled cavities (ABDALLATIF et al. 2015: 512). GPR setup: 100, 250 and 500 MHz antennas. ERT setup: IRIS SYSCAL Pro / SYSCAL R1 Switch resistivity meter, Wenner-Schlumberger array, 2 m electrode spacing.

In the karst area of Kleśnica valley, Sudetes, southwestern Poland, the application of GPR and 2D ERT, in combination with high-resolution LiDAR DTM data and cave underground mapping, revealed the existence and the distribution of both known and previously unknown **karst voids in crystalline limestones** (KASPRZAK et al. 2015: 75f.). GPR setup: 250 MHz antenna. ERT setup: Wenner-Schlumberger array, 5 m electrode spacing.

In a study area at the western border of the Potiguar Basin, northeastern Brazil, where seismic sections were not practicable due to the occurrence of significant spatial heterogeneities on a subseismic scale in deeply buried carbonate strata, ERT and GPR sections were acquired to obtain the complex spatial distribution of a collapsed paleocave system and of the limestone host rocks (REIS JÚNIOR et al. 2015: 369f.). In conjunction with available exposures, previous geophysical studies and petrophysical laboratory tests on rock samples, the ERT and GPR measurements in 2D / 3D allowed a clear delineation between an underlying fractured **calciferous sandstone** (3 – 190 Ωm), the **karstified limestone host rock** (190 – 1250 Ωm) and a covering layer of **tufas** containing the collapsed **paleocaves** up to a depth of approximately 10 m (> 1300 – 3500 Ωm) (REIS JÚNIOR et al. 2015: 371ff., 380). Although the spatial distribution of the collapsed paleocave

system was well reproduced in both data, the GPR method, however, enabled a more accurate imaging of the internal geometry of each paleocave and, furthermore, showed that the paleocaves are partially isolated in depth; in contrast, no isolated paleocave could be mapped using the ERT method (REIS JÚNIOR et al. 2015: 378). In addition, the GPR data revealed moderately bedded layers of tufa deposited within the paleocaves and indicated regions characterized by the collapse of the cave ceilings and walls with fractured speleothems, brecciated materials and vugs in a chaotic distribution (REIS JÚNIOR et al. 2015: 371, 375, 380). ERT setup: IRIS SYSCAL Pro Switch resistivity meter, Wenner-Schlumberger array, 1 – 2 m electrode spacing, smoothness-constrained least-squares inversion, RMS error: 6.5 % for a maximum of 16 iterations. GPR setup: 200 MHz antenna, recording time: 220 ns, 50 traces per meter, 512 samples per trace, various processing adjustments.

7. Special investigations on the Swabian Alb high plain, new line Wendlingen–Ulm, southwestern Germany

In order to determine the dimension of karstification of the Swabian Alb high plain, comprehensive, independent and complementary indirect geophysical investigations including microgravimetric and seismic methods were previously conducted at the excavation bottom level by the construction company. These were part of a multi-phase exploration concept, which was designed to treat the karst building ground effectively, inter alia composed of: preliminary and main site investigations, ground investigations during construction (engineering geological mapping, indirect geophysical surveys, dynamic preloading of the ground), direct probing investigations (core drillings, destructive drillings, trial pits etc.) depending on the geophysical results, and collation of all available investigation results with holistic evaluations (KIELBASSA et al. 2015a: 131f.). In the course of the present research work, electrical resistivity tomography (ERT) measurements were performed at the excavation bottom level in addition to the investigation program of the construction company. The aim was to (i) explore geological defective karst voids and other karstic features including their geometry (size, shape, spatial distribution) and their type of filling (non, partially or almost completely filled with soil material and/or water) and to (ii) test the effectiveness of an inverse Wenner-Schlumberger array for geoelectrical karst (void) reconnaissance in a highly heterogeneous karstic environment.

7.1. Geoelectrical karst reconnaissance at the study site

The following content has been published as PRINS et al. (2017).

Introduction

In the course of the first research study, 2D electrical resistivity tomography (ERT) measurements were conducted at the excavation bottom level. The 2D ERT results were subsequently compared with the results of the microgravimetric and seismic methods of the construction company. Direct probing investigations served for calibration: 1 exploration drilling, 2 core drillings and 13 destructive drillings.

Methodology

The acquisition system used for the 2D ERT survey was composed of an ABEM Terrameter SAS 1000, an ES10-64C electrode selector and 41 electrodes in one layout. The survey contained one 150 m long profile (2.5 m inter-electrode spacing, 150 m maximum field layout) along the northeastern line track (direction Ulm to Stuttgart) (Fig. 20). Electrode locations/elevations were obtained by differential GPS measurements. The Wenner-Schlumberger and the Dipole-dipole electrode arrays were applied. The Wenner-Schlumberger protocol used and exhibited in this chapter totaled 1133 measurement points. For each array, the acquisition time was 0.1 s and the delay time was 0.1 s. The injection intensity ranged between 100 and 200 mA according to the ground resistance. During acquisition, the measurement was stacked up to two times.

The 2D apparent resistivity pseudosections were matched using a finite-difference forward modeling subroutine and inverted with a non-linear least-squares optimization technique

(DEGROOT-HEDLIN & CONSTABLE 1990, LOKE & BARKER 1996). The 2D finite-element inversion program RES2DINV ver. 3.54 (LOKE & BARKER 1996, LOKE 2004a) was used to automatically subdivide the subsurface into a large number of rectangular cells of calculated apparent resistivity values (with dimensions in the order of the electrode spacing). RES2DINV iteratively changed the resistivity of the model cells in order to minimize the difference between the measured and calculated apparent resistivity values; this difference was quantified by the Root-Mean-Square (RMS) error, respectively. Only a few bad datum points were gradually removed and model cells with widths of one unit electrode spacing were used. Further model refinements (meaning the use of model cells with widths of half the unit electrode spacing) were not applied, because this approach produced small near-surface artifacts, which significantly disturbed the data set. In comparison with the smoothness-constrained least-squares method (L2-norm criterion) (DEGROOT-HEDLIN & CONSTABLE 1990), the robust inversion routine (L1-norm criterion) (FARQUHARSON & OLDENBURG 1998, LOKE et al. 2003) yielded consistently more accurate results with significantly lower RMS errors and, therefore, was used to invert the acquired resistivity data.

Fig. 20: Photograph of the 2D ERT survey layout, with one 150 m long profile (2.5 m inter-electrode spacing, 150 m maximum field layout) along the northeastern line track (direction Ulm to Stuttgart).

Results and Discussion

The 2D ERT results are shown with the used electrode array, the number of iterations required for the solution and the RMS error (Fig. 21). The used Wenner-Schlumberger array (2.5 m inter-electrode spacing) allowed an investigation depth of up to 38 m. The average RMS error was 5.2 % after 5 iterations.

Three more or less extensive, conductive zones in the shallow subsurface (< 15 m) with low resistivity values (< 60 Ωm) are indicated in the 2D ERT section. These conductive zones were interpreted as clay / loam deposits, whose existence could subsequently be confirmed by directly adjoining boreholes (2 core drillings, 13 destructive drillings). These conductive zones were clearly distinguishable from the more resistive surrounding with resistivity values ranging from 60 to 240 Ωm, respectively. In conjunction with the available borehole investigations, this more resistive environment could be assigned to an intensely fractured and/or highly weathered limestone bedrock. Its comparatively low resistivity values were most probably caused by frequently recurring clayey / loamy (and thus conductive) fracture and void infillings with increasing depth, as indicated by the superimposed borehole logs; these observations also coincide with the results presented by ISMAIL & ANDERSON (2012: 287f.). Only in areas where the limestone bedrock is of high quality (i.e. with very few fractures / unweathered), the ERT section would show a continuing increase in resistivity with depth (ROTH et al. 1999: 299). Two more resistive zones with resistivity values between 240 and 960 Ωm could be delineated from the surrounding and were interpreted as moderately fractured and/or medium weathered limestone bedrock, respectively. Near-surface and spatially limited resistive zones with high resistivity values (> 1000 Ωm) are associated with the presence of compact limestone boulders, occasionally outcropping at the surface. The resistivity data suggested the general absence of air-filled voids (which would have been indicated by resistivity values of typically more than 2000 Ωm), which was in absolute accordance with the borehole logs. The depth to intact, largely unweathered limestone bedrock could not be derived from the resistivity results.

As illustrated above, the 2D ERT data generally agreed with the results gathered from the direct probing investigations. Only directly adjoining borings (less than 4 m for exploration and core drillings / less than 1 m for destructive drillings) were superimposed on the ERT section and used for interpretation. In a highly heterogeneous karstic environment, however, drilling only a few decimeters apart can easily result in a completely different borehole record. The few points where the drilling and resistivity data disagreed are thus probably caused by the distance between a drilling location and the ERT profile, respectively, or due to bedrock weathering on a scale too fine to be resolved. Boring data, in general, are spatially much more localized than the apparent resistivity data and local small-scale irregularities are often obscured by the volume-averaging method inherent in the ERT technique (ZHOU et al. 2002: 926ff.).

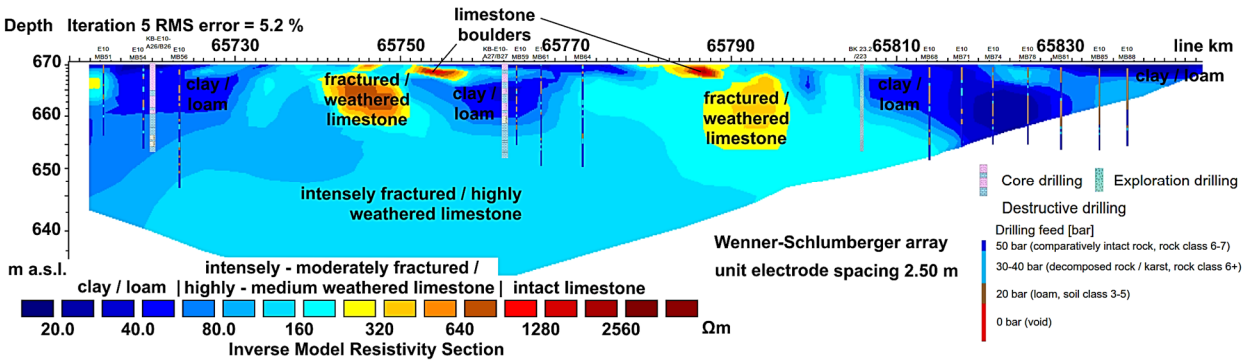

Fig. 21: Interpreted 2D ERT results, obtained from the 150 m long profile along the northeastern line track (direction Ulm to Stuttgart). Directly adjoining exploration drillings, core drillings and destructive drillings (indicating the drilling feed) were incorporated onto the ERT section.

The microgravimetric results of the previously conducted investigation program of the construction company coincides with the 2D ERT data to a great extent. The microgravimetry (Scintrex CG-5 autograv microgravity meter, resolution: 0.005 mGal, nominal grid: 2 m, residual Bouguer gravity, error: 0.002 mGal) indicated the location, size and planar extent of three gravity lows (from −0.025 to –0.015 mGal) and two gravity highs (< +0.045 mGal) (Fig. 22, ARGE NBS WENDLINGEN–ULM 2017a: 8ff.). While the gravity lows correlate with the conductive zones, interpreted as clay / loam deposits, the gravity highs correspond to the more resistive zones, interpreted as moderately fractured and/or medium weathered limestone bedrock, by means of 2D ERT, respectively. However, the exact spatial distribution with depth as well as the internal structure of these anomalies could only be obtained from the 2D ERT data. In addition, the microgravimetric survey alone was not able to clearly delineate compact rock from loosened zones (ARGE NBS WENDLINGEN–ULM 2017a: 13). While the microgravimetric data suggest the presence of air-filled voids with dimensions of 2.5 m x 2.5 m x 2.5 m up to a depth of 5 m and air-filled voids with dimensions of 5 m x 5 m x 5 m up to a depth of 15 m (ARGE NBS WENDLINGEN–ULM 2017a: 14), the 2D ERT data, in contrast, suggested the general absence of air-filled voids, which was, as mentioned before, in absolute accordance with the borehole investigations. This major difference might be caused by the fact that microgravimetry alone is often incapable of discriminating between an air-filled void and local bedrock loosening, both possibly producing very similar gravity anomalies (depending on the depth); microgravimetry is thus always interpreted with complementary geophysical (e.g. seismic) and/or boring data (ARGE NBS WENDLINGEN–ULM 2017a: 14, GOLDSCHEIDER & DREW 2007: 182).

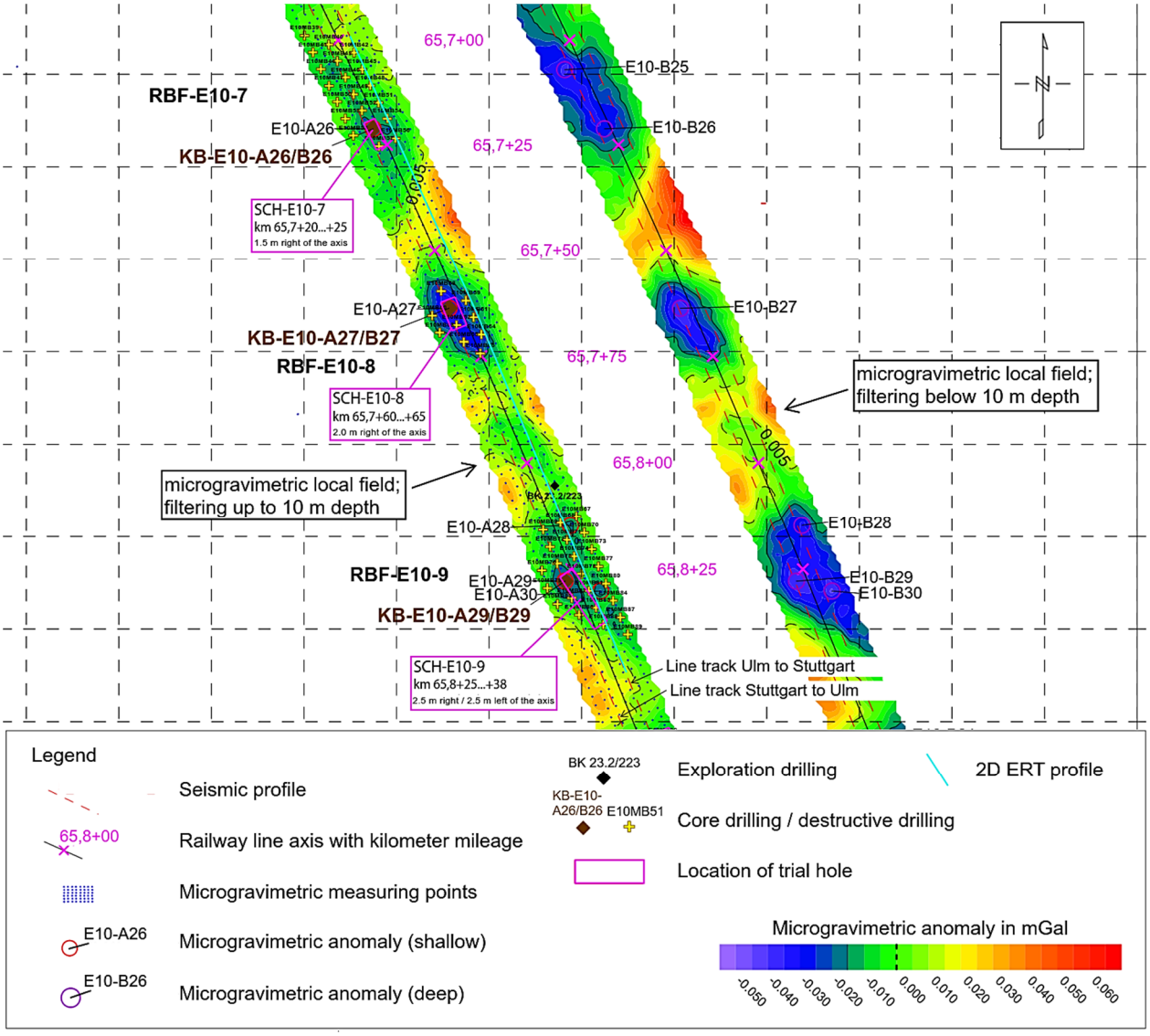

Fig. 22: Micrograviметric results of the previously conducted investigation program of the construction company (modified after ARGE NBS WENDLINGEN–ULM 2017a). The location of the 2D ERT profile, the seismic lines and the individual drillings can also be gathered from the figure.

The seismic results of the previously conducted investigation program of the construction company also coincides with the 2D ERT data to a high degree. The seismic profile along the northeastern line track (direction Ulm to Stuttgart) with combined high-resolution refraction/reflection seismics (Geometrics Geode 72-channel system, 4.5 Hz geophones, 2 m geophone spacing, 2 m shot spacing, source: 5 kg sledgehammer stroke with at least 3 individual hammer blows per shot location, vertical stacking used to enhance signal-to-noise ratio) divided the subsurface in an overlying, approximately 3 – 7 m thick, low velocity zone (v_p = 300 – 1000 m/s), an approximately 7 – 20 m thick, medium velocity transition zone (v_p = 1000 – 1700 m/s) and an underlying higher velocity zone (v_p = 1700 – 2250 m/s) (Fig. 23, ARGE NBS WENDLINGEN–ULM 2017a: 6f., 11ff., KIELBASSA et al. 2015a: 133). The overlying low velocity zone was interpreted as quaternary,

highly cohesive loam deposit and/or completely weathered limestone bedrock (soil class 4/5, DIN 18300) (ARGE NBS WENDLINGEN–ULM 2017a: 12f., 31). In contrast to the 2D ERT profiling, the seismic data were thus not able to distinguish between highly cohesive loam deposits and completely weathered limestone bedrock within the shallow subsurface (< 10 m). This major difference might be caused by the fact that seismic refraction tomography exhibits only a moderate precision for subtle substrate changes and thus is limited in determining the internal stratification of overlying layers and in delineating smaller karst features from comparatively solid bedrock (SIART et al. 2011: 319, 331, SIART et al. 2013: 1141). The medium velocity transition zone was interpreted as medium to highly weathered limestone bedrock (rock class 6, DIN 18300), whereas the underlying higher velocity zone was interpreted as lowly weathered to intact limestone bedrock (rock class 7, DIN 18300) (ARGE NBS WENDLINGEN–ULM 2017a: 12f., 31). The v_p = 1000 m/s-seismic line constituted the boundary between soil class 4/5 and rock class 6, even if in zones with a high degree of fracturing and/or void occurrences with mostly clayey / loamy infillings, respectively, the rock class 6 could often only be found in depths with seismic velocities between v_p = 1350 and 1700 m/s (ARGE NBS WENDLINGEN–ULM 2017a: 12f., 31). The v_p = 1700 m/s-seismic line constituted the boundary between rock class 6 and 7 (ARGE NBS WENDLINGEN–ULM 2017a: 12f., 31), which was in absolute accordance with the borehole logs. This seismic line showed the bedrock surface even more precisely than the 2D ERT data; an observation that coincides with the results presented by SIART et al. (2011: 331).

While the vertical seismic velocity gradient was moderately pronounced between line km 65+700 and 65+775, it was weakly developed from line km 65+775 to 65+850 with seismic velocities of less than v_p = 1800 m/s (km 65+775 – 65+835) and less than v_p = 1700 m/s (km 65+835 – 65+850) at the maximum penetration depth of approximately 21 m, respectively (ARGE NBS WENDLINGEN–ULM 2017a: 12). While the lower seismic velocity gradients correlate with the conductive zones, interpreted as clay / loam deposits, and the resistive environment, interpreted as intensely fractured and/or highly weathered limestone bedrock, the higher seismic velocity gradients correspond to the more resistive zones, interpreted as moderately fractured and/or medium weathered limestone bedrock / compact limestone boulders, by means of 2D ERT, respectively. However, the exact spatial distribution with depth as well as the internal structure of these anomalies (clay / loam deposits, moderately fractured and/or medium weathered limestone bedrock, compact limestone boulders) could again only be obtained from the 2D ERT data.

The seismic survey provided a highly heterogeneous subsurface image with frequently occurring, deep-reaching karstic zones and only limited weathered bedrock occurrences, reaching near-surface areas (ARGE NBS WENDLINGEN–ULM 2017a: 16). While the microgravimetric data suggested the potential presence of air-filled voids by three gravity lows, the seismic as well as the 2D ERT survey, in contrast, suggested the general absence of air-filled voids (ARGE NBS WENDLINGEN–ULM 2017a: 18f.); the latter was subsequently confirmed by extensive direct probing investigations (ARGE NBS WENDLINGEN–ULM 2017a: 25).

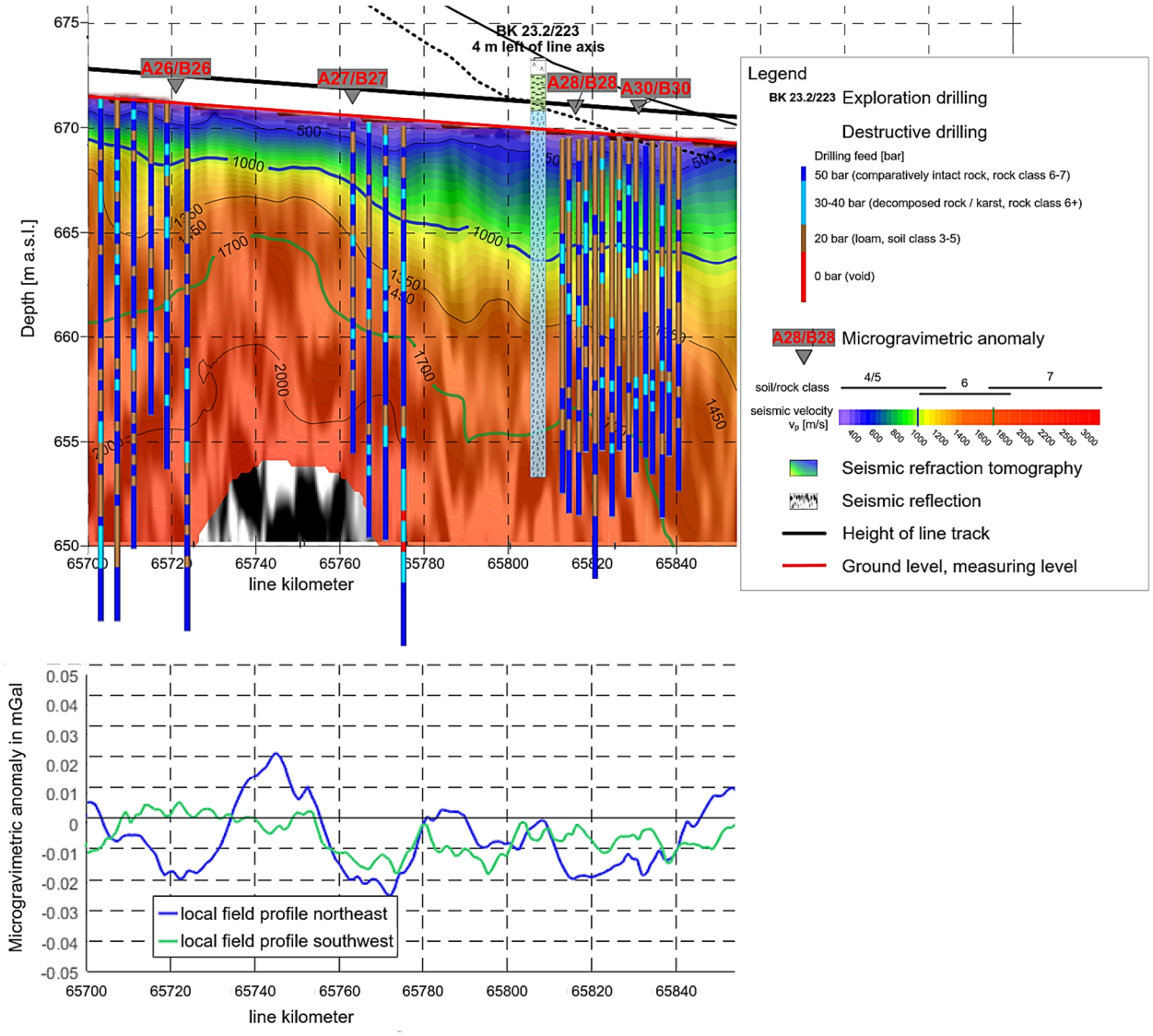

Fig. 23: Seismic and microgravimetric results of the previously conducted investigation program of the construction company (modified after ARGE NBS WENDLINGEN–ULM 2017a). Directly adjoining exploration drillings and destructive drillings (indicating the drilling feed) are incorporated onto the seismic section. Furthermore, a correlation between the drilling feed / seismic P-wave velocity and the associated soil/rock class is shown in the legend, respectively.

Conclusion

The 2D ERT survey provided a high-resolution, consistent and reliable image of the subsurface and accurately revealed (i) three conductive zones (< 60 Ωm, interpreted as clay / loam deposits, existence confirmed by 2 core drillings / 13 destructive drillings), (ii) a more resistive surrounding (60 – 240 Ωm, assigned to an intensely fractured and/or highly weathered limestone bedrock, in conjunction with boreholes), (iii) two more resistive zones (240 – 960 Ωm, interpreted as moderately fractured and/or medium weathered limestone bedrock) and (iv) near-surface and spatially limited resistive zones (> 1000 Ωm, associated with the presence of compact limestone

boulders). The 2D ERT data generally agreed with the results gathered from the direct probing investigations. Moreover, the 2D ERT results largely coincided with the microgravimetric and seismic results of the previously conducted investigation program of the construction company. The seismic line showed the bedrock surface even more precisely than the 2D ERT data. The exact spatial distribution with depth as well as the internal structure of the detected anomalies (clay / loam deposits, moderately fractured and/or medium weathered limestone bedrock, compact limestone boulders) could, however, only be obtained from the 2D ERT data. In contrast to the microgravimetric data, which suggested the potential presence of air-filled voids, the seismic as well as the 2D ERT survey suggested the general absence of air-filled voids, whereby the latter was subsequently confirmed by the direct probing investigations. In direct comparison, the resistivity method was thus superior in detecting zones with low ground load-bearing capacity and in delineating them from zones, generally capable of bearing weight.

7.2. The effectiveness of an inverse Wenner-Schlumberger array for geoelectrical karst reconnaissance at the study site

The following content has been published as PRINS et al. (2018).

Introduction

In the course of the second research study, 2D electrical resistivity tomography (ERT) measurements were conducted with an inverse Wenner-Schlumberger array. The 2D ERT results were subsequently compared with the results of the microgravimetric and seismic methods of the construction company. Direct probing investigations served for calibration and discussion: 1 exploration drilling, 4 core drillings, 19 destructive drillings and 2 trial pits.

Methodology

The acquisition system used for the 2D ERT survey was composed of an ABEM Terrameter SAS 4000, an ES10-64C electrode selector and 41 electrodes in one layout. The survey contained one 320 m long profile (2.0 m inter-electrode spacing, 120 m maximum field layout) along the southwestern line track (direction Stuttgart to Ulm) (Fig. 24). Electrode locations/elevations were obtained by differential GPS measurements. An inverse Wenner-Schlumberger electrode array was applied. The inverse Wenner-Schlumberger protocol totaled 2516 measurement points. The acquisition time was 0.5 s and the delay time was 0.3 s. The injection intensity ranged between 100 and 200 mA according to the ground resistance. During acquisition, the measurement was stacked up to two times.

The 2D apparent resistivity pseudosections were matched using a finite-difference forward modeling subroutine and inverted with a non-linear least-squares optimization technique (DEGROOT-HEDLIN & CONSTABLE 1990, LOKE & BARKER 1996). The 2D finite-element inversion program RES2DINV ver. 3.54 (LOKE & BARKER 1996, LOKE 2004a) was used to automatically subdivide the subsurface into a large number of rectangular cells of calculated apparent resistivity values (with dimensions in the order of the electrode spacing). RES2DINV iteratively changed the resistivity of the model cells in order to minimize the difference between the measured and calculated apparent resistivity values; this difference was quantified by the Root-Mean-Square

(RMS) error, respectively. Only a few bad datum points were gradually removed and model cells with widths of one unit electrode spacing were used. Further model refinements (meaning the use of model cells with widths of half the unit electrode spacing) were not applied, because this approach produced small near-surface artifacts, which significantly disturbed the data set. In comparison with the smoothness-constrained least-squares method (L2-norm criterion) (DEGROOT-HEDLIN & CONSTABLE 1990), the robust inversion routine (L1-norm criterion) (FARQUHARSON & OLDENBURG 1998, LOKE et al. 2003) yielded consistently more accurate results with lower RMS errors and, therefore, was used to invert the acquired resistivity data.

Fig. 24: Photograph of the 2D ERT survey layout, with one 320 m long profile (2.0 m inter-electrode spacing, 120 m maximum field layout) along the southwestern line track (direction Stuttgart to Ulm).

Results and Discussion

The 2D ERT results are shown with the used electrode array, the number of iterations required for the solution and the RMS error (Fig. 25). The used inverse Wenner-Schlumberger array (2.0 m inter-electrode spacing) allowed an investigation depth of up to 30 m. The average RMS error was 1.61 % after 5 iterations.

Numerous near-surface and a few deep-reaching, spatially limited conductive zones with low resistivity values (< 60 Ωm) are indicated in the 2D ERT section. These conductive zones were interpreted as clayey / loamy deposits, whose existence could subsequently be confirmed by visual inspection of the excavation bottom level and by directly adjoining boreholes (3 core drillings, 13 destructive drillings). These conductive zones were distinguishable from the more resistive surrounding with resistivity values ranging from 60 to 240 Ωm, respectively. In conjunction with the available borehole and trial pit investigations, this more resistive environment could be assigned to an intensely fractured and/or highly weathered limestone bedrock. Its comparatively low resistivity values were most probably caused by frequently recurring clayey / loamy (and thus conductive) fracture and void infillings with increasing depth, as indicated by the superimposed borehole logs; these observations also coincide with the results presented by ISMAIL & ANDERSON (2012: 287f.) and PRINS et al. (2017: 376). Only in areas where the limestone bedrock is of high quality (i.e. with very few fractures / unweathered), the ERT section would show a continuing increase in resistivity with depth (ROTH et al. 1999: 299). Several resistive zones in the shallow subsurface (< 10 m) with resistivity values between 240 and 960 Ωm could be delineated from the surrounding and were interpreted as moderately fractured and/or medium weathered limestone bedrock, respectively; 5 destructive drillings subsequently served as a confirmation. The resistivity data suggested the general absence of intact limestone bedrock and air-filled voids (which would have been indicated by resistivity values of typically more than 1000 Ωm and 2000 Ωm), which was in accordance with the borehole logs. The depth to intact, largely unweathered limestone bedrock could thus not be derived from the resistivity results.

As illustrated above, the 2D ERT data generally agreed with the results gathered from the direct probing investigations. Only directly adjoining borings (less than 2.5 m for exploration and core drillings / less than 1 m for destructive drillings) and crossing trial pits were superimposed on the ERT section and used for interpretation. In a highly heterogeneous karstic environment, however, drilling only a few decimeters apart can easily result in a completely different borehole record. On a few locations, the drilling and resistivity data disagreed, which might at least partly be caused by the distance between a drilling location and the ERT profile, respectively.

(i) Between line km 63+740 and 63+765, the 2D ERT survey was not able to reveal an intensely fractured and/or highly weathered limestone bedrock (rock class 6, DIN 18300), which was subsequently exposed by 1 core drilling and 4 destructive drillings below a depth of approximately 15 m. This divergence was most probably caused by frequently recurring clayey / loamy (and thus conductive) fracture and void infillings with increasing depth, reducing the apparent resistivity values significantly (PRINS et al. 2017: 376).

(ii) Occasionally occurring, very gravely to very cobbly layers / limestone fragments within the conductive clayey / loamy deposits were detected in 4 of 4 core drillings. They may explain the partly increased resistivity values of the clayey / loamy deposits of up to 160 Ωm and thus the deviation between the drilling and resistivity data on a few drilling locations; these observations coincide with the remarks given by ROTH et al. (2000: 362).

(iii) At line km 63+958, 1 core drilling encountered an air-filled void between a depth of approximately 696.5 and 697 m a.s.l (~ 10 m below the excavation bottom level), which was not shown in the 2D ERT profile; an air-filled void on a scale too fine to be resolved with the used inter-electrode spacing of 2.0 m.

(iv) Between line km 63+937 and 63+944, 3 destructive drillings disagreed with the resistivity data at a depth of approximately 4 – 8 m below the excavation bottom level. While the destructive drilling results suggested the presence of clayey / loamy deposits by drilling feeds of less than 20 bar, the 2D ERT profile indicated the existence of a moderately fractured and/or medium weathered limestone bedrock by resistivity values between 240 and 960 Ωm. It is believed that the destructive drillings entered narrow soil-filled fractures within the limestone bedrock, which did not show up in the 2D ERT profile. Local small-scale irregularities are often obscured by the volume-averaging method inherent in the ERT technique and boring data, in general, are spatially much more localized than the apparent resistivity data (ROTH & NYQUIST 2003: 6, ZHOU et al. 2002: 926ff.). However, borings located in a fracture are often misleadingly be used to infer bedrock depths much greater than the average bedrock surface, whereas rock ledges / lenses might be interpreted as areas of shallow bedrock if they caused refusal of the drilling pipe (ISMAIL & ANDERSON 2012: 292, ROTH et al. 2000: 362). In this context, it is also worth mentioning that the human operation of a drilling rig exerts a considerable influence on the resulting boring data; a circumstance, which should not be neglected when interpreting (especially destructive) drilling records.

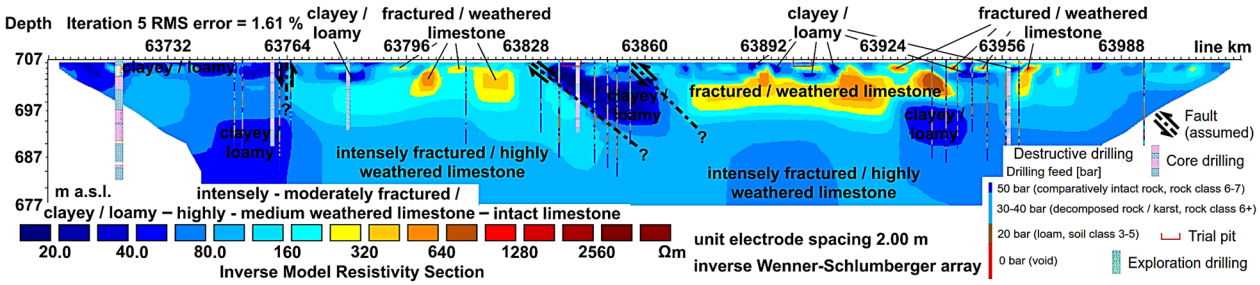

Fig. 25: Interpreted 2D ERT results, obtained from the 320 m long profile along the southwestern line track (direction Stuttgart to Ulm). Directly adjoining exploration drillings, core drillings, destructive drillings (indicating the drilling feed) and crossing trial pits were incorporated onto the ERT section.

The microgravimetric results of the previously conducted investigation program of the construction company coincides with the 2D ERT data to a great extent. The microgravimetry (Scintrex CG-5 autograv microgravity meter, resolution: 0.005 mGal, nominal grid: 2 m, residual Bouguer gravity, error: 0.008 mGal) indicated the location, size and planar extent of five gravity lows (from −0.035 to –0.015 mGal) and two gravity highs (< +0.025 mGal) (Fig. 26, ARGE NBS WENDLINGEN–ULM 2017b: 7ff.). While the gravity lows correlate with the conductive zones, interpreted as clayey / loamy deposits, the gravity highs correspond to the more resistive zones, interpreted as moderately fractured and/or medium weathered limestone bedrock, by means of 2D ERT, respectively. However, the exact spatial distribution with depth as well as the internal structure of these anomalies could only be obtained from the 2D ERT data. In addition, the microgravimetric survey alone was not able to clearly delineate compact rock from loosened zones (ARGE NBS

WENDLINGEN–ULM 2017b: 12). While the microgravimetric data suggested the presence of air-filled voids with dimensions of 2.5 m x 2.5 m x 2.5 m up to a depth of 5 m and air-filled voids with dimensions of 5 m x 5 m x 5 m up to a depth of 15 m (ARGE NBS WENDLINGEN–ULM 2017b: 13), the 2D ERT data, in contrast, suggested the general absence of air-filled voids, which was, as mentioned before, in accordance with the borehole investigations. This major difference might be caused by the fact that microgravimetry alone is often incapable of discriminating between an air-filled void and local bedrock loosening, both possibly producing very similar gravity anomalies (depending on the depth); microgravimetry is thus always interpreted with complementary geophysical (e.g. seismic) and/or boring data (ARGE NBS WENDLINGEN–ULM 2017b: 13, GOLDSCHEIDER & DREW 2007: 182).

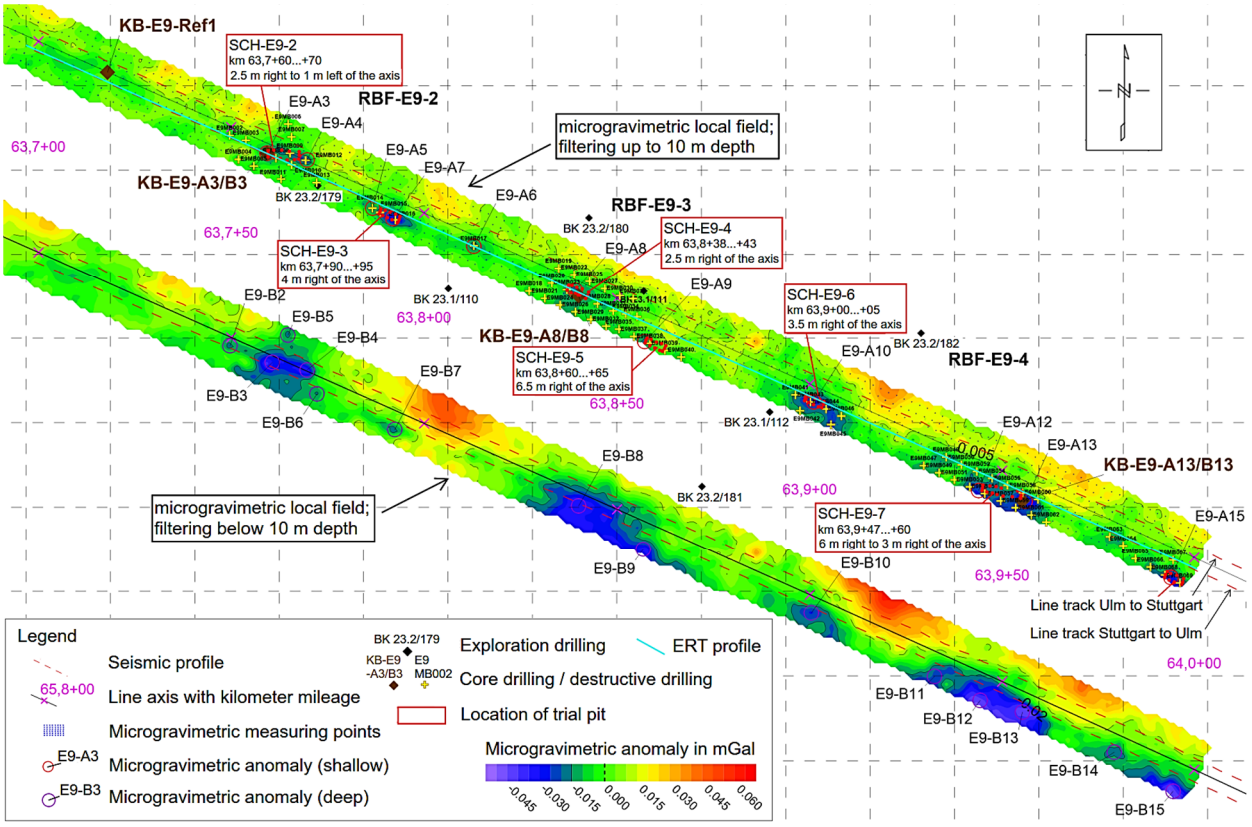

Fig. 26: Microgravimetric results of the previously conducted investigation program of the construction company (modified after ARGE NBS WENDLINGEN–ULM 2017b). The location of the 2D ERT profile, the seismic lines, the individual drillings and the trial pits can also be gathered from the figure.

The seismic results of the previously conducted investigation program of the construction company also coincides with the 2D ERT data to a high degree. The seismic profile along the southwestern line track (direction Stuttgart to Ulm) with combined high-resolution refraction/reflection seismics (Geometrics Geode 72-channel system, 4.5 Hz geophones, 2 m geophone spacing, 2 m shot spacing, source: 5 kg sledgehammer stroke with at least 3 individual hammer blows per shot location, vertical stacking used to enhance signal-to-noise ratio) divided the subsurface in an overlying, approximately 2 – 5 m thick, low velocity zone (v_p = 300 – 1000 m/s), an approximately 5 – 12 m thick, medium velocity transition zone (v_p = 1000 – 1700 m/s) and an underlying higher

velocity zone (v_p = 1700 – 2600 m/s) (Fig. 27, ARGE NBS WENDLINGEN–ULM 2017b: 7f., 10ff., KIELBASSA et al. 2015a: 133). The overlying low velocity zone was interpreted as quaternary, highly cohesive loam deposit and/or completely weathered limestone bedrock (soil class 4/5, DIN 18300) (ARGE NBS WENDLINGEN–ULM 2017b: 11f., 26). In contrast to the 2D ERT profiling, the seismic data were thus not able to distinguish between highly cohesive loamy deposits and completely weathered limestone bedrock within the shallow subsurface (< 5 m). This major difference might be caused by the fact that seismic refraction tomography exhibits only a moderate precision for subtle substrate changes and thus is limited in determining the internal stratification of overlying layers and in delineating smaller karst features from comparatively solid bedrock (SIART et al. 2011: 319, 331, SIART et al. 2013: 1141). The medium velocity transition zone was interpreted as medium to highly weathered limestone bedrock (rock class 6, DIN 18300), whereas the underlying higher velocity zone was interpreted as lowly weathered to intact limestone bedrock (rock class 7, DIN 18300) (ARGE NBS WENDLINGEN–ULM 2017b: 11f., 26). The v_p = 1000 m/s-seismic line constituted the boundary between soil class 4/5 and rock class 6, even if in zones with a high degree of fracturing and/or void occurrences with mostly clayey / loamy infillings, respectively, the rock class 6 could often only be found in depths with seismic velocities between v_p = 1350 and 1700 m/s (ARGE NBS WENDLINGEN–ULM 2017b: 11f., 26). The v_p = 1700 m/s-seismic line constituted the boundary between rock class 6 and 7 (ARGE NBS WENDLINGEN–ULM 2017b: 11f., 26), which was not in absolute accordance with the borehole logs. As was the case with the 2D ERT profiling, also the seismic survey had difficulties in showing the bedrock surface precisely. This inefficiency was also most probably caused by the frequently recurring clayey / loamy fracture and void infillings with increasing depth, reducing the seismic velocities significantly.

While the vertical seismic velocity gradient was weakly developed between line km 63+700 and 63+780 and between line km 63+830 and 63+860, it was moderately pronounced between line km 63+780 and 63+830 and between line km 63+880 and 64+020 (ARGE NBS WENDLINGEN–ULM 2017b: 11). While the lower seismic velocity gradients correspond to the conductive zones, interpreted as clayey / loamy deposits, the higher seismic velocity gradients correlate with the more resistive environment and the resistive zones, interpreted as moderately to intensely fractured and/or medium to highly weathered limestone bedrock, by means of 2D ERT, respectively. However, the exact spatial distribution with depth as well as the internal structure of these anomalies (clayey / loamy deposits, moderately fractured and/or medium weathered limestone bedrock) could again only be obtained from the 2D ERT data.

The seismic survey provided a heterogeneous subsurface image with frequently occurring, shallow karstic zones and only limited weathered bedrock occurrences, reaching near-surface areas (ARGE NBS WENDLINGEN–ULM 2017b: 15). While the microgravimetric data suggested the potential presence of air-filled voids by five gravity lows, the seismic as well as the 2D ERT survey, in contrast, suggested the general absence of air-filled voids (ARGE NBS WENDLINGEN–ULM 2017b: 17); only the latter was in accordance with extensive direct probing investigations (ARGE NBS WENDLINGEN–ULM 2017b: 21).

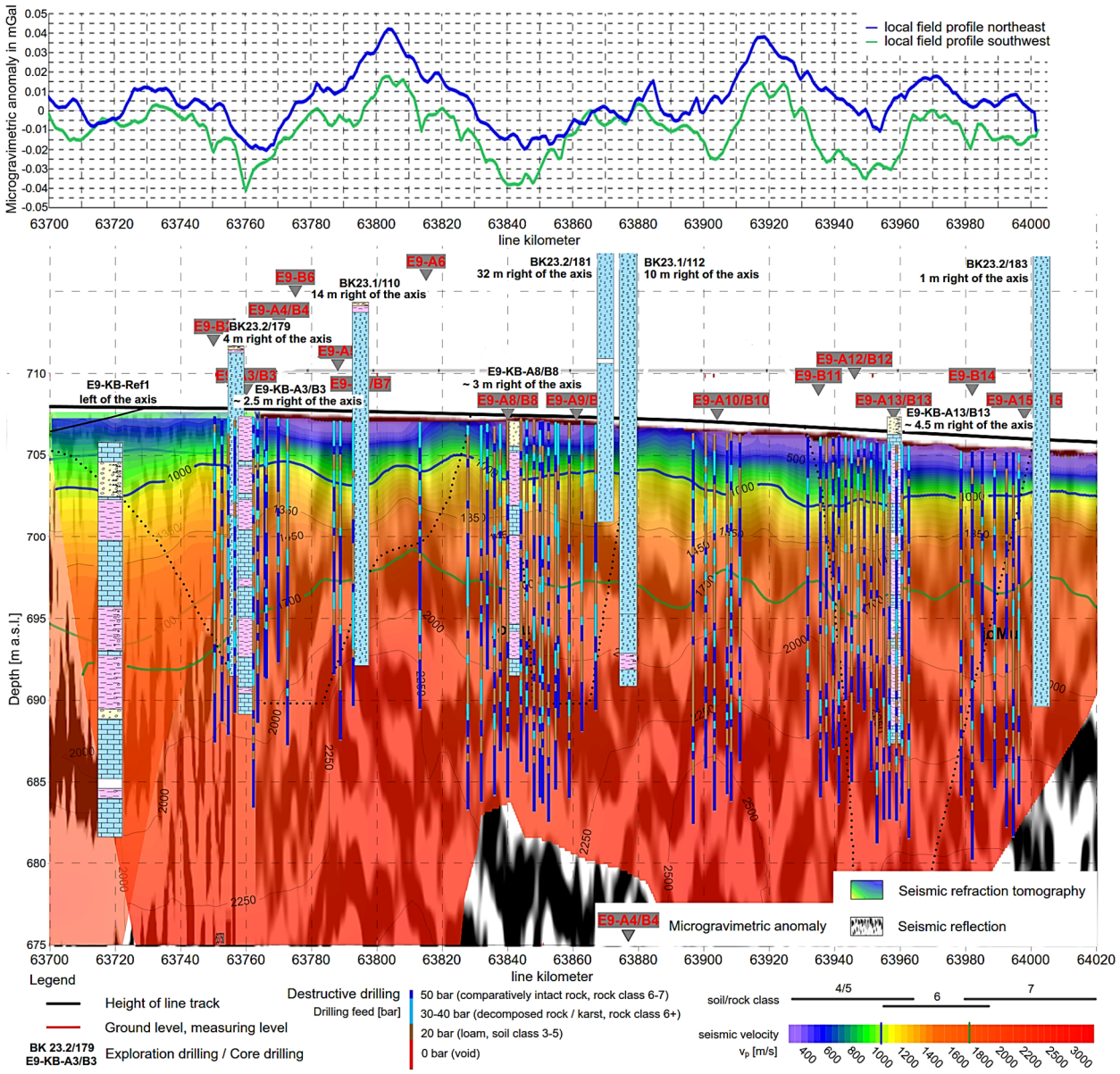

Fig. 27: Seismic and microgravimetric results of the previously conducted investigation program of the construction company (modified after ARGE NBS WENDLINGEN–ULM 2017b). Directly adjoining exploration drillings, core drillings and destructive drillings (indicating the drilling feed) are incorporated onto the seismic section. Furthermore, a correlation between the drilling feed / seismic P-wave velocity and the associated soil/rock class is shown in the legend, respectively.

Conclusion

The 2D ERT survey conducted with an inverse Wenner-Schlumberger array provided a high-resolution, consistent and reliable image of the subsurface and revealed (i) numerous near-surface and a few deep-reaching, spatially limited conductive zones (< 60 Ωm, interpreted as clayey / loamy deposits, existence confirmed by visual inspection of the excavation bottom level / 3 core drillings / 13 destructive drillings), (ii) a more resistive surrounding (60 – 240 Ωm, assigned to an

intensely fractured and/or highly weathered limestone bedrock, in conjunction with borehole and trial pit investigations) and (iii) several resistive zones (240 – 960 Ωm, interpreted as moderately fractured and/or medium weathered limestone bedrock, existence confirmed by 5 destructive drillings). The 2D ERT data generally agreed with the results gathered from the direct probing investigations. On the few locations, where the drilling and resistivity data disagreed, the divergences were explained and possible causes discussed. Moreover, the 2D ERT results largely coincided with the microgravimetric and seismic results of the previously conducted investigation program of the construction company. As was the case with the 2D ERT profiling, also the seismic survey had difficulties in showing the bedrock surface precisely. The exact spatial distribution with depth as well as the internal structure of the detected anomalies (clayey / loamy deposits, moderately fractured and/or medium weathered limestone bedrock) could only be obtained from the 2D ERT data. In contrast to the microgravimetric data, which suggested the potential presence of air-filled voids, the seismic as well as the 2D ERT survey suggested the general absence of air-filled voids, whereby only the latter was in accordance with the direct probing investigations. In direct comparison, the resistivity method was thus superior in detecting zones with low ground load-bearing capacity and in delineating them from zones, generally capable of bearing weight.

7.3. The effectiveness of an inverse Wenner-Schlumberger array for geoelectrical karst void reconnaissance at the study site

The following content has been published as PRINS et al. (2019).

Introduction

In the course of the third research study, 2.5D electrical resistivity tomography (ERT) measurements (meaning the use of parallel 2D lines) were conducted with an inverse Wenner-Schlumberger array. Extensive direct probing investigations served for calibration and discussion: 1 core drilling with camera inspection, 29 destructive drillings with 14 camera inspections and 2 laser scans as well as 1 excavation pit.

Methodology

The acquisition system used for the 2.5D ERT survey was composed of an ABEM Terrameter SAS 4000, an ES10-64C electrode selector and 41 electrodes in one layout. The survey contained six independent, 60 m long profiles (P01 – P06, 0.75 m inter-electrode spacing, 45 m maximum field layout, 1.5 m line spacing) oriented perpendicular to the long axis of an oval-shaped collapse doline and the most prominent voids (Fig. 28). Electrode locations/elevations were obtained by differential GPS measurements. An inverse Wenner-Schlumberger electrode array was applied. The inverse Wenner-Schlumberger protocols totaled 698 – 729 measurement points. The acquisition time was 0.5 s and the delay time was 0.3 s. The injection intensity ranged between 100 and 200 mA according to the ground resistance. During acquisition, the measurement was stacked up to two times.

A complete 3D ERT survey (meaning the use of orthogonal cross-lines in addition to the six parallel 2D lines) was not carried out due to the following restrictive circumstances:

(i) The directly adjoining slopes with angles of approximately 45° might easily have led to terrain anomalies and errors in estimating the depth and the resistivity in the model. The terrain effect increases with surface relief and can only be seen as insignificant for slopes of less than 10° (TELFORD et al. 1990: 532, chapter 6.2). In general, it should be focused on removing or at least minimizing the terrain effect.

(ii) Distortions in the resistivity model might also be produced by the influence of even moderately anisotropic media on the results of the resistivity inversion assuming isotropic conditions (e.g. GREENHALGH et al. 2010, HERWANGER et al. 2004). When using a 3D ERT survey in an anisotropic media, these distortions might be even more momentous due to differing lateral resistivities in different line directions (chapter 6.7). This anisotropic effect of resistivity should be minimized to a maximum possible degree, especially in a highly anisotropic karstic environment.

The 2D apparent resistivity pseudosections were matched using a finite-difference forward modeling subroutine and inverted with a non-linear least-squares optimization technique (DEGROOT-HEDLIN & CONSTABLE 1990, LOKE & BARKER 1996). The 2D finite-element inversion program RES2DINV ver. 3.54 (LOKE & BARKER 1996, LOKE 2004a) was used to automatically subdivide the subsurface into a large number of rectangular cells of calculated apparent resistivity values (with dimensions in the order of the electrode spacing). RES2DINV iteratively changed the resistivity of the model cells in order to minimize the difference between the measured and calculated apparent resistivity values; this difference was quantified by the Root-Mean-Square (RMS) error, respectively. Only a few bad datum points were gradually removed and model cells with widths of one unit electrode spacing were used. Further model refinements (meaning the use of model cells with widths of half the unit electrode spacing) were not applied, because this approach produced small near-surface artifacts, which significantly disturbed the data set. The smoothness-constrained least-squares method (L2-norm criterion) (DEGROOT-HEDLIN & CONSTABLE 1990) and the robust inversion routine (L1-norm criterion) (FARQUHARSON & OLDENBURG 1998, LOKE et al. 2003) were used to invert the acquired resistivity data; while the first was more suitable in areas where the subsurface resistivity values changed in a smooth manner (e.g. profile P01), the latter yielded more accurate results for regions that were piecewise constant and separated by relatively sharp boundaries (e.g. profile P05).

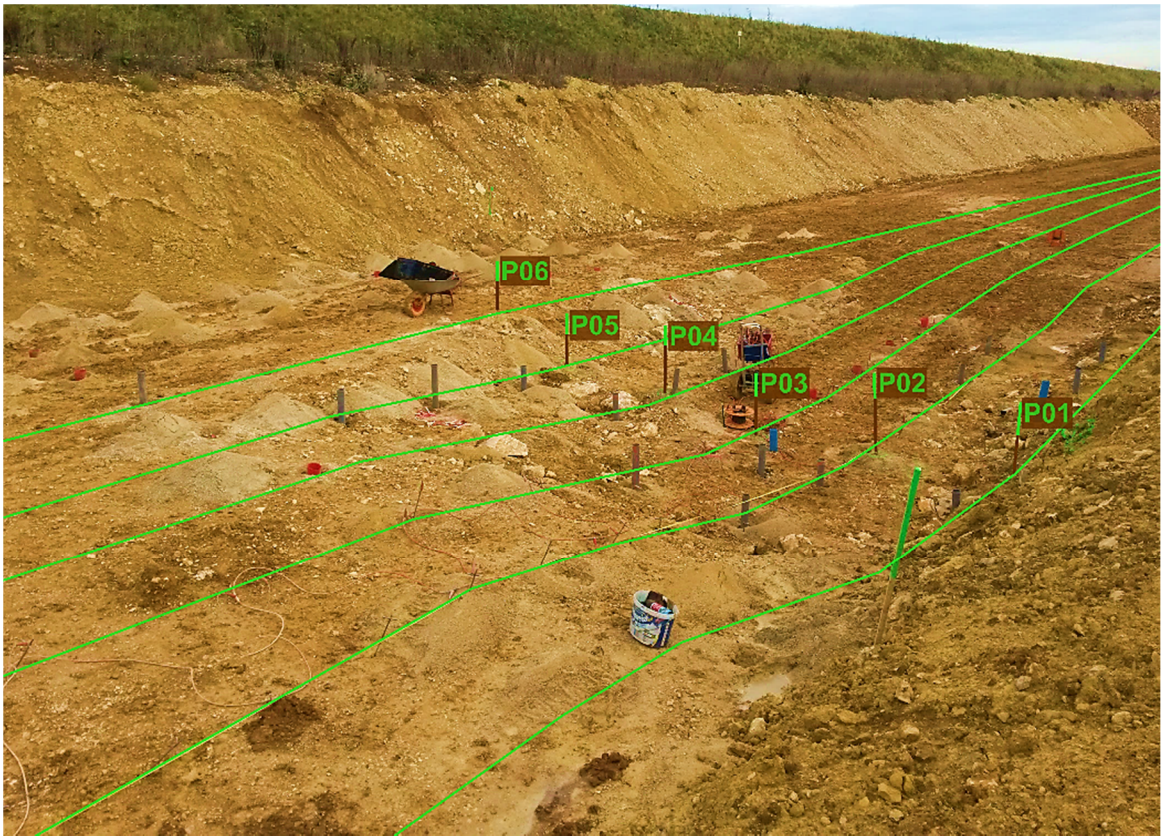

Fig. 28: Photograph of the 2.5D ERT survey layout, with six 60 m long profiles (P01 – P06, 0.75 m inter-electrode spacing, 45 m maximum field layout, 1.5 m line spacing) oriented perpendicular to the long axis of an oval-shaped collapse doline and the most prominent voids (viewing direction from west/Stuttgart to east/Ulm).

Results and Discussion

The 2.5D ERT results are shown for the profiles P01, P03 and P05 with the used electrode array and inversion routine, the number of iterations required for the solution and the RMS error, respectively (Fig. 29, Appendix A.2). The used inverse Wenner-Schlumberger array (0.75 m inter-electrode spacing, 45 m maximum field layout) allowed an investigation depth of up to 15 m. The average RMS error was between 1.60 and 3.2 % after 5 iterations. Only directly adjoining borings (less than 0.75 m for core drillings / less than 0.2 m for destructive drillings (except MB-D03/D02 and MB-D03/E03 in profile P03 with less than 0.75 m and 0.35 m)) and the excavation pit were used for calibration and discussion.

In profile P01, the resistivity values ranged from 7.5 to 160 Ωm within the excavation pit area, between line km 69+056 and 69+071. The overlying soil, a binder-stabilized mixture of gravel and silt, showed resistivity values between 15 and 120 Ωm. Between line km 69+056 and 69+064, moderately fractured and medium weathered marls and marlstones with resistivity values between 7.5 and 80 Ωm were exposed beneath the soil cover, underlain by a coarsely fractured and lowly to medium weathered limestone bedrock with resistivity values ranging from 20 to 120 Ωm; a clear demarcation between these geological units was not possible by means of ERT. Between line km 69+064 and 69+071, an oval-shaped collapse doline (composed of cobbly, blocky limestone

fragments embedded in a loamy matrix) with resistivity values between 15 and 160 Ωm was encountered beneath the soil cover; the continuing increase in resistivity with depth might be indicative of looser clastic limestone fragments with a small volume of voids within the deeper raveling zone, as was detected by 4 destructive drilling logs, 1 camera inspection and during pit excavation. Again, a clear demarcation between the collapse doline and the adjoining geological units was not possible by means of ERT. This inefficiency might be caused (i) by the very similar and thus indistinguishable geoelectrical properties of, for example, the soil cover and the underlying marls / marlstones and (ii) by the high amount of fine-grained material within the excavation pit area, reducing the apparent resistivity values of the adjacent limestone bedrock significantly; this observation complements the results of PRINS et al. (2017: 376) and PRINS et al. (2018).

In profile P03, the resistivity values ranged from 10 to 2000 Ωm within the excavation pit area. The overlying soil, a not binder-stabilized mixture of gravel and silt, showed resistivity values between 40 and approximately 2000 Ωm at line km 69+065. It is believed that an air-filled and thus high-resistive void has formed within the loose soil cover at a depth of approximately 1 m, due to the existence of the underlying air-filled void 1 developed within the limestone bedrock. The comparatively more resistive anomaly of the potential void was already indicated within the binder-stabilized soil cover of profile P01 (in its main feature, but to a much lesser extent). Between line km 69+056 and 69+062, moderately fractured and medium weathered marls and marlstones with resistivity values between 10 and 80 Ωm were again exposed beneath the soil cover, also underlain by a coarsely fractured and lowly to medium weathered limestone bedrock with resistivity values ranging from 20 to 320 Ωm; a clear demarcation between these geological units was again not possible by means of ERT. The air-filled void 1 (open fracture, depth: 4 – 10 m, maximum horizontal opening width: 1.5 m) within the limestone bedrock was not shown but rather hidden in the ERT profile; most probably due to the influence of the overlying high-resistive anomaly (potential void) within the soil cover. It seems that the ERT method gives, in general, greater importance to shallow, especially high-resistive anomalies. Between line km 69+065 and 69+071, the collapse doline (composed of cobbly, blocky limestone fragments embedded in a loamy matrix) with resistivity values between 20 and 320 Ωm was encountered beneath the soil cover; the overlying high-resistive anomaly (potential void) within the soil also seemed to exert a considerable influence on the apparent resistivity values of the underlying collapse doline.

In profile P05, the resistivity values ranged from 15 to 960 Ωm within the excavation pit area. The overlying soil, a not binder-stabilized mixture of gravel and silt, showed resistivity values between 30 and 640 Ωm at line km 69+065; the high-resistive anomaly of profile P03 was also recognizable in profile P05, to a lesser extent but still with a considerable influence on the apparent resistivity values at the transition zone to the underlying, moderately fractured and medium weathered marls and marlstones. The latter with resistivity values between 15 and 120 Ωm were again exposed beneath the soil cover, underlain by the coarsely fractured and lowly to medium weathered limestone bedrock with resistivity values ranging from 60 to 960 Ωm; a clear and even non-transitional demarcation between these geological units was possible by means of ERT. While the air-filled void 2 (cavity, depth: 4 – 9 m, maximum horizontal opening width: 0.7 m) with resistivity

values between 120 and 240 Ωm was not distinguishable from the surrounding limestone bedrock, the air-filled void 3 (cavity, partly backfilled loosely with stone and other debris, depth: 4 – 7 m, maximum horizontal opening width: 1.2 m) was clearly visible and shown as a high-resistive anomaly with resistivity values between 320 and 960 Ωm. The air-filled void 2 was probably not resolved by means of ERT because of its comparatively small maximum horizontal opening width of 0.7 m in comparison to the used inter-electrode spacing of 0.75 m. The air-filled void 3 with a maximum horizontal opening width of 1.2 m (and thus approximately 1.5 times the inter-electrode spacing) could be derived accurately in location and roughly in size and shape from the ERT profile. Note that the effective geoelectrical size of the void is larger than its true size because of the surrounding fractured and weathered limestone bedrock, creating a larger anomalous volume; a circumstance, which ultimately favors the detection of the void (CHALIKAKIS et al. 2011: 1172f., MCGRATH et al. 2002: 554). Between line km 69+070 and 69+071, the collapse doline (composed of cobbly, blocky limestone fragments embedded in a loamy matrix) with resistivity values between 20 and 160 Ωm was encountered beneath the soil cover in the edge region of the excavation pit; the continuing increase in resistivity with depth might again be indicative of looser clastic limestone fragments with a small volume of voids within the shallow raveling zone at a depth of approximately 2 – 4 m.

Fig. 30 conclusively illustrates the ground conditions within the excavation pit area, between line km 69+056 and 69+071.

The microgravimetry (Scintrex CG-5 autograv microgravity meter, resolution: 0.005 mGal, nominal grid: 2 m, residual Bouguer gravity, error: 0.004 mGal) of the previously conducted investigation program of the construction company indicated the location, size and planar extent of one gravity low (from −0.015 to –0.050 mGal) (ARGE NBS WENDLINGEN–ULM 2018: 7). This gravity low largely coincided with the extent of the oval-shaped collapse doline; a gross demarcation between the collapse doline and the surrounding geological units was thus possible by means of microgravimetry. In contrast to the 2.5D ERT profiling, the microgravimetric survey did not reveal any of the three air-filled voids developed within the limestone bedrock in the nearest surrounding of the collapse doline; the microgravimetry was thus not able to delineate smaller-scale air-filled voids from comparatively compact rock.

The seismic profile of the previously conducted investigation program of the construction company (along the southwestern line track, direction Stuttgart to Ulm) with combined high-resolution refraction/reflection seismics (Geometrics Geode 72-channel system, 4.5 Hz geophones, 2 m geophone spacing, 2 m shot spacing, source: 5 kg sledgehammer stroke with at least 3 individual hammer blows per shot location, vertical stacking used to enhance signal-to-noise ratio) indicated an overlying, maximum 3 m thick, low velocity zone (v_p = 700 – 1000 m/s) between line km 69+020 and 69+095, underlain by higher seismic velocities (v_p = 1000 – 2700 m/s) (ARGE NBS WENDLINGEN–ULM 2018: 6, KIELBASSA et al. 2015a: 133). This overlying low velocity zone encompassed an area of approximately five times the excavation pit area, where the collapse doline and the air-filled voids were detected; a gross demarcation between the collapse doline and the surrounding geological units was thus not possible and the seismic survey was not able to reveal any of the three air-filled voids.

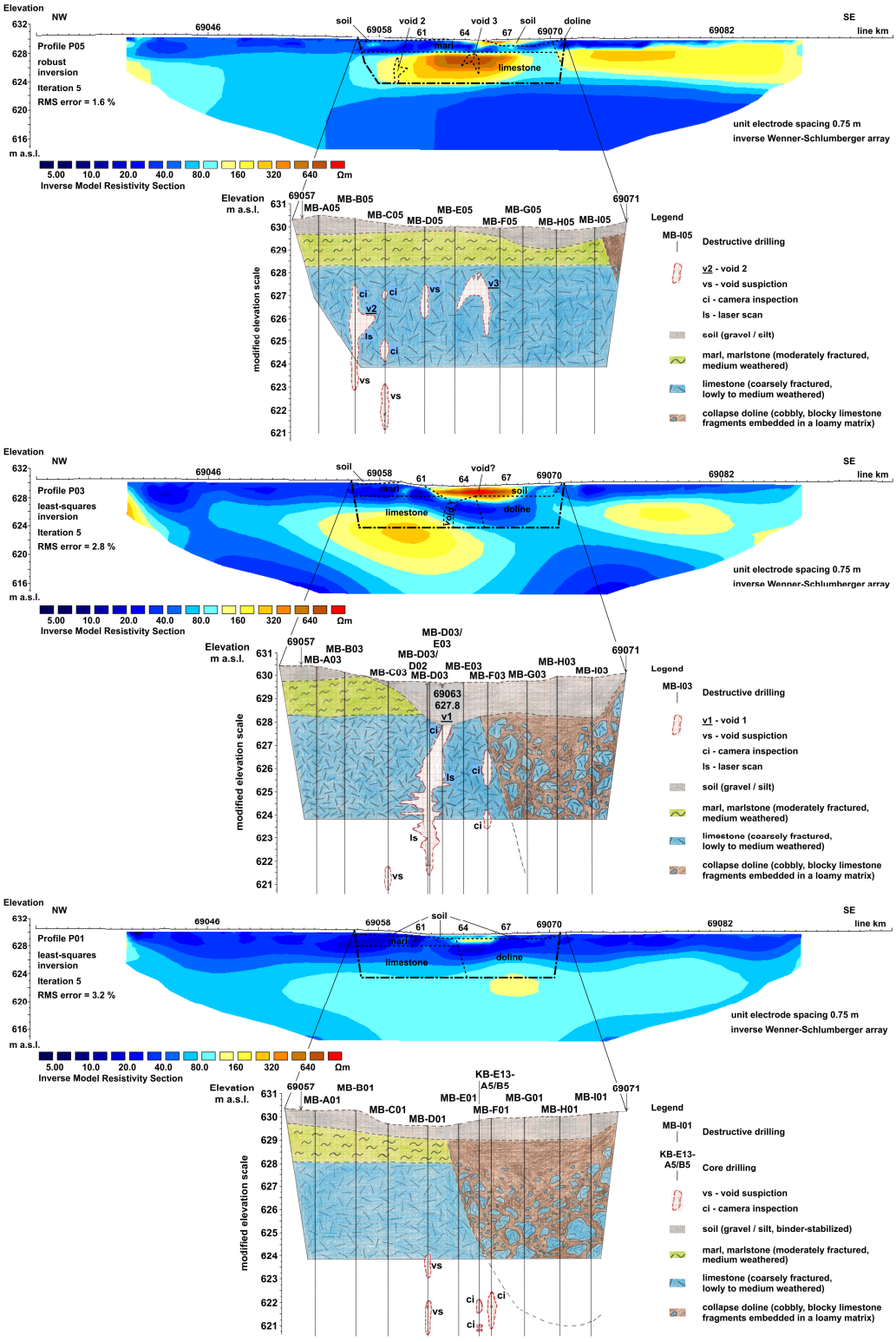

Fig. 29: Interpreted 2.5D ERT results, obtained from the three 60 m long profiles P01, P03 and P05 oriented perpendicular to the long axis of an oval-shaped collapse doline and the most prominent voids. The results of directly adjoining core drillings and destructive drillings (with camera inspections and laser scans) and an excavation pit were incorporated onto the figure.

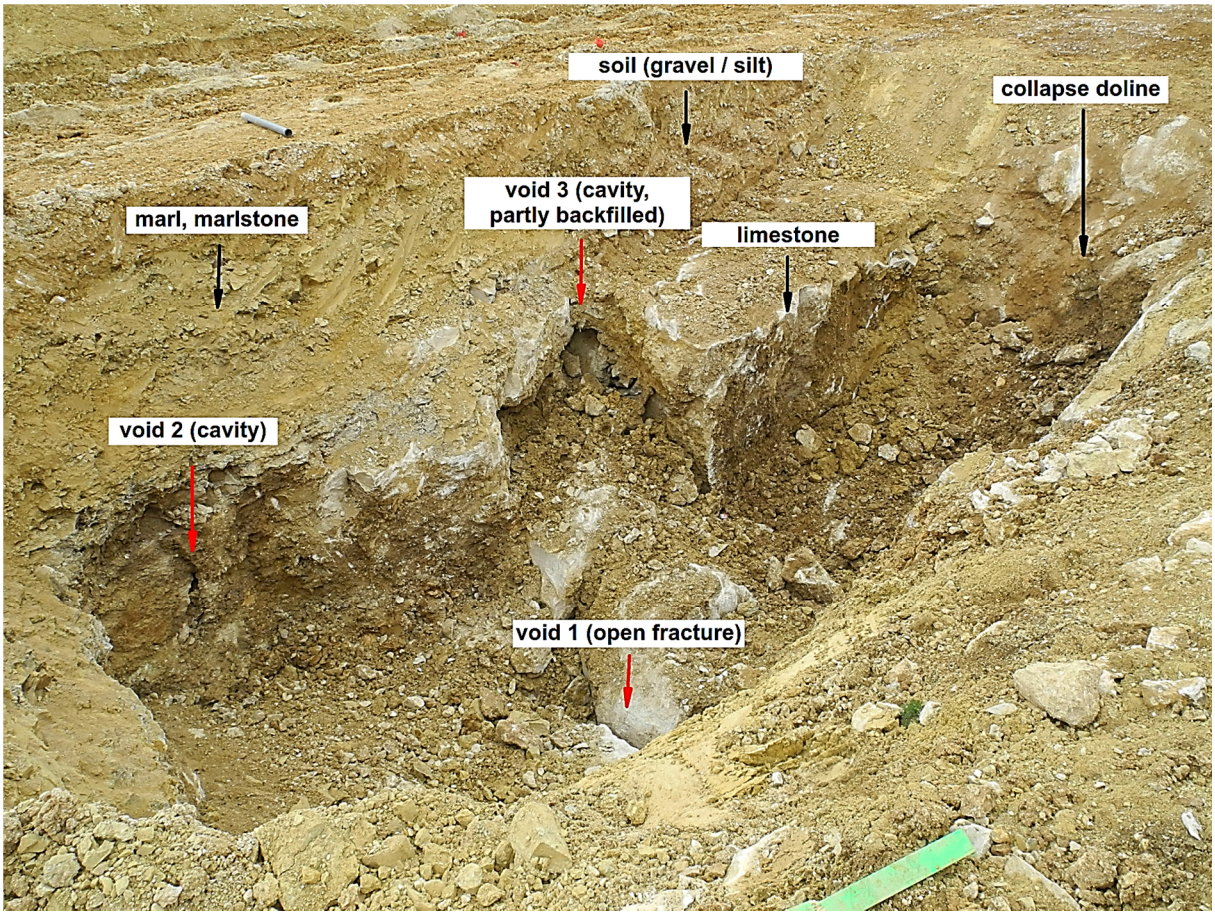

Fig. 30: Ground conditions within the excavation pit area, between line km 69+056 and 69+071 (viewing direction from west/Stuttgart to east/Ulm).

Conclusion

The 2.5D ERT survey conducted with an inverse Wenner-Schlumberger array provided resistivity values of (i) moderately fractured and medium weathered marls and marlstones (7.5 – 120 Ωm), (ii) a coarsely fractured and lowly to medium weathered limestone bedrock (20 – 960 Ωm), (iii) a collapse doline composed of cobbly, blocky limestone fragments embedded in a loamy matrix (15 – 320 Ωm) and of (iv) an air-filled cavity, partly backfilled loosely with stone and other debris (320 – 960 Ωm). A clear demarcation between the marls and marlstones and the limestone bedrock was only possible in one of three ERT profiles (P05) and outside the area of influence of the collapse doline. The latter could not be exactly delineated from the adjoining geological units and its internal structure could only be assumed but not revealed by means of ERT; in contrast to the microgravimetric survey of the previously conducted investigation program of the construction company, which allowed at least a gross demarcation between the collapse doline and the surrounding geological units.

The 2.5D ERT survey conducted with an inverse Wenner-Schlumberger array was partially effective in detecting air-filled voids. The air-filled void 1 (open fracture) within the limestone bedrock was overlain by a soil cover with a high-resistive anomaly and not shown but rather hidden

in the ERT profile, despite its maximum horizontal opening width of 2 times the inter-electrode spacing. Based on the results gained within this research study, the ERT method seems to give greater importance to shallow, especially high-resistive anomalies. When an air-filled void is located beneath a high-resistive anomaly (e.g. another void), the underlying air-filled void might not be detected anymore. The air-filled void 2 (cavity) within the limestone bedrock was not resolved by means of ERT, probably because of its comparatively small maximum horizontal opening width of only 1 time the used inter-electrode spacing. The air-filled void 3 (cavity, partly backfilled loosely with stone and other debris) could be derived accurately in location and roughly in size and shape from the ERT profile, with a maximum horizontal opening width of approximately 1.5 times the inter-electrode spacing. The microgravimetric and seismic surveys, in contrast, were not able to reveal any of the three air-filled voids within the comparatively compact limestone bedrock.

8. Overall conclusions of the research work

8.1. Investigated karst hazard scenario and detected karst phenomena at the study site

As stated in chapter 1, karstic rock can cause a wide range of hazard scenarios that (i) do not or only to a small extent exist in other rock types and that (ii) have a considerable impact on tunnel and underground constructions. In the course of this Ph.D. thesis, the following **karst hazard scenario** (Tab. 7) for tunnel constructions (cut-and-cover method) was investigated:

Tab. 7: Investigated karst hazard scenario for tunnel constructions in the course of this Ph.D. thesis.

Hazard scenario	Karst void filled with air	Karst void filled with water	Karst void filled with soil material	Hazard to the entire construction	Hazard to the environment	Hazard during the construction phase	Hazard during the operation phase
Disturbance of ground load-bearing capacity due to differences in rock and soil resistance/stiffness, especially over pinnacles or dolines	X	X	X	X		X	X

The **study site** – the Swabian Alb high plain, on the new high-speed railway line Wendlingen–Ulm – was a highly heterogeneous karstic environment, which can be described as mature (cf. Tab. 4, Fig. 7). The excavation bottom and thus the measuring level on the Alb high plain was situated in the epikarst zone (cf. Tab. 2, Tab. 3, Fig. 5) and composed of limestones of the Upper Jurassic. These primarily thick-bedded, massive, mechanically strong, coarsely fractured and weathered limestones showed (i) a highly irregular rockhead, (ii) strongly loosened zones with corrosively widened fissures and conduits, (iii) rather small and mostly subvertical, air-/soil-filled cavities and (iv) rather less soil but predominantly boulders and debris. One remarkable example of various surface and subsurface karst forms was an oval-shaped, 12 m deep collapse doline (classified after WALTHAM & FOOKES (2003: 106)) aligned along the strike of the limestones, characterized by subvertical sides and composed of cobbly, blocky limestone fragments embedded in a loamy matrix. The spatial orientation of the doline provided indications on the geometry of the underground conduit network; the statements of GOLDSCHEIDER & DREW (2007: 21), GOEPPERT et al. (2011: 293) and BENSON & YUHR (2016: 22) can thus be confirmed. In the nearest surrounding of the doline, isolated air-filled voids with maximum horizontal opening widths of 1.5 m were detected (cf. chapter 7.3); the development of these dissolution voids was not random but referred to discontinuities within the limestone rock. This finding coincides with the research carried out by karst scientists during the last 40 years (KIRALY 1968, RAUCH & WHITE 1970, WALTHAM 1971, PALMER 1989, KLIMCHOUK & FORD 2000, FILIPPONI & JEANNIN 2006, FILIPPONI 2009). Discontinuities such as bedding planes, joints and faults (often collectively referred to as fractures**)** pervade karstic rock and host and guide almost all parts of the underground solution conduit networks (cf. chapter 3.3).

8.2. Criterion of exclusion of the GPR method for karst reconnaissance at the study site

GPR (or other EM) methods were not part of the previously conducted investigation program of the construction company. As described in chapter 5.5 and 5.6, GPR is well-adapted to the analysis of the near-surface (< 30 m depth) structure of karst (AL-FARES et al. 2002) and useful in the case of air-filled cavities or sinkholes in a limestone bedrock environment (BILLI et al. 2016: 70, VADILLO et al. 2012: 153). However, its penetration depth is significantly limited in the presence of electrically conductive zones (ABDALLATIF et al. 2015: 510, ABDELTAWAB 2013: 268, CARRIÈRE et al. 2013: 39, CHALIKAKIS et al. 2011: 1175, GOLDSCHEIDER & DREW 2007: 194, ROTH & NYQUIST 2003: 1, chapter 5.5, 5.6). On the Swabian Alb high plain, the radar signal would most probably have been absorbed and attenuated due to numerous near-surface and deep-reaching zones composed of clayey / loamy and thus electrically conductive deposits; as was also the case at other karst sites, e.g. at the study site Perry Farm Park in Bourbonnais, east-central Illinois, USA (AHMED & CARPENTER 2003: 705ff., 710), at a study area in the Sang Run quadrangle, Garrett County, Maryland, USA (GRGICH et al. 2004: 5ff.) or at the Tournaisis area at Gaurain-Ramecroix, south-eastern Belgium (KAUFMANN & DECEUSTER 2014: 17f., 21f.) (cf. chapter 6.9). This is the main reason why the GPR method was not used for karst reconnaissance on the Swabian Alb high plain.

8.3. Evaluation of the microgravimetry method for karst reconnaissance at the study site

The microgravimetry (Scintrex CG-5 autograv microgravity meter, resolution: 0.005 mGal, nominal grid: 2 m, residual Bouguer gravity, error: 0.002 – 0.008 mGal) of the previously conducted investigation program of the construction company was able to indicate the location, size and planar extent of zones with lower and higher **ground load-bearing capacity**, respectively; this effectiveness of the microgravimetric method coincides with the statements of CHALIKAKIS et al. (2011: 1175) and with the results of MCGRATH et al. (2002: 552, 555). The exact spatial distribution with depth as well as the internal structure of these zones could not be obtained from the microgravimetric data (cf. chapter 7.1 and 7.2). Moreover, the microgravimetric survey alone was not able to clearly delineate compact rock from loosened zones.

On the one hand, the microgravimetric data suggested the presence of **air-filled voids** by various gravity lows, which could not be confirmed by direct probing investigations (cf. chapter 7.1 and 7.2). Microgravimetry alone is often incapable of discriminating between an air-filled void and local bedrock loosening, both possibly producing very similar gravity anomalies (depending on the depth) (GOLDSCHEIDER & DREW 2007: 182). On the other hand, the microgravimetry was not able to delineate smaller-scale air-filled voids from a comparatively compact limestone rock (cf. chapter 7.3). The assertion of CHALIKAKIS et al. (2011: 1175f.) that microgravity remains one of the geophysical methods best suited to the detection of voids, even when these voids might be relatively small, can thus not be confirmed by means of the present measurements. An unequivocal anomalous response (as described by VAN SCHOOR (2002: 393) and CARRIÈRE et al. (2013: 32)) was not caused by the existing, but ultimately not construction-relevant air-filled voids. In this respect, the microgravimetric results complement the findings of ROTH et al. (2000: 359), which illustrated the difficulty to distinguish gravity anomalies caused by shallow voids from those

caused by abrupt changes in bedrock depth; fluctuations observed in the gravity data in areas without voids were of a similar magnitude to those observed in areas with voids, at a karst site in Northampton County, northeastern Pennsylvania, USA (cf. chapter 6.9).

The microgravimetry indicated the location, size and planar extent of an oval-shaped collapse **doline** and allowed a gross demarcation between the collapse doline and the surrounding geological units (cf. chapter 7.3); the statement of CHALIKAKIS et al. (2011: 1175) that microgravity is able to detect large dolines or those located close to the ground surface can thus be confirmed. Also ARGENTIERI et al. (2015) applied the microgravity technique successfully in the detection of dolines and in differentiating their geological structure in the northern Acque Albule Basin, northeast of Rome, central Italy, where the density of the doline's filling material was markedly lower than the density of the host rock (cf. chapter 6.9).

8.4. Evaluation of the seismic method for karst reconnaissance at the study site

The seismic profiles along the line tracks with combined high-resolution refraction/reflection seismics (Geometrics Geode 72-channel system, 4.5 Hz geophones, 2 m geophone spacing, 2 m shot spacing, source: 5 kg sledgehammer stroke with at least 3 individual hammer blows per shot location, vertical stacking used to enhance signal-to-noise ratio) of the previously conducted investigation program of the construction company allowed a rough division of the subsurface in zones of highly cohesive loam deposit / completely weathered limestone bedrock, medium weathered limestone bedrock and intact limestone bedrock, respectively. The seismic data were not able to distinguish between highly cohesive loam deposits and completely weathered limestone bedrock within the shallow subsurface (< 10 m) (cf. chapter 7.1 and 7.2). In certain areas, the seismic survey showed the **bedrock surface** precisely (cf. chapter 7.1). These findings coincide with the indications of CHALIKAKIS et al. (2011: 1176) and the results of SIART et al. (2011: 319, 331) and SIART et al. (2013: 1139, 1143ff.) at the archaeological site of Zominthos and at Kroustas, Crete, Greece, where seismic refraction tomography (SRT) performed rather moderately in determining the internal stratification of a loose unconsolidated overburden, but allowed the detection of the actual limestone and dolomite bedrock surface (cf. chapter 6.9). Also at the Tournemire test site, Aveyron, France, seismic reflection clearly identified the interfaces between an overlying clay-rock and underlying carbonate formations (GÉLIS et al. 2010: 1407, 1416) (cf. chapter 6.9).

The seismic survey was not able to reveal any of three **air-filled voids** within a comparatively compact limestone bedrock (cf. chapter 7.3). This observation coincides with the results of KAUFMANN & DECEUSTER (2014: 23) at the Tournaisis area at Gaurain-Ramecroix, south-eastern Belgium, where smaller palaeokarst slots encountered at a highly weathered limestone bedrock were not detected by means of SRT; probably due to their limited width compared to the geophone spacing and to their vertical structure that is often poorly reconstructed, especially by surface SRT (cf. chapter 6.9). In contrast, seismic tomography measurements at the Poumeyssen test site, southwestern France, provided the location and width of a 5 – 9 m wide, 10 – 15 m deep, water-filled (and thus with lower acoustic impedance contrast compared to air-filled) conduit to within a few meters, whose location and shape in compact limestone were known from cave mapping work

(GUÉRIN et al. 2009: 816) (cf. chapter 6.9). On the Swabian Alb high plain, the used seismic source (5 kg sledgehammer stroke) was comparatively weak (despite at least 3 individual hammer blows per shot location) and a poor signal-to-noise ratio possibly prevented the detection of the three air-filled, but ultimately not construction-relevant voids. Also GÉLIS et al. (2010: 1407, 1416) described that their seismic reflection data failed in revealing faults in a carbonate / clay-rock formation, inter alia due to the poor signal-to-noise ratio at shallow depths, at the Tournemire test site, Aveyron, France (cf. chapter 6.9).

A gross demarcation between the collapse **doline** and the surrounding geological units was not possible by means of refraction/reflection seismics (cf. chapter 7.3). On the one hand, these results are comparable to those of KAUFMANN & DECEUSTER (2014: 22f.) at the Tournaisis area at Gaurain-Ramecroix, south-eastern Belgium, where SRT was unsuccessful and seismic reflection only moderately suitable for delineating doline locations (cf. chapter 6.9). On the other hand, SRT measurements at the archaeological site of Zominthos, Central Crete, Greece, were able to highlight a buried doline filled with fine-grained material, developed within an intensively karstified limestone and dolomite bedrock and overlain by an extremely coarse-grained covering possibly comprised of numerous debris fragments (SIART et al. 2011: 322f.) (cf. chapter 6.9). Also in the northern Acque Albule Basin, northeast of Rome, central Italy, SRT was inter alia capable of delineating a doline depression from the surrounding travertine lithoid and the sedimentary sequence with highlighting an asymmetric deepening of the depression (ARGENTIERI et al. 2015: 44f.) (cf. chapter 6.9). Beside these recent and relatively successful applications, SRT and seismic reflection are yet rather rarely used in terms of doline detection.

8.5. Evaluation of the ERT method for karst reconnaissance at the study site

In advance: as first described in chapter 7.1, drilling only a few decimeters apart in a highly heterogeneous karstic environment can easily result in a completely different borehole record; deviations between the drilling and resistivity data might at least partly be caused by the distance between a drilling location and the ERT profile (cf. chapter 7.2). Therefore, it is recommended to use only directly adjoining **direct probing investigations** for ERT calibration and interpretation; less than 4 m for exploration and core drillings and less than 1 m for destructive drillings proved reasonably good (cf. chapter 7.1). However, at many karst sites, the true ground conditions are not discovered until foundations are excavated (cf. chapter 7.3).

The **first 2D ERT survey** (ABEM Terrameter SAS 1000, Wenner-Schlumberger array, 2.5 m electrode spacing, roll-along technique, robust inversion, RMS error: 5.2 % for a maximum of 5 iterations) accurately revealed the size, shape and spatial distribution of conductive clay / loam deposits (< 60 Ωm) and delineated them from an intensely fractured and/or highly weathered limestone bedrock (60 – 240 Ωm), respectively (cf. chapter 7.1); this outcome (high spatial resolution at shallow depths < 15 m) confirms the indications of Tab. 5 and correlates with the results of SIART et al. (2011: 319ff., 323ff.), SIART et al. (2013: 1139ff., 1144), ISMAIL & ANDERSON (2012: 281, 285, 289), KAUFMANN & DECEUSTER (2014: 22f.) and CARRIÈRE et al. (2013: 31, 34f., 37ff.) (cf. chapter 6.9). Especially in areas with a fractured and/or weathered to intact limestone bedrock underground, the results of the ERT survey were reliable and made

additional direct probing investigations dispensible. The acquired **resistivity values** of (i) the clay / loam deposits (< 60 Ωm) and the limestone bedrock (60 – 960 Ωm, depending on degree of fracturing / weathering) (cf. chapter 7.1) are within the range reported in chapter 6.3 and Tab. 6 and correspond with those given by ISMAIL & ANDERSON (2012: 281, 285, 289), KAUFMANN & DECEUSTER (2014: 22f.), PUTIŠKA et al. (2014: 155ff., 162), REIS JÚNIOR et al. (2015: 371ff., 380) and KIDANU et al. (2016: 107) at other karst sites, respectively (cf. chapter 6.9). The comparatively low resistivity values of the intensely fractured and/or highly weathered limestone bedrock (60 – 240 Ωm) were most probably caused by frequently recurring clayey / loamy (and thus conductive) fracture and void infillings with increasing depth; these observations coincided with the results presented by ISMAIL & ANDERSON (2012: 287f.) (cf. chapter 7.1). Such low resistivity values of a limestone bedrock (fractured / weathered) might not be an exception but may occur more frequently in karstic environments. The main **limitations** of the ERT survey were (pursuant to chapter 6.8) (i) the rapid reduction of resolution with distance from the electrodes and (ii) the limited sensitivity to resistive zones beneath conductive zones. Hence, the ERT section did not show a continuing increase in resistivity with depth, despite the higher quality of the limestone bedrock in depth; an observation, which complements the findings of ROTH et al. (1999: 299) and HARRO & KRUSE (2014: 213) (cf. chapter 6.9).

The **Wenner-Schlumberger** and the **Dipole-dipole** electrode arrays were applied for data acquisition (as recommended by ZHOU et al. (2002), chapter 6.5), but only the Wenner-Schlumberger protocol was exhibited in chapter 7.1. This was the case because there were no significant differences in the respective 2D apparent resistivity pseudosections; the two electrode arrays delivered nearly identical results. The approach of **model refinements** (meaning the use of model cells with widths of half the unit electrode spacing) produced small near-surface artifacts, which significantly disturbed the data set (cf. chapter 7.1). Even if SASAKI (1992) and LOKE (2012) recommend the use of a model cell-size of half the unit electrode spacing (cf. chapter 6.7), which is often used in practice (e.g. CARRIÈRE et al. 2013, chapter 6.9), it was not expedient in the present research work, for unclear reasons. The adjustment of inversion parameters including the damping factor and flatness filter (LOKE 2004b: 56ff., DAHLIN & ZHOU 2004: 387, cf. chapter 6.6) had no appreciable impact on the apparent resistivity pseudosections.

The **second 2D ERT survey** (ABEM Terrameter SAS 4000, inverse Wenner-Schlumberger array, 2.0 m electrode spacing, roll-along technique, robust inversion, RMS error: 1.61 % for a maximum of 5 iterations) also revealed the size, shape and spatial distribution of conductive clayey / loamy deposits (< 60 Ωm) and delineated them from an intensely fractured and/or highly weathered limestone bedrock (60 – 240 Ωm), respectively (cf. chapter 7.2). In contrast to the first survey, an **inverse Wenner-Schlumberger** electrode array was used for data acquisition, which can be applied in a multi-channel system and thus reduces the survey time significantly (cf. chapter 6.5). As previously described, the only significant disadvantage of this array in comparison to the standard Wenner-Schlumberger array is the increased telluric noise / the possibly minimized resolution at large potential electrode spacings. However, comparative measurements on the Swabian Alb high plain over a length of approximately 100 m have shown that the inverse Wenner-Schlumberger array delivered the same results as those obtained from the standard Wenner-

Schlumberger array; a larger potential electrode spacing had no negative effect on the resistivity results.

The **2.5D ERT survey** (ABEM Terrameter SAS 4000, inverse Wenner-Schlumberger array, 0.75 m electrode spacing, lines oriented perpendicular to the long axis of an oval-shaped collapse doline and the most prominent voids, 1.5 m line spacing, smoothness-constrained least-squares / robust inversion, RMS error: 1.60 – 3.20 % for a maximum of 5 iterations) provided **resistivity values of** (i) moderately fractured and medium weathered **marls** and **marlstones** (7.5 – 120 Ωm), (ii) a coarsely fractured and lowly to medium weathered **limestone bedrock** (20 – 960 Ωm), (iii) a collapse **doline** composed of cobbly, blocky limestone fragments embedded in a loamy matrix (15 – 320 Ωm) and of (iv) an **air-filled cavity**, partly backfilled loosely with stone and other debris (320 – 960 Ωm) (cf. chapter 7.3). These resistivity values are largely within the range reported in chapter 6.3 and Tab. 6 and correspond with those given by ROTH et al. (2002: 226ff.), GÉLIS et al. (2010: 1409ff.), SIART et al. (2011: 319ff., 323ff.), FESTA et al. (2012: 143f.), ISMAIL & ANDERSON (2012: 281, 285ff., 289), KAUFMANN & DECEUSTER (2014: 22f.), PUTIŠKA et al. (2014: 155ff., 162), ARGENTIERI et al. (2015: 41, 43f.), REIS JÚNIOR et al. (2015: 371ff., 380) and KIDANU et al. (2016: 107) at other karst sites, respectively (cf. chapter 6.9). Again conspicuous are the comparatively low resistivity values of the coarsely fractured and lowly to medium weathered limestone bedrock. Also the acquired resistivity values of the air-filled cavity are lower than typically expected (more than 2000 Ωm, chapter 6.3) and as observed in other karst terrains (e.g. NYQUIST et al. 2007: 139f., 142f., ORTEGA et al. 2010: 236f., 242, YOUSSEF et al. 2012b: 655, 659ff., REDHAOUNIA et al. 2015: 1289, 1294ff., cf. chapter 6.9). Based on the current research work on the Swabian Alb high plain, it can be concluded that air-filled cavities can be characterized by even lower resistivity values (< 1000 Ωm) and that the resistivity value alone may not be sufficient to conclude that a void is present (cf. ROTH & NYQUIST 2003: 9).

A clear **demarcation** between (i) the marls and marlstones and the limestone bedrock and between (ii) the collapse doline and the adjoining geological units was not possible by means of ERT within the area of influence of the collapse doline (cf. chapter 7.3). This inefficiency might have been caused (i) by the very similar and thus indistinguishable geoelectrical properties of, for example, the soil cover and the underlying marls / marlstones and (ii) by the high amount of fine-grained material within the excavation pit area, reducing the apparent resistivity values of the adjacent limestone bedrock significantly; this observation complemented the results of PRINS et al. (2017: 376) and PRINS et al. (2018) (cf. chapter 7.3). As outlined in chapter 6.8, the overall effectiveness of ERT profiling in karst environments is based on the contrast of different resistivity values, particularly between the limestone host rock and detrital sediments/clayey soils due to porosity and moisture content (BERMEJO et al. 2017: 393, FORD & WILLIAMS 2007: 148f., ZHOU et al. 2000: 761). However, based on the present research work on the Swabian Alb high plain, it can be concluded that this statement is only true if there are perceptible variations in the resistivity values of the different geological units/karst features; otherwise, the ERT method is limited in differentiating a highly heterogeneous karstic environment within narrow space (cf. chapter 7.3).

Outside the area of influence of the collapse doline, a clear demarcation between the marls and marlstones and the limestone bedrock was possible (cf. chapter 7.3). As mentioned in chapter 6.7,

a smoothing effect is often identifiable in the resistivity results when compared to the actual bedrock depth (ROTH et al. 2000: 362) and even a sharply contrasting limestone/clay boundary will, in general, appear transitional on the processed resistivity images (ZHOU et al. 2000: 762). Contrary to these indications, the actual **limestone bedrock surface** was depicted clear and even non-transitional by means of the used inverse Wenner-Schlumberger array (cf. chapter 7.3). This effectiveness of the ERT method in detecting the (for common) irregular limestone bedrock surface is consistent with the specifications of Tab. 5 and correlates with the results of ZHOU et al. (2000: 760ff.), ROTH et al. (2000: 359ff., 365), ROTH et al. (2002: 226ff.), ROTH & NYQUIST (2003: 1ff.), AHMED & CARPENTER (2003: 709ff.), NYQUIST et al. (2007: 139f., 142f.), ORTEGA et al. (2010: 236f., 242), SIART et al. (2011: 319ff., 323ff.), ISMAIL & ANDERSON (2012: 281, 285ff., 289), KAUFMANN & DECEUSTER (2014: 22f.), FADHLI et al. (2015: 349f., 353) and KIDANU et al. (2016: 107) at other karst sites, respectively (cf. chapter 6.9).

As stated before, the collapse **doline** could not be exactly delineated from the adjoining geological units and its internal structure could only be assumed but not revealed by means of ERT (cf. chapter 7.3). Even if the ERT technique is well suited to mapping dolines due to its ability to detect resistive features and discriminate subtle resistivity variations in karst environments (FESTA et al. 2012: 140), exploring the geometrical and geophysical properties of dolines proved to be complex and unpredictable since dolines may have differentiated morphologic properties at different scales (SIART et al. 2011: 331) (cf. chapter 6.7). Nevertheless, ERT measurements allowed the reliable detection of dolines at the Tournaisis area at Gaurain-Ramecroix, south-eastern Belgium (KAUFMANN & DECEUSTER 2014: 22f.), in Komberek, western Slovakia (PUTIŠKA et al. 2014: 155ff., 162), in the sedimentary Acque Albule Basin, northeast of Rome, central Italy (BILLI et al. 2016: 63, 75ff.) and at a highway construction site in Jefferson County, Missouri, USA (ISMAIL & ANDERSON 2012: 281, 285, 289), for instance (cf. chapter 6.9). At further karst sites, e.g. in Frederick County, Maryland, USA (ZHOU et al. 2002: 925ff.), at the study site Perry Farm Park in Bourbonnais, east-central Illinois, USA (AHMED & CARPENTER 2003: 709ff.), at the archaeological site of Zominthos, Central Crete, Greece (SIART et al. 2011: 315, 323, 325f.), at Masseria Forte di Morello, Salento Peninsula, southern Italy (FESTA et al. 2012: 143f.) and in the northern Acque Albule Basin, northeast of Rome, central Italy (ARGENTIERI et al. 2015: 41, 43f.), ERT surveys (primarily conducted with **Dipole-dipole** and **Wenner-Schlumberger** arrays) effectively delineated dolines from their surroundings, respectively (cf. chapter 6.5, 6.9); in this context, the Dipole-dipole array (followed by the Wenner-Schlumberger array) provided the highest precision, due to its greater sensitivity to vertical resistivity boundaries (e.g. ZHOU et al. 2002: 925ff.).

The 2.5D ERT survey conducted with an **inverse Wenner-Schlumberger** array was partially effective in detecting **air-filled voids**. An air-filled void 1 (open fracture) within the limestone bedrock was overlain by a soil cover with a high-resistive anomaly and not shown but rather hidden in the ERT profile, despite its maximum horizontal opening width of 2 times the inter-electrode spacing; the ERT method seemed to give greater importance to shallow, especially **high-resistive anomalies** (cf. chapter 7.3). It could be concluded that when an air-filled void is located beneath a high-resistive anomaly (e.g. another void), the underlying air-filled void might not be detected anymore (cf. chapter 7.3). Also GÉLIS et al. (2010: 1412, 1417) illustrated the ineffectiveness of the ERT method in imaging karst features, when an overlying high-resistive anomaly is present, at

the Tournemire test site, Aveyron, France (cf. chapter 6.9). The overlying high-resistive anomaly of chapter 7.3 also seemed to exert a considerable influence on the apparent resistivity values of the underlying collapse doline and at the transition zone to the underlying marls and marlstones; therefore, caution should be taken when interpreting inverted resistivity sections in comparable karst site conditions.

An air-filled void 2 (cavity) within the limestone bedrock was not resolved by means of ERT, probably because of its comparatively small maximum horizontal **opening width** of only 1 time the used **inter-electrode spacing** (cf. chapter 7.3). In this regard, reference can also be made to chapter 7.2, in which 1 core drilling encountered an air-filled void, which did not show up in the ERT profile; again an air-filled void on a scale too fine to be resolved with the used inter-electrode spacing. Based on the findings of the present research work, the use of an inter-electrode spacing of 0.5 m and thus 0.33 times the opening width of construction-relevant voids is recommended, in order to obtain sufficient safety in karst building ground evaluation.

An air-filled void 3 (cavity, partly backfilled loosely with stone and other debris) within the limestone bedrock (and outside the area of influence of the collapse doline) could be derived accurately in location and roughly in size and shape from the ERT profile, with a maximum horizontal opening width of approximately 1.5 times the inter-electrode spacing; this effective outcome coincides with the indications of Tab. 5 and correlates with the results of VAN SCHOOR (2002: 398), NYQUIST et al. (2007: 139f., 142f.), ABU-SHARIAH (2009: 239f., 243), ORTEGA et al. (2010: 236f., 242), GAMBETTA et al. (2011: 11ff.), YOUSSEF et al. (2012b: 655, 659ff.), PUTIŠKA et al. (2014: 155ff., 162), FADHLI et al. (2015: 349f., 353), REDHAOUNIA et al. (2015: 1289, 1294ff.) and ABD EL AAL (2017: 220f.) at other karst sites, respectively (cf. chapter 6.9). However, while the **location of a void** can often be derived from ERT surveys (e.g. NYQUIST et al. 2007: 139f., 142f., ABU-SHARIAH 2009: 239f., 243, ORTEGA et al. 2010: 236f., 242, ABD EL AAL 2017: 220f., chapter 6.9), exploring its **three-dimensional geometry** often remains extraordinarily complex (e.g. ROTH et al. 2002: 231, ABU-SHARIAH 2009: 239f., 243, REIS JÚNIOR et al. 2015: 378, chapter 6.9). Nevertheless, there have been some reasonably good examples of detecting known air-filled cavities and determining their three-dimensional volume by means of ERT; for instance in a case study at Al Eitaliyah, northeast of Ar Riyad City, Kingdom of Saudi Arabia (YOUSSEF et al. 2012b: 655, 659ff.) (cf. chapter 6.9).

As elucidated in chapter 6.7, the effectiveness of the ERT method in exploring geological defective karst voids depends on (i) the orientation of the test line, (ii) the horizontal offset from the karst void to the test line and (iii) on the quality of the bedrock surrounding the karst void (ROTH & NYQUIST 2003: 1, 8). By ensuring **lines** are **oriented perpendicular to** the **strike** of elongated structures, distortion effects in the resistivity model can be reduced (LOKE et al. 2013: 149, ZHOU et al. 2000: 763). In this regard, the 2.5D ERT survey held a good precondition with lines oriented perpendicular to the long axis of the oval-shaped collapse doline and the most prominent voids (cf. chapter 7.3); as was also effectively done by ISMAIL & ANDERSON (2012: 281, 285, 289), at a highway construction site in Jefferson County, Missouri, USA (cf. chapter 6.9). In addition, the 2.5D ERT survey was conducted with a **line spacing** of 1.5 m and thus no more than two times the electrode spacing of 0.75 m, as recommended by CHAMBERS et al. (2002), ROTH et al. (2002) and

GHARIBI & BENTLEY (2005) (cf. chapter 6.7). Based on the findings of the present research work, a line spacing of 1 m and thus two times the advised inter-electrode spacing of 0.5 m is recommended, in order to detect construction-relevant karst voids and to obtain sufficient safety in karst building ground evaluation. It is generally true that the likelihood of locating a void will be increased and distortion effects will be reduced by using a **3D ERT survey** approach in complex karst settings (ROTH & NYQUIST 2003: 11, LOKE et al. 2013: 149) (cf. chapter 6.7). However, a 3D ERT survey (meaning the use of orthogonal cross-lines in addition to parallel 2D lines) should not be applied, if restrictive circumstances (e.g. terrain effect, anisotropic effect etc.) are present and may disturb the data set, significantly; as described in chapter 7.3. The epikarst zone affords the advantage of not being a fully saturated medium and often provides a sharp **resistivity contrast** between **air-filled voids** and the **limestone bedrock** (VADILLO et al. 2012: 153f.) (cf. chapter 4). However, despite this good precondition, the 2.5D ERT survey showed no or only a moderately defined resistivity contrast between the air-filled voids and the limestone bedrock, respectively (cf. chapter 7.3). Also GUÉRIN et al. (2009: 816) stated that it was a moderately defined resistivity contrast between a void (water-filled conduit) and the limestone host rock, which affected their electrical measurements, at the Poumeyssen test site, southwestern France (cf. chapter 6.9). Besides the higher resistivity value in comparison to the limestone bedrock, air-filled voids may only be detected by the relatively abrupt transition from lower to higher resistivity values and by a subcircular-shaped, elliptical-shaped or tabular-shaped progression of the isoohms, depending on the shape of the void. If the void within the limestone bedrock is comparatively small, its effect on the resistivity section will be insignificant (cf. chapter 7.3), unless its resistivity is extremely high (suppression principle, chapter 6.2).

The **smoothness-constrained least-squares method** (L2-norm criterion) (DEGROOT-HEDLIN & CONSTABLE 1990) and the **robust inversion routine** (L1-norm criterion) (FARQUHARSON & OLDENBURG 1998, LOKE et al. 2003) were used to invert the acquired resistivity data; while the first was more suitable in areas where the subsurface resistivity values changed in a smooth manner (e.g. profile P01, chapter 7.3), the latter yielded more accurate results for regions that were piecewise constant and separated by relatively sharp boundaries (e.g. profile P05, chapter 7.3). Based on the results of the current research work, the robust inversion routine was more suitable for detecting the limestone bedrock surface and air-filled voids; an observation, which complements the indications of PUTIŠKA et al. (2014: 158) and ZHU et al. (2011: 529) (cf. chapter 6.6).

In terms of detecting geological defective karst voids, an electrode array responding best to the material change between the karst void and its non-karstic/karstic surrounding is primarily required (cf. chapter 6.5). The 2.5D ERT survey could reliably be used to test the effectiveness of an **inverse Wenner-Schlumberger** array for exploring the geometry of known **air-filled voids**; one of three air-filled voids could be derived accurately in location and roughly in size and shape from the ERT measurements (cf. chapter 7.3). In this regard, the **Dipole-dipole** array would possibly have been more suitable for delineating the mainly subvertical, tabular-shaped air-filled voids due to its better horizontal data coverage and its greater sensitivity to vertical resistivity boundaries (LABUDA & BAXTER 2001: 10, LOKE 2004b: 30f., ZHOU et al. 2002: 925ff., chapter 6.5); note that voids with

subvertical, tabular-shaped cross-sections are in general more difficult to be detected than those with equant cross-sections, by means of ERT (GOLDSCHEIDER & DREW 2007: 174). Some recent applications of the ERT method demonstrated the effectiveness of the Dipole-dipole array in delineating air-filled cavities, for instance at two sinkhole sites near Centurion, south of Pretoria, South Africa (VAN SCHOOR 2002: 398), at the karst research area Metzgar Field, eastern Pennsylvania, USA (NYQUIST et al. 2007: 139f., 142f.) and in a case study at Al Eitaliyah, northeast of Ar Riyad City, Kingdom of Saudi Arabia (YOUSSEF et al. 2012b: 655, 659ff.) (cf. chapter 6.9). As outlined in chapter 6.5, ZHOU et al. (2002: 926) directly compared the Dipole-dipole and the Wenner-Schlumberger arrays in locating a water-saturated void in Maryville, Tennessee, USA, where the Dipole-dipole array was superior in delineating the water-saturated void. At the Torcas-Cueva Mayor endokarst system, Sierra de Atapuerca, Burgos, Spain, in contrast, the Wenner-Schlumberger array provided more realistic results of existing air-filled cavities (ORTEGA et al. 2010: 236f., 242) (cf. chapter 6.9). Compared to the Dipole-dipole array, the Wenner-Schlumberger array will be more suitable for delineating subhorizontal, elliptical-shaped or tabular-shaped air-filled voids (e.g. void 3, chapter 7.3), due to its greater sensitivity to horizontal resistivity boundaries; it is these subhorizontal air-filled voids, which have a major impact on the ground load-bearing capacity in karstic environments.

In chapter 6.5, it was elucidated that the Wenner-Schlumberger array (compared to the Dipole-dipole array) affords the advantage of (i) a significantly higher signal strength / larger median depth of investigation (LOKE 2004b: 33), (ii) its comparatively lower susceptibility to near-surface inhomogenities (MILSOM 2003: 106) (while its resistivity results in turn are generally less affected by artifacts (CARRIÈRE et al. 2013: 34)) and (iii) its greater sensitivity to horizontal resistivity boundaries (MILSOM 2003: 106); the actual limestone bedrock surface of chapter 7.3 would most probably not have been resolved non-transitional by means of a Dipole-dipole array. An inverse Wenner-Schlumberger array affords the same advantages as the standard Wenner-Schlumberger array (if it is ensured that the larger potential electrode spacing has no negative effect on the resistivity results), but, in addition, reduces the survey time significantly when applied in a multi-channel system (cf. chapter 6.5). Based on their results in Frederick County, Maryland, and Maryville, Tennessee, both USA, ZHOU et al. (2002) concluded that a combination of the Dipole-dipole (preferred) and the Wenner-Schlumberger array should be used for ERT data acquisition in karst terrains. Based on the findings of the present research work on the Swabian Alb high plain, a **combination of** an **inverse Wenner-Schlumberger** and the **Dipole-dipole** array can be recommended for data acquisition in a highly heterogeneous karstic environment, with different geological units/karst features within narrow space.

Conclusively, the following questions should conscientiously be answered: What is the **main outcome** of the 2D / 2.5D ERT measurements on the Swabian Alb high plain and what recommendations can be given for future ERT applications in karstic environments?

The **2D ERT surveys** (conducted with Wenner-Schlumberger, Dipole-dipole and inverse Wenner-Schlumberger electrode arrays) have proved to be robust and consistent in revealing the size, shape and spatial distribution of clayey / loamy deposits (< 60 Ωm) and in delineating them from a fractured and/or weathered limestone bedrock (60 – 960 Ωm). The ERT method was thus effective in detecting zones with low ground load-bearing capacity and in delineating them from zones, generally capable of bearing weight. Especially in areas with a fractured and/or weathered to intact limestone bedrock underground, the results of the ERT survey were reliable and made additional direct probing investigations dispensible. The comparatively low resistivity values of the limestones can be seen as possible geoelectrical indicators of the limestone host rock in karstic environments.

Comparative measurements have shown that the inverse Wenner-Schlumberger array delivered the same results as those obtained from the standard Wenner-Schlumberger array; a larger potential electrode spacing had no negative effect on the resistivity results.

Model refinements (meaning the use of model cells with widths of half the unit electrode spacing) produced small near-surface artifacts, which significantly disturbed the data set; this approach was not expedient, for unclear reasons. The adjustment of inversion parameters including the damping factor and flatness filter had no appreciable impact on the apparent resistivity pseudosections.

The **2.5D ERT survey** (parallel 2D lines, conducted with an inverse Wenner-Schlumberger electrode array) provided resistivity values of:

(i) marls and marlstones (fractured, weathered): 7.5 – 120 Ωm,
(ii) limestone bedrock (coarsely fractured, lowly to medium weathered): 20 – 960 Ωm,
(iii) collapse doline (cobbly, blocky limestone fragments in loamy matrix): 15 – 320 Ωm,
(iv) air-filled cavity (partly backfilled loosely with stone / other debris): 320 – 960 Ωm.

It could be concluded that air-filled cavities can be characterized by lower resistivity values than typically expected (< 1000 Ωm).

Exploring the geometrical and geophysical properties of dolines still remains complex due to their differentiated morphologic properties at different scales.

Outside the area of influence of the collapse doline, the actual limestone bedrock surface was depicted clear and even non-transitional by means of the used inverse Wenner-Schlumberger array.

The 2.5D ERT survey could reliably be used to test the effectiveness of an inverse Wenner-Schlumberger array for exploring the geometry of known air-filled voids; one of three air-filled voids could be derived accurately in location and roughly in size and shape from the ERT profiles. In general, the ERT method gave greater importance to shallow, especially high-resistive anomalies.

In order to obtain sufficient safety in karst building ground evaluation, the use of

(i) an inter-electrode spacing of 0.5 m and thus 0.33 times the opening width of construction-relevant voids and
(ii) a line spacing of 1 m and thus two times the advised inter-electrode spacing of 0.5 m

is recommended.

The robust inversion routine was more suitable for detecting the limestone bedrock surface and the air-filled voids.

The used inverse Wenner-Schlumberger array (applied in the multi-channel system ABEM Terrameter SAS 4000) afforded the same advantages as the standard Wenner-Schlumberger array, but, in addition, reduced the survey time significantly (by a factor of almost 4). If it is ensured that the larger potential electrode spacing has no negative effect on the resistivity results, a combination of an inverse Wenner-Schlumberger and the Dipole-dipole array can be recommended for data acquisition in a highly heterogeneous karstic environment, with different geological units/karst features within narrow space.

Based on the findings of the present research work / of previous ERT studies at other karst sites, **future research priorities** for ERT applications in karstic environments should primarily deal with the following question:

> How can the ERT technique (including electrode arrays) be further improved in exploring the exact three-dimensional geometry and the characteristics of shallow/deep geological defective karst voids and other smaller-scale karst features underground?

The **bottom line** of this research work: The 2D / 2.5D ERT measurements (conducted with an inverse Wenner-Schlumberger array) complemented the microgravimetric and seismic results of the previously conducted investigation program of the construction company and provided a reliable and consistent contribution to karst (void) reconnaissance and building ground evaluations in a highly heterogeneous karstic environment like the Swabian Alb high plain, on the new line Wendlingen–Ulm.

9. References

9.1. Literature references

ABD EL AAL, A. (2017): Identification and characterization of near surface cavities in Tuwaiq Mountain Limestone, Riyadh, KSA, "detection and treatment". – Egypt. J. Petrol., **26** (1): 215–223.

ABDALLATIF, T., KHAFAGY, A.-S.A.B. & KHOZYM, A. (2015): Geophysical Investigation to Delineate Hazardous Cavities in Al-Hassa Karstic Region, Kingdom of Saudi Arabia. – In: LOLLINO, G., MANCONI, A., GUZZETTI, F., CULSHAW, M., BOBROWSKY, P. & LUINO, F. (Eds.): Engineering Geology for Society and Territory – Volume 5. Urban Geology, Sustainable Planning and Landscape Exploitation: 507–514, Switzerland (Springer).

ABDELTAWAB, S. (2013): Karst Limestone Geohazards in Egypt and Saudi Arabia. – International Journal of Geoengineering Case Histories, **2** (4): 258–269.

ABU-SHARIAH, M.I.I. (2002): Imaging subsurface structure & geohazard evolution of selected limestone sites in Peninsular Malaysia using integrated geophysical techniques & geoelectrical resistivity computer tomography modeling. – Ph.D. thesis, Universiti Kebangsaan Malaysia.

ABU-SHARIAH, M.I.I. (2009): Determination of cave geometry by using a geoelectrical resistivity inverse model. – Eng. Geol., **105**: 239–244.

AHMED, S. & CARPENTER, P.J. (2003): Geophysical response of filled sinkholes, soil pipes and associated bedrock fractures in thinly mantled karst, east-central Illinois. – Environ. Geol., **44**: 705–716.

ALEY, T. (1997): Groundwater tracing in the epikarst. – In: BECK, B. & STEPHENSON, J.B. (Eds.): The Engineering Geology and Hydrogeology of Karst Terranes: Proceedings of the Sixth Multidisciplinary Conference on Sinkholes and the Engineering and Environmental Impacts of Karst, pp. 207–211, Springfield, Missouri (Balkema).

AL-FARES, W. (2014): Application of ERT technique for characterizing leakage problem in Abu Baara Earth Dam, Syria. – International Journal of Geophysics, 2014, 9 pp.

AL-FARES, W., BAKALOWICZ, M., GUÉRIN, R. & DUKHAN, M. (2002): Analysis of the karst aquifer structure of the Lamalou area (Hérault, France) with ground penetrating radar. – J. Appl. Geophys., **51**: 97–106.

ARCHIE, G.E. (1942): The electric resistivity log as an aid in determining some reservoir characteristics. – Trans. AIME, **146**: 54–62.

ARGE NBS WENDLINGEN–ULM (2017a): Dokumentation und Bewertung der Ergebnisse der geophysikalischen Erkundung Karst, der Nacherkundung sowie Gründungsempfehlungen, Einschnitt E10: km 65,1+35 – 65,8+65, Großprojekt Stuttgart–Ulm, NBS Wendlingen–Ulm, PFA 2.3 Albhochfläche, 2. Streckenabschnitt km 61,4+45 – 68,0+43, 33 pp., Februar 2017 (in German, unpublished report).

ARGE NBS WENDLINGEN–ULM (2017b): Dokumentation der Ergebnisse der geophysikalischen Erkundung Karst, der Nacherkundung sowie Gründungsempfehlungen, Einschnitt E9 – Teil 1: km 63,6+66 – 64,0+41,5, Großprojekt Stuttgart–Ulm, NBS Wendlingen–Ulm, PFA 2.3 Albhochfläche, 2. Streckenabschnitt km 61,4+45 – 68,0+43, 28 pp., Juli 2017 (in German, unpublished report).

ARGE NBS WENDLINGEN–ULM (2018): E13Mitte – Erkundung „Karstloch" – Aktennotiz, Großprojekt Stuttgart–Ulm, NBS Wendlingen–Ulm, PFA 2.3 Albhochfläche, 1. Streckenabschnitt km 68,0+43 – 74,9+00, 190 pp., Januar 2018 (in German, unpublished report).

ARGENTIERI, A., CARLUCCIO, R., CECCHINI, F., CHIAPPINI, M., CIOTOLI, G., DE RITIS, R., DI FILIPPO, M., DI NEZZA, M., MARCHETTI, M., MARGOTTINI, S., MATERNI, V., MELONI, F., NARDI, A., ROTELLA, G., SAPIA, V. & VENUTI, A. (2015): Early stage sinkhole formation in the Acque Albule basin of central Italy from geophysical and geochemical observations. – Eng. Geol., **191**: 36–47.

BAKER, G.S., SCHMEISSNER, C., STEEPLES, D.W. & PLUMB, R.G. (1999): Seismic reflections from depths of less than two meters. – Geophys. Res. Lett., **26**: 279–282.

BALLARD, R.F., CUENOD, Y. & JENNI, J.P. (1983): Detection of karst cavities by geophysical methods. – Bull. Int. Assoc. Eng. Geol., **26–27**: 153–157.

BATAYNEH, A.T. (2013): A Case Study of High-Resolution Gravity and Wenner-Schlumberger Resistivity for Geotechnical Engineering: An Example from North Jordan. – Res. J. Appl. Sci. Eng. Technol., **5** (4): 1377–1382.

BAUER, M. & THURO, K. (2005): Regionale und historische Geologie entlang der Neubaustrecke Nürnberg-Ingolstadt. – Felsbau, **23** (1): 1–9.

BENSON, R.C. & YUHR, L.B. (2016): Site Characterization in Karst and Pseudokarst Terraines. Practical Strategies and Technology for Practicing Engineers, Hydrologists and Geologists. – 421 pp., Dordrecht (Springer).

BENTLEY, L.R. & GHARIBI, M. (2004): Two- and three-dimensional electrical resistivity imaging at a heterogeneous remediation site. – Geophysics, **69** (3): 674–680.

BERMEJO, L., ORTEGA, A.I., GUÉRIN, R., BENITO-CALVO, A., PÉREZ-GONZÁLEZ, A., PARÉS, J.M., ARACIL, E., BERMÚDEZ DE CASTRO, J.M. & CARBONELL, E. (2017): 2D and 3D ERT imaging for identifying karst morphologies in the archaeological sites of Gran Dolina and Galería Complex (Sierra de Atapuerca, Burgos, Spain). – Quat. Int., **433**: 393–401.

BERNER, R.A. & MORSE, J.W. (1974): Dissolution kinetics of calcium carbonate in seawater. IV. Theory of calcite solution. – Am. J. Sci., **274**: 108–134.

BHATTACHARYYA, B.B. & SEN, M.K. (1981): Depth of investigation of colinear electrode arrays over homogeneous anisotropic half-space in direct current methods. – Geophysics, **46**: 768–780.

BILLI, A., DE FILIPPIS, L., PONCIA, P.P., SELLA, P. & FACCENNA, C. (2016): Hidden sinkholes and karst cavities in the travertine plateau of a highly-populated geothermal seismic territory (Tivoli, central Italy). – Geomorphology, **255**: 63–80.

BLACK, T.J. (1997): Evaporite karst of northern lower Michigan. – Carbonates and Evaporites, **12**: 81–83.

BONACCI, O. (1987): Karst Hydrology. With Special Reference to the Dinaric Karst. – 184 pp., New York (Springer).

BOUCHEDDA, A., CHOUTEAU, M., BINLEY, A. & GIROUX, B. (2012): 2-D joint structural inversion of cross-hole electrical resistance and ground penetrating radar data. – J. Appl. Geophys., **78**: 52–67.

BUTLER, D.K. (1984): Microgravimetric and gravity gradient techniques for detection of subsurface cavities. – Geophysics, **49** (7): 1084–1096.

CALAFORRA, J.M. & PULIDO-BOSCH, A. (2003): Evolution of the gypsum karst of Sorbas (SE Spain). – Geomorphology, **50**: 173–180.

CARDARELLI, E., MARRONE, C. & ORLANDO, L. (2003): Evaluation of tunnel stability using integrated geophysical methods. – J. Appl. Geophys., **52** (2–3): 93–102.

CARDARELLI, E., DI FILIPPO, G. & TUCCINARDI, E. (2006): Electrical resistivity tomography to detect buried cavities in Rome: a case study. – Near Surface Geophysics, **4**: 387–392.

CARDARELLI, E., CERCATO, M., CERRETO, A. & DI FILIPPO, G. (2010): Electrical resistivity and seismic refraction tomography to detect buried cavities. – Geophys. Prospect., **58**: 685–695.

CARRIÈRE, S.D., CHALIKAKIS, K., SÉNÉCHAL, G., DANQUIGNY, C. & EMBLANCH, C. (2013): Combining Electrical Resistivity Tomography and Ground Penetrating Radar to study geological structuring of karst Unsaturated Zone. – J. Appl. Geophys., **94**: 31–41.

CARRIÈRE, S.D., CHALIKAKIS, K., DANQUIGNY, C., CLÉMENT, R. & EMBLANCH, C. (2015): Feasibility and Limits of Electrical Resistivity Tomography to Monitor Water Infiltration Through Karst Medium During a Rainy Event. – In: ANDREO, B., CARRASCO, F., DURÁN, J.J., JIMÉNEZ, P. & LAMOREAUX, J.W. (Eds.): Hydrogeological and Environmental Investigations in Karst Systems: Environ. Earth Sci., **1**: 45–55, Berlin (Springer).

CAVINATO, G.P., DI LUZIO, E., MOSCATELLI, M., VALLONE, R., AVERARDI, M., VALENTE, A. & PAPALE, S. (2006): The new Col di Tenda tunnel between Italy and France: integrated geological investigations and geophysical prospections for preliminary studies on the Italian side. – Eng. Geol., **88**: 90–109.

CHALIKAKIS, K., PLAGNES, V., GUÉRIN, R., VALOIS, R. & BOSCH, F.P. (2011): Contribution of geophysical methods to karst-system exploration: an overview. – Hydrogeol. J., **19**: 1169–1180.

CHAMBERS, J.E., OGILVY, R.D., KURAS, O., CRIPPS, J.C. & MELDRUM, P.I. (2002): 3D electrical imaging of known targets at a controlled environmental test site. – Environ. Geol., **41** (6): 690–704.

CLEMENS, T., HUCKINGHAUS, D., LIEDL, R. & SAUTER, M. (1999): Simulation of the development of karst aquifers: role of the epikarst. – Int. J. Earth Sci., **88** (1): 157–162.

COGGON, J.H. (1971): Electromagnetic and electrical modeling by the finite element method. – Geophysics, **36** (1): 132–155.

COLLINS, M.E., PUCKETT, W.E., SCHELLENTRAGER, G.W. & YUST, N.A. (1990): Using GPR for micro-analyses of soils and karst features on the Chiefland Limestone Plain in Florida. – Geoderma, **47** (1–2): 159–170.

CRAWFORD, N.C., LEWIS, M.A., WINTER, S.A. & WEBSTER, J.A. (1999): Microgravity techniques for subsurface investigations of sinkhole collapses and for detection of groundwater flow paths through karst aquifers. – In: BECK, B.F., PETTIT, A.J. & HERRING, J.G. (Eds.): Hydrology and Engineering Geology of Sinkholes and Karst: 203–218, Rotterdam (Balkema).

CUNNINGHAM, K.J. (2004): Application of ground-penetrating radar, digital optical borehole images, and cores for characterization of porosity hydraulic conductivity and paleokarst in the Biscayne aquifer, southeastern Florida, USA. – J. Appl. Geophys., **55** (1–2): 61–76.

DAHLIN, T. (2000): Short note on electrode charge-up effects in DC resistivity data acquisition using multi-electrode arrays. – Geophys. Prospect., **48** (1): 181–187.

DAHLIN, T. & ZHOU, B. (2004): A numerical comparison of 2D resistivity imaging with ten electrode arrays. – Geophys. Prospect., **52** (5): 379–398.

DAHLIN, T. & ZHOU, B. (2006): Multiple gradient array measurements for multi-channel 2D resistivity imaging. – Near Surface Geophysics, **4** (2): 113–123.

DAHLIN, T., BJELM, L. & SVENSSON, C. (1999): Use of electrical imaging in site investigations for a railway tunnel through the Hallandsås Horst, Sweden. – Q. J. Eng. Geol., **32** (2): 163–172.

DAHLIN, T., BERNSTONE, C. & LOKE, M.H. (2002): A 3D resistivity investigation of a contaminated site at Lernacken in Sweden. – Geophysics, **60** (6): 1682–1690.

DANIELS, J. (1988): Locating caves, tunnels and mines. – Geophysics, **7**: 32–37.

DANIELSEN, B.E (2010): The applicability of geoelectrical methods in pre-investigation for construction in rock. – Ph.D. thesis, Lund University, Lund (Media-Tryck).

DANIELSEN, B.E. & DAHLIN, T. (2009): Comparison of geoelectrical imaging and tunnel documentation at the Hallandsås Tunnel, Sweden. – Eng. Geol., **107**: 118–129.

DAVIS, K.J., DOVE, P.M. & DE YOREO, J.J. (2000): The role of Mg^{2+} as an impurity in calcite growth. – Science, **290** (5494): 1134–1137.

DE WAELE, J., PLAN, L. & AUDRA, P. (2009): Recent developments in surface and subsurface karst geomorphology: an introduction. – Geomorphology, **106**: 1–8.

DEGROOT-HEDLIN, C. & CONSTABLE, S. (1990): Occam's inversion to generate smooth, two-dimensional models from magnetotelluric data. – Geophysics, **55** (12): 1613–1624.

DEY, A. & MORRISON, H.F. (1979a): Resistivity modelling for arbitrarily shaped two-dimensional structures. – Geophys. Prospect., **27** (1): 106–136.

DEY, A. & MORRISON, H.F. (1979b): Resistivity modeling for arbitrarily shaped three-dimensional shaped structures. – Geophysics, **44** (4): 753–780.

DOOLITTLE, J.A. & COLLINS, M.E. (1998): A comparison of EM induction and GPR methods in areas of karst. – Geoderma, **85** (1): 83–102.

DREYBRODT, W. (1988): Processes in Karst Systems. Physics, Chemistry, and Geology. – 288 pp., Berlin (Springer).

DUNSCOMB, M.H. & REHWOLDT, E. (1999): Two-dimensional resistivity profiling; geophysical weapon of choice in karst terrain for engineering applications. – In: BECK, B.F., PETTIT, A.J. & HERRING, J.G. (Eds.): Hydrogeology and engineering geology of Sinkholes and Karst: 219–224, Rotterdam, Netherlands (Balkema).

EDELHOFF, D., TORKHANI, J., BREIDENSTEIN, M. & HANDKE, D. (2015): The Boßler Tunnel – the longest Tunnel on the new Line Wendlingen–Ulm. – Tunnel, **7**: 16–31.

ERASO, A. (1985): Método de Predicción de las Direcciones Principales de Drenaje en el Karst. – KOBIE (Serie Ciencias Naturales), **15**: 15–165.

ESTEBAN, M. & WILSON, J.L. (1993): Introduction to karst systems and paleokarst reservoirs. – In: FRITZ, R.D., WILSON, J.L. & YUREWICZ, D.A. (Eds.): Paleokarst related hydrocarbon reservoirs: SEPM Core Workshop, **18**: 1–9.

EVANS, R.L. & LIZARRALDE, D. (2003): Geophysical evidence for karst formation associated with offshore groundwater transport: an example from North Carolina. – Geochem. Geophys. Geosyst., **4** (8): 1069–1077.

FADHLI, Z., SAAD, R., NORDIANA, M.M., AZWIN, N. & BERY, A.A. (2015): Mapping Subsurface Karst Formation Using 2-D Electrical Resistivity Imaging (2-DERI). – EJGE, **20**: 349–358.

FAROOQ, M., PARK, S., SONG, Y.S., KIM, J.H., TARIQ, M. & ABRAHAM, A.A. (2012): Subsurface cavity detection in a karst environment using electrical resistivity (er): a case study from yongweol-ri, South Korea. – Earth Sci. Res. J., **16** (1): 75–82.

FARQUHARSON, C.G. (2008): Constructing piecewise-constant models in multidimensional minimum-structure inversions. – Geophysics, **73** (1): K1–K9.

FARQUHARSON, C.G. & OLDENBURG, D.W. (1998): Nonlinear inversion using general measures of data misfit and model structure. – Geophys. J. Int., **134** (1): 213–227.

FASCHING, A., VANEK, R., STADLMANN, T., REICHL, P., DOMBERGER, G., FORSTINGER, G. & WAGNER, O.K. (2010): New Semmering Base Tunnel – the investigation programme 2008/2009 and the knowledge gained in the areas of geology, hydrogeology and geotechnical engineering. – Geomechanics and Tunnelling, **3** (2): 119–129.

FERAHTIA, J., DJARFOUR, N., BADDARI, K. & GUÉRIN, R. (2009): Application of signal dependent rank-order mean filter to the removal of noise spikes from 2D electrical resistivity imaging data. – Near Surface Geophysics, **7** (3): 159–169.

FESTA, V., FIORE, A., PARISE, M. & SINISCALCHI, A. (2012): Sinkhole evolution in the Apulian Karst of Southern Italy: a case study, with some considerations on Sinkhole Hazards. – J. Cave Karst Stud., **74** (2): 137–147.

FIELD, M.S. (2002): A Lexicon of Cave and Karst Terminology with Special Reference to Environmental Karst Hydrology. – EPA/600/R-02/003, 214 pp., Washington, D.C (U.S. Environmental Protection Agency).

FILIPPONI, M. (2009): Spatial analysis of karst conduit networks and determination of parameters controlling the speleogenesis along preferential lithostratigraphic horizons. – Ph.D. thesis, Ecole polytechnique fédérale, 166 pp., Lausanne.

FILIPPONI, M. & JEANNIN, P.-Y. (2006): Is it possible to predict karstified horizons in tunneling?. – Austrian J. Earth Sci., **99**: 24–30.

FILIPPONI, M. & JEANNIN, P.-Y. (2010): Karst-ALEA: a Scientific Based Karst Risk Assessment for Underground Engineering. – In: ANDREO, B., CARRASCO, F., DURÁN, J.J. & LAMOREAUX, J.W. (Eds.): Advances in Research in Karst Media: 435–440, Heidelberg (Springer).

FILIPPONI, M., JEANNIN, P.-Y. & TACHER, L. (2009): Evidence of inception horizons in karst conduit networks. – Geomorphology, **106**: 86–99.

FILIPPONI, M., PARRIAUX, A., SCHMASSMANN, S. & JEANNIN, P.-Y. (2012): KarstALEA: Wegleitung zur Prognose von karstspezifischen Gefahren im Untertagbau. – Forschungsprojekt FGU 2009/003 des Bundesamt für Strassen ASTRA, Schweizerischer Verband der Strassen- und Verkehrsfachleute (VSS), 200 pp., Zürich, Schweiz.

FORD, D.C. & WILLIAMS, P.W. (1989): Karst Geomorphology and Hydrology. – 601 pp., London (Unwin Hyman).

FORD, D.C. & WILLIAMS, P.W. (2007): Karst Hydrogeology and Geomorphology. – 2nd ed., 576 pp., West Sussex, England (John Wiley & Sons).

FOX, R.C., HOHMANN, G.W., KILLPACK, T.J. & RIJO, L. (1980): Topographic effects in resistivity and induced polarization surveys. – Geophysics, **45**: 75–93.

FRIEDEL, S. (2003): Resolution, stability and efficiency of resistivity tomography estimated from a generalized inverse approach. – Geophys. J. Int., **153** (2): 305–316.

GAMBETTA, M., ARMADILLO, E., CARMISCIANO, C., STEFANELLI, P., COCCHI, L. & TONTINI, F.C. (2011): Determining geophysical properties of a near-surface cave through integrated microgravity vertical gradient and electrical resistivity tomography measurements. – J. Cave Karst Stud., **73** (1): 11–15.

GAN, F., CHEN, Y., ZHAO, W., CHEN, Y. & LIU, W. (2013): Integrated geophysical methods for groundwater exploration in a karst area with or without thin cover – a case study from Tai'an City, Shandong Province, China. – In: LAND, L., DOCTOR, D.H. & STEPHENSON, J.B. (Eds.): Sinkholes and the Engineering and Environmental Impacts of Karst: Proceedings of the Thirteenth Multidisciplinary Conference, May 6–10, pp. 255–261, NCKRI Symposium 2, Carlsbad, New Mexico (National Cave and Karst Research Institute).

GANERØD, G.V., RØNNING, J.S., DALSEGG, E., ELVEBAKK, H., HOLMØY, K., NILSEN, B. & BRAATHEN, A. (2006): Comparison of geophysical methods for sub-surface mapping of faults and fracture zones in a section of the Viggja road tunnel, Norway. – Bull. Eng. Geol. Environ., **65** (3): 231–243.

GÉLIS, C., REVIL, A., CUSHING, M.E., JOUGNOT, D., LEMEILLE, F., CABRERA, J., DE HOYOS, A. & ROCHER, M. (2010): Potential of Electrical Resistivity Tomography to Detect Fault Zones in

Limestone and Argillaceous Formations in the Experimental Platform of Tournemire, France. – Pure Appl. Geophys., **167** (11): 1405–1418.

GHARIBI, M. & BENTLEY, L.R. (2005): Resolution of 3-D electrical resistivity images from inversions of 2-D orthogonal lines. – J. Environ. Eng. Geophys., **10** (4): 339–349.

GIBSON, P.J., LYLE, P. & GEORGE, D.M. (2004): Application of resistivity and magnetometry geophysical techniques for near-surface investigations in karstic terranes in Ireland. – J. Cave Karst Stud., **66** (2): 35–38.

GIRMSCHEID, G. (2013): Bauprozesse und Bauverfahren des Tunnelbaus. – 3rd ed., 694 pp., Berlin (Wilhelm Ernst & Sohn).

GOLDSCHEIDER, N. & DREW, D. (2007): Methods in Karst Hydrogeology. – 264 pp., London (Taylor & Francis).

GOLDSCHEIDER, N. & GÖPPERT, N. (2004): Hydrogeologie der alpinen Karstlandschaften Vorarlbergs. – Vorarlberger Naturschau, **15**: 41–62.

GÖPPERT, N., GOLDSCHEIDER, N. & SCHOLZ, H. (2011): Karst geomorphology of carbonatic conglomerates in the Folded Molasse zone of the Northern Alps (Austria/Germany). – Geomorphology, **130**: 289–298.

GRANDORI, R., BIENIAWSKI, Z.T., VIZZINO, D., LIZZADRO, L., ROMUALDI, P. & BUSILLO, A. (2011): Hard rock extreme conditions in the first 10 km of TBM driven Brenner Exploratory Tunnel. – In: REDMOND, S. & ROMERO, V. (Eds.): Rapid Excavation and Tunneling Conference Proceedings: 667–685.

GREENHALGH, S., WIESE, T. & MARESCOT, L. (2010): Comparison of DC sensitivity patterns for anisotropic and isotropic media. – J. Appl. Geophys., **70** (2): 103–112.

GRGICH, P., HAMMACK, R., HARBERT, W., SAMS, J., VELOSKI, G. & ACKMAN, T. (2004): Delineating the subsurface: using surface geophysics to identify groundwater flow paths in a carbonate aquifer. – J. Environ. Hydrol., **12** (12): 1–10.

GRIFFITHS, D.H. & BARKER, R.D. (1993): Two-dimensional resistivity imaging and modelling in areas of complex geology. – J. Appl. Geophys., **29**: 211–226.

GROVES, C. & MEIMAN, J. (2005): Weathering, geomorphic work, and karst landscape evolution in the Cave City groundwater basin, Mammoth Cave, Kentucky. – Geomorphology, **67**: 115–126.

GUÉRIN, R., BALTASSAT, J.-M., BOUCHER, M., CHALIKAKIS, K., GALIBERT, P.-Y., GIRARD, J.-F., PLAGNES, V. & VALOIS, R. (2009): Geophysical characterisation of karstic networks - application to the Ouysse system (Poumeyssen, France). – C. R. Geoscience, **341**: 810–817.

GÜNTHER, T. & RÜCKER, C. (2009): Advanced inversion strategies using a new geophysical inversion and modelling library. – Near Surface Geoscience 2009: Proceedings of the 15th European Meeting of Environmental and Engineering Geophysics, Sept. 7–9, pp. B14 (253–258), Dublin, Ireland.

HAMDAN, H., ECONOMOU, N., KRITIKAKIS, G., ANDRONIKIDIS, N., MANOUTSOGLOU, E., VAFIDIS, A., PANGRATIS, P. & APOSTOLIDOU, G. (2012): 2D and 3D imaging of the metamorphic carbonates at Omalos plateau/polje, Crete, Greece by employing independent and joint inversion on resistivity and seismic data. – Int. J. Speleol., **41** (2): 199–209.

HARRO, D. & KRUSE, S. (2014): Improved imaging of covered karst with the multi-electrode resistivity implant technique. – In: LAND, L., DOCTOR, D.H. & STEPHENSON, J.B. (Eds.): Sinkholes and the Engineering and Environmental Impacts of Karst: Proceedings of the Thirteenth Multidisciplinary Conference, May 6–10, pp. 255–261, NCKRI Symposium 2, Carlsbad, New Mexico (National Cave and Karst Research Institute).

HAUCK, C., BÖTTCHER, M. & MAURER, H. (2011): A new model for estimating subsurface ice content based on combined electrical and seismic data sets. – The Cryosphere, **5**: 453–468.

HERWANGER, J.V., PAIN, C.C., BINLEY, A., DE OLIVEIRA, C.R.E. & WORTHINGTON, M.H. (2004): Anisotropic resistivity tomography. – Geophys. J. Int., **158** (2): 409–425.

HOFFMANN, R. & DIETRICH, P. (2004): An approach to determine equivalent solutions to the geoelectrical 2D inversion problem. – J. Appl. Geophys., **56** (2): 79–91.

HOLCOMBE, H.T. & JIRACEK, G.R. (1984): 3D terrain corrections in resistivity surveys. – Geophysics, **49** (4): 439–452.

INMAN, J.R. (1975): Resistivity inversion with ridge regression. – Geophysics, **40** (5): 798–817.

ISMAIL, A. & ANDERSON, N. (2012): 2-D and 3-D Resistivity Imaging of Karst Sites in Missouri, USA. – Environ. Eng. Geosci., **18** (3): 281–293.

JACKSON, P.D., NORTHMORE, K.J., ENTWISLE, D.C., GUNN, D.A., MILODOWSKI, A.E., BOARDMAN, D.I., ZOURMPAKIS, A., ROGERS, C.D.F., JEFFERSON, I. & DIXON, N. (2006): Electrical resistivity monitoring of a collapsing meta-stable soil. – Q. J. Eng. Geol. Hydrogeol., **39**: 151–172.

JOHNSON, S.B. & STIEGLITZ, R.D. (1990): Karst features of a glaciated dolomite peninsula, Door County, Wisconsin. – Geomorphology, **4**: 37–54.

KASPRZAK, M., SOBCZYK, A., KOSTKA, S. & HACZEK, A. (2015): Surface geophysical surveys and LiDAR DTM analysis combined with underground cave mapping – an efficient tool for karst system exploration: Jaskinia Niedźwiedzia case study (Sudetes, SW Poland). – In: JASIEWICZ, J., ZWOLIŃSKI, Z., MITASOVA, H. & HENGL, T. (Eds.): Geomorphometry for Geosciences: International Society for Geomorphometry, Adam Mickiewicz University, Institute of Geoecology and Geoinformation, pp. 75–78, Poznań, Poland (Bogucki Wydawnictwo Naukowe).

KAUFMANN, O. & DECEUSTER, J. (2014): Detection and mapping of ghost-rock features in the Tournaisis area through geophysical methods – an overview. – GEOLOGICA BELGICA, **17** (1): 17–26.

KAUFMANN, O., DELGRANCHE, J. & DECEUSTER, J. (2006): Geophysics for physical planning over covered karstic areas in the Walloon region of Belgium. – In: WERKEMA, D.D. (Ed.):

Proceedings of the 19th Symposium on the Application of Geophysics to Engineering and Environmental Problems (SAGEEP), April 2–6, pp. 51–59, Seattle, Washington, USA.

KELLER, G.V. & FRISCHKNECHT, F.C. (1966): Electrical methods in geophysical prospecting. – 519 pp., Oxford (Pergamon Press).

KIDANU, S.T., TORGASHOV, E.V., VARNAVINA, A.V. & ANDERSON, N.L. (2016): ERT-based Investigation of a Sinkhole in Greene County, Missouri. – AIMS Geosciences, **2** (2): 99–115.

KIELBASSA, S., PRISCHMANN, F. & BEER, N. (2015a): Karst investigation and treatment measures for the high-speed track on the Swabian Jura. – Geomechanics and Tunnelling, **8** (2): 129–145.

KIELBASSA, S., REINHARDT, A., GERING, A. & DB PROJEKT STUTTGART–ULM GMBH (2015b): Albabstieg Tunnel: Karst Probing and Treatment Measures. – Tunnel, **4**: 26–37.

KIRALY, L. (1968): Eléments structuraux et alignement des phénomènes karstiques (région du gouffre du Petit-Pré de St-Livres, Jura vaudois). – Bull. soc. neuchâtel. sci. nat., **91**: 127–146.

KIRALY, L. (1975): Rapport sur l'état actuel des connaissances dans le domaines des caractères physiques des roches karstiques. – In: BURGER, A. & DUBERTRET, L. (Eds): Hydrogeology of karstic terrains: Int. Union of Geol. Sciences, B, **3**: 53–67.

KLIMCHOUK, A.B. (1995): Karst morphogenesis in the epikarstic zone. – Cave and Karst Science, **21** (2): 45–50.

KLIMCHOUK, A.B. & FORD, D.C. (2000): Lithologic and Structural Controls of Dissolutional Cave Development. – In: KLIMCHOUK, A.B., FORD, D.C., PALMER, A.N. & DREYBRODT, W. (Eds.): Speleogenesis. Evolution of Karst Aquifers: 54–64, Huntsville, Alabama, USA (National Speleological Society, Inc.).

KLIMCHOUK, A.B., FORD, D.C., PALMER, A.N. & DREYBRODT, W. (2000): Speleogenesis. Evolution of Karst Aquifers. – 527 pp., Huntsville, Alabama, USA (National Speleological Society, Inc.).

KLOSE, C.D., LOEW, S., GIESE, R. & BORM, G. (2007): Spatial predictions of geological rock mass properties based on in-situ interpretations of multi-dimensional seismic data. – Eng. Geol., **93**: 99–116.

KNÖDEL, K., KRUMMEL, H. & LANGE, G. (2005): Handbuch zur Erkundung des Untergrundes von Deponien und Altlasten. – **3**, 1102 pp., Berlin (Springer Verlag).

KRAUTBLATTER, M., VERLEYSDONK, S., FLORES-OROZCO, A. & KEMNA, A. (2010): Temperature-calibrated imaging of seasonal changes in permafrost rock walls by quantitative electrical resistivity tomography (Zugspitze, German/Austrian Alps). – J. Geophys. Res., **115** (F02003): 1–15.

LABRECQUE, D.J., MILETTO, M., DAILY, W., RAMIREZ, A. & OWEN, E. (1996): The effects of noise on Occam's inversion of resistivity tomography data. – Geophysics, **61** (2): 538–548.

LABUDA, T.Z. & BAXTER, A.C. (2001): Mapping Karst Conditions Using 2D and 3D Resistivity Imaging Methods. – Symposium on the Application of Geophysics to Engineering and Environmental Problems, 2001, 11 pp.

LAMOREAUX, P.E., WILSON, B.M. & MEMON, B.A. (1984): Guide to the Hydrology of Carbonate Rocks. – 345 pp., Paris (UNESCO).

LANKSTON, R.W. (1990): High-Resolution Refraction Seismic Data Acquisition and Interpretation. – In: WARD, S.H. (Ed.): Geotechnical and Environmental Geophysics: 45–74 (Society of Exploration Geophysicists).

LEHMANN, B., ORLOWSKY, D. & MISIEK, R. (2009): Exploration of Tunnel Alignment using Geophysical Methods to Increase Safety for Planning and Minimizing Risk. – J. Rock Mech. Rock Eng., **43**: 105–116.

LI, Y. & OLDENBURG, D.W. (1992): Approximate inverse mappings in DC resistivity problems. – Geophys. J. Int., **109** (2): 343–362.

LI, L., LI, S., ZHOU, Z., XU, Z., SHI, S., ZHANG, Q., ZHOU, Y. & HU, C. (2013): Geological defect and its geophysical prediction method in Karst Tunnel. – PRZEGLĄD LEKTROTECHNICZNY, **89** (1b**)**: 116–119.

LI, S., LI, S., ZHANG, Q., XUE, Y., LIU, B., SU, M., WANG, Z. & WANG, S. (2010): Predicting geological hazards during tunnel construction. – Journal of Rock Mechanics and Geotechnical Engineering, **2** (3): 232–242.

LOKE, M.H. (1994): The Inversion of Two-Dimensional Resistivity Data. – Ph.D. thesis, University of Birmingham, 122 pp., Birmingham, United Kingdom.

LOKE, M.H. (2004a): RES2DINV version 3.54. Rapid 2-D resistivity & IP inversion using the least-squares method. – Computer Disk and Manual, Penang, Malaysia (Geotomo Software).

LOKE, M.H. (2004b): Tutorial – 2D and 3D electrical imaging surveys. – 128 pp., Malaysia (Geotomo Software).

LOKE, M.H. (2012): Tutorial: 2-D and 3-D Electrical Imaging Surveys. – Malaysia (Geotomo Software).

LOKE, M.H. & BARKER, R.D. (1996): Rapid least-squares inversion of apparent resistivity pseudosections using a quasi-Newton method. – Geophys. Prospect., **44** (1): 131–152.

LOKE, M.H. & DAHLIN, T. (2010): Methods to reduce banding effects in 3-D resistivity inversion. – In: Near Surface Geoscience 2010: Proceedings of the 16th European Meeting of Environmental and Engineering Geophysics, Sept. 6–8, pp. A16 (76–80), Zurich, Switzerland.

LOKE, M.H. & LANE JR., J.W. (2004): Inversion of data from electrical resistivity imaging surveys in water-covered areas. – Explor. Geophys., **35** (4): 266–271.

LOKE, M.H., ACWORTH, I. & DAHLIN, T. (2003): A comparison of smooth and blocky inversion methods in 2D electrical imaging surveys. – Explor. Geophys., **34** (3): 182–187.

LOKE, M.H., CHAMBERS, J.E., RUCKER, D.F., KURAS, O. & WILKINSON, P.B. (2013): Recent developments in the direct-current geoelectrical imaging method. – J. Appl. Geophys., **95**: 135–156.

LOWE, D.J. (1992): The origin of limestone caverns: an inception horizon hypothesis. – Ph.D. thesis, Manchester Polytechnic, 512 pp., United Kingdom.

LOWE, D.J. (2000): Role of stratigraphic elements in speleogenesis: the speleoinception concept. – In: KLIMCHOUK, A.B., FORD, D.C., PALMER, A.N. & DREYBRODT, W. (Eds.): Speleogenesis. Evolution of Karst Aquifers: 65–75, Huntsville, Alabama, USA (National Speleological Society, Inc.).

LÜTH, S., GIESE, R., OTTO, P., KRÜGER, K., MIELITZ, S. & BORM, G. (2005): Seismische Vorauserkundung im Tunnelbau mit konvertierten Oberflächenwellen. – In: Zweijahresbericht 2004/2005, GeoForschungsZentrum Potsdam, pp. 97–102.

LÜTH, S., GIESE, R. & RECHLIN, A. (2008): A seismic exploration system around and ahead of tunnel excavation – Onsite. – In: KANJLIA, V.K., RAMAMURTHY, T., WAHI, P.P. & GUPTA, A.C. (Eds.): Proceedings of the World Tunnel Congress 2008: Underground Facilities for Better Environment and Safety, Sept. 22–24, pp. 119–125, Agra, India.

MCGRATH, R.J., STYLES, P., THOMAS, E. & NEALE, S. (2002): Integrated high-resolution geophysical investigations as potential tools for water resource investigations in karst terrain. – Environ. Geol., **42**: 552–557.

MCMECHAN, G.A., LOUCKS, R.G., ZENG, X. & MESCHER, P. (1998): Ground penetrating radar imaging of a collapsed paleocave system in the Ellenburger dolomite, central Texas. – J. Appl. Geophys., **39**: 1–10.

MERRIAM, J.B. (2005): Injection electrode overprinting. – J. Environ. Eng. Geoph., **10** (4): 365–370.

MILSOM, J. (2003): Field Geophysics. The geological field guide series. – 3rd ed., 233 pp., Sussex (Wiley).

MOCHALES, T., CASAS, A.M., PUEYO, E.L., PUEYO, O., ROMÁN, M.T., POCOVÍ, A., SORIANO, M.A. & ANSÓN, D. (2007): Detection of underground cavities by combining gravity, magnetic and ground penetrating radar surveys: a case study from the Zaragoza area, NE Spain. – Environ. Geol., **53**: 1067–1077.

MORSE, J.W. & MACKENZIE, F.T. (1990): Geochemistry of Sedimentary Carbonates. – 706 pp. (Elsevier).

NEAL, A. (2004): Ground-penetrating radar and its use in sedimentology: principles, problems and progress. – Earth-Sci. Rev., **66**: 261–330.

NEUKUM, C., GRÜTZNER, C., AZZAM, R. & REICHERTER, K. (2010): Mapping buried karst features with capacitive-coupled resistivity system (CCR) and ground penetrating radar (GPR). – In: ANDREO, B., CARRASCO, F., DURÁN, J.J. & LAMOREAUX, J.W. (Eds.): Advances in Research in Karst Media: Environ. Earth Sci., **3**: 429–434.

NEWTON, J.G. (1976): Early detection and correlation of sinkhole problems in Alabama with a preliminary evaluation of remote sensing applications. – Alabama Highway Research Report, **76**, 83 pp.

NEWTON, J.G. (1987): Development of Sinkholes Resulting from Man's Activities in the Eastern United States. – U.S. Geol. Surv. Circ., **968**, 57 pp., Reston, Virginia.

NIMMER, R.E., OSIENSKY, J.L., BINLEY, A.M. & WILLIAMS, B.C. (2008): Three-dimensional effects causing artifacts in two-dimensional, cross-borehole, electrical imaging. – J. Hydrol., **359** (1–2): 59–70.

NYQUIST, J.E., PEAKE, J.S. & ROTH, M.J.S. (2007): Case History. Comparison of an optimized resistivity array with dipole-dipole soundings in karst terrain. – Geophysics, **72** (4): 139–144.

ODUM, J.K., STEPHENSON, W.J., WILLIAMS, R.A., PRATT, T.L., TOTH, D.J. & SPECHLER, R.M. (1999): Shallow high-resolution seismic-reflection imaging of karst structures within the Floridan aquifer system, northeastern Florida. – J. Environ. Eng. Geophys., **4** (4): 251–261.

OLHOEFT, G.R. (2000): Maximizing the information return from ground penetrating radar. – J. Appl. Geophys., **43**: 175–187.

ORTEGA, A.I., BENITO-CALVO, A., PORRES, J., PÉREZ-GONZÁLES, A. & MARTÍN MERINO, M.A. (2010): Applying Electrical Resistivity Tomography to the Identification of Endokarstic Geometries in the Pleistocene Sites of the Sierra de Atapuerca (Burgos, Spain). – Archaeol. Prospect., **17**: 233–245.

PALMER, A.N. (1989): Stratigraphic and Structural Control of Cave Development and Groundwater Flow in the Mammoth Cave Region. – In: WHITE, W.B. & WHITE, E.L. (Eds.): Karst Hydrology. Concepts from the Mammoth Cave Area: 293–316, Van Nostrand Reinhold, New York (Springer).

PALMER, A.N. (2007): Cave Geology. – 454 pp., Dayton, Ohio (Cave Books).

PARK, S.K. & VAN, G.P. (1991): Inversion of pole–pole data for 3-D resistivity structures beneath arrays of electrodes. – Geophysics, **56** (7): 951–960.

PARK, M.K., PARK, S., YI, M.-J., KIM, C., SON, J.-S., KIM, J.-H. & ABRAHAM, A.A. (2014): Application of electrical resistivity tomography (ERT) technique to detect underground cavities in a karst area of South Korea. – Environ. Earth Sci., **71**: 2797–2806.

PATTERSON, D.A., DAVEY, J.C., COOPER, A.H. & FERRIS, J.K. (1995): The investigation of dissolution subsidence incorporating microgravity geophysics at Ripon, Yorkshire. – Q. J. Eng. Geol., **28**: 83–94.

PAZDIREK, O. & BLAHA, V. (1996): Examples of resistivity imaging using ME-100 resistivity field acquisition system. – In: Extended Abstracts Book: Proceedings of the EAGE 58th Conference and Technical Exhibition, June 3–7, P050, Amsterdam, Netherlands.

PELLERIN, L. & WANNAMAKER, P.E. (2005): Multi-dimensional electromagnetic modeling and inversion with application to near-surface earth investigations. – Comput. Electron. Agric., **46** (1–3): 71–102.

PESENDORFER, M. (2006): Hydrogeologic Exploration and Tunneling in a Karstified and Fractured Limestone Aquifer (Lötschberg Base Tunnel, Switzerland). – Ph.D. thesis, Swiss Federal Institute of Technology Zurich, 303 pp., Zurich, Switzerland.

PIDLISECKY, A., KNIGHT, R. & HABER, E. (2006): Cone-based electrical resistivity tomography. – Geophysics, **71** (4): G157–G167.

PIDLISECKY, A., HABER, E. & KNIGHT, R. (2007): RESINVM3D: a 3D resistivity inversion package. – Geophysics, **72** (2): H1–H10.

PLINNINGER, R.J., AMADORI, T. & ECKSTALLER, W. (2005): Baubegleitende Karsterkundung und -sanierung in den Felseinschnitten des Bauloses Süd. – Felsbau, **23** (1): 41–47.

PLUMMER, L.N. & BUSENBERG, E. (1982): The solubilities of calcite, aragonite and vaterite in CO_2-H_2O solutions between 0 and 90°C, and an evaluation of the aqueous model for the system $CaCO_3$-CO_2-H_2O. – Geochim. Cosmochim. Acta, **46** (6): 1011–1040.

PLUMMER, L.N. & WIGLEY, T.M.L. (1976): The dissolution of calcite in CO_2 saturated solutions at 25°C and 1 atmosphere total pressure. – Geochim. Cosmochim. Acta, **40** (2): 191–202.

PLUMMER, L.N., WIGLEY, T.M.L. & PARKHURST, D.L. (1978): The kinetics of calcite dissolution in CO_2 – water systems at 5° to 60°C and 0.0 to 1.0 atm CO_2. – Am. J. Sci., **278**: 179–216.

PRINS, C., THURO, K. & KRAUTBLATTER, M. (2017): Geoelectrical karst reconnaissance on the Swabian Alb high plain, new line Wendlingen–Ulm, southwestern Germany. – In: THURO, K. (Ed.): Tagungsband der 20. Tagung für Ingenieurgeologie mit Forum für junge Ingenieurgeologen, Congress Centrum Würzburg, Fachsektion Ingenieurgeologie, Deutsche Gesellschaft für Geotechnik, Sept. 6–8, pp. 374–397, Würzburg, Germany.

PRINS, C., THURO, K. & KRAUTBLATTER, M. (2018): The effectiveness of an inverse Wenner-Schlumberger array for geoelectrical karst reconnaissance, on the Swabian Alb high plain, new line Wendlingen–Ulm, southwestern Germany. – In: SHAKOOR, A. & CATO, K. (Eds.): IAEG/AEG Annual Meeting Proceedings – Volume 3. Mining, Aggregates, Karst: 115–122, Sept. 15–23, San Francisco, California, USA (Springer Nature Switzerland AG).

PRINS, C., THURO, K., KRAUTBLATTER, M. & SCHULZ, R. (2019): Testing the effectiveness of an inverse Wenner-Schlumberger array for geoelectrical karst void reconnaissance, on the Swabian Alb high plain, new line Wendlingen–Ulm, southwestern Germany. – Eng. Geol., **249**: 71–76.

PRINZ, H. & STRAUß, R. (2011): Ingenieurgeologie. – 5th ed., 738 pp., Heidelberg (Spektrum).

PUEYO-ANCHUELA, O., CASAS-SAINZ, A.M., SORIANO, M.A. & POCOVÍ-JUAN, A. (2009): Mapping subsurface karst features with GPR: results and limitations. – Environ. Geol., **58** (2): 391–399.

PUTIŠKA, R., KUŠNIRÁK, D., DOSTÁL, I., LAČNÝ, A., MOJZEŠ, A., HÓK, J., PAŠTEKA, R., KRAJŇÁK, M. & BOŠANSKÝ, M. (2014): Integrated geophysical and geological investigations of karst structures in Komberek, Slovakia. – J. Cave Karst Stud., **76** (3): 155–163.

RAITHEL, M., KIELBASSA, S. & BAUMBUSCH, J. (2015): Bau der Strecke Wendlingen–Ulm in verkarstetem Baugrund. – EI-Spezial Tiefbau, **10**: 18–25.

RAUCH, H.W. & WHITE, W.B. (1970): Lithologic controls on the development of solution porosity in carbonate aquifers. – Water Reservoir Research, **6**: 1175–1192.

RECHLIN, A., LÜTH, S., GIESE, R., POLOM, U., BOHLEN, T., JETSCHNY, S. & HEIDER, S. (2011): Seismic Observations for Underground Development (SOUND). – GEOTECHNOLOGIEN Science Report, **18**: 14–23.

REDHAOUNIA, B., ILONDO, B.O., GABTNI, H., SAMI, K. & BÉDIR, M. (2015): Electrical Resistivity Tomography (ERT) Applied to Karst Carbonate Aquifers: Case Study from Amdoun, Northwestern Tunisia. – Pure Appl. Geophys., **173** (4): 1289–1303.

REHBOCK-SANDER, M., WIELAND, G. & JESEL, T. (2014): Advance probing measures on the TBM drives of the south contrasts of the Gotthard Base Tunnel – experience and implications for other projects. – Geomechanics and Tunnelling, **7** (5): 551–561.

REIS JÚNIOR, J.A., DE CASTRO, D.L., CASAS, A., HIMI, M. & LIMA-FILHO, F.P. (2015): ERT and GPR survey of collapsed paleocave systems at the western border of the Potiguar Basin in northeast Brazil. – Near Surface Geophysics, **13**: 369–381.

REYNOLDS, J.M. (2011): An Introduction to Applied and Environmental Geophysics. – 2nd ed., 710 pp. (John Wiley & Sons).

RODRIGUEZ, R. (1995): Mapping karst solution features by the integrated geophysical method. – In: BECK, B.F. (Ed.): Karst Geohazards: 443–449, Rotterdam (Balkema).

RODRÍGUEZ ESTRELLA, T. (2002): Acuíferos kársticos profundos. – In: ANDREO, B. & DURÁN, J.J. (Eds.): Investigaciones en sistemas kársticos españoles: Hidrogeología y Aguas Subterráneas, **12** (IGME).

ROTH, M.J.S. & NYQUIST, J.E. (2003): Evaluation of Multi-Electrode Earth Resistivity Testing in Karst. – Geotechnical Testing Journal, **26** (2): 1–12.

ROTH, M.J.S., MACKEY, J.R. & NYQUIST, J.E. (1999): A case study of the use of earth resistivity in thinly mantled karst. – In: POWERS, M.H., IBRAHIM, A.-B. & CRAMER, L. (Eds.): Proceedings of the 12th Symposium on the Application of Geophysics to Environmental and Engineering Problems (SAGEEP 1999), pp. 293–302, Oakland, California, USA.

ROTH, M.J.S., NYQUIST, J.E. & GUZAS, B. (2000): Locating subsurface voids in karst: a comparison of multi-electrode earth resistivity testing and gravity testing. – In: POWERS, M.H., IBRAHIM, A.-B. & CRAMER, L. (Eds.): Proceedings of the 13th Symposium on the Application of Geophysics to Environmental and Engineering Problems (SAGEEP 2000), Feb. 20–24, pp. 359–365, Arlington, Virginia, USA.

ROTH, M.J.S., MACKEY, J.R., MACKEY, C. & NYQUIST, J.E. (2002): A case study of the reliability of multielectrode earth resistivity testing for geotechnical investigations in karst terrains. – Eng. Geol., **65**: 225–232.

ROQUES, H. (1962): Considérations théoriques sur la chimie des carbonates. – Ann. Speleol., **17**: 11–41, 241–284, 463–467.

ROQUES, H. (1964): Contribution à l'étude statique et cinétique des systèmes gaz carbonique-eau-carbonate. – Ann. Speleol., **19** (2): 255–484.

RUCKER, D.F., LEVITT, M.T. & GREENWOOD, W.J. (2009): Three-dimensional electrical resistivity model of a nuclear waste disposal site. – J. Appl. Geophys., **69** (3–4): 150–164.

RUSSELL, E.J.F. & BARKER, R.D. (2010): Electrical properties of clay in relation to moisture loss. – Near Surface Geophysics, **8** (2): 173–180.

SASAKI, Y. (1992): Resolution of resistivity tomography inferred from numerical simulation. – Geophys. Prospect., **40** (4): 453–464.

SCHAER, J.P., STETTLER, R., ARAGNO, P.O., BURKHARD, M. & MEIA, J. (1998): Géologie du Creux du Van et des Gorges de l'Areuse. – In: Nature au Creux du Van, Editions du Club Jurassien: 143–215.

SCHMID, S.M., FUGENSCHUH, B., KISSLING, E. & SCHUSTER, R. (2004): Tectonic map and overall architecture of the Alpine orogen. – Eclogae Geol. Helv., **97** (1): 93–117.

SCHOLZ, H. & STROHMENGER, M. (1999): Dolinenartige Sackungsstrukturen in den Molassebergen des südwestbayerischen Alpenvorlandes. – Jahresberichte und Mitteilungen des Oberrheinischen Geologischen Vereins, **81**: 275–283.

SHARIFI, F., ARAB-AMIRI, A.R. & KAMKAR-ROUHANI, A. (2014): Karstic water exploration using the Schlumberger VES and dipole–dipole resistivity profiling surveys in the Tepal area, west of Shahrood, Iran. – Journal of Mining & Environment, **5** (1): 1–12.

SIART, C., HECHT, S., BRILMAYER BAKTI, B. & HOLZHAUER, I. (2011): Analysis and 3D visualization of Mediterranean subsurface karst features based on tomographic mapping (Zominthos, Central Crete). – Z. Geomorphol., **55** (3): 315–335.

SIART, C., FORBRIGER, M., NOWACZINSKI, E., HECHT, S. & HÖFLE, B. (2013): Fusion of multi-resolution surface (terrestrial laser scanning) and subsurface geodata (ERT, SRT) for karst landform investigation and geomorphometric quantification. – Earth Surf. Process. Landforms, **38**: 1135–1147.

SMITH, D.V. (2005). The state of the art of geophysics and karst: a general literature review. – In: KUNIANSKY, E.L. (Ed.): U.S. Geological Survey Karst Interest Group proceedings: USGS Scientific Investigations Report, Sept. 12–15, 296 pp., Rapid City, South Dakota.

SLABE, T. (1995): Cave Rocky Relief and its Speleogenetical Significance. – Zbirka ZRC, **10**, 128 pp., Ljubljana (Založba ZRC).

SLOB, E., SATO, M. & OLHOEFT, G. (2010): Surface and borehole ground-penetrating-radar developments. – Geophysics, **75** (5): 103–120.

SONG, K.-I., CHO, G.-C. & CHANG, S.-B. (2012): Identification, remediation, and analysis of karst sinkholes in the longest railroad tunnel in South Korea. – Eng. Geol., **135–136**: 92–105.

SOWERS, G.F. (1996): Building on Sinkholes. Design and Construction of Foundations in Karst Terrain. – 202 pp., Reston (ASCE Press).

STEEPLES, D.W. & MILLER, R.D. (1990): Seismic reflection methods applied to engineering, environmental, and groundwater problems. – In: WARD, S.H. (Ed.): Geotechnical and Environmental Geophysics: 1–30 (Society of Exploration Geophysicists).

STEFANELLI, P., CARMISCIANO, C., CARATORI TONTINI, F., COCCHI, L., BEVERINI, N., FIDECARO, F. & EMBRIACO, D. (2008): Microgravity vertical gradient measurement in the site of Virgo interferometric antenna (Pisa Plain, Italy). – Annals of Geophysics, **51** (5–6): 877–886.

STUMMER, P., MAURER, H. & GREEN, A.G. (2004): Experimental design: Electrical resistivity data sets that provide optimum subsurface information. – Geophysics, **69**: 120–139.

ŠUMANOVAC, F. & WEISSER, M. (2001): Evaluation of resistivity and seismic methods for hydrogeological mapping in karst terrains. – J. Appl. Geophys., **47**: 13–28.

TELFORD, W.M., GELDART, L.P. & SHERIFF, R.E. (1990): Applied Geophysics. – 2nd ed., 770 pp., Cambridge (Cambridge University Press).

THIENERT, C. & LEISMANN, F. (2015): Auswirkungen von Karst-Hohlräumen auf die Bemessung von Tunneln. – In: PULSFORT, M. (Ed.): Festschrift anlässlich des 60. Geburtstages von Matthias Pulsfort: Berichte des Lehr- und Forschungsgebietes Geotechnik, **34**: 73–84, Bergische Universität Wuppertal.

THIENERT, C., DOMBROWSKI, B., LEISMANN, F. & MALKUS, J. (2016): Anforderungen an die Erkundung von Karst-Hohlräumen. – 8 pp.

THIERRY, P., DEBEBLIA, N. & BITRI, A. (2005): Geophysical and geological characterization of karst hazards in urban environments: application to Orleáns (France). – Bull. Eng. Geol. Environ., **64**: 139–150.

ULUSAY, R. (2015): The ISRM Suggested Methods for Rock Characterization, Testing and Monitoring: 2007–2014. – 293 pp., Switzerland (Springer).

VADILLO, I., BENAVENTE, J., NEUKUM, C., GRÜTZNER, C., CARRASCO, F., AZZAM, R., LIÑÁN, C. & REICHERTER, K. (2012): Surface geophysics and borehole inspection as an aid to characterizing karst voids and vadose ventilation patterns (Nerja research site, S. Spain). – J. Appl. Geophys., **82**: 153–162.

VAN DER PLUIJM, B.A. & MARSHAK, S. (2003): Earth structure. An Introduction to Structural Geology and Tectonics. – 2nd ed., 672 pp. (WW Norton & Company).

VAN SCHOOR, M. (2002): Detection of sinkholes using 2D electrical resistivity imaging. – J. Appl. Geophys., **50**: 393–399.

VOUILLAMOZ, J.M., LEGCHENKO, A., ALBOUY, Y., BAKALOWICZ, M., BALTASSAT, J.M. & AL-FARES, W. (2003): Localization of saturated karst aquifer with magnetic resonance sounding and resistivity imagery. – Ground Water, **41** (5): 578–586.

WAGNER, H., HANDKE, D., MATTER, J., FABBRI, D. & KEIPER, K. (2009): Concepts to overcome squeezing geological conditions at the Koralm tunnel. – Geomechanics and Tunnelling, **2** (5): 601–611.

WALTHAM, A.C. (1971): Controlling factors in the development of caves. – Transactions of the Cave Research Group of Great Britain, **13** (2): 73–80.

WALTHAM, A.C. & FOOKES, P.G. (2003): Engineering classification of karst ground conditions. – Q. J. Eng. Geol. Hydrogeol., **36**: 101–118.

WALTHAM, T., BELL, F.G. & CULSHAW, M.G. (2005): Sinkholes and Subsidence. Karst and Cavernous Rocks in Engineering and Construction. – 384 pp., Chichester, UK (Springer–Praxis Publishing).

WHITE, W.B. (1977a): The role of solution kinetics in the development of karst aquifers. – In: TOLSON, J.S. & DOYLE, F.L. (Eds.): Karst Hydrogeology: International Association of Hydrogeologists, Memoir **12**: 503–517, Huntsville, Alabama (UAH Press).

WHITE, W.B. (1977b): Conceptual models for carbonate aquifers: revisited. – In: DILAMARTER, R.R. & CSALLANY, S.C. (Eds.): Hydrologic Problems in Karst Regions: 176–187, Bowling Green, Western Kentucky (Western Kentucky University Press).

WHITE, W.B. (1988): Geomorphology and Hydrology of Karst Terrains. – 464 pp., New York (Oxford University Press).

WHITE, W.B. (2002): Karst hydrology: recent developments and open questions. – Eng. Geol., **65**: 85–105.

WILKINSON, P.B., CHAMBERS, J.E., LELLIOTT, M., WEALTHALL, G.P. & OGILVY, R.D. (2008): Extreme sensitivity of crosshole electrical resistivity tomography measurements to geometric errors. – Geophys. J. Int., **173** (1): 49–62.

WILKINSON, P.B., CHAMBERS, J.E., MELDRUM, P.I., GUNN, D.A., OGILVY, R.D. & KURAS, O. (2010): Predicting the movements of permanently installed electrodes on an active landslide using time-lapse geoelectrical resistivity data only. – Geophys. J. Int., **183** (2): 543–556.

WILKINSON, P.B., LOKE, M.H., MELDRUM, P.I., CHAMBERS, J.E., KURAS, O., GUNN, D.A. & OGILVY, R.D. (2012): Practical aspects of applied optimized survey design for electrical resistivity tomography. – Geophys. J. Int., **189** (1): 428–440.

WISEN, R., AUKEN, E. & DAHLIN, T. (2005): Combination of 1D laterally constrained inversion and smooth inversion of resistivity data with a priori data from boreholes. – Near Surface Geophysics, **3** (2): 71–78.

WITTHÜSER, K. (2002): Untersuchungen zum Stofftransport in geklüfteten Festgesteinen unter besonderer Berücksichtigung der Matrixdiffusion. – Schr. Angew. Geol. Karlsruhe, **64**, 145 pp.

WIWATTANACHANG, N. & GIAO, P.H. (2011): Monitoring crack development in fiber concrete beam by using electrical resistivity imaging. – J. Appl. Geophys., **75** (2): 294–304.

XU, Y., CHEN, Z., ZUO, C. & LUO, L. (2013): Research on the mechanism of Karst Disaster and Risk Reduction of Carbonate Buried Tunnel in Fault Zone. – 10 pp., Wuhan, China.

YASSIN, R.R., MUHAMMAD, R.F., TAIB, S.H. & AL-KOURI, O. (2014): Application of ERT and Aerial Photographs Techniques to Identify the Consequences of Sinkholes Hazards in Constructing Housing Complexes Sites over Karstic Carbonate Bedrock in Perak, Peninsular Malaysia. – J. Geogr. Geol., **6** (3): 55–89.

YILMAZ, O. (2001): Seismic data analysis. Processing, Inversion and Interpretation of Seismic Data. – 2nd ed., 2065 pp. (Society of Exploration Geophysicists).

YOUSSEF, A.M., EL-KALIOUBY, H.M. & ZABRAMAWI, Y.A. (2012a): Integration of remote sensing and electrical resistivity methods in sinkhole investigation in Saudi Arabia. – J. Appl. Geophys., **87**: 28–39.

YOUSSEF, A.M., EL-KALIOUBY, H.M. & ZABRAMAWI, Y.A. (2012b): Sinkhole detection using electrical resistivity tomography in Saudi Arabia. – J. Geophys. Eng., **9**: 655–663.

ZHAO, Y., LI, P. & TIAN, S. (2013): Prevention and treatment technologies of railway tunnel water inrush and mud gushing in China. – J. of Rock Mechanics and Geotechnical Engineering, **5**: 468–477.

ZHOU, B. & DAHLIN, T. (2003): Properties and effects of measurement errors on 2D resistivity imaging surveying. – Near Surface Geophysics, **1** (3): 105–117.

ZHOU, W. & BECK, B.F. (2011): Engineering Issues on Karst. – In: VAN BEYNEN, P.E. (Ed.): Karst Management: 9–45, New York (Springer).

ZHOU, W., BECK, B.F. & STEPHENSON, J.B. (2000): Reliability of dipole-dipole electrical resistivity tomography for defining depth to bedrock in covered karst terranes. – Environ. Geol., **39** (7): 760–766.

ZHOU, W., BECK, B.F. & ADAMS, A.L. (2002): Effective electrode array in mapping karst hazards in electrical resistivity tomography. – Environ. Geol., **42**: 922–928.

ZHU, J., CURRENS, J.C. & DINGER, J.S. (2011): Challenges of using electrical resistivity method to locate karst conduits – A field case in the Inner Bluegrass Region, Kentucky. – J. Appl. Geophys., **75**: 523–530.

ZISMAN, E.D. (2001): Application of a standard method of sinkhole detection in the Tampa, Florida, area. – In: BECK, B.F. & HERRING, J.G. (Eds.): Geotechnical and Environmental Applications of Karst Geology and Hydrology: 187–192, Lisse, Netherlands (Balkema).

9.2. URL references

www-01: http://www.vdhk.de/ueber-hoehlen/karst-in-deutschland.html, accessed on 15.02.2016.

www-02: http://www.tiefenhoehle.de, accessed on 27.02.2016.

www-03: http://web.env.auckland.ac.nz/our_research/karst/, accessed on 03.06.2016.

Appendix

Appendix A.1. Overview of the new high-speed railway line Wendlingen–Ulm (in German, DB Projekt Stuttgart–Ulm GmbH © 2015).

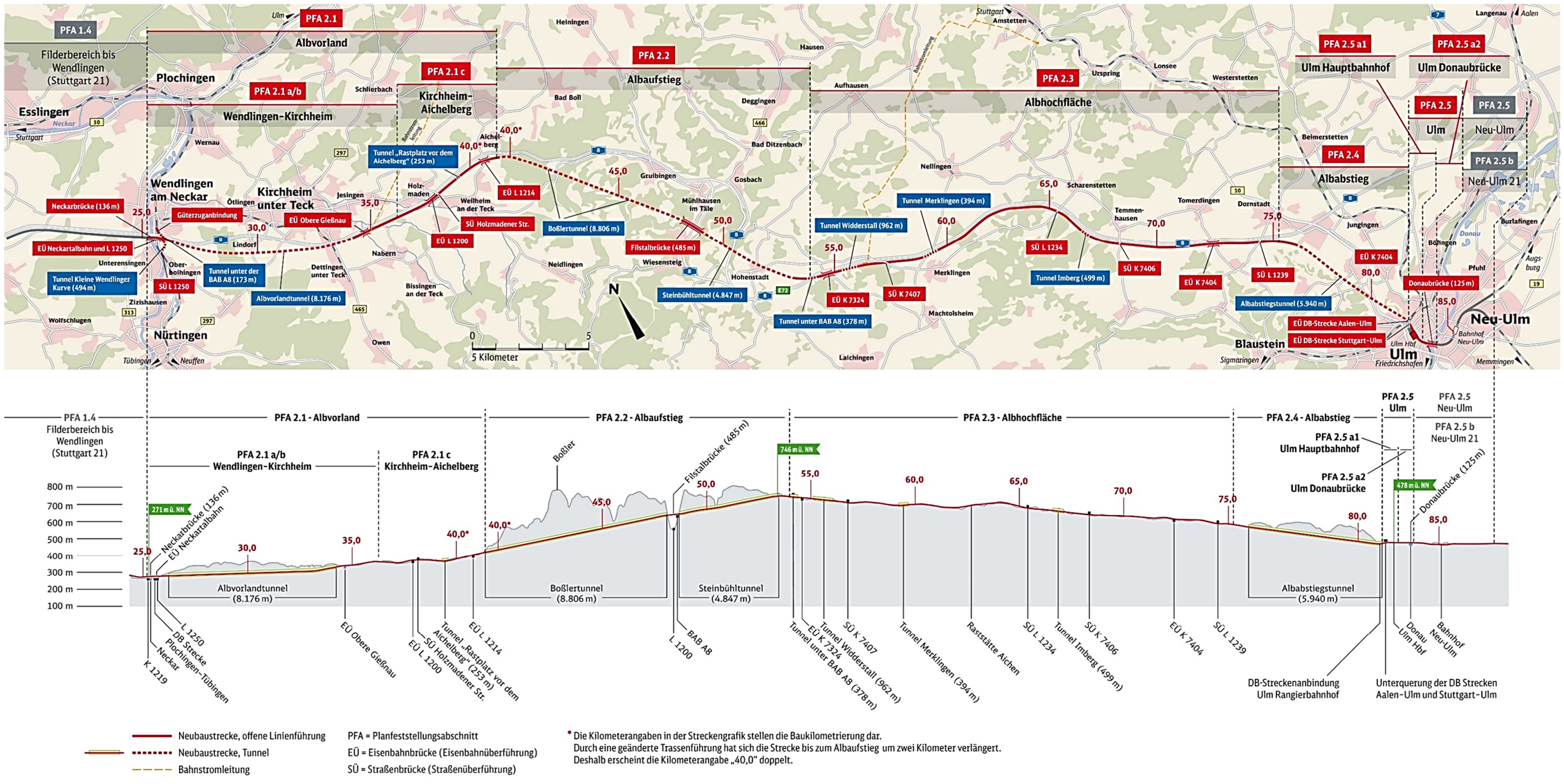

Neubaustrecke, offene Linienführung
Neubaustrecke, Tunnel
Bahnstromleitung

PFA = Planfeststellungsabschnitt
EÜ = Eisenbahnbrücke (Eisenbahnüberführung)
SÜ = Straßenbrücke (Straßenüberführung)

* Die Kilometerangaben in der Streckengrafik stellen die Baukilometrierung dar.
Durch eine geänderte Trassenführung hat sich die Strecke bis zum Albaufstieg um zwei Kilometer verlängert.
Deshalb erscheint die Kilometerangabe „40,0" doppelt.

Appendix A.2. Enlarged interpreted 2.5D ERT results, obtained from the three 60 m long profiles P01, P03 and P05 of chapter 7.3 (Prins et al. 2019).